Motility of Swimming Bacteria

Hydrodynamics and Statistics

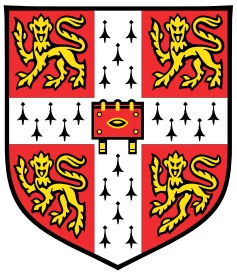

Christian Esparza López

Department of Applied Mathematics and Theoretical Physics
University of Cambridge

This dissertation is submitted for the degree of
Doctor of Philosophy

Churchill College May 2021

I would like to dedicate this thesis to my loving parents who have always offered me their unconditional support.

Declaration

This dissertation is the result of my own work and includes nothing which is the outcome of work done in collaboration except as declared below and specified in the text. It is not substantially the same as any that I have submitted, or, is being concurrently submitted for a degree or diploma or other qualification at the University of Cambridge or any other University or similar institution except as declared below and specified in the text. I further state that no substantial part of my thesis has already been submitted, or, is being concurrently submitted for any such degree, diploma or other qualification at the University of Cambridge or any other University or similar institution except as declared below and specified in the text. It does not exceed the prescribed word limit for the relevant Degree Committee.

Chapter 3 is an adaptation of C. Esparza López and E. Lauga, "Hydrodynamic model for *Spiroplasma* motility", Phys. Rev. Fluids **5**, 093102 (2020). The author of this thesis is also the primary investigator an author of this paper.

Chapter 4 is an adaptation of the manuscript C. Esparza López, J. Gonzalez-Gutierrez, F. Solorio-Ordaz, E. Lauga and R. Zenit, "Dynamics of a helical swimmer crossing viscosity gradients", arXiv:2012.04788 [physics.flu-dyn] (2020). A revised version of this manuscript has been submitted to Physical Review Fluids and is currently being considered for publication. The author of this thesis is also the author of the theoretical modelling in this manuscript. The experimental work was done at the National University of Mexico (UNAM) by Jorge Gonzalez under the supervision of Roberto Zenit at Brown University.

Chapter 5 is an adaptation of C. Esparza López, A. Théry and E. Lauga, "A stochastic model for bacteria-driven micro-swimmers", Soft Matter **15**, 2605-2616 (2019). The author of this thesis is also the primary investigator an author of this paper.

The work in Chapter 6 is being prepared for submission. The author of this thesis is the primary investigator and author of this manuscript.

Chapter 1 contains extracts from the introductory material of each of the above articles.

Christian Esparza López
May 2021

Motility of Swimming Bacteria
Hydrodynamics and Statistics

Christian Esparza López

The present work contains original research on the field of biophysics, specifically the study of swimming bacteria. Swimming microorganisms can be modeled as active particles moving at low Reynolds number ($Re \ll 1$) and subject to different sources of noise. The term "active" means that they are self-propelled, while $Re \ll 1$ implies that their motion is dominated by viscous stresses, therefore relying on non-reciprocal deformations in time, in order to achieve movement. Noise arises from thermal fluctuations and the inherent stochasticity of their propelling machinery, as a result, bacteria follow random trajectories. Nevertheless, bacteria have evolved to display a number of strategies to overcome randomness and achieve directed locomotion, known as "taxis". Here, we explore the mechanisms involved in the propulsion and navigation of swimming bacteria, using low Reynolds number flow techniques and random walks.

First, we introduce the physical principles that govern the dynamics of a low Reynolds number swimmer. We pay special attention to the random walk model for the description of the swimming trajectories, since it allows to quantify motility in terms of statistical measures, such as diffusivity and drift velocity, which can be measured experimentally. After a general discussion of the model, we demonstrate its use by applying it to the dynamics of bacteria-driven microswimmers, which are active particles that use bacteria as a propulsion mechanism. We show in particular, that the diffusivity of such particles increases with the square of their size and that the microswimmers inherit the chemotactic capabilities from the bacteria that propel them. These results are in agreement with experiments and can be useful to improve the design of these artificial microswimmers.

Next, we investigate the motility properties of *Spiroplasma melliferum*, which is special among bacteria, as it can swim without flagella. Instead, *Spiroplasma* can switch the handedness of its helical body and in the process, the helical domains rotate generating propulsion. Based on experimental observations, we develop a hydrodynamic model to describe *Spiroplasma* motility. We obtain expressions for the total linear and angular displacements of the cell body per swimming stroke. Observing that the cell body does not reorient at the end of one period, we define an effective swimming speed and a hydrodynamic efficiency. Then, we show that the helical shape that maximises speed and efficiency has a pitch angle close to that of *Spiroplasma*, $\phi \simeq 35°$, in agreement with experimental observations and with previous numerical simulations.

Finally, we explore the dynamics of a low Reynolds number swimmer crossing a viscosity gradient. This is a work in collaboration with experimental groups in the National University of Mexico (UNAM) and Brown University. The experiments aim to shed light on the dynamics of the bacterium Helicobacter pylori, which inhabits the human gut and is capable of penetrating the mucus layer that protects the stomach. Experimentally, a magnetic swimmer is immersed in a stratified solution of miscible fluids with different viscosities. The swimmer consists of a helical tail and a cylindrical head that rotate at a fixed rate due to the action of an external magnetic field. As the swimmer advances, it accelerates or slows down, depending on its orientation with respect to the gradient. In general, the experimental results show that it is harder for a pusher-like swimmer to swim up the gradient, whereas for a puller-like swimmer it is the opposite. We rationalize this mathematically by assuming that the forces acting on the swimmer depend on the local viscosity that it experiences. This allows us to calculate the swimming speed as a function of the swimmer's position along the gradient. The predictions of the model are in good agreement with the experimental observations. The results also suggest that viscotaxis is possible without viscoreceptors, and in fact governed solely by the motility pattern of the swimmer.

Together, the results presented in this thesis contribute to the understanding of bacterial motility and low Reynolds number swimmers in general. Furthermore, these results may be useful for future developments in biophysics, including applications to targeted drug delivery and microrobotics.

Acknowledgements

I would like to thank all those who have supported me during my time at the University of Cambridge. I am especially grateful to Eric Lauga, I consider myself lucky to have had him as my supervisor. I would like to thank my collaborators Roberto Zenit and Jorge González; my friends and colleagues at DAMTP, in particular Albane Théry, Debasish Das, Mariia Dvoriashyna, Davide Parise, Øyvind Borthne and Loren Held; my friends at the University: Guillermo Caballero, Paola Velasco, Alejandro Guizar, Mauro Velasco, Fernando León, Harris Farooq, Christiane Goßen, and the mexican society. I am also thankful to my old friends: Alfonso Libreros, Sergio Mayesell and especially Ana Vásquez for always being there when I needed a friend. Finally, I would like to thank Sol Lim for her infinite patience and love.

My work has been funded by the European Research Council (ERC) under the European Union's Horizon 2020 research and innovation programme (grant agreement 682754 to EL).

Table of contents

List of figures **xv**

List of tables **xvii**

1 Introduction **1**
1.1 Low-*Re* swimming 1
1.2 Swimming without flagella 2
1.3 Swimming across viscosity gradients 4
1.4 Bacteria-driven microswimmers 6
1.5 Near-surface bacterial chemotaxis 8

2 Physics of Low-*Re* swimming **11**
2.1 Hydrodynamics of Low-*Re* Swimming 11
2.1.1 Stokes Equations of Creeping Flow 11
2.1.2 Flagellar swimming 13
2.1.2.1 The fundamental solution of Stokes equations 13
2.1.2.2 Resistive-force theory 14
2.2 Statistical aspects of Low-*Re* Swimming 16
2.2.1 Run-and-tumble 17
2.2.1.1 Diffusion 17
2.2.2 Bacterial chemotaxis 18
2.2.3 Thermal fluctuations 19
2.2.4 Generality of the model 21

3 *Spiroplasma* Motility **23**
3.1 Introduction 23
3.2 Setup and model 24
3.2.1 Geometry and notation 24
3.2.2 Dynamics 25

3.2.3 Swimming stroke . . . 27
3.2.3.1 First stage . . . 28
3.2.3.2 Second stage . . . 30
3.2.3.3 Third stage . . . 31
3.2.4 Helical geometry: Coarse-grained model . . . 31
3.2.4.1 Helical propulsion . . . 31
3.2.4.2 Effective drag ratio . . . 32
3.3 Planar motion, no helical geometry . . . 35
3.3.1 Kinematics . . . 35
3.3.2 No net rotation . . . 37
3.3.3 Swimming speed and efficiency . . . 37
3.4 Planar motion, bistable helix . . . 40
3.5 Asymptotic and numerical results . . . 42
3.6 Discussion . . . 44

4 Swimming Across Viscosity Gradients 49
4.1 Introduction . . . 49
4.2 Experimental setup . . . 50
4.2.1 Evolution of the viscosity gradient in time . . . 52
4.2.2 Four different swimmer-viscosity interactions . . . 53
4.3 Experimental results . . . 55
4.3.1 Case I: Head-first, positive viscosity gradient . . . 55
4.3.2 Case II: Tail-first, positive viscosity gradient . . . 56
4.3.3 Case III: Head-first, negative viscosity gradient . . . 57
4.3.4 Case IV: Tail-first, negative viscosity gradient . . . 58
4.4 Discrete interface model . . . 59
4.4.1 Sharp viscosity gradient . . . 60
4.4.2 Head-first interaction . . . 61
4.4.2.1 Head crossing . . . 61
4.4.2.2 Tail crossing . . . 63
4.4.2.3 Summary . . . 63
4.4.3 Swimmer position . . . 64
4.4.4 Buoyancy . . . 65
4.5 Continuous interface model . . . 66
4.5.1 Head-first vs tail-forward approach . . . 68
4.5.2 Model predictions: Parameter dependence . . . 68
4.6 Comparison with experiments . . . 73

4.6.1 Low to high viscosity . . . 73
4.6.2 High to low viscosity . . . 76
4.7 Conclusions . . . 80

5 Diffusion and Chemotaxis of Bacteria-Driven Micro-swimmers 83
5.1 Introduction . . . 83
5.2 Mathematical model and numerical simulations . . . 84
5.2.1 Micro-swimmers in homogeneous environments . . . 84
5.2.2 Run-and-tumble dynamics . . . 87
5.2.3 Chemotaxis of bacteria-driven microswimmers . . . 88
5.3 Theoretical and numerical results . . . 89
5.3.1 Three-dimensional trajectories of bacteria-driven microswimmers . . . 89
5.3.2 Coarse-grained modelling . . . 91
5.3.2.1 Effective speed . . . 93
5.3.2.2 Rotational diffusion coefficient . . . 94
5.3.2.3 Long-time diffusion of bacteria-driven microswimmers . . . 98
5.3.3 Chemotaxis of bacteria-driven microswimmers . . . 99
5.3.3.1 Chemotactic drift speed . . . 100
5.4 Discussion . . . 103

6 Near-surface run-and-tumble 105
6.1 Introduction . . . 105
6.2 Free-swimming run-and-tumble . . . 106
6.2.1 Equations of Motion . . . 106
6.2.2 The generalised Fokker–Planck equation . . . 107
6.2.2.1 Run-and-tumble diffusion . . . 109
6.3 Run-and-tumble chemotaxis . . . 111
6.3.1 Non-adaptive chemotaxis . . . 112
6.3.2 Adaptive chemotaxis . . . 114
6.4 Run-and-tumble near boundaries . . . 117
6.4.1 Diffusion . . . 117
6.4.2 Chemotaxis . . . 119
6.5 Discussion . . . 122

7 Conclusions 129
7.1 Summary . . . 129
7.2 Outlook: Run-and-tumble models for higher organisms . . . 134

7.3 Conclusions 137

References **141**

List of figures

1.1 *Spiroplasma* swimming gait 3
1.2 Conceptual design of bacteria-driven microswimmer 7

2.1 Microswimmer mode classification 13

3.1 *Spiroplasma* geometry 25
3.2 Schematics of *Spiroplasma* motility 26
3.3 *Spiroplasma* swimming stroke, first stage 27
3.4 *Spiroplasma* swimming stroke, second stage 29
3.5 Continuity condition at the kink of a bistable helix 33
3.6 No net rotation on *spiroplasma* swimming stroke 38
3.7 *Spiroplasma* swimming trajectory 40
3.8 Symmetries in *spiroplasma* motility 41
3.9 *Spiroplasma* swimming speed and hydrodynamic efficiency 43

4.1 Swimming across viscosity gradients, experimental setup 51
4.2 Diffuse viscosity profile 53
4.3 Swimmer-viscosity interaction configurations 54
4.4 Case I: pusher swimming up the viscosity gradient 56
4.5 Case I: swimmer's position and speed 56
4.6 Case II: puller swimming up the viscosity gradient 57
4.7 Case II: swimmer's position and speed 57
4.8 Case III: pusher swimming down the viscosity gradient 58
4.9 Case III: swimmer's position and speed 58
4.10 Case IV: puller swimming down the viscosity gradient 59
4.11 Case IV: swimmer's position and speed 59
4.12 Helical swimmer crossing a sharp viscosity gradient 61
4.13 Helical swimmer crossing a continuous viscosity gradient 67
4.14 Swimming speed in a linear viscosity gradient 70

4.15 Swimming speed and position in a diffusive viscosity gradient 71
4.16 Swimming speed and position dependence on viscosity ratio 72
4.17 Swimming speed and position dependence on tail to head size ratio 74
4.18 Case I: comparison with experiments 75
4.19 Case II: comparison with experiments 76
4.20 Viscous entrainment 77
4.21 Case III: comparison with experiments 78
4.22 Case IV: comparison with experiments 79

5.1 Bacteria-driven microswimmer 84
5.2 Location and orientation of each bacterium on the surface of the bacteria-driven microswimmer 85
5.3 Run-and-tumble as a two-state Markov chain 86
5.4 Typical trajectories of bacteria-driven microswimmers 90
5.5 Bacteria-driven microswimmers coarse-grain trajectories 92
5.6 Mean squared displacement of bacteria-driven microswimmers 97
5.7 Velocity correlation function of a bacteria-driven microswimmer 99
5.8 Effective diffusion coefficient of bacteria-driven microswimmers 100
5.9 Drift speed of bacteria-driven microswimmers as a function of the bead radius 101
5.10 Drift speed of bacteria-driven microswimmers as a function of the gradient intensity 102

6.1 Two-dimensional run-and-tumble 107
6.2 Run-and-Tumble pattern for a circle swimmer 117
6.3 Chemotactic drift for circle swimming RTPs 123
6.4 Down gradient bias for a circle swimming RTP 123

7.1 Run-and-tumble particle geodesic displacement on a spherical surface . . . 132
7.2 Run-and-tumble particle chemotaxis on a spherical surface 133
7.3 The nematode *Caenorhabditis elegans* 134
7.4 Behavioral mechanisms in *C. elegans* and *E. coli* chemotaxis 136

List of tables

4.1 The four possible swimmer-viscosity interactions 54

Chapter 1

Introduction

1.1 Low-*Re* swimming

For a microorganism, locomotion is essential for a number of tasks, such as foraging, escaping predators or moving away from harmful environments [1]. Swimming microorganisms have to overcome physical constrains in order to move effectively. For starters, they are found in liquid environments and their world may appear strange to our everyday experience. This is the realm of low Reynolds number (*Re*) flow, where inertia is negligible and viscous forces dominate. The strategies to achieve locomotion in such an environment are different from those we know for macroscopic swimming creatures. In particular, a small organism such as a bacterium must move in a non-reciprocal fashion (i.e. its motion is different when observed forward in time as compared to backwards in time) in order to achieve net locomotion [2].

A natural way to achieve non-reciprocal deformation is by propagating waves [3]. Indeed, most swimming microorganisms have evolved to grow slender appendages called flagella, that can be deformed into flexible waves or rotated in apparent waves [4–6]. In fact, flagellar locomotion is known to be among the most efficient ones when it comes to low-*Re* swimming [5, 7–10]. Therefore, scientist have tried to replicate flagellar motion in the design of artificial microswimmers, either by fabricating chiral microstructures [11–14] or by integrating biological systems and inorganic devices [15–25].

Another important constrain is the fact that fluctuations are significant at small scales. Swimming cells are subject to different sources of noise such as thermal fluctuations and variations in the distribution and sizes of their flagella. As a result, the trajectory of a swimming cell appears erratic, very much like a passive particle undergoing Brownian motion [26]. Nevertheless, swimming cells have evolved to display a number of strategies to overcome randomness and achieve directed locomotion, known as “taxis”. For example, the bacterium *Escherichia coli*, which is probably the most studied and understood microorganism on

Earth [9, 27], is capable of responding to chemical stimuli [28]. This is known as chemotaxis, and is essential for the successful colonisation of a host [29, 30].

Among low-*Re* swimmers, bacteria are of particular importance for the scientific community. Firstly, the recent decrease in novel antibiotics and the spread of multidrug-resistant bacteria are of great economic and health concern. Since infectivity is known to be strongly correlated to flagellar motility, understanding bacterial motility in depth may lead to the development of new anti-infectious drugs [29]. Secondly, from the engineering perspective, bacteria represent a paradigm for the design of micromachines [18, 31]. A bacterium is not only capable of self-powered locomotion, it can also perform complex tasks such as self-replication, cargo transport and respond to external stimuli such as light and temperature [32]. Finally, from a fundamental point of view, swimming bacteria constitute a model system for active matter and far from equilibrium thermodynamics [31, 33, 34].

The work presented here addresses both aspects of bacterial motility, hydrodynamics and statistics. A general discussion of the fundamental physical principles that govern swimming at low *Re* is given in Chapter 2. The following two chapters are dedicated to the study of bacterial propulsion using hydrodynamic models. The second part of the thesis on the other hand, focuses on the statistical aspects of bacterial locomotion, particularly diffusion and chemotaxis. Although Chapters 3 and 4 are concerned mainly with the propulsion mechanisms of swimming bacteria, the results offer insight on the physics behind taxis techniques displayed by different bacteria. Similarly, Chapters 5 and 6 focus on the statistical aspects of bacterial motility, but they build on the hydrodynamic constrains of bacterial locomotion.

I have done most of the work independently, except for the study on Chapter 4, which is the result of a collaboration with the experimental groups of Jorge Gonzalez-Gutierrez at the National University of Mexico (UNAM) and Roberto Zenit at Brown University. The expressions for the diffusivity and the swimming speed of bacteria-driven microswimmers in Chapter 5 were previously derived by Albane Théry during a research internship at the University of Cambridge. These results were used as validation for the results here presented. Therefore, in what follows I use the author's we for convenience. In the rest of this chapter, we introduce the different model systems studied in this thesis.

1.2 Swimming without flagella

Many species of bacteria, such as *Escherichia coli* (*E. coli*), use helical flagellar filaments and rotate them along their axes. As a result, the helical filaments push on the surrounding fluid and generate propulsion in the opposite direction [9]. There exist however some bacteria that do not rely on flagella to achieve locomotion. This is the case of the marine bacterium

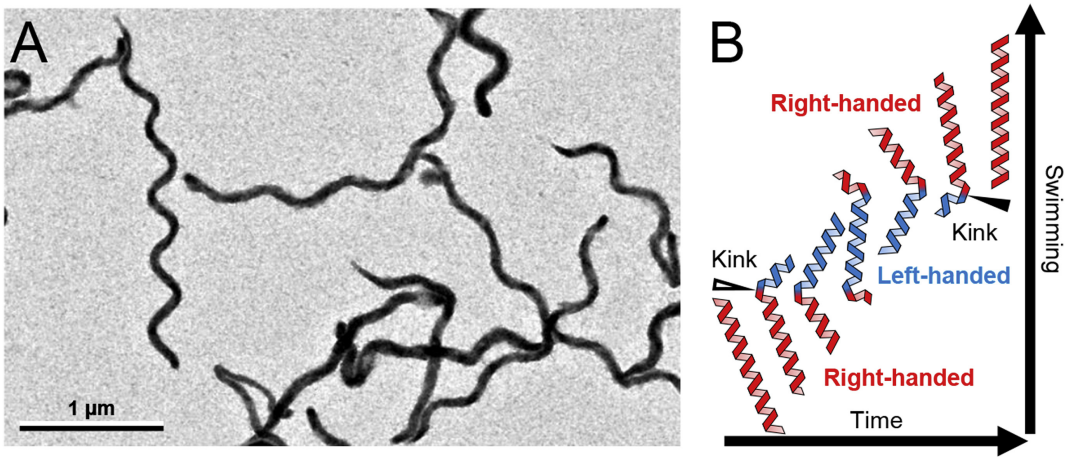

Fig. 1.1 *Spiroplasma* swimming gait. (A) Electron microscopy of the bacterium *Spiroplasma eriocheiris*. (B) Swimming gait, the bacterium changes from a right-handed to a left-handed helical configuration. A kink propagates along the body and the different helical domains rotate in opposite senses propelling the bacterium in the opposite direction to the kink. Reproduced and adapted from [51].

Synechococcus, whose swimming strategy is still under debate [35, 36], and the better known *Spiroplasma* which swims by deforming its helical body [37, 38] (see illustration in Fig. 1.1).

As opposed to the *Spirochetes*, which have internal flagella [39], *Spiroplasma* is a wall-less bacterium (termed a mollicute) with an internal, flexible flat ribbon cytoskeleton. The cell deforms its cytoskeleton into a helix whose chirality is allowed to progressively shift [40–47]. The change in geometry gives rise to a wall domain, *i.e.* a kink, which propagates along the cell body from one end to the other. The chirality is then reverted in a similar fashion completing a swimming stroke [38, 48–50]. The whole deformation is non-reciprocal, therefore movement at low Reynolds number is possible, and indeed, the bacterium is observed to move in the direction opposite to the kink pair propagation.

The cell body has a definite polarity, as one of its ends is tapered, usually called the tip (or head) while the other untapered end is termed the tail. It has been observed that kinks appear most of the times at the tip [46]. As a consequence, *Spiroplasma* swims predominantly in the direction of the head. The morphological change is stochastic in nature and the motion of the kinks is altered by the presence of different amino acids [46, 52, 53]. Analogously to the well-studied *E. coli* chemotaxis [9], modulation of the rate of chirality transformations allows *Spiroplasma* to follow chemical concentration gradients. However, studies have yet to discover the genes involved [46], and therefore the precise mechanism that controls chemotaxis remains unclear.

Hydrodynamic models used to describe the locomotion of *Spiroplasma* motility have been previously developed [48–50]. These studies show three main results: (i) the cell moves in the

direction opposite to the kink pair propagation, with a speed proportional to the kink speed; (ii) the helical pitch of *Spiroplasma* (angle $\phi \simeq 35^\circ$) maximises the hydrodynamic swimming efficiency; and (iii) at the optimum pitch angle, the inter-kink distance that maximises the swimming speed is $D/L \approx 1/3$ [48–50], where L is the total axial length of the helical cell. These results are obtained mostly numerically and were supported by theoretical predictions using some fitting parameters.

In Chapter 3 we propose a hydrodynamic model to describe *Spiroplasma* motility. By coarse-graining the geometry of the cell body, we avoid the use of fitting parameters and unveil an underlying symmetry of the bacterium swimming gait. We show mathematically that the cell body does not reorient at the end of one period, which allows us to define an effective swimming speed, v_s. We then use v_s to calculate the energy dissipated in one stroke, $\dot{W}$, and to define a hydrodynamic efficiency, $\eta = \dot{W}_0/\dot{W}$, where $\dot{W}_0$ is the power spent by a straight filament moving at the same speed v_s. We show that the helical shape of the cytoskeleton that maximises both v_s and η are helices of pitch angles ϕ close to that of *Spiroplasma*, $\phi \simeq 35^\circ$, in agreement with experimental observations and with previous numerical simulations.

1.3 Swimming across viscosity gradients

Taxis is the capability of biological cells to respond to an external stimulus, such as light or chemical gradients, and as a result move towards or away from it [32]. In nature, the adaptability of microorganisms to respond to a variety of cues has been demonstrated in gradients of light intensity (phototaxis) [54–58], magnetic fields (magnetotaxis) [59–61], temperature (thermotaxis) [62–64], a gravitational potential (gravitaxis) [65–67] and chemical stimuli (chemotaxis) [68].

A mechanical example of taxis, viscotaxis, emerges when a cell adapts its motion in response to viscosity gradients. Some microorganisms, such as *Spiroplasma* [52] and *Leptospira interrogans* [69–71], have indeed the ability to respond to changes in viscosity. A particularly important example for human health is the colonization of the stomach by the bacterium *Helicobacter pylori*, which turns out to be a consequence of the ability to move in viscosity gradients [72, 73]. Indeed, *H. pylori* is the only known bacteria to be capable of penetrating the intestinal mucus layer and reach the stomach wall [72, 73], thanks to an enzymatic degradation of the stomach mucosa [31, 74]. This leads to severe inflammation that can result in ulcerogenesis or neoplasia. Since the bacterium infects about 50% of the human population it is important to understand its pathogenesis [75].

Some understanding already exists on the impact of viscosity gradients on the dynamics

of both passive and active (swimming) particles. For example, through cross-streamline migration in viscosity gradients, it is possible to sort soft passive particles in microflows [76]. Heated particles create temperature gradients, which induce local variations in viscosity in the surroundings of the particle [77]. For simple swimmers composed of a small number of active spheres, viscotaxis has been recently shown to arise from a mismatch in the viscous forces acting on the different parts of the swimmer, allowing both positive and negative viscotaxis in Newtonian fluids [78]. Although that mechanism does not account for the possible existence of biological viscoreceptors [79], the positive viscotaxis in *Spiroplasma* [52] and *Leptospira* [69–71] can be explained in these terms.

Using the classical squirmer model microswimmer [80–82], work coupling the concentration of nutrients to the viscosity of the fluid showed qualitative differences in the dynamics of swimming, in contrast to fluids with constant viscosity [83]. The squirmer model has also allowed to study theoretically the effect of weak viscosity gradients on the motion of general spherical swimmers, showing in particular how the swimmer 'mode' (i.e. whether the swimmer acts as a pusher or a puller in the far field, [see §2.1]) is critical in setting the sign of the viscotaxis response [84]. However, and despite a good understanding of locomotion of bacteria in Newtonian fluids [85], a theory that explains how viscosity gradients affect the swimming of helical swimmers is currently not available.

Synthetic swimmers have often been proposed as one modelling approach to study the motility of microorganisms. Self-phoretic Janus colloids, for example, can be made to move through the generation of chemical, electrostatic or thermal gradients [86]. Another example are helical swimmers, which typically consist of a rigid magnetic head fixed to a metallic helical tail [13]. The whole body is made to rotate by an external magnetic field, propulsion arises as a result of the chirality of the helical tail, in close analogy to the swimming of flagellated bacteria, e.g. *E. coli* [9]. Synthetic helical swimmers preserve the basic physical characteristics that allow locomotion in low–Re environments. Specially the coupling between rotation and translation. Under this framework, many control parameters can be explored experimentally to quantify the swimming motion in complex environments [87, 88].

In Chapter 4 we present a joint theoretical-experimental study that explores the dynamics of a low-*Re* swimmer moving in a fluid of variable viscosity. This is the result of a collaboration with experimental groups at UNAM and Brown University. Experimentally, a linear viscosity gradient is prepared by superposing two miscible fluids and a helical swimmer is made to move perpendicular to the initial fluid-fluid interface. It is observed that the swimmer slows down or accelerates as it crosses the gradient, depending on its orientation. We propose a hydrodynamic model to explain the dynamics. Assuming that the classical resistive-force theory of slender filaments is locally valid along the helical propeller, we

calculate the swimming speed as a function of the position of the swimmer, relative to the initial fluid-fluid interface. The predictions of the model agree well with experiments for the case of up the gradient motion. When moving down the gradient, gravitational forces in the experiment become important, therefore we modify the model to include buoyancy, which improves the agreement with experiments. In general our results show that it is harder for a pusher swimmer (see §2.1) to cross from low to high viscosity, whereas for a puller the opposite happens. This suggest that collective viscotaxis is possible without viscoreceptors and it is governed solely by the motility pattern of the swimmer.

1.4 Bacteria-driven microswimmers

Miniaturisation of actuators and efficient power sources are two of the biggest technical challenges in the design and fabrication of microscopic robots [18, 89]. As is often the case, Nature can offer insight into overcoming these challenges. Flagellated bacteria, such as the well-studied *E. coli*, are known to be efficient swimmers with intricate sensing capabilities [9] and they have inspired scientists to integrate living cells and synthetic components into bio-hybrid devices [16–25]. Bacteria-driven microswimmers have received special attention due to their potential applications in medicine such as targeted drug delivery [16, 90–96]. Commonly, a microswimmer of this type consists of a synthetic substrate such as a micro-plate [17, 97] or a micro-bead [16, 93, 94, 98] with just a few or many bacteria attached to their surfaces (see example in Fig. 1.2). The attachment of the cells to the surface is often random but can be controlled by patterning the substrate using chemical or physical techniques [19, 99].

The dynamics of a passive bead driven by surface-attached bacteria is a result of the precise behaviour of each cell. Of particular importance is the ability of bacteria to bias its motion in response to a chemical gradient. It is possible for the individual chemotactic response of each bacterium to contribute to a collective response, so that the microswimmer displays chemotaxis itself [90, 100]. Indeed, there are many other taxis techniques which can be used to control the trajectories of synthetic microswimmers, such as phototaxis [101] and magnetotaxis [102]. However, for medical applications chemotaxis appears to be the most natural, as not only it does not require the use of external force fields but can also be linked to the ubiquitous presence of chemical gradients in the human body.

Helical trajectories of particles with surface-attached bacteria have been observed in experiments with small beads on which only one or two bacteria can be attached [92, 103]. This suggests that the cells, despite being attached to a surface, still follow a run-and-tumble dynamics (see §2.2.1), and each bacterium applies a constant force and constant torque to

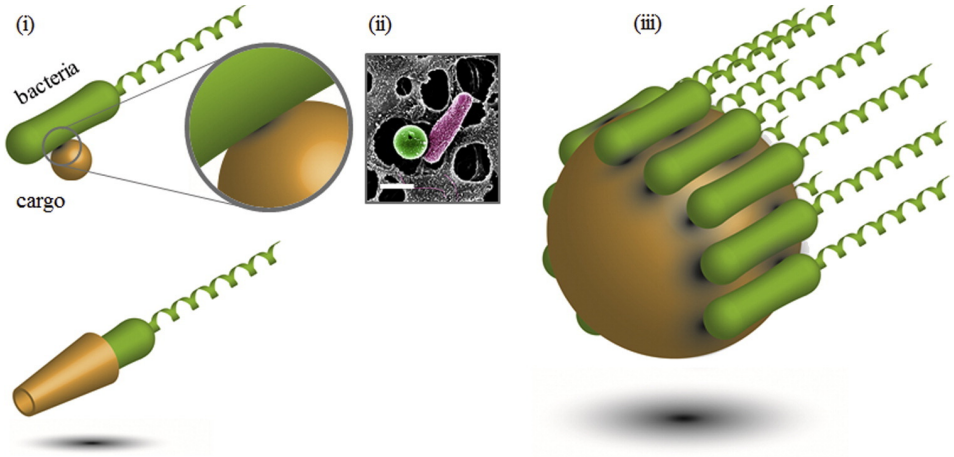

Fig. 1.2 Conceptual design of bacteria-driven microswimmer, (i) single cell biohybrid systems with spherical or cone cargo, (ii) scanning electron micrograph of single-cell biohybrid system, (iii) multi-cell biohybrid system. Reproduced and adapted from [20] by permission from Elsevier.

the bead. Following this observation, a number of mathematical models have been proposed to describe the motion of bacteria-driven microswimmers [17, 91, 92]. The swimmers are modelled as spherical particles actuated by random forces and torques that result from the combination of the individual forces and torques applied by each bacterium. Although these models have been validated numerically against experimental results [16, 90–93], very few analytical expressions have been derived. For example, it is known that for large number of surface-attached bacteria N, the swimming speed increases as $\sqrt{N}$ [91, 93] but the dependence on the size of the microswimmer is unclear.

In Chapter 5 we propose a stochastic fluid dynamic model to describe analytically and computationally the dynamics of microscopic particles driven by surface-attached bacteria undergoing run-and-tumble motion. We compute analytical expressions for the rotational diffusion coefficient, the swimming speed and the effective diffusion coefficient. At short times, the mean squared displacement (MSD) is proportional to the square of the swimming speed, which is independent of the particle size (for fixed density of attached bacteria) and scales linearly with the number of attached bacteria; in contrast, at long times the MSD scales quadratically with the size of the swimmer and is independent of the number of bacteria. We then extend our result to the situation where the surface-attached bacteria perform chemotaxis within the linear response regime. We demonstrate that bacteria-driven particles are capable of performing artificial chemotaxis, with a chemotactic drift velocity linear in the chemical concentration gradient and independent of the size of the particle.

1.5 Near-surface bacterial chemotaxis

Microorganisms are often encountered in environments where their motion is limited to confined micrometer-size spaces such as wet soil, filters and mucous membranes. This is relevant for the study of swimming bacteria as it is well known that their spatial distribution and motility pattern is altered by the presence of a surface [104–106]. Bacteria such as *E. coli* for example, tend to accumulate on surfaces [107–109]. It has been recently shown that the physical mechanisms that account for the accumulation near solid boundaries are a combination of steric forces and hydrodynamic interactions between the cell body and the wall [110]. At first, hydrodynamic interactions slow down the cell as it approaches the boundary, then at contact, the cell body is reoriented in the parallel direction to the surface and finally, near field hydrodynamic interactions account for a tilt towards the wall, which effectively traps the cell. As a result of these processes, *E. coli* bacteria swim at a stable distance from a solid boundary and it is well known that their trajectories in this case become left handed circles [111, 112]. The additional reorientation due to the hydrodynamic interaction with the wall hinders the ability of bacteria to explore effectively the surface.

It has been shown before that the diffusivity of circle swimmers that follow a run-and-tumble strategy is always less than that of swimmers that follow straight runs [113–115]. It has also been observed that the tumbling rate plays a key role in the diffusion of circle swimmers. As in the free swimming case a high tumbling rate prevents the cell from swimming long distances without changing its direction of motion. On the other hand, a low tumbling rate implies that the bacterium spends more time swimming in closed circular trajectories which leads to low diffusivity, as opposed to the free swimming case in which the diffusion coefficient increases monotonically with decreasing tumbling rate. In fact, for circle swimmers there is an optimum tumbling rate that maximizes the diffusivity and which depends on the angular velocity and the tumbling angle [114, 116]. We should expect a similar balance between tumbling rate and angular velocity to be determining in the chemotactic strategy of *E. coli*, although this has not been properly tested, neither theoretically nor experimentally. One of the only few observations is that of Berg et al. in their experiments on chemotaxis of bacteria in capillary arrays [113], they observed that both diffusivity and chemotactic drift reduced when the size of the capillaries increased and this could be a consequence of the bacteria being entrapped in circular trajectories.

In Chapter 6 we describe the motion of a run-and-tumble particle (RTP) using a Fokker-Planck-like approach. We analyse both, motion in free space and motion near a solid boundary. We start by considering stochastic differential (Langevin) equations for the evolution of the position and orientation of the particle. Initially we ignore thermal fluctuations, in this case run-and-tumble is the only source of noise and can be modeled as a jump diffusion process.

Using the Langevin equations for position and orientation we derive an evolution equation for the probability distribution $P(\mathbf{x},\mathbf{p},t)$ of finding the particle at position $\mathbf{x}$, with orientation $\mathbf{p}$ at time t. We refer to this equation as the *generalised Fokker–Planck equation* given its similarity with the classic Fokker–Planck equation for Brownian diffusion. We solve for P using a Fourier expansion in the moments of the orientation, this allows us to obtain the marginal distribution $P(\mathbf{x},t)$. We can then compute the moments of the position and obtain analytical expressions for the diffusion coefficient D_e and the decorrelation time τ_r of the RTP. We include chemotaxis by allowing the tumbling rate to change with the position of the RTP, according to a chemical concentration field $C(\mathbf{x})$. Using a perturbative approach, we calculate the first moment of the position and we use it to define the chemotactic drift. We perform all the calculations in the free swimming case, recovering previous results. Finally, we generalise to the case in which the RTP perform circular runs, due to hydrodynamic interactions with a boundary. We show that diffusion and chemotaxis are always lower for a circle swimmer.

Chapter 2

Physics of Low-*Re* swimming

In this chapter we introduce the physical principles that govern the dynamics of swimming bacteria. In §2.1 we present the Navier-Stokes equations for incompressible flow in a Newtonian fluid. We discuss how inertia is unimportant for swimming microorganisms, in this case the Navier-Stokes equations simplify to the steady Stokes equations of creeping flow. We point out the implication of the mathematical properties of the Stokes equations for the motility of swimming microorganisms. Specifically, force free-swimming, non-reciprocal locomotion and drag anisotropy. We elaborate on the last property and introduce the resistive-force theory for slender filaments in §2.1.2.2, as a model for flagellar propulsion. The second part of this chapter is devoted to the statistical aspects of bacterial motility. We present the run-and-tumble model in §2.2.1 which allows us to calculate the diffusion coefficient of bacteria with different motility patterns. Then, we introduce the *de Gennes* model for bacterial chemotaxis in §2.2.2 and derive a general expression for the chemotactic drift. Finally, we discuss the effects of thermal fluctuations in §2.2.3 and the generality of the run-and-tumble model in §2.2.4.

2.1 Hydrodynamics of Low-*Re* Swimming

2.1.1 Stokes Equations of Creeping Flow

The motion of a particle immersed in a Newtonian fluid of viscosity μ is described by the Navier–Stokes equations

$$\nabla \cdot \mathbf{u} = 0 \tag{2.1}$$

$$\rho \left(\frac{\partial}{\partial t} + \mathbf{u} \cdot \nabla \right) \mathbf{u} = \nabla \cdot \boldsymbol{\sigma} + \mathbf{f}, \tag{2.2}$$

where ρ is the fluid mass density, $\mathbf{f}$ a body force per unit volume such as gravity for example, $\mathbf{u}$ is the flow field surrounding the particle and $\boldsymbol{\sigma}$ is the stress tensor, with isotropic part proportional to the hydrodynamic pressure, $\boldsymbol{\sigma}_{iso} = -p\mathbf{1}$, and deviatoric part proportional to the symmetric part of the velocity gradient, $\boldsymbol{\sigma}_{dev} = \mu\left(\nabla\mathbf{u} + (\nabla\mathbf{u})^T\right)$. Equation (2.1) states that the fluid is incompressible, while Eq. (2.2) is an statement of local conservation of momentum, a continuum version of Newton's second law. Usually, boundary conditions for equations Eq. (2.1) and Eq. (2.2) are continuity of the velocity and stress fields at interfaces. Considering characteristics scales L, U, LU^{-1} for length, speed and time it is possible to compare the inertial and viscous terms in Eq. (2.2) and define the dimensionless Reynolds number

$$Re = \frac{\text{Inertial stress}}{\text{Viscous stress}} = \frac{\rho U^2}{\mu U/L} = \frac{\rho UL}{\mu}. \tag{2.3}$$

For our systems of interest, that is microswimmers, the typical length and speeds are $L \sim 10^{-5}$ m, $U \sim 10^{-5}\,\mathrm{m\,s^{-1}}$, and they are often found in viscous environments with densities and viscosities $\rho \sim 10^3\,\mathrm{kg\,m^{-3}}$ and $\mu \sim 10^{-3}$ Pa s or larger. Therefore, $Re \sim 10^{-4} \ll 1$ which means that the microswimmer is virtually inertialess and its motion is described by the Stokes equations Eq. (2.1) and

$$\mu\Delta\mathbf{u} = \nabla p - \mathbf{f}, \tag{2.4}$$

where $\Delta = \nabla\cdot\nabla$ is the Laplace operator. In other words, the motion of a microswimmer is overdamped, Eq. (2.4) simply states that the forces acting on the particle balances instantaneously. This property, and the fact that the Stokes equations are linear in the velocities and forces, have two important consequences: rate independence and time reversibility [117]. Together, both conditions lead to the so called *Purcell's scallop theorem* [2, 118], which states that a swimmer that generates propulsion by deforming its body periodically, cannot achieve net displacement if its deformation is invariant under a time reversal, regardless of the rate of deformation. This physical constraint underlies the prevalence of wave-like structures in the realm of swimming microorganisms.

As a final remark, the linearity of Stokes equations allows for superposition of solutions, very much like the solutions of Maxwell equations for electromagnetic fields. It is therefore possible to describe any flow field in terms of the Green's function, termed the Stokeslet, and its derivatives. Physically the Stokeslet correspond to the flow generated by a point force and its derivatives to multipoles whose flow magnitude decay increasingly fast far away from the point singularity. In an otherwise quiescent and unbounded fluid, Eq. (2.4) implies that in the absence of external forces, $\mathbf{f} = \mathbf{0}$, a microswimmer moves force- and torque-free, therefore the multipolar expansion of the flow that it generates cannot contain a Stokeslet

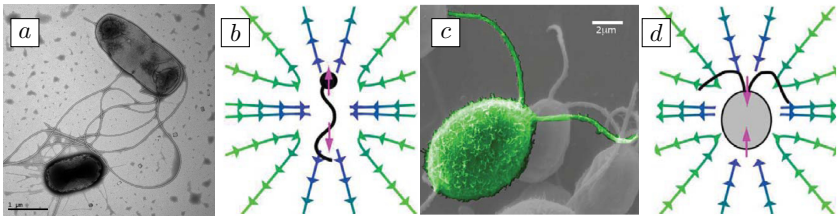

Fig. 2.1 Microswimmer mode classification. The bacterium *E. coli*, (a) electron micrography and (b) schematic pusher flow field. The green alga *C. reinhardtii*, (c) electron micrography and (d) schematic puller flow field. The scale bars correspond to 1 μm and 2 μm in (a) and (b), respectively. Panel (a) is adapted from https://www.eurekalert.org, panels (b)-(d) are adapted from [31] by permission of IOP.

or an antisymmetric force dipole, instead the leading order contribution comes from the symmetric dipole. There are two possible configurations in which we can build a force-free symmetric dipole, this allows for a general classification of microswimmers in *pushers* and *pullers* [see Fig. 2.1(b) and (d)]. The former move generating thrust behind them while the latter do it generating thrust in front of them.

A classical example of a puller is the micro algae *Chlamydomonas reinhardtii* [Fig. 2.1 (c)] that performs a breaststroke-like gait with its two active (eukaryotic) flagella. On the other hand, the classical example of a pusher is the bacterium *Escherichia coli* [Fig. 2.1 (a)], which has a number of passive (prokaryotic) flagella that rotate by the action of molecular motors embedded in its cell wall. The bacterial motors switch stochastically from anticlockwise to clockwise rotation and back, leading to the so called *run-and-tumble* motility pattern, which we described in detail in §2.2.1 below.

2.1.2 Flagellar swimming

2.1.2.1 The fundamental solution of Stokes equations

As mention above, any flow with $Re = 0$ can be expressed as a linear superposition of singularities, which derive from the Green's function of Stokes equations Eq. (2.1) and Eq. (2.4). The fundamental solution is obtained by considering a point force $\mathbf{F}$ acting at $\mathbf{x} = \mathbf{x}'$, that is $\mathbf{f} = \delta(\mathbf{x} - \mathbf{x}')\mathbf{F}$, with $\delta(\mathbf{x})$ the Dirac delta. Denoting by $\mathbf{u}_\mathbf{k}$ and $p_\mathbf{k}$ the Fourier transforms of the velocity and pressure fields, we find $\mathbf{k} \cdot \mathbf{u}_\mathbf{k} = 0$ for the continuity equation and $-\mu k^2 \mathbf{u}_\mathbf{k} = i\mathbf{k} p_\mathbf{k} - e^{-i\mathbf{k}\cdot\mathbf{x}'}\mathbf{F}$ for the momentum equation, with $k^2 = \mathbf{k} \cdot \mathbf{k}$. Therefore the pressure field is given by

$$p(\mathbf{x}) = -\frac{i}{(2\pi)^3}\mathbf{F} \cdot \int \frac{\mathbf{k}}{k^2} e^{i\mathbf{k}\cdot(\mathbf{x}-\mathbf{x}')}\, \mathrm{d}\mathbf{k} = -\frac{\mathbf{F}}{(2\pi)^3} \cdot \nabla \int \frac{e^{i\mathbf{k}\cdot(\mathbf{x}-\mathbf{x}')}}{k^2}\, \mathrm{d}\mathbf{k}$$

$$= -\frac{\mathbf{F}}{4\pi}\cdot\nabla\left(\frac{1}{|\mathbf{x}-\mathbf{x}'|}\right) = \frac{\mathbf{F}}{4\pi}\cdot\frac{\mathbf{x}}{|\mathbf{x}-\mathbf{x}'|^3}. \tag{2.5}$$

The velocity contains the solution to the pressure above and the inverse of the tensor $e^{-i\mathbf{k}\cdot\mathbf{x}'}\mathbf{k}\mathbf{k}/k^4$, which is

$$\begin{aligned}\mathscr{F}_{\mathbf{k}}^{-1}\left[\frac{\mathbf{k}\mathbf{k}}{k^4}\right] &= \frac{1}{(2\pi)^3}\int e^{i\mathbf{k}\cdot(\mathbf{x}-\mathbf{x}')}\frac{\mathbf{k}\mathbf{k}}{k^4}\,\mathrm{d}\mathbf{k} = \frac{1}{(2\pi)^3}\nabla^2\int\frac{e^{i\mathbf{k}\cdot(\mathbf{x}-\mathbf{x}')}}{k^4}\,\mathrm{d}\mathbf{k}\\ &= \frac{1}{8\pi}\nabla^2\left(|\mathbf{x}-\mathbf{x}'|\right) = \frac{1}{8\pi|\mathbf{x}-\mathbf{x}'|}\left(\mathbf{1}-\mathbf{k}\mathbf{k}\right),\end{aligned} \tag{2.6}$$

therefore, the velocity field is given by the *Stokeslet*

$$\mathbf{u}(\mathbf{x}) = \frac{\mathbf{F}}{8\pi\mu}\cdot\left(\frac{\mathbf{1}}{|\mathbf{x}-\mathbf{x}'|}+\frac{(\mathbf{x}-\mathbf{x}')(\mathbf{x}-\mathbf{x}')}{|\mathbf{x}-\mathbf{x}'|^3}\right) = \mathbf{F}\cdot\mathbf{H}(\mathbf{x}-\mathbf{x}'), \tag{2.7}$$

where $\mathbf{H}$ is called the Oseen tensor. Now let us denote by $\mathbf{n}$ the direction of the point force $\mathbf{F}$. The velocity $\mathbf{u}_{\parallel}$ along the line generated by $\mathbf{n}$ at a distance r from $\mathbf{x}'$, and the velocity $\mathbf{u}_{\perp}$ on the plane $\mathbf{x}\cdot\mathbf{n}=0$ at the same distance r have magnitudes $u_{\parallel}(r) = F/4\pi\mu = 2u_{\perp}(r)$. This anisotropy of the Stokeslet is fundamental for the propulsion of flagellated microorganisms, as we will see below.

2.1.2.2 Resistive-force theory

Most swimming microorganisms propel themselves by beating or rotating long thin filaments, called flagella or cilia. The physical principle underlying this mechanism is the anisotropy of the viscous drag on the filaments. Since it is easier to pull a thin rod along its axis than perpendicular to it, the rod will tend to drift sideways when it settles down at a slant angle to the vertical in a viscous flow. Indeed, it is possible to show that the hydrodynamic drag per unit length on a thin filament is given by

$$\mathbf{f} = -\zeta_{\parallel}\mathbf{u}_{\parallel} - \zeta_{\perp}\mathbf{u}_{\perp}, \tag{2.8}$$

where $\mathbf{u}_{\parallel,\perp}$ is the local fluid velocity along and perpendicular to the filament surface[4, 5, 119]. The drag coefficients $\zeta_{\parallel,\perp}$ satisfy $\zeta_{\perp}\simeq 2\zeta_{\parallel}$, a reminiscent of the anisotropy of the Stokeslet. We can demonstrate Eq. (2.8) for a thin rod of radius b and length L, such that $b \ll L$. In this case we can think of the rod as a collection of small spheres of radius b. If the rod moves at velocity $\mathbf{u}$ and rotates at rate $\boldsymbol{\omega}$, then the velocity $\mathbf{u}_n$ of the n-th sphere is

$$\mathbf{u}_n = \mathbf{u} + 2nb\boldsymbol{\omega}\times\mathbf{p}, \tag{2.9}$$

where $\mathbf{p}$ is a unit vector along the rod's axis and $-N/2 \leq n \leq N/2$, with $N = L/2b$. We can also express $\mathbf{u}_n$ in terms of the forces $\mathbf{F}_m$ acting on the remaining $n-1$ spheres using Eq. (2.7) as follows

$$\mathbf{u}_n = \sum_{m \neq n} \mathbf{H}_{nm} \cdot \mathbf{F}_m = \sum_{m \neq n} \frac{1}{16\pi\mu b|m-n|} (\mathbf{1} + \mathbf{pp}) \cdot \mathbf{F}_m. \tag{2.10}$$

Considering the fact that the flow decays rapidly as $|n-m|$ increases and that for a translating very long rod $\mathbf{F}_m$ is constant, we may approximate $\mathbf{H}_{nm}$ as follows [120]

$$\mathbf{H}_{nm} \simeq \frac{\ln(N/2)\delta_{nm}}{8\pi\mu b} (\mathbf{1} + \mathbf{pp}), \tag{2.11}$$

where δ_{nm} is the Kroenecker delta. We can now invert Eq. (2.10) to determine the total force acting on the rod $\mathbf{F} = \sum_n \mathbf{F}_n = \sum_{n,m} \mathbf{H}_{nm}^{-1} \cdot \mathbf{u}$, where the term proportional to $\boldsymbol{\omega}$ vanishes due to the symmetry of the Oseen tensor $\mathbf{H}_{nm} = \mathbf{H}_{-n-m}$ and its inverse. We can define the translational resistance tensor $\boldsymbol{\zeta}_t$ so that $\mathbf{F} = \boldsymbol{\zeta}_t \cdot \mathbf{u}$ and

$$\boldsymbol{\zeta}_t = \sum_{n,m} \mathbf{H}_{nm}^{-1} \simeq N \frac{8\pi\mu b}{\ln(N/2)} (\mathbf{1} + \mathbf{pp})^{-1} = \frac{4\pi\mu L}{\ln(L/4b)} \left(\mathbf{1} - \frac{\mathbf{pp}}{2}\right). \tag{2.12}$$

From this we deduce that the drag coefficients per unit length are $\zeta_\perp = 4\pi\mu/\ln(L/2b) = 2\zeta_\parallel$. The hydrodynamic drag is obtained by force balance, $\mathbf{F} + L\mathbf{f} = \mathbf{0}$, which leads to Eq. (2.8).

But how do microorganisms exploit this mechanism? They do it by propagating waves along the filaments. Indeed, consider a filament undergoing a small deformation $y(x,t) = y(x-ct)$, $|y| \ll 1$. In this case, we can approximate the tangential vector to the filament by $\mathbf{e}_x$ and the propulsion force by the perpendicular component of the drag [117]

$$\mathbf{F}_p \simeq (\zeta_\perp - \zeta_\parallel) \int_0^L \frac{\partial y}{\partial t} \frac{\partial y}{\partial x} \mathrm{d}x \mathbf{e}_x = -c(\zeta_\perp - \zeta_\parallel) \int_0^L \left(\frac{\partial y}{\partial \xi}\right) \mathrm{d}\xi \mathbf{e}_x. \tag{2.13}$$

This means that all the elements along the filament push the organism in the opposite direction to the wave propagation.

There a few limitations of the resistive-force theory (RFT) Eq. (2.8), in particular, it requires exponentially thin filaments. More accurate expressions for the drag coefficients have been derived [5, 121] and a more sophisticated technique called *slender-body theory* [119] offers expressions valid for thin filaments of order $b/L \sim \varepsilon^q$ ($q \in \mathbb{Q}$) rather than $b/L \sim e^{-1/\varepsilon}$, $\varepsilon \ll 1$ [117]. Nevertheless, RFT is very useful, it allows us to calculate analytical expressions for the swimming velocities of microorganisms and in some cases, it offers more physical insight on the swimming dynamics than more sophisticated techniques which

are mathematically more involved. We demonstrate this in Chapter 3 where an RFT model allows us to uncover the symmetries of the swimming gait of the bacterium *Spiroplasma*, and in Chapter 4 where we use RFT to explain the variations in the speed of a Low-*Re* swimmer moving across a viscosity gradient.

2.2 Statistical aspects of Low-*Re* Swimming

Most low-*Re* swimmers have submillimiter sizes, therefore their motion is highly sensitive to fluctuations. There are two major sources of noise: i) thermal fluctuations, caused by the constant collisions of the molecules in the surrounding fluid with the swimmer's body and ii) the inherent stochasticity of the machinery that allows them to swim. For example, the rotation sense of a bacterial motor depends on the concentration of CheY molecules which most likely varies in space and time, additionally, a bacterium will have a variable number of flagella with different sizes and randomly located around their body.

The action of noise renders the otherwise deterministic trajectories of a low-*Re* swimmer stochastic. Knowing the initial position and velocity of the swimmer is not sufficient to precisely predict its location at a later time. At best, we can tell on average where the swimmer will be found. Therefore, we need a probabilistic description of the trajectories. There are several options, one is to consider the swimmer as a particle that performs a random walk and calculate the moments of the position. Another option is to consider random forces acting on the swimmer and derive a stochastic differential equation for the position, called the *Langevin equation*, which can in turn be transformed into an evolution equation for the probability density of finding the swimmer at a certain position in time, sometimes called the *Fokker-Planck equation*. Ultimately, both approaches allow us to compute macroscopic properties such as diffusivity and flux velocities that can be experimentally measured.

In this section we describe the first approach, the so called run-and-tumble model. Although this model was originally developed to describe the trajectories of *E. coli* [122], it is possible to describe the individual (coarse-grain) trajectories of different microorganisms and artificial microswimmers by tuning a small number of parameters [115, 123]. Therefore, we focus on the run-and-tumble dynamics of *E. coli* and only point out how does this relate to other motility patterns.

2.2.1 Run-and-tumble

When free swimming, a peritrichous bacterium[1] such as *E. coli* moves in a series of nearly straight paths ('runs'), interrupted by quick changes in orientation ('tumbles'). This so-called run-and-tumble motion consists therefore of two stages: (i) the running phase, in which all the helical flagellar filaments rotate counterclockwise (when measured from behind the cell) and form a bundle which aligns with the cell body and whose rotation in the fluid propels the cell forward; (ii) the tumble phase, in which at least one flagellar filament rotates in the clockwise direction and leaves the bundle resulting in a reorientation of the whole cell [9, 124]. During the running phase, the bacterium experiences a constant propulsive force and torque along the same direction. Both force and torque balance with the corresponding hydrodynamic translational and rotational drags, so that the cell is overall force- and torque-free. In contrast, in the tumbling phase the bacterium experiences no propulsive force but a torque which reorients the cell body [92].

The number of running and tumbling events for *E. coli* are well approximated by a Poisson distribution [125] with each run lasting for approximately one second while tumbles last just a tenth of a second [124]. These times can be altered by chemical concentration gradients in the environment surrounding the cell. Bacteria such as *E. coli* can measure temporal differences in concentration of certain chemicals during their locomotion, for example aspartate, and reduce their tumbling rate if moving up the gradient [126, 127]. As a result, the trajectory of a swimming bacterium is an isotropic random walk in homogeneous environments and a biased random walk when in the presence of a chemical gradient (if the cell is sensitive to it). The bias in the direction of motion is known as chemotaxis.

2.2.1.1 Diffusion

The random trajectories of *E. coli*, and in general of any run-and-tumble particle (RTP), result in a diffusive behavior in the long term, this means that the position of the particle, $\mathbf{x}(t)$ has zero mean but finite variance that grows quadratically in t at short times and linear in t for long time scales. Classically, this is rationalised by modelling the trajectories as a random chain with links of equal length $v_0\lambda_T$, where v_0 and λ_T are the swimming speed and tumbling rate of *E. coli*. The angle θ between consecutive links is such that $\langle \mathbf{p}_i \cdot \mathbf{p}_{i+1} \rangle = \langle \cos\theta \rangle = \alpha$, where $\langle \cdots \rangle$ stand for the average over the configurations of the chain, $\mathbf{p}_i$ is a unit vector determining

[1] Flagellated bacteria are classified according to the distribution of its flagella around their body. The root *tricho* derives from the Greek word for hair, $\theta\rho\acute{\iota}\xi$ (*thríx*). Therefore, monotrichous, amphitrichous and peritrichous stand for bacteria with a single flagellum, flagella on both poles and flagella all around their body, for example.

the direction of the i-th link and α is called the persistence parameter. In polymer physics, a mathematically-identical setup is used in the freely-rotating chain model of a polymer and it is thus a textbook result that the orientation correlation function satisfies [122, 128, 129]

$$\begin{aligned} c(t) \equiv \langle \mathbf{p}(0)\cdot\mathbf{p}(t)\rangle &= \sum_{n=0}^{\infty} P_n(t)\,\langle \mathbf{p}_0\cdot\mathbf{p}_n\rangle \\ &= \sum_{n=0}^{\infty} P_n(t)\,\langle\cos\theta\rangle^n = \sum_{n=0}^{\infty} P_n(t)\alpha^n, \end{aligned} \tag{2.14}$$

where $P_n(t)$ is the probability of observing n tumbles before time t. In the case of Poisson distributed tumbling events with rate λ_T, we have $P_n = (\lambda_T t)^n e^{-\lambda_T t}/n!$ and the sum in Eq. (2.14) can be done explicitly, the result is

$$c(t) = e^{-\lambda_T(1-\alpha)t} = e^{-t/\tau_r}, \tag{2.15}$$

where $\tau_r^{-1} = \lambda_T(1-\alpha)$ is called the randomisation or correlation time. The variance of the position, also termed the mean squared displacement (MSD), is obtained by integrating $c(t)$ twice in time, the result is

$$\left\langle |\mathbf{x}|^2 \right\rangle = 2v_0^2\tau_r^2\left(\frac{t}{\tau_r} + e^{-t/\tau_r} - 1\right), \tag{2.16}$$

which is the classical result derived by Chandrasekhar for the MSD of a particle diffusing in free space [130]. For $t \ll \tau_r$ the MSD is ballistic, $\left\langle |\mathbf{x}|^2 \right\rangle \simeq v_0^2 t^2$, whereas for $\tau_r \ll t$ the MSD is diffusive, $\left\langle |\mathbf{x}|^2 \right\rangle \simeq 6D_e t$, where $D_e = v_0^2\tau_r/3$ is the diffusion constant for an RTP. For *E. coli* $v_0 \sim 20-30$ μm/s, $\lambda_T^{-1} \sim 1$ s and $\alpha \sim 1/3$, hence $D_e \sim 200-450$ μm^2/s in close agreement with experimental value $D_e \simeq 500$ μm$^2/s$ [28, 113, 122].

2.2.2 Bacterial chemotaxis

Bacteria such as *E. coli* are able to navigate through chemical gradients by using an inhibition of the mechanism that inverts the polarity of their bacterial motor when the cell swims in a favourable direction [9]. Polarity inversion is responsible for tumbling events, and therefore runs are extended when swimming up (down) the chemoattractant (repellent) gradient [131]. Classically, a bacterium is assumed to be equipped with an internal sensor that responds to temporal variations in the chemical concentration of its environment by modifying the tumbling rate, λ_T, i.e. the expected rate at which running cells stop moving and transition to a tumble [127]. For weak chemical concentrations $C(t)$, the variation in λ_T is captured by a linear response as $\lambda_T(t) = \lambda_T^{(0)}(1-Q(t))$, where $\lambda_T^{(0)}$ is the tumbling rate in a homogeneous

environment and the fraction Q depends on the history of the RTP trajectory as

$$Q(t) = \int_{-\infty}^{t} K(t-s)C(\mathbf{x}(s))\mathrm{d}s. \tag{2.17}$$

The kernel $K(t)$ is usually considered to be a bilobed function such that $\int K\mathrm{d}t = 0$, a property which accounts for adaptation and it is customary to approximate the memory kernel by a sum of impulses $K(t) = \sum k_i \delta(t - T_i)$, where k_i is the intensity of the response at time T_i and satisfies $\sum k_i = 0$ [132, 133]. The effect of the chemoattractant on the motion of the organism is measured by a drift speed defined as the average length of a run, x, travelled in the direction of the gradient, divided by the average run time $\left(\lambda_T^{(0)}\right)^{-1}$, that is

$$v_d = \lambda_T^{(0)} \langle x \rangle = \lambda_T^{(0)} \left\langle \int_0^{\infty} x(t)p(t)\mathrm{d}t \right\rangle_{\mathbf{p}}, \tag{2.18}$$

where $p(t) = \exp\left(-\int_0^t \lambda_T(t')\,\mathrm{d}t'\right)$ is the probability of stopping at time t. The integral above represents the average over possible run lengths and $\langle\cdots\rangle_{\mathbf{p}}$ denotes the average over possible initial orientations. For shallow concentration gradients, $|Q(t)| \ll 1$ we can expand $p(t)$ in powers of Q and find [132, 134]

$$v_d = \frac{v_0^2 |\nabla C| \lambda_T^{(0)} (1-\alpha)\tau_r^2}{3} \int_0^{\infty} e^{-T/\tau_r} K(T)\,\mathrm{d}T, \tag{2.19}$$

where $\tau_r^{-1} = \lambda_T^{(0)}(1-\alpha)$. This result has been confirmed by numerical simulations for different values of α [134] and for the case of circle swimming induced by a shear flow [135].

2.2.3 Thermal fluctuations

The constant collision of the molecules surrounding the bacterium will exert forces and torques on the bacterium that will make it drift and rotate. The drift direction and the rotation sense appear to be random due to fluctuations in the number of particles an the amount of momentum that they transfer to the bacterium as they collide. Therefore, the trajectories of the bacterium will display additional tortuosity. It is customary to assume that thermal fluctuations are independent from the run-and-tumble dynamics. In this case, we can model the trajectory of the bacterium as a sum of two random chains, one for translational diffusion due to thermal fluctuations and another one for rotational diffusion due to both thermal noise and run-and-tumble dynamics.

In a homogeneous medium there will be no preferential orientation, therefore the average

force exerted at any time should vanish. Usually the duration of a collision is much smaller than the viscous damping timescale, therefore we can assume instantaneous collisions. Moreover, given the large amount of molecules in the medium and the fact that the size of the bacterium is much larger than that of the molecules, we can assume that each collision will be independent of each other, therefore thermal forces at two different times will be uncorrelated.

Under this assumptions, we can model the trajectory for translational diffusion as a random chain of equal length links $\mathbf{x} = \ell \mathbf{p}_i$ with $\mathbf{p}_i$ a unit vector such that $\langle \mathbf{p}_i \rangle = \mathbf{0}$ and $\langle \mathbf{p}_i \mathbf{p}_j \rangle = \delta_{ij}$. Therefore the mean vanishes and the MSD is $\langle |\mathbf{x}|^2 \rangle = N\ell^2$, where N is the number of links at time t. Using the viscous relaxation time $\tau = m/\zeta$, where m is the mass of the bacterium and ζ its resistance coefficient, we can write $\ell = v\tau$ and $N = t/\tau$, where the speed v follows from the equipartion of energy $mv^2 = k_B\Theta$, with k_B the Boltzmann constant and Θ the absolute temperature of the fluid medium. Therefore $\langle |\mathbf{x}|^2 \rangle = 6D_T t$ with the translational thermal diffusion coefficient $D_T = k_B T/\zeta$, this is the classical Einstein-Stokes relation.

Since the thermal energy is proportional to $k_B\Theta \sim 10^{-21}$ J and the viscous work over a length scale of the size of the bacterium is $\mu L^2 U \sim 10^{-18}$ J, we can expect the rotation due to thermal fluctuations to be much smaller than that of a tumble. However there will be a large number of thermal rotations before a tumble happens, therefore it is possible to have a large overall reorientation due to thermal fluctuations at the end of a run. This suggest that we can coarse-grain the fast jiggling due to thermal noise in such a way that the trajectory can be represented by a random chain similar to that in §2.2.1 above, but with an average angle between consecutive links $\theta + \theta'$, where θ is due to run-and-tumble and θ' due to thermal noise. Since we are considering run-and-tumble dynamics and thermal noise to be independent processes, the correlation function can be split into the product

$$c(t) \equiv \langle \mathbf{p}(0) \cdot \mathbf{p}(t) \rangle = \langle \cos\theta \rangle \left\langle \cos\theta' \right\rangle = e^{-\lambda_T (1-\alpha) t} \left\langle \cos\theta' \right\rangle . \tag{2.20}$$

The average over thermal fluctuations can be calculated by assuming that the evolution of the probability density of finding the particle with orientation $\mathbf{p}$ at time t, satisfies the diffusion equation with diffusivity D_r [134, 136]. Alternatively, we can think of rotational diffusion as a run-and-tumble dynamics with rate D_r and persistence parameter $\alpha' = 0$, the latter follows from the fact that we assumed thermal fluctuations to be uncorrelated. In any case we find $\langle \cos\theta' \rangle = e^{-2D_r t}$, with the rotational diffusivity given by the Stokes-Einstein relation $D_r = k_B\Theta/\zeta_r$, with ζ_r the rotational drag coefficient of the swimmer [120]. Putting all together, we find the MSD of a run-and-tumble swimmer, undergoing thermal translational

and rotational diffusion to be given by

$$\left\langle |\mathbf{x}|^2 \right\rangle = 6D_T t + 2v_0^2 \tau_r \left(\frac{t}{\tau_r} + e^{-t/\tau_r} - 1 \right), \tag{2.21}$$

where the randomisation time is given by $\tau_r^{-1} = \lambda_T(1-\alpha) + 2D_r$. Notice that thermal rotation reduces the effective diffusivity $D_e = 2v_0^2\tau_r$ by accelerating the loss of orientation memory. Although thermal translations contribute to an increase of the total diffusivity $D = D_T + D_e$, it is negligible compared to the run-and-tumble activity and we can ignore it. Using the same coarse-graining of the trajectory, we can show that the chemotactic drift is given by Eq. (2.19) with $\tau_r^{-1} = \lambda_T(1-\alpha) + 2D_r$.

2.2.4 Generality of the model

As mention before, different motility patterns can be described with the run-and-tumble model by changing the value of the persistence parameter. For example, the bacterium *Helicobacter pylori* reverses its direction of motion when its motor switch polarity [137]. This motility pattern is called run-reverse and is prevalent in many marine bacteria such as *Pseudomonas aeruginosa*. Run-reverse can be modelled simply by setting $\alpha = -1$. More complicated patterns can also be included if we allow runs to have different values of α. The bacterium *Vibrio alginolyticus* follows a strategy similar to run-reverse, with an extra reorientation event. When the bacterial motor switches from clockwise to counterclockwise rotation, *V. alginolyticus* flagellum becomes unstable and bends generating a torque, as a result the bacterium "flicks" [138]. The average turning angle during a flick is 90°, therefore the trajectory is described by two persistence parameters $\alpha_1 = \langle \mathbf{p}_i \cdot \mathbf{p}_{i+1} \rangle = -1$ and $\alpha_2 = \langle \mathbf{p}_i \cdot \mathbf{p}_{i+2} \rangle = 0$ [123].

A wider variety of strategies arise within the model if we also vary the swimming speed and the tumbling rates. However, it might not be possible to calculate the diffusivity and the drift analytically with the method described here. In such cases, more sophisticated techniques are required. Continuous time random walks (CTRW) generalise the run-and-tumble model and allow to calculate diffusivity and drift for multimodal motility patterns and trajectories with different running times distributions, not necessarily Poissonian [115].

In Chapter 6 we present a different approach for the statistical description of bacterial motility. We model run-and-tumble as a compound Poisson process and derive a evolution equation for the probability distribution P of finding an RTP at a certain position in time. Using a perturbative method, we calculate diffusivity and chemotactic drift from the master equation for P.

Chapter 3

Spiroplasma Motility

3.1 Introduction

In this chapter, we propose a coarse-grained model for the swimming of *Spiroplasma* avoiding the use of fitting parameters. In the spirit of previous studies, we model *Spiroplasma* as a deformable body whose motion in fluids can be described by the resistive-force theory of slender filaments [119] (see §2.1.2.2). We derive analytical expressions for the swimming speed and the swimming efficiency, which we then optimise.

The chapter is organised as follows. In §3.2 we develop the mathematical model. We present first the geometry of *Spiroplasma* and the kinematics and dynamics of the motion. We then describe the swimming gait in detail and compute the resistance matrix for the slender body using resistive-force theory. At the end of §3.2 we introduce our coarse-grained model allowing to take into account the helical geometry of *Spiroplasma*.

The theoretical results derived from our model are then presented in §3.3 and §3.4. First we consider the non-helical case in §3.3, where we replace the cell body by a straight rod located at the position of the original helical axis. The rod is allowed to bend similarly to *Spiroplasma*, producing a kink that propagates from end to end and propels the rod (i.e. the cell) in the opposite direction. In this case, we demonstrate that the average orientation of the cell body is unchanged by the swimming stroke, which allows us to define an effective swimming speed and a hydrodynamic efficiency. We next show in §3.4 that this conclusion is robust to the inclusion of the helical geometry at a coarse-grained level and therefore the cell undergoes no periodic reorientation.

The results of our models are presented in §3.5 and numerical solutions are compared to asymptotic results in the limit of small-inter-kink distance. We compute in particular the optimum pitch angle and show that it is close to the experimental value of $\phi \approx 35^\circ$. We

finally summarise our results and discuss their relevance to cell diffusion and chemotaxis in §3.6.

3.2 Setup and model

3.2.1 Geometry and notation

The bacterium *Spiroplasma melliferum* has a right-handed helical body of radius $R \simeq 0.5\,\mu$m, pitch $P \simeq 1\,\mu$m and $4-6$ helical repeats [41] (see notation in Fig. 3.1). The cell body is therefore roughly ten times longer than it is wide. As mentioned above, the cytoskeleton allows the cell to change its chirality from right-handed to left-handed. It has been observed that the change occurs in the absence of external stress, therefore the body displays a kink with angle $\theta = \pi - 2\phi \simeq 110^\circ$ where $\phi \simeq 35^\circ$ is the pitch angle of the helical body [38, 50, 139, 140]. The angle θ is therefore the angle between the axes of the helical domains with opposite handedness. The time between chirality changes is observed to be exponentially distributed in experiments, with rate $\lambda_k = 1\,\mathrm{s}^{-1}$ while the time between a kink pair follows a normal distribution with mean $\tau_p = 0.26$s. The kink pair propagates along the helical filament with average speed $v_k \simeq 10.5 \pm 0.3\,\mu\mathrm{m/s}$ which is linearly related to the swimming velocity $v_s \simeq 3.3 \pm 0.2\,\mu\mathrm{m/s}$ [38].

A chirality transformation under the stress-free constraint allows for two kind of kinematic modes, namely the "crankshafting" and the "speedometer cable" mode [140]. In the former, one of the domains revolve around the other, while in the later, both domains spin around their axes. Scaling arguments for the energy dissipated on each mode suggest that the "speedometer cable" transformations are predominant, as observed in experiments [38, 50]. Given the aspect ratio of the cell body, we model the organism as a deformable rod that represents the location of the axes of the helical domains and that performs the speedometer swimming stroke illustrated in Fig. 3.2. The details of the helical geometry are included by allowing the drag on the rod to depend on the pitch angle of the original helical body and by including the hydrodynamic propulsive forces that originate from the rotation of the helical domains in the "speedometer cable" swimming mode. After one stroke, the position of the head $\mathbf{H}$ will be denoted by $\mathbf{H}(T) = \mathbf{H}(0) + \mathbf{X}_T$, where $\mathbf{H}(0)$ is the initial position of the head and $\mathbf{X}_T$ the net displacement after one period. The orientation at the end of the stroke will be $\mathbf{n}(T) = \mathbf{R}_T \cdot \mathbf{n}(0)$ where $\mathbf{R}_T$ is a rotation matrix and $\mathbf{n}(0)$ a unit vector that defines the initial orientation of the cell body (assumed to be straight at the beginning of the stroke). The linear and angular displacements, $\mathbf{X}_T$ and $\varphi_T = \cos^{-1}(\mathbf{n}(T) \cdot \mathbf{n}(0))$, are obtained by computing the force and torque acting on the body.

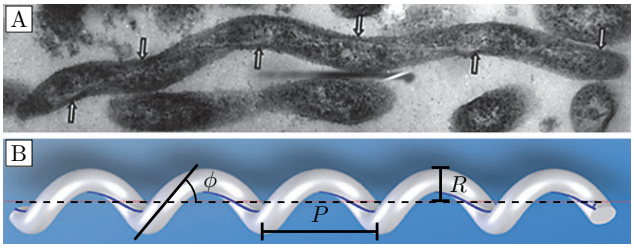

Fig. 3.1 The bacterium *Spiroplasma* with its characteristic helical shape. (A) Electron micrograph of *Spiroplasma*, with the arrows showing the cytoskeleton along the shortest helical path. (B) A three-dimensional model of an average cell with helical radius R and pitch $P = 2\pi R \cot\phi$, where ϕ is the pitch angle. Reprinted from Ref. [44] and modified from Ref. [40]. With permission from S. Karger AG and John Wiley and Sons.

3.2.2 Dynamics

Using the resistive-force theory for slender filaments subject to viscous flows [119] (see §2.1.2.2), we decompose the hydrodynamic force acting on the model rod, in parallel and perpendicular components to the filament as

$$\mathbf{f} = -\zeta_{\perp}\left[\beta\boldsymbol{\tau}\boldsymbol{\tau} + (\mathbf{1} - \boldsymbol{\tau}\boldsymbol{\tau})\right]\cdot\mathbf{v}, \tag{3.1}$$

where $\mathbf{f}$ is the hydrodynamic force per unit length, $\mathbf{v} = \mathbf{U} + \boldsymbol{\Omega}\times\mathbf{x} + \dot{\mathbf{x}}$ is the velocity of the fluid at a point $\mathbf{x}(s,t)$ along the centre-line of the rod (i.e. the axis of the helical domains) and where $\mathbf{U}$ and $\boldsymbol{\Omega}$ denote the linear and angular velocities of the body in the laboratory frame of reference. Here $\mathbf{x}(s,t)$ is a suitable parametrisation of the cell body in terms of the arclength s, in a frame of reference co-moving with some arbitrary point of the cell body at time t. In the following section we divide the swimming stroke in different stages, and we specify the parametrisation and the frame of reference used in each one of them.

We use primes to denote spatial derivatives along the arclength of the rod, and dots for time derivatives so the tangent vector at $\mathbf{x}$ is denoted by $\boldsymbol{\tau} \equiv \mathbf{x}'$ and $\dot{\mathbf{x}}$ is the velocity of deformation. In Eq. (3.1) the identity tensor is represented by $\mathbf{1}$, the drag coefficient per unit length, perpendicular to the body is denoted by $\zeta_{\perp}$ and $\beta = \zeta_{\parallel}/\zeta_{\perp}$ is the ratio of the parallel to the perpendicular drag coefficients.

The total force $\mathbf{F}$ and torque $\mathbf{N}$ acting on the body at a given time is obtained by integrating Eq. (3.1) along the arclength of the model rod $\mathbf{x}(s,t)$, i.e.

$$\mathbf{F}(t) = \int_{\mathbf{x}(s,t)} \mathbf{f}(s,t)\,\mathrm{d}s, \tag{3.2}$$

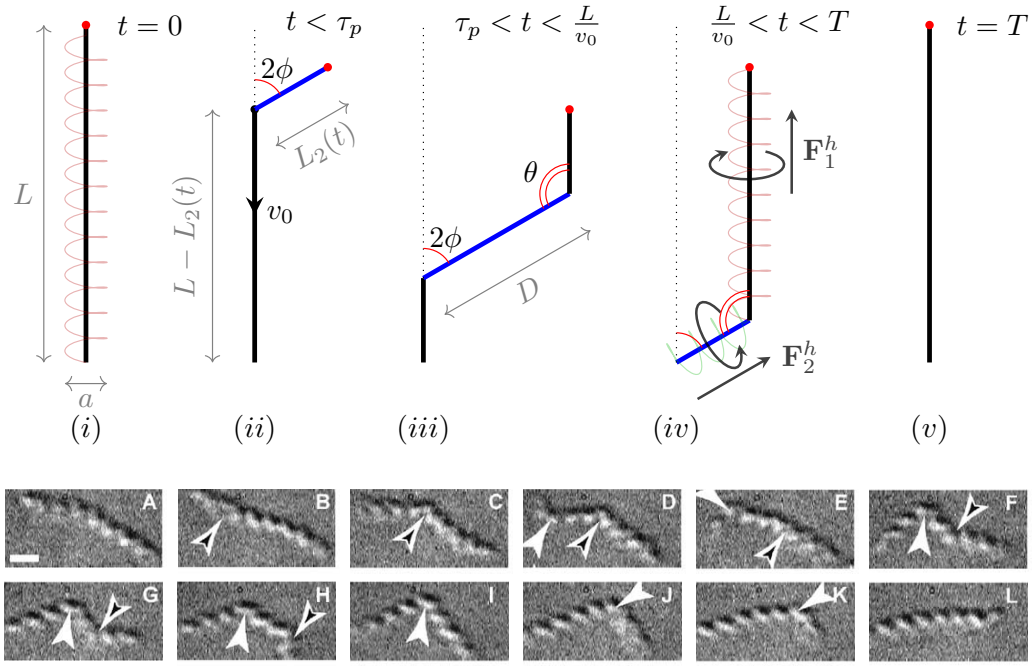

Fig. 3.2 Illustration of the swimming stroke of *Spiroplasma*. (A-L): Experiments (reprinted from Ref. [38] with permission from Elsevier). (*i-v*): Our mathematical model where we consider the helical axis of the swimmer as made of one, two or three straight rods (thick lines). The stroke is described in the frame of reference in which the tail (the untapered end) is static. (A, *i*): Initially the cell body has a right-handed helical shape. (B, C, *ii*): A kink appears at $t = 0$ and propagates from head (red circle) to tail along the body of axial length L at speed $v_0 = v_k \cos\phi$. In that case, the deformed rod has two domains of size $L_2(t)$ and $L_1(t) = L - L_2(t)$. (D-H, *iii*): The second kink forms at $t = \tau_p$, the maximum distance between kinks is denoted by $D = v_0\tau_p$. The deformed rod has now three domains. (I-K, *iv*): The configuration is similar to that of (*ii*), with reversed signs of the forces and torques acting on the body, the blue segment has now left-handed chirality and rotates clockwise, while the right-handed segment rotates anticlockwise. The arrows shows the induced force. (L, *v*): The stroke finishes at $T = \tau_p + L/v_0$.

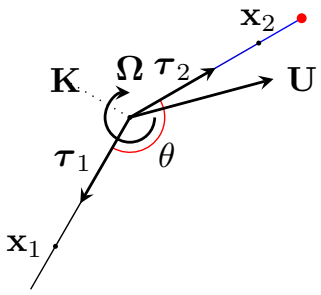

Fig. 3.3 First stage of the swimming stroke in the interval $0 \leq t \leq \tau_p$. We describe the motion in a frame of reference in which the tail appears to be fixed, with instantaneous origin at the location of the kink, $\mathbf{K}(t)$. The body moves with linear velocity $\mathbf{U}(t)$ and rotates with angular velocity $\boldsymbol{\Omega}(t)$. Material points on the axis of the right-handed and left-handed domains are denoted by $\mathbf{x}_1$, $\mathbf{x}_2$ respectively. The unit tangent vectors along the domains are denoted by $\boldsymbol{\tau}_1$ and $\boldsymbol{\tau}_2$.

$$\mathbf{N}(t) = \int_{\mathbf{x}(s,t)} \mathbf{x}(s,t) \times \mathbf{f}(s,t)\, \mathrm{d}s. \tag{3.3}$$

Assuming free swimming, drag and thrust must balance, and therefore we have the constraints $\mathbf{F} = \mathbf{0}$ and $\mathbf{N} = \mathbf{0}$. Consequently, $\mathbf{U}$ and $\boldsymbol{\Omega}$ can be expressed in terms of integrals of $\dot{\mathbf{x}}$. Then $\mathbf{X}_T$, $\mathbf{R}_T$ can be obtained by integration over one stroke as

$$\mathbf{X}_T = \int_0^T \dot{\mathbf{H}}(t)\, \mathrm{d}t, \tag{3.4}$$

$$(R_T)_{ij} = \mathscr{T} \exp\left[\varepsilon_{ikj} \int_0^T \Omega_k(t)\, \mathrm{d}t\right], \tag{3.5}$$

where ε_{ijk} are the components of the Levi–Civita pseudo tensor and $\dot{\mathbf{H}}(t)$ depends on $\mathbf{U}$ and $\boldsymbol{\Omega}$ in a non-trivial way. The operator $\mathscr{T}$ is called the time ordering operator, which ensures that the infinitesimal rotations $\varepsilon_{ijk}\Omega_k(t)$, in the Taylor expansion of the exponential function, appear from left to right in decreasing order of time evaluation.

In the next section we describe in detail the model for the swimming stroke depicted in Fig. 3.2 and calculate the forces and torques acting on the body in each stage.

3.2.3 Swimming stroke

The motion of the cell starts at $t = 0$ when a kink appears [see arrows in Fig. 3.2B and C] and starts propagating from head (tapered end) to tail at speed $v_0 = v_k \cos(\phi) = v_k \sin(\theta/2)$, which is the projected speed on the axis of the helical body. This is the first stage, which ends at time τ_p when a second kink appears [Fig. 3.2(*i*)-(*ii*) and A-C]. During the second

stage, the kink pair propagates along the body with a fixed distance $D = v_0\tau_p$ between the kinks [Fig. 3.2(*iii*) and D-H]. The third stage starts when the first kink reaches the tail at time $t = L/v_0$, and during this stage the second kink continues propagating until it reaches the tail. At the end of the third stage the geometry of the cell reverts to its original straight configuration [Fig. 3.2(*iv*)-(*v*) and I-L].

3.2.3.1 First stage

We start the calculation of the swimming velocity by obtaining the thrust in the first stage of the swimming stroke, that is for times $0 \leq t \leq \tau_p$ where we assume that a single kink propagates from head to tail at velocity $v_0\boldsymbol{\tau}_1$ (see Fig. 3.3).

Using a frame of reference in which the tail appears fixed and instantaneously centred at the location of the kink, the positions of material points in the different domains are given by

$$\mathbf{x}_i = s_i\boldsymbol{\tau}_i, \tag{3.6}$$

where $i = 1,2$, $\boldsymbol{\tau}_i$ is the tangent vector along each domain and $s_i \in [0, L_i]$ is the distance moving away from the kink with L_i the length of the corresponding domain (no Einstein summation notation). In this frame of reference, we have $\dot{\mathbf{x}}_1 = \mathbf{0}$ and the deformation velocity of the second domain, $\dot{\mathbf{x}}_2$, can be obtained by noting that after a small interval of time δt, the kink moves along $\boldsymbol{\tau}_1$ a distance $v_0\delta t$ and the distance from the kink to $\mathbf{x}_2$ increases by $v_0\delta t$ along $\boldsymbol{\tau}_2$, hence

$$\dot{\mathbf{x}}_2 = v_0\left(\boldsymbol{\tau}_1 + \boldsymbol{\tau}_2\right). \tag{3.7}$$

The hydrodynamic force per unit length is therefore

$$\begin{aligned}\mathbf{f}_i = \mathbf{f}_i^h &- \zeta_\parallel \mathbf{U}\cdot\boldsymbol{\tau}_i\boldsymbol{\tau}_i - \zeta_\perp\left[\mathbf{U} - \mathbf{U}\cdot\boldsymbol{\tau}_i\boldsymbol{\tau}_i + s_i\boldsymbol{\Omega}\times\boldsymbol{\tau}_i\right] \\ &- \delta_{i,2}v_0\left[\zeta_\parallel(1+\cos\theta)\boldsymbol{\tau}_i + \zeta_\perp(\boldsymbol{\tau}_1 - \boldsymbol{\tau}_2\cos\theta)\right],\end{aligned} \tag{3.8}$$

where $\mathbf{f}_i^h$ is the hydrodynamic force due to helical rotation (see §3.2.4). Substitution of Eq. (3.8) in equations Eq. (3.2) and Eq. (3.3) yields

$$\mathbf{F}_i = \mathbf{F}_i^h - \zeta_\perp v_0 L\left[\ell_i\left(\beta\mathbf{A}_i + \mathbf{B}_i\right)\cdot\mathbf{u} + \frac{\ell_i^2}{2}\mathbf{C}_i\cdot\boldsymbol{\omega}\right] - \delta_{i,2}\zeta_\perp v_0 L\ell_2\mathbf{d}_2, \tag{3.9}$$

$$\mathbf{N}_i = \mathbf{N}_i^h - \zeta_\perp v_0 L^2\left[\frac{\ell_i^2}{2}\mathbf{C}_i^T\cdot\mathbf{u} + \frac{\ell_i^3}{3}\mathbf{B}_i\cdot\boldsymbol{\omega}\right] - \delta_{i,2}\zeta_\perp v_0 L^2\frac{\ell_2^2}{2}\mathbf{e}_2, \tag{3.10}$$

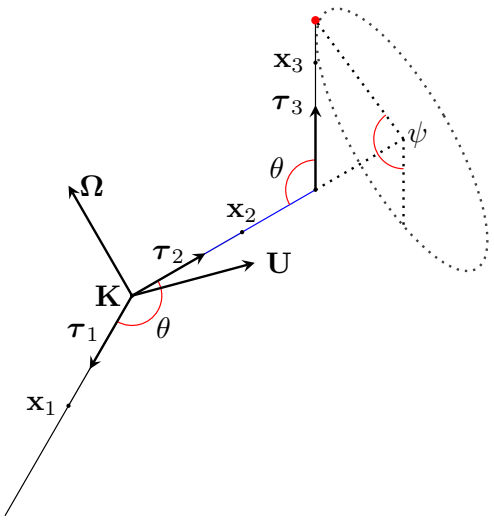

Fig. 3.4 Second stage of the swimming stroke in the interval $\tau_p \leq t \leq L/v_0$. We describe the motion in a frame of reference in which the tail appears to be fixed, with instantaneous origin at the location of the kink, $\mathbf{K}(t)$. The body moves with linear velocity $\mathbf{U}(t)$ and rotates with angular velocity $\boldsymbol{\Omega}(t)$. Material points and tangent vectors in each domain axis are denoted by $\mathbf{x}_i$ and $\boldsymbol{\tau}_i$ respectively. It is possible for the third helical domain to be tilted at an angle ψ away from the plane generated by $\boldsymbol{\tau}_1$ and $\boldsymbol{\tau}_2$.

where $\ell_i = L_i/L$, $\mathbf{u} = \mathbf{U}/v_0$, $\boldsymbol{\omega} = \boldsymbol{\Omega}L/v_0$ are, respectively, the dimensionless length of the domains, linear and angular velocities of the body. We have also made use of the tensors $\mathbf{A}_i = \boldsymbol{\tau}_i\boldsymbol{\tau}_i$ (no Einstein summation notation), $\mathbf{B}_i = \mathbf{1} - \boldsymbol{\tau}_i\boldsymbol{\tau}_i$, $\mathbf{C}_i = \boldsymbol{\varepsilon}\cdot\boldsymbol{\tau}_i$, with $\boldsymbol{\varepsilon}$ the Levi–Civita pseudo tensor, the superscript T denotes transposition and the vectors $\mathbf{d}_2$ and $\mathbf{e}_2$ are given by

$$\mathbf{d}_2 = \boldsymbol{\tau}_1 + [\beta + \cos\theta(\beta - 1)]\,\boldsymbol{\tau}_2, \tag{3.11}$$

$$\mathbf{e}_2 = \boldsymbol{\tau}_2 \times \boldsymbol{\tau}_1. \tag{3.12}$$

The free-swimming constraint, i.e. $\mathbf{F}_1 + \mathbf{F}_2 = \mathbf{0}$, $\mathbf{N}_1 + \mathbf{N}_2 = \mathbf{0}$, then leads to

$$\begin{aligned}\mathbf{J}_2 \cdot \begin{pmatrix} \mathbf{u} \\ \boldsymbol{\omega} \end{pmatrix} &= \begin{pmatrix} \sum_i \ell_i\,(\beta\mathbf{A}_i + \mathbf{B}_i) & \frac{1}{2}\sum_i \ell_i^2\mathbf{C}_i \\ \frac{1}{2}\sum_i \ell_i^2\mathbf{C}_i^T & \frac{1}{3}\sum_i \ell_i^3\mathbf{B}_i \end{pmatrix} \cdot \begin{pmatrix} \mathbf{u} \\ \boldsymbol{\omega} \end{pmatrix} \\ &= -\begin{pmatrix} \ell_2\mathbf{d}_2 - \sum_i \hat{\mathbf{F}}_i^h \\ \frac{\ell_2^2}{2}\mathbf{e}_2 - \sum_i \hat{\mathbf{N}}_i^h \end{pmatrix},\end{aligned} \tag{3.13}$$

where the sums are over $i = 1, 2$ and $\hat{\mathbf{F}}_i^h$, $\hat{\mathbf{N}}_i^h$ are the dimensionless forces and torques induced by the helical rotation (see §3.2.4).

3.2.3.2 Second stage

During the second stage of the swimming stroke, we need to compute the force per unit length on the third segment, this has tangent vector $\boldsymbol{\tau}_3$, which forms an angle ϑ with $\boldsymbol{\tau}_1$ such that $\boldsymbol{\tau}_1 \cdot \boldsymbol{\tau}_3 = \cos\vartheta = \sin^2\theta(1-\cos\psi) - 1$, as illustrated in Fig. 3.4. The position of the material point is given by $\mathbf{x}_3 = D\boldsymbol{\tau}_2 + s_3\boldsymbol{\tau}_3$, where $s_3 \in [0, L_3]$ is the distance moving away from the second kink. Using an argument similar to the one we used to derive $\dot{\mathbf{x}}_2$, we obtain the velocity of the third domain as

$$\dot{\mathbf{x}}_3 = v_0(\boldsymbol{\tau}_1 + \boldsymbol{\tau}_3), \tag{3.14}$$

and the hydrodynamic force per unit length is

$$\begin{aligned}\mathbf{f}_3 = \mathbf{f}_3^h &- \zeta_{\|}\left[\mathbf{A}_3 \cdot \mathbf{U} + v_0(1+\cos\vartheta)\boldsymbol{\tau}_3 + L_2\mathbf{A}_3 \cdot \mathbf{C}_2 \cdot \boldsymbol{\Omega}\right] \\ &- \zeta_{\perp}\left[\mathbf{B}_3 \cdot \mathbf{U} + s_3\mathbf{C}_3 \cdot \boldsymbol{\Omega} + v_0(\boldsymbol{\tau}_1 - \boldsymbol{\tau}_3\cos\vartheta) + L_2\mathbf{B}_3 \cdot \mathbf{C}_2 \cdot \boldsymbol{\Omega}\right].\end{aligned} \tag{3.15}$$

Hence, the total force and torque on the third portion of the body (measured with respect to **K**) is

$$\begin{aligned}\hat{\mathbf{F}}_3 - \hat{\mathbf{F}}_3^h &= -\ell_3\left(\beta\mathbf{A}_3 + \mathbf{B}_3\right)\cdot\mathbf{u} - \ell_3\mathbf{d}_3 \\ &\quad - \left(\frac{\ell_3^2}{2}\mathbf{C}_3 + \ell_2\ell_3\left(\beta\mathbf{A}_3 + \mathbf{B}_3\right)\cdot\mathbf{C}_2\right)\cdot\boldsymbol{\omega},\end{aligned} \tag{3.16}$$

$$\begin{aligned}\hat{\mathbf{N}}_3 - \hat{\mathbf{N}}_3^h &= -\frac{\ell_3^2}{2}\mathbf{C}_3^T\cdot\mathbf{u} - \left(\frac{\ell_3^3}{3}\mathbf{B}_3 + \frac{\ell_2\ell_3^2}{2}\mathbf{C}_3^T\cdot\mathbf{C}_2\right)\cdot\boldsymbol{\omega} \\ &\quad - \frac{\ell_3^2}{2}\mathbf{e}_3 + \ell_2\mathbf{C}_2^T\cdot\left(\hat{\mathbf{F}}_3 - \hat{\mathbf{F}}_3^h\right),\end{aligned} \tag{3.17}$$

where we have defined the vectors $\mathbf{d}_3 = \boldsymbol{\tau}_1 + [\beta + \cos\vartheta(\beta-1)]\boldsymbol{\tau}_3$ and $\mathbf{e}_3 = \boldsymbol{\tau}_3 \times \boldsymbol{\tau}_1$ as in equations Eq. (3.11) and Eq. (3.12). Applying the free swimming conditions, $\sum_i \mathbf{F}_i = \mathbf{0}$, $\sum_i \mathbf{N}_i = \mathbf{0}$, we now obtain

$$\left(\mathbf{J}_3 + \mathbf{K}_3\right)\cdot\begin{pmatrix}\mathbf{u}\\ \boldsymbol{\omega}\end{pmatrix} = -\begin{pmatrix}\ell_2\mathbf{d}_2 + \ell_3\mathbf{d}_3 - \sum_i \hat{\mathbf{F}}_i^h \\ \frac{\ell_2^2}{2}\mathbf{e}_2 + \frac{\ell_3^2}{2}\mathbf{e}_3 + \ell_2\ell_3\boldsymbol{\tau}_2\times\mathbf{d}_3 - \sum_i \hat{\mathbf{N}}_i^h\end{pmatrix}, \tag{3.18}$$

where the matrix $\mathbf{J}_3$ is as in Eq. (3.13) but with now sums over all three indices $i = 1,2,3$ and where

$$\mathbf{K}_3 = \ell_2\ell_3\begin{pmatrix}\mathbf{0} & \left(\beta\mathbf{A}_3 + \mathbf{B}_3\right)\cdot\mathbf{C}_2 \\ \mathbf{C}_2^T\cdot\left(\beta\mathbf{A}_3 + \mathbf{B}_3\right) & \ell_3\left(\mathbf{C}_2^T\cdot\mathbf{C}_3\right)^S + \ell_2\mathbf{C}_2^T\cdot\left(\beta\mathbf{A}_3 + \mathbf{B}_3\right)\cdot\mathbf{C}_2\end{pmatrix}, \tag{3.19}$$

where the superscript S denotes symmetrisation of the given tensor, i.e. $\mathbf{Q}^S = (\mathbf{Q}+\mathbf{Q}^T)/2$ for any tensor $\mathbf{Q}$.

3.2.3.3 Third stage

Using the symmetry of the stroke between the first and the third stages, the linear and angular velocities in the third stage of the motion can be obtained from Eq. (3.13) with the identification $\{\boldsymbol{\tau}_1, \ell_1\} \mapsto \{-\boldsymbol{\tau}_2, \ell_2\}$ and $\{\boldsymbol{\tau}_2, \ell_2\} \mapsto \{\boldsymbol{\tau}_3, \ell_3\}$. In this case, the frame of reference is chosen so that the second domain appears fixed and is centred at the location of the second kink. Note that the information about the orientation of the cell, carried by $\boldsymbol{\tau}_1$, is not lost since, as the kink angle θ is fixed, the same information is contained in the vector $\boldsymbol{\tau}_2$.

3.2.4 Helical geometry: Coarse-grained model

3.2.4.1 Helical propulsion

As the kink propagates along the bacterial body, as explained above the domains with different handedness rotate in opposite senses and therefore both propel the bacteria in the same direction. To account for the hydrodynamic effect of helical propulsion, we follow the treatment of Wada and Netz [50]. We consider a coarse-grained model in which we ignore end effects so that the hydrodynamic force per unit length acting on any of the helical domains is the same that acts on an infinite helix rotating around its axis. Following resistive-force theory, we know that the swimming velocity U^h of an infinite helix of radius R and pitch angle ϕ rotating with angular velocity ω_φ around its axis is given by [50]

$$U^h(\omega_\varphi) = \frac{R(1-\beta^h)\sin\phi\cos\phi}{(\beta^h + (1-\beta^h)\sin^2\phi)}\omega_\varphi, \tag{3.20}$$

where β^h is the ratio of the parallel to the perpendicular drag coefficient of the slender filament making up the helix. Therefore, the hydrodynamic force acting on each of the individual helical domains, and due to the rotation of the helical domain, has magnitude $|\mathbf{F}_i^h| \simeq \zeta_\parallel L_i U^h$, acting along the helical axis.

We next need to determine the angular velocity at which the domains rotate. Using a frame of reference in which the junction point (the kink) is fixed and the domains appear to grow and shrink, respectively, we parametrise the helical domains explicitly as (see Fig. 3.5)

$$\frac{\mathbf{x}_1^h}{R} = \cos\varphi_1 \mathbf{e}_x - \sin\varphi_1 \mathbf{e}_y - \frac{\varphi_1}{\tan\phi}\mathbf{e}_z, \tag{3.21}$$

$$\frac{\mathbf{x}_2^h}{R} = \cos\varphi_2 \mathbf{e}_x + \left(\frac{\varphi_2}{\tan\phi}\sin(2\phi) - \sin\varphi_2\cos(2\phi)\right)\mathbf{e}_y + \left(\frac{\varphi_2}{\tan\phi}\cos(2\phi) + \sin\varphi_2\sin(2\phi)\right)\mathbf{e}_z, \tag{3.22}$$

where $\varphi_i = \Phi_i(t) - \tilde{\varphi}_i = \Phi_{i_0} + (-1)^{i-1}\omega_{\varphi_i} t - \tilde{\varphi}_i$, with $\tilde{\varphi}_i \in [0, \Phi_i(t)]$, and Φ_{i_0} sets the initial length of the domains $L_{i_0} = \Phi_{i_0}/\tan\phi$. Hence the angular velocity at φ_i is $\dot{\varphi}_i = (-1)^{i-1}\omega_{\varphi_i}$. By continuity at the junction point ($\varphi_i = 0$) we have

$$\begin{aligned}\mathbf{e}_z \cdot (\dot{\mathbf{x}}_1^h + \dot{\mathbf{x}}_2^h) &= -R\left[\frac{\omega_{\varphi_1}}{\tan\phi} + \omega_{\varphi_2}\left(\frac{\cos(2\phi)}{\tan\phi} + \sin(2\phi)\right)\right] \\ &= -\frac{R(\omega_{\varphi_1} + \omega_{\varphi_2})}{\tan\phi}.\end{aligned} \tag{3.23}$$

During the first stage of the motion, in a small interval of time δt the kink moves a distance $(-1)^{i-1} R\omega_{\varphi_i}\cot\phi\,\delta t$ along the axis of the corresponding helical domains. As the kink travels at speed v_0 this same distance must be equal to $v_0\delta t$. Thus, we obtain the kinematic relationship $R(\omega_{\varphi_1} + \omega_{\varphi_2}) = 2v_0\tan\phi$. Furthermore, the torque on each of the domains is proportional to their arclength and their angular velocity, hence by torque balance we have $\omega_1 L_1 \simeq \omega_2 L_2$. Combining this with Eq. (3.20) and Eq. (3.23) leads to the helical hydrodynamic forces on each domain for the first stage of the swimming stroke

$$\begin{aligned}\hat{\mathbf{F}}_i^h &= (-1)^i \frac{2\beta(1-\beta^h)\cos^2(\theta/2)}{\beta^h + (1-\beta^h)\cos^2(\theta/2)}\ell_2(1-\ell_2)\boldsymbol{\tau}_i \\ &= \beta f(\beta^h, \theta)\ell_2(1-\ell_2)(-1)^i\boldsymbol{\tau}_i,\end{aligned} \tag{3.24}$$

with $i = 1, 2$ (no Einstein summation). Here we have used the condition $\ell_1 + \ell_2 = 1$, with $\ell_i = L_i/L$ and the continuity condition $2\phi = \pi - \theta$ (see Fig. 3.5).

In the second stage of the swimming stroke, the analysis is similar but the torque condition is now written $\omega_1(\ell_1 + \ell_3) = \omega_2\ell_2$ instead, hence $\hat{\mathbf{F}}_1^h = -f\beta\ell_1 d\boldsymbol{\tau}_1$, $\hat{\mathbf{F}}_2^h = f\beta(1-d)d\boldsymbol{\tau}_2$ and $\hat{\mathbf{F}}_3^h = -f\beta\ell_3 d\boldsymbol{\tau}_1$.

Finally the configuration in the third stage is analogous to that in the first stage discussed above, but now with $\hat{\mathbf{F}}_2^h = \beta f\ell_2(1-\ell_2)\boldsymbol{\tau}_1$ and $\hat{\mathbf{F}}_3^h = -\beta f\ell_2(1-\ell_2)\boldsymbol{\tau}_1$.

3.2.4.2 Effective drag ratio

A slender filament in a viscous fluid has a drag ratio $\beta_\infty = 1/2$ in the asymptotic limit of small cross sectional length relative to the filament length. Our effective rod model has a drag ratio β that captures the effective ratio of tangential to perpendicular drag and whose

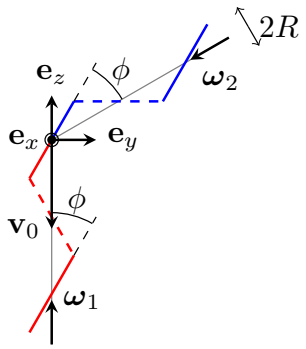

Fig. 3.5 Side view of the helical domains in the vicinity of the kink. The bottom left segment (red) represents the centreline of a right-handed helix while the top right segment (blue) represents the centreline of a left-landed helix. Both helices have the same radius R and pitch angle ϕ. The different domains rotate in opposite direction with angular velocities ω_1 and ω_2.

value should of course depend on the geometry of the helical body. In order to include more detail of the helical geometry of *Spiroplasma* in our calculation, we can derive the values of the parallel and perpendicular drag coefficients by considering the hydrodynamic forces acting on an infinitely long helix that is translating along its axis and perpendicular to it, respectively. We parametrise the material points on the helix as

$$\mathbf{x}^h = \mathbf{e}_x R\cos\varphi + \mathbf{e}_y R\sin\varphi + \mathbf{e}_z \frac{R\varphi}{\tan\phi}, \tag{3.25}$$

where the angle φ is related to the arclength by $s = R\varphi/\sin\phi$. The unit tangent vector to the helix centreline $\boldsymbol{\tau}^h$ is obtained by taking the derivative with respect to the arclength, and thus

$$\boldsymbol{\tau}^h = -\mathbf{e}_x \sin\varphi\sin\phi + \mathbf{e}_y\cos\varphi\sin\phi + \mathbf{e}_z\cos\phi. \tag{3.26}$$

We first calculate the force that acts on the helix when it moves along its axis at speed V. Using resistive-force theory we obtain the hydrodynamic force density

$$\begin{aligned}\mathbf{f}_a^{\parallel} &= -\left[\zeta_\perp^h(V\mathbf{e}_z - V\boldsymbol{\tau}^h\boldsymbol{\tau}^h\cdot\mathbf{e}_z) + \zeta_\parallel^h V\boldsymbol{\tau}^h\boldsymbol{\tau}^h\cdot\mathbf{e}_z\right]\\ &= -\left[(\zeta_\parallel^h - \zeta_\perp^h)V\cos\phi\,\boldsymbol{\tau}^h + \zeta_\perp^h V\mathbf{e}_z\right],\end{aligned} \tag{3.27}$$

where $\zeta_\perp^h$, $\zeta_\parallel^h$ are the drag coefficients perpendicular and parallel to the centreline of the helical filament. By definition, the coarse-grained parallel drag coefficient is the ratio between

longitudinal force per unit length and speed, i.e.

$$\zeta_{\parallel} \simeq -\frac{1}{LV}\int_0^L \mathbf{f}_a^{\parallel}\cdot\mathbf{e}_z\,\mathrm{d}s = \zeta_{\parallel}^h\cos^2\phi + \zeta_{\perp}^h\sin^2\phi. \tag{3.28}$$

Similarly, to derive the perpendicular drag coefficient we calculate the hydrodynamic force density acting on the helix when it moves perpendicular to the helical axis as

$$\begin{aligned}\mathbf{f}_a^{\perp} &= -\left[\zeta_{\perp}^h(V\mathbf{e}_x - V\boldsymbol{\tau}^h\boldsymbol{\tau}^h\cdot\mathbf{e}_x) + \zeta_{\parallel}^h V\boldsymbol{\tau}^h\boldsymbol{\tau}^h\cdot\mathbf{e}_x\right]\\ &= -\left[-(\zeta_{\parallel}^h-\zeta_{\perp}^h)V\sin\varphi\sin\phi\,\boldsymbol{\tau}^h + \zeta_{\perp}^h V\mathbf{e}_x\right].\end{aligned} \tag{3.29}$$

The coarse-grained perpendicular drag coefficient is thus given by

$$\begin{aligned}\zeta_{\perp} &\simeq -\frac{1}{LV}\int_0^L \mathbf{f}_a^{\perp}\cdot\mathbf{e}_x\,\mathrm{d}s\\ &= \frac{(\zeta_{\parallel}^h-\zeta_{\perp}^h)\sin^2\phi}{L}\int_0^L \sin^2\varphi(s)\,\mathrm{d}s + \zeta_{\perp}^h\\ &= \frac{\zeta_{\parallel}^h}{2}\sin^2\phi + \frac{\zeta_{\perp}^h}{2}(1+\cos^2\phi).\end{aligned} \tag{3.30}$$

Hence the drag ratio for the coarse-grained helical body is obtained as

$$\beta = \frac{\zeta_{\parallel}}{\zeta_{\perp}} = 2\frac{\beta^h\sin^2\phi+\cos^2\phi}{\beta^h\sin^2\phi+(1+\cos^2\phi)}. \tag{3.31}$$

Assuming an asymptotically slender helical filament, we may assume $\beta^h = \zeta_{\parallel}^h/\zeta_{\perp}^h = 1/2$. As a result, the effective helix drag ratio β is obtained as a function of $\theta \equiv \pi - 2\phi$ as

$$\beta = 2\left(\frac{3+\cos\theta}{7-\cos\theta}\right). \tag{3.32}$$

In the case where $\theta = \pi$, the helix becomes a straight filament ($\phi = 0$) and we recover $\beta = 1/2$ as expected. In the other extreme, $\theta = 0$ the helix becomes a circle and $\beta = 4/3$, indeed it is easier to move such filament in the plane that contains it than in the perpendicular direction. As a caveat, we note that Eq. (3.32) is strictly valid only for a helix with a large number of turns. Nevertheless, it is known that resistive-force theory approximates the actual force per unit length acting on a finite helical filament with good accuracy (error within 2%) [141], except for normal forces acting on the tips of the helix; these should however average as the helix rotates so as to account for negligible effects.

3.3 Planar motion, no helical geometry

We first analyse the model ignoring the helical geometry (i.e. we ignore the contributions from $\mathbf{F}_i^h$ and $\mathbf{N}_i^h$). Given that previous numerical results have shown that the swimming trajectories follow almost straight lines [50], we will also assume that the cell motion is planar. We will demonstrate that, under these assumptions, the orientation of the cell body does not change after one period of the swimming stroke. This allows us to define an effective swimming speed and a hydrodynamic efficiency with no ambiguity.

3.3.1 Kinematics

We start by considering the case in which the model cell moves in a plane, i.e. $\psi = 0$ or $\boldsymbol{\tau}_3 = -\boldsymbol{\tau}_1$. In this case we can define normal vectors $\boldsymbol{\nu}_i \equiv \hat{\mathbf{z}} \times \boldsymbol{\tau}_i$ where the unit vector $\hat{\mathbf{z}}$ is given by $(\sin\theta)\hat{\mathbf{z}} = \boldsymbol{\tau}_1 \times \boldsymbol{\tau}_2$. Defining $\boldsymbol{\tau} \equiv \boldsymbol{\tau}_1$, $\boldsymbol{\nu} \equiv \boldsymbol{\nu}_1$ we have $\boldsymbol{\tau}_2 = \cos\theta\boldsymbol{\tau} + \sin\theta\boldsymbol{\nu}$ and $\boldsymbol{\nu}_2 = -\sin\theta\boldsymbol{\tau} + \cos\theta\boldsymbol{\nu}$, hence we can express equations Eq. (3.13) and Eq. (3.18) for the components of the linear and angular velocities parallel and perpendicular to $\boldsymbol{\tau}_1$ as

$$\left(\tilde{\mathbf{J}} + \mathbb{I}_{\ell_2=d}\tilde{\mathbf{K}}\right) \cdot \begin{pmatrix} u_\tau \\ u_\nu \\ \omega \end{pmatrix} = \begin{pmatrix} -\ell_2\left[1 + (\beta - (1-\beta)\cos\theta)\cos\theta\right] \\ -\ell_2\left(\beta - (1-\beta)\cos\theta\right)\sin\theta \\ \ell_2^2 \sin\theta/2 \end{pmatrix}, \tag{3.33}$$

where $d = v_0\tau_p/L$ and $\mathbb{I}_{x=y}$ is an indicator function, which is 1 if $x = y$ and 0 otherwise. The symmetric matrices $\tilde{\mathbf{J}}$ and $\tilde{\mathbf{K}}$ have components

$$\tilde{J}_{11} = \ell_2(1-\beta)\sin^2\theta + \beta, \tag{3.34}$$
$$\tilde{J}_{12} = -\ell_2(1-\beta)\sin\theta\cos\theta, \tag{3.35}$$
$$\tilde{J}_{13} = -\ell_2^2\sin\theta/2, \tag{3.36}$$
$$\tilde{J}_{22} = 1 - \ell_2(1-\beta)\sin^2\theta, \tag{3.37}$$
$$\tilde{J}_{23} = \left[\ell_1^2 + \ell_2^2\cos\theta\right]/2, \tag{3.38}$$
$$\tilde{J}_{33} = \left[\ell_1^3 + \ell_2^3\right]/3, \tag{3.39}$$

while the nonzero components of $\tilde{\mathbf{K}}$ are

$$\tilde{K}_{13} = -d\ell_3\beta\sin\theta, \tag{3.40}$$
$$\tilde{K}_{23} = \ell_3\left(d\cos\theta - \ell_3/2\right), \tag{3.41}$$
$$\tilde{K}_{33} = \ell_3\left[\ell_3^2/3 + d^2\cos^2\theta(1-\beta)\right] + \ell_3\left[\beta d^2 - d\ell_3\cos\theta\right]. \tag{3.42}$$

Notice that due to the normalization condition $\ell_1+\ell_2+\ell_3=1$, the components of $\tilde{\mathbf{J}}$ in the second stage of the swimming stroke are the same as those in the first stage if we simply take $\ell_2=d$, where $d=v_0\tau_p/L$ is the normalised inter-kink distance. Further, as mentioned above, the linear and angular velocities in the third stage can be obtained from those in the first stage of the motion. Therefore we only need to solve Eq. (3.33) for $\{u_\tau,u_\nu,\omega\}$ and integrate to obtain the angular and linear displacements. Solving Eq. (3.33) in the first and second stages we find the angular and linear velocities in the body frame, $\{u_\tau^{(j)},u_\nu^{(j)},\omega^{(j)}\}$, where the superscript denotes the swimming stage, i.e. $j=1,2$.

Assuming that at the beginning of each stage of the motion $\boldsymbol{\tau}^{(j)}=-\hat{\mathbf{y}}$ and denoting by $\alpha^{(j)}(\ell)$ the angle that $\boldsymbol{\tau}^{(j)}$ makes with the $-y$ axis at $\ell_2=\ell$ for $j=1$ or $\ell_3=\ell$ for $j=2$, we have $\boldsymbol{\tau}(\alpha)=\sin\alpha\hat{\mathbf{x}}-\cos\alpha\hat{\mathbf{y}}$, $\boldsymbol{\nu}(\alpha)=\cos\alpha\hat{\mathbf{x}}+\sin\alpha\hat{\mathbf{y}}$ and the Cartesian components of the velocity are

$$u_x=u_\tau\sin\alpha+u_\nu\cos\alpha, \tag{3.43}$$

$$u_y=-u_\tau\cos\alpha+u_\nu\sin\alpha, \tag{3.44}$$

where we omit the superscript for simplicity. The angular displacement $\alpha^{(j)}$ is obtained by integrating the angular velocity $\omega^{(j)}$ in time, and therefore

$$\alpha^{(1)}(\ell)=\int_0^\ell\omega^{(1)}(\ell_2)\,\mathrm{d}\ell_2, \tag{3.45}$$

$$\alpha^{(2)}(\ell)=\alpha^{(1)}(d)+\int_0^\ell\omega^{(2)}(\ell_3)\,\mathrm{d}\ell_3. \tag{3.46}$$

In order to obtain the displacement $\mathbf{x}_T=\mathbf{X}_T/L$, we first calculate the position of the head during the first stage at $\ell_2=\ell$, i.e. $\mathbf{h}^{(1)}(\ell)=\mathbf{k}^{(1)}(\ell)+\ell\boldsymbol{\tau}^{(1)}(\ell)$. Here $\mathbf{h}^{(1)}$ is the dimensionless position of the head and $\mathbf{k}^{(1)}$ that of the kink, which is given by

$$\mathbf{k}^{(1)}(\ell)=\int_0^\ell\left[\mathbf{u}^{(1)}(\ell_2)+\boldsymbol{\tau}^{(1)}(\ell_2)\right]\mathrm{d}\ell_2. \tag{3.47}$$

The position of the head during the second stage at $\ell_3=\ell$ is

$$\mathbf{h}^{(2)}(\ell)=\mathbf{k}^{(2)}(\ell)+d\boldsymbol{\tau}_2^{(2)}(\ell)-(1-d)\boldsymbol{\tau}^{(2)}(\ell), \tag{3.48}$$

where $\mathbf{k}^{(2)}$ is the position of the first kink and is given by

$$\mathbf{k}^{(2)}(\ell)=\mathbf{k}^{(1)}(d)+\int_0^\ell\left[\mathbf{u}^{(2)}(\ell_3)+\boldsymbol{\tau}^{(2)}(\ell_3)\right]\mathrm{d}\ell_3. \tag{3.49}$$

It only remains to calculate the displacement of the head in the last stage of the motion $\mathbf{h}^{(3)}$. Using a symmetry argument, we will show below that this displacement is the same as that of the tail in the first stage.

3.3.2 No net rotation

Under our modelling assumptions, we notice that the swimming stroke is symmetric under a rotation by 180° in the plane of motion and a time reversal $t \mapsto T - t$ (see illustration in Fig. 3.6). Given that Stokes flows are reversible in time, changing the signs of the forces and torques acting on the body, or equivalently reversing time, changes the signs of the linear and angular velocity. Therefore, the angular displacement γ in the first half of the stroke [Fig. 3.6(a)-(b)] is the opposite of that obtained by reversing the propagation of the kink [Fig. 3.6(b')-(c')]. By the symmetry of the motion this is the same angular displacement as that of the second half of the stroke [Fig. 3.6(b)-(c)]. Therefore by reversibility of the Stokes equations, the total angular displacement at the end of the swimming stroke vanishes. The fact that the cell orientation does not change after one complete cycle is confirmed by numerical solutions of Eq. (3.45) and Eq. (3.46) shown in the bottom-left inset of Fig. 3.6 and displaying the angular displacement as a function of time for different values of the inter-kink distance.

Using the same symmetry argument, we deduce that the total displacement during the third stage of the motion is the same as the total displacement of the tail in the first stage. The later is given by $\mathbf{t}^{(1)}(d) = \mathbf{k}^{(1)}(d) + (1-d)\boldsymbol{\tau}^{(1)}(d) - \mathbf{t}^{(1)}(0)$. Therefore, after one stroke, the total linear and angular displacements are $\mathbf{x}_T = \mathbf{h}^{(2)}(1-d) + \mathbf{t}^{(1)}(d)$ (with $\mathbf{h}(t=0) = \mathbf{0}$) and $\phi_T = 0$ respectively.

We illustrate in Fig. 3.7 the trajectory of the centre of mass of the cell (black solid line), obtained by numerical solution of Eq. (3.33), in the case $d = 0.25$. The time evolution of the deformation is represented by the red (right-handed part of the cell) and blue (left-handed) shades, while the circles denote the end of each stroke and the cross the initial position of the centre of mass. Darker shades denote an increase in time. The kink travels in the negative y direction, while the cell swims in the positive y direction (see Movie 1 in Supplemental Material).

3.3.3 Swimming speed and efficiency

Since the body orientation does not change after one swimming stroke, we may define an effective swimming speed v_s as the ratio of the total distance travelled in one cycle to the

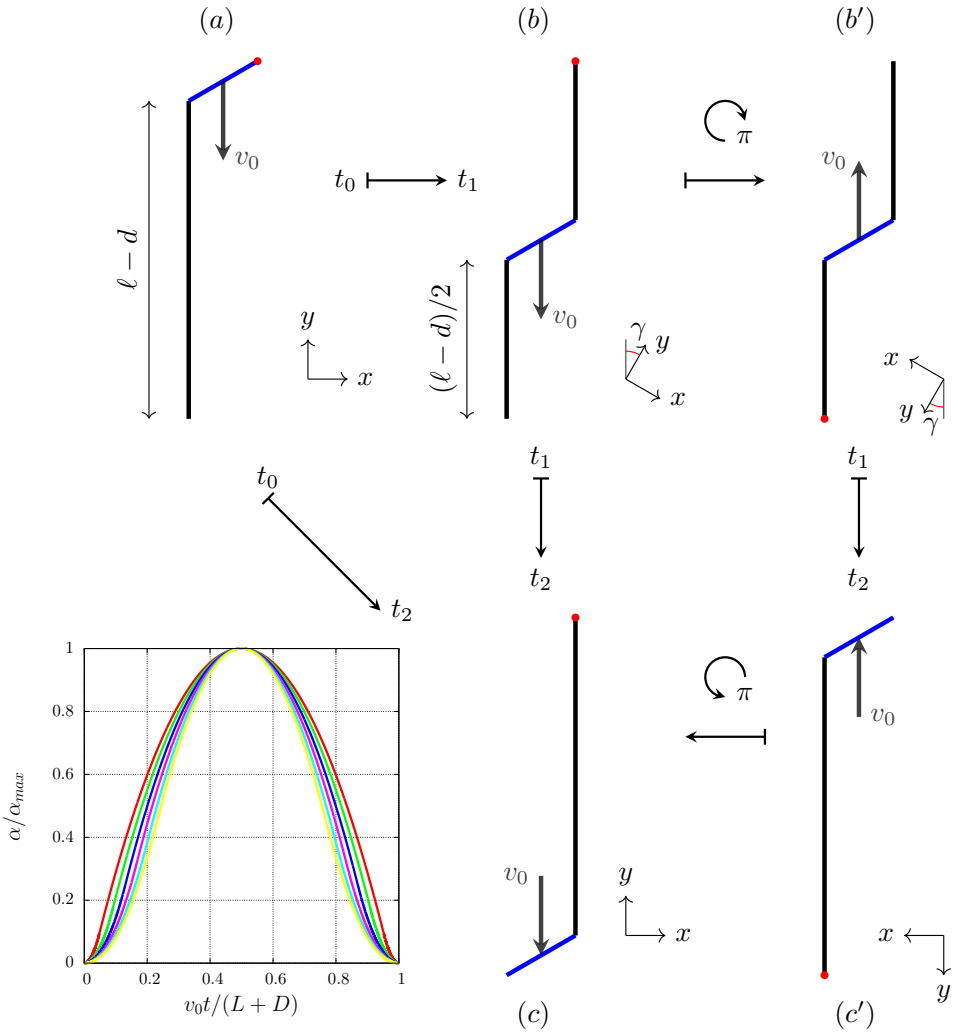

Fig. 3.6 Total angular displacement during the periodic stroke. Due to the time-reversibility of Stokes flow, the angular displacement γ during the first half of the stroke – i.e. going from configuration (a) to (b) – is the opposite of that occurring during the second half – i.e. going from (b') to (c'), or equivalently from (b) to (c). Hence the total angular displacement during the complete stroke vanishes. Bottom-left inset: Instantaneous angular displacements for $\theta = 110°$, $\beta = 1/2$ and values of d ranging from $d = 0.05$ (top) to $d = 0.3$ (bottom) with increments of 0.05 as obtained by a numerical integration of Eq. (3.33) using a midpoint Euler method.

period of the stroke, i.e.

$$v_s^2 \equiv \frac{L^2}{T^2}\left(x_T^2+y_T^2\right) = \frac{v_k^2\sin^2(\theta/2)}{(1+d)^2}\left(x_T^2+y_T^2\right). \tag{3.50}$$

We may also compute the average rate of energy dissipation (i.e. power) during one swimming stroke as

$$\dot{W} = \frac{1}{T}\int_0^T\int_0^L \mathbf{f}(s,t)\cdot\mathbf{v}(s,t)\,\mathrm{d}s\,\mathrm{d}t, \tag{3.51}$$

where the hydrodynamic force density $\mathbf{f}$ is given in Eq. (3.1) and where $\mathbf{v}$ is the instantaneous velocity of each helical domain axis. We can split the time integral from Eq. (3.51) in three parts, $\dot{W} = \dot{W}_1 + \dot{W}_2 + \dot{W}_3$, with each one corresponding to the three different stages of the swimming motion discussed in § 3.2.3. By symmetry of the stroke, we have $\dot{W}_1 = \dot{W}_3$ and thus $\dot{W} = 2\dot{W}_1 + \dot{W}_2$. Dividing by $\zeta_\perp L v_0^2$, the non-dimensional rates of energy dissipation in each stage are given by

$$\begin{aligned}\hat{\dot{W}}_1 = \frac{1}{1+d}\Bigg[&\int_0^d\int_0^{1-\ell_2}\mathbf{u}_1^{(1)}(\ell_2,\ell)\cdot\left(\beta\mathbf{A}_1^{(1)}+\mathbf{B}_1^{(1)}\right)\cdot\mathbf{u}_1^{(1)}(\ell_2,\ell)\mathrm{d}\ell\mathrm{d}\ell_2\\ &+\int_0^d\int_0^{\ell_2}\mathbf{u}_2^{(1)}(\ell_2,\ell)\cdot\left(\beta\mathbf{A}_2^{(1)}+\mathbf{B}_2^{(1)}\right)\cdot\mathbf{u}_2^{(1)}(\ell_2,\ell)\mathrm{d}\ell\mathrm{d}\ell_2\Bigg],\end{aligned} \tag{3.52}$$

$$\begin{aligned}\hat{\dot{W}}_2 = \frac{1}{1+d}\Bigg[&\int_0^{1-d}\int_0^{1-d-\ell_3}\mathbf{u}_1^{(2)}(\ell_3,\ell)\cdot\left(\beta\mathbf{A}_1^{(2)}+\mathbf{B}_1^{(2)}\right)\cdot\mathbf{u}_1^{(2)}(\ell_3,\ell)\mathrm{d}\ell\mathrm{d}\ell_3\\ &+\int_0^{1-d}\int_0^{d}\mathbf{u}_2^{(2)}(\ell_3,\ell)\cdot\left(\beta\mathbf{A}_2^{(2)}+\mathbf{B}_2^{(2)}\right)\cdot\mathbf{u}_2^{(2)}(\ell_3,\ell)\mathrm{d}\ell\mathrm{d}\ell_3\\ &+\int_0^{1-d}\int_0^{\ell_3}\mathbf{u}_3^{(2)}(\ell_3,\ell)\cdot\left(\beta\mathbf{A}_1^{(2)}+\mathbf{B}_1^{(2)}\right)\cdot\mathbf{u}_3^{(2)}(\ell_3,\ell)\mathrm{d}\ell\mathrm{d}\ell_3\Bigg],\end{aligned} \tag{3.53}$$

where $\mathbf{A}_i^{(j)} = \boldsymbol{\tau}^{(j)}\boldsymbol{\tau}^{(j)}$ and

$$\mathbf{u}_1^{(j)}(\ell',\ell) = u_\tau^{(j)}(\ell')\boldsymbol{\tau}^{(j)}(\ell') + \left(u_\nu^{(j)}(\ell')+\omega^{(j)}(\ell')\ell\right)\boldsymbol{\nu}^{(j)}(\ell'), \tag{3.54}$$

$$\begin{aligned}\mathbf{u}_2^{(j)}(\ell',\ell) = &\left(u_\tau^{(j)}(\ell') - \omega^{(j)}(\ell')\ell\sin\theta + 1 + \cos\theta\right)\boldsymbol{\tau}^{(j)}(\ell')\\ &+\left(u_\nu^{(j)}(\ell')+\omega^{(j)}(\ell')\ell\cos\theta+\sin\theta\right)\boldsymbol{\nu}^{(j)}(\ell'),\end{aligned} \tag{3.55}$$

$$\begin{aligned}\mathbf{u}_3^{(j)}(\ell',\ell) = &\left(u_\tau^{(j)}(\ell') - \omega^{(j)}(\ell')d\sin\theta\right)\boldsymbol{\tau}^{(j)}(\ell')\\ &+\left(u_\nu^{(j)}(\ell')+\omega^{(j)}(\ell')(d\cos\theta-\ell)\right)\boldsymbol{\nu}^{(j)}(\ell').\end{aligned} \tag{3.56}$$

Here the subscript $j = 1,2$ denotes the swimming stage and $(u_\tau^{(j)}, u_\nu^{(j)}, \omega^{(j)})$ are obtained by solving Eq. (3.33). As is commonly done in low-Reynolds number swimming, we compare

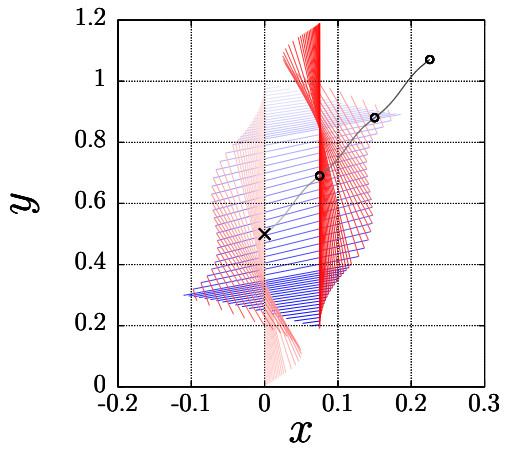

Fig. 3.7 Snapshots of swimming trajectory for the case $d = 0.25$ with darker shades denoting an increase in time. The instantaneous location of the centre of mass is represented by the black solid line. The trajectory over three strokes is shown. The shades represent the deformation of the cell body during the stroke (only the first stroke is shown) with the axis of the right-handed domain(s) shown in red and that of the left-handed domain represented in blue. The cross indicates the initial position of the centre of mass and the circles its position of the end of a stroke (See Movie 1 in Supplemental Material).

the dissipated power in one stroke, against the power dissipated by a straight model cell of length L dragged at speed v_s along its axis, i.e. $\hat{\dot{W}}_0 = \beta(v_s/v_0)^2$. The efficiency is then defined as the ratio

$$\eta \equiv \frac{\hat{\dot{W}}_0}{\hat{\dot{W}}} = \frac{\beta v_s^2}{v_0^2(2\hat{\dot{W}}_1 + \hat{\dot{W}}_2)}. \tag{3.57}$$

In the next section we include the additional forces and torques resulting from the helical geometry modelled at the coarse-grained level. We show that the cell does not rotate in that case either and therefore both Eq. (3.50) and Eq. (3.57) will remain applicable.

3.4 Planar motion, bistable helix

Now we turn our attention to the coarse-grained model in which we include the details of the helical geometry. The symmetry argument we used to deduce that the bacterium does not change its orientation after one stroke remains valid when we add the forces due to the rotation of the helical domains. Indeed as represented in Fig. 3.8, the swimming stroke is still symmetric under a rotation by 180° and time reversal. To every configuration with velocities $\{\mathbf{U}, \boldsymbol{\Omega}\}$ at time t it corresponds therefore a configuration $\{\mathbf{U}, -\boldsymbol{\Omega}\}$ at time $T - t$, hence the orientation remains unchanged after one stroke. From Eq. (3.24) and the condition

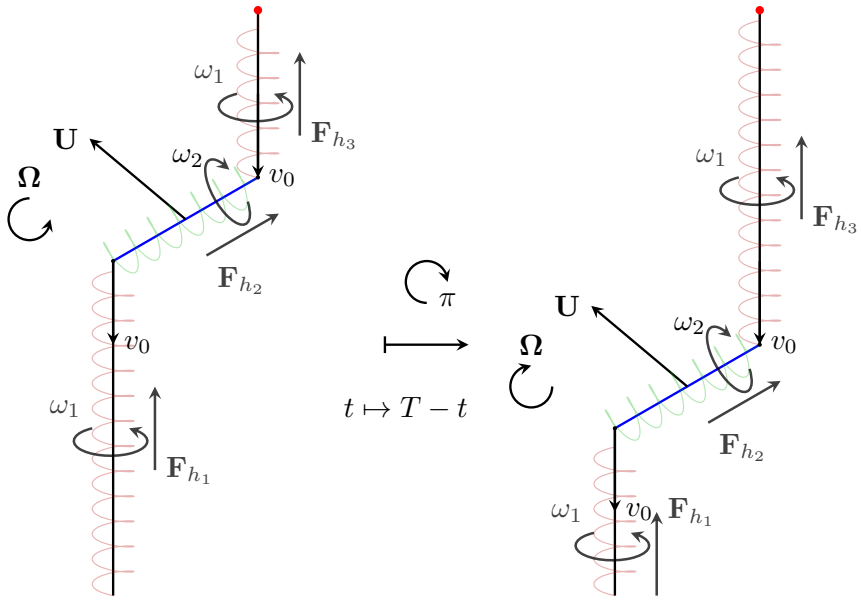

Fig. 3.8 The swimming gait remains symmetric even when the helical domains are included. Given a configuration with instantaneous linear and angular velocity $\{\mathbf{U}, \mathbf{\Omega}\}$ at time t it is possible to find the linear and angular velocities of the configuration at time $T - t$, where T is the period of the stroke, by rotating one half revolution and reversing the signs of the instantaneous forces.

$\ell_1 + \ell_2 + \ell_3 = 1$, the extra forces and torques due to the helical rotation are given by

$$\sum_i \hat{\mathbf{F}}_i^h = \beta f(\theta)(1-\ell_2)\ell_2 \left[\boldsymbol{\tau}(\cos\theta - 1) + \boldsymbol{\nu}\sin\theta\right], \tag{3.58}$$

$$\sum_i \hat{\mathbf{N}}_i^h = \beta f(\theta)\ell_2^2\ell_3 \sin\theta \hat{\mathbf{z}}, \tag{3.59}$$

in all three swimming stages. These extra terms enter on the right-hand side of Eq. (3.33) and therefore only $\{u_\tau, u_\nu, \omega\}$ are modified. Hence, equations Eq. (3.43)-Eq. (3.49) and the expressions for the swimming speed and the dissipated energy, Eq. (3.50) and Eq. (3.51) respectively, remain unchanged. Note that both equations, Eq. (3.52) and Eq. (3.53), are also valid in the case in which we consider helical propulsion. There is however an extra contribution to the dissipated energy that comes from the product $\mathbf{f}^h \cdot \mathbf{v}$. The total dissipated energy becomes therefore $\hat{W}^{(h)} = 2\hat{W}_1 + \hat{W}_2 + 2\hat{W}_1^{(h)} + \hat{W}_2^{(h)}$, where

$$\hat{W}_1^{(h)} = \frac{\beta f}{1+d}\int_0^d \left[\int_0^{1-\ell_2} -\ell_2 \boldsymbol{\tau}^{(1)}(\ell_2)\cdot \mathbf{u}_1^{(1)}(\ell_2,\ell)\,\mathrm{d}\ell + \int_0^{\ell_2} \ell_1 \boldsymbol{\tau}_2^{(1)}(\ell_2)\cdot \mathbf{u}_2^{(1)}(\ell_2,\ell)\,\mathrm{d}\ell\right]\mathrm{d}\ell_2, \tag{3.60}$$

$$\hat{W}_2^{(h)} = \frac{\beta f}{1+d}\int_0^{1-d}\left[\int_0^{1-d-\ell_3} -d\boldsymbol{\tau}^{(2)}(\ell_3)\cdot\mathbf{u}_1^{(2)}(\ell_3,\ell)\,\mathrm{d}\ell + \int_0^{d}(1-d)\boldsymbol{\tau}_2^{(2)}(\ell_3)\cdot\mathbf{u}_2^{(2)}(\ell_3,\ell)\,\mathrm{d}\ell - \int_0^{\ell_3} d\boldsymbol{\tau}^{(2)}(\ell_3)\cdot\mathbf{u}_3^{(2)}(\ell_3,\ell)\,\mathrm{d}\ell\right]\mathrm{d}\ell_3. \tag{3.61}$$

3.5 Asymptotic and numerical results

We now explore the results of our models, compare the predictions of asymptotic expansions to numerical simulations, and predict the optimal cell shape. Since the body does not reorient during each stroke, in order to obtain the swimming speed, we only need to calculate the linear displacement, $\mathbf{x}_T$. It is possible, in principle, to find an explicit solution to Eq. (3.33) (or its helical modification) and obtain $\{u_\tau^{(j)}, u_\nu^{(j)}, \omega^{(j)}\}$ as rational functions in ℓ_2 and ℓ_3 for $j=1$ and $j=2$ respectively. However, an analytical integration of such functions does not appear to be possible as the coefficients in these polynomials depend in a non-trivial way on β and θ.

We can however make some asymptotic progress by considering $d = D/L$ to be small, an assumption supported by experiments. Indeed according to Shaevitz et al. [38], $v_0 = v_k\cos\phi \approx 7.5\ \mu\mathrm{m/s}$, $\tau_p \approx 0.25\ s$ and $L \approx 6\ \mu\mathrm{m}$ hence $d \approx 1/3$. Moreover, as observed a posteriori in our simulations in Fig. 3.9, both the swimming speed and the efficiency depend only weakly in the inter-kink distance, and therefore the maximum swimming speed and efficiency are achieved at almost the same value of θ, for any value of d.

We therefore consider the asymptotic limit $d \ll 1$ and expand $\mathbf{x}_T$ in powers of d. To leading order, the components of the total displacement are obtained as

$$x_T^{(h)} = [(1-\beta)(1+\cos\theta)\sin\theta + \beta f\sin\theta]\,d + \mathscr{O}\left(d^2\right), \tag{3.62}$$

$$y_T^{(h)} = \left[(1-\beta)\sin^2\theta + \beta f(1-\cos\theta)\right]\frac{d}{\beta} + \mathscr{O}\left(d^2\right). \tag{3.63}$$

Substituting Eq. (3.32) into equations Eq. (3.62) and Eq. (3.63), with f as given in Eq. (3.24) and $\beta^h = 1/2$, and further substitution into Eq. (3.50), gives access to the asymptotic solution for the swimming speed as

$$\left(\frac{v_s^{(h)}}{v_k}\right)^2 = \frac{\sin^4\theta(5-3\cos\theta)^2(85-3\cos\theta+43\cos^2\theta+3\cos^3\theta)}{8(7-\cos\theta)^2(3+\cos\theta)^2}d^2 + \mathscr{O}\left(d^3\right). \tag{3.64}$$

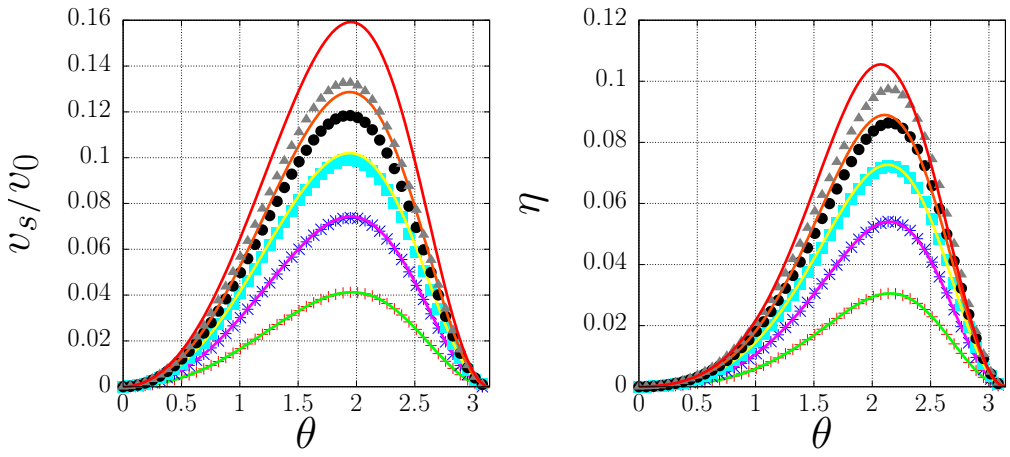

Fig. 3.9 Average swimming speed (left) and efficiency (right) of the model *Spiroplasma* as a function of the kink angle, θ. Top: Comparison between the full numerical solution (symbols) and the asymptotic expansion (line) for the swimming speed, Eq. (3.64), with d increasing from bottom to top from 0.05 to 0.25 in steps of 0.05. Bottom: Comparison between the full numerical solution (symbols) and the asymptotic expansion (line), for the efficiency Eq. (3.66), for the same values of d. In both cases that the dependence on d is very weak.

Furthermore, the total dissipated energy is given, at leading order in d, by

$$\hat{W}^{(h)} = \frac{(1+\cos\theta)(17+4\cos\theta+3\cos^2\theta)}{7-\cos\theta} d + \mathscr{O}\left(d^2\right). \tag{3.65}$$

The swimming efficiency is then obtained by substituting equations Eq. (3.64) and Eq. (3.65) into Eq. (3.57), and we obtain

$$\eta^{(h)} = \frac{\sin^2\theta(5-3\cos\theta)^2(85-3\cos\theta+43\cos^2\theta+3\cos^3\theta)}{2(7-\cos\theta)^2(3+\cos\theta)(17+4\cos\theta+3\cos^2\theta)} d + \mathscr{O}\left(d^2\right). \tag{3.66}$$

We illustrate in Fig. 3.9 the comparison between the full numerical solutions of our model and the asymptotic expansion up order d^3, for values of the inter-kink distance between $d = 0.05$ and $d = 0.25$. Although the agreement is quantitative only for the smallest values of d, both the swimming speed and the efficiency depend only weakly on d and the maxima are achieved at approximately the same value of θ for all d. The bending angle, $\theta^*_{v_s}$, that maximises the swimming speed (at leading order in d) satisfies $g_{v_s}(\cos\theta^*_{v_s}) = 0$, where

$$\begin{aligned} g_{v_s}(\xi) = {} & 14425 + 24343\xi - 19895\xi^2 + 25631\xi^3 \\ & - 15229\xi^4 - 4963\xi^5 + 219\xi^6 + 45\xi^7, \end{aligned} \tag{3.67}$$

whose only real root of modulus less than unity is $\xi \simeq -0.391$ which corresponds to optimal values of $\theta_{v_s}^* \simeq 113^\circ$ or $\phi_{v_s}^* \simeq 33.5^\circ$. On the other hand, for the swimming efficiency, the angle θ_η^* that maximises $\eta^{(h)}$ (at leading order in d) satisfies $g_\eta(\cos\theta_\eta^*) = 0$, where

$$\begin{aligned} g_\eta(\xi) = {} & 115175 + 116603\xi - 80524\xi^2 + 132372\xi^3 \\ & - 73638\xi^4 - 40830\xi^5 - 18348\xi^6 - 3372\xi^7 \\ & - 9\xi^8 + 27\xi^9, \end{aligned} \tag{3.68}$$

whose only real root of modulus less than unity is $\xi \simeq -0.539$ which corresponds to an optimum of $\theta_\eta^* \simeq 122^\circ$ or $\phi_\eta^* \simeq 29^\circ$. Our mathematical model predicts therefore optimal shapes for *Spiroplasma* that are close to those seen experimentally ($\phi \simeq 35^\circ$).

3.6 Discussion

Summary

In this chapter we derived a hydrodynamic model to describe the motility of *Spiroplasma*. Our simple model includes details of the helical geometry of the bacterium at a coarse-grained level and is able to capture the main features of *Spiroplasma* swimming motion. Our results confirm those of previous numerical simulations [49, 50] which also agree with experimental observations [38, 40–46]. In detail, our model predicts that: (i) *Spiroplasma* swims in the direction opposite to the kink pair propagation, with a swimming speed v_s proportional to the kink speed v_0; (ii) For values of the dimensionless inter-kink distance $d = D/L$ in the experimental range, the swimming speed is $v_s \simeq 1 - 2\,\mu\mathrm{m/s}$; (iii) In the case in which the motion occurs in a plane, we found that *Spiroplasma* does not reorient after one complete stroke; (iv) The maximum swimming efficiency is achieved for a pitch angle of $\phi_\eta^* \simeq 29^\circ$ whilst the maximum swimming speed is attained at $\phi_{v_s}^* = 33.5^\circ$.

Comparison with experiments

Experimental values for the swimming speed range between $v_s \simeq 1 - 3\,\mu\mathrm{m/s}$ while the kink speed lies between $v_k \simeq 10 - 40\,\mu\mathrm{m/s}$. Similar values are also reported in the numerical study of Wada and Netz [50]. Therefore our theoretical results are consistent both with experiments and previous computational models.

The numerical simulations of our model show that both the swimming speed and the efficiency depend only weakly on the inter-kink distance, which allowed us to determine the position of their maxima by considering only the lowest order term in their asymptotic expansions in powers of d. Our model predicts that the maximum swimming speed is attained

at a pitch angle $\phi^*_{v_s} = 33.5^\circ$ very close to the experimental measured one, $\phi = 35^\circ$. Although the maximum efficiency is not achieved at the same value of ϕ, the value of the efficiency $\eta(\phi = 35^\circ)$ is not far from the maximum. For the case $d = 0.25$ for instance, $\eta(\phi = 35^\circ) \simeq 0.13$ which differ in 7% with respect to the maximum $\eta_{max} \simeq 0.14$. Considering the fact that we are modelling the dynamics of the helical domains only at a coarse-grained level, we regard this agreement as excellent, and it is also consistent with previous numerical models [49, 50].

Kink propagation *vs* wave propagation

Wave like motion is commonly observed in biological microswimmers and it is often the preferred choice for mathematical modelling of flagellar motion [3, 5]. It is therefore natural to ask how does motion by kink-pair propagation compares to wave propagation in terms of speed and efficiency. Note first that kink-pair propagation is itself a non-reciprocal deformation, therefore locomotion in our model is possible even without considering the external forces $\mathbf{F}_{h_i}$. Indeed a deforming rod propagating kinks along its body is similar to the Purcell's 3-link swimmer [2]. Previous studies have explored the optimal gait for low-*Re* swimmers consisting of multiple links. In particular Alouges et al. [142] found that the displacement for a finite size multi-link swimmer of fixed size L scales as $\Delta x \sim L/N$. Therefore, for a fixed gait of period T, the speed $v = \Delta x/T$ of a multi-link swimmer decays as the number of links increases. In terms of efficiency, it has been shown that for a filament beating in a plane, the optimum flagellar shape is that of a travelling sawtooth wave [143]. These result ignore the fact that most of the energy required to deform an active flagellum is lost in irreversible deformation of the filament rather than through viscous dissipation in the surrounding fluid. When this fact is taken into consideration the optimal shape turns out to be a regularisation of the sawtooth wave consisting of arcs of constant curvature joined by straight filament segments, in agreement with experimental observations of flagellated microorganisms [144]. In the case of spiroplasma however, most of the propulsive force is due to the rotation of the helical domains rather than the propagation of kinks, as suggested by the model of Wada and Netz that ignores kink propagation and still predicts the correct swimming speed and efficiency [50]. Note as well that internal dissipation is not considered in our model. Throughout the chirality transformation, the helical domains remain undeformed away from the kink. Therefore most of the internal dissipation is localised at the kink and it is safe to ignore it in the definition of the hydrodynamic efficiency.

Motion in three dimensions

In previous numerical simulations, it has been observed that *Spiroplasma* trajectories are

almost rectilinear [49, 50], a result which is consistent with our theoretical prediction of no reorientation in the case of planar motion. Movement in a plane will take place only if the right-handed domains are parallel, in other words, there is planar motion only if the angle ψ in §3.2.3 vanishes. In the case where we have $D = nP$ with $n \in \mathbb{N}$ then the axes of the right-handed domains are parallel. According to experiments $d \simeq 1/3$ (see §3.4) which means that $D \simeq 2\,\mu$m. On the other hand, the pitch of the cell body is $P \simeq 1\,\mu$m, hence $D \simeq 2P$. Therefore, the assumption of planar motion is the biologically-relevant limit.

Fluctuations in the time between chirality transformations may be accounted by considering the angle ψ to be non-vanishing but small. In this case we can expand the linear and angular velocities in powers of ψ, $\mathbf{u} = \mathbf{u}_0 + \psi\mathbf{u}_1 + \mathscr{O}(\psi^2)$ and $\boldsymbol{\omega} = \boldsymbol{\omega}_0 + \psi\boldsymbol{\omega}_1 + \mathscr{O}(\psi^2)$, where $(\mathbf{u}_0, \boldsymbol{\omega}_0)$ correspond to the planar motion presented above. By expanding the resistance matrix and the right-hand side of Eq. (3.18), it is possible to show that $\mathbf{u}_0 \cdot \mathbf{u}_1 = \boldsymbol{\omega}_0 \cdot \boldsymbol{\omega}_1 = 0$. As a consequence, for small enough values of ψ, the motion corresponds to a helix with a large radius $R_h \sim \psi^{-1}$ and the trajectories are effectively straight. Note that for out-of-plane deformations, the absolute distance travelled by the centre of mass of *Spiroplasma* in one cycle is expected to be smaller to that of a cell deforming on the plane, due to the extra curvature of the trajectory. Since the stroke period is the same, we expect a cell undergoing planar deformation to always swim faster than a cell moving out of plane. This suggest that *Spiroplasma* might have evolved to regulate the time between kinks so that the inter-kink distance closely matches an integer number of helical turns.

Diffusion

Experimental observations reveal that the kink propagation can be reversed, and in homogeneous media this reversal rate is constant [46]. According to our model, the cell body does not reorient after one stroke. Moreover, by reversibility of Stokes flow, we know that the cell body traces back its path when the chirality transformation is reversed. The consequence is rather severe as it means that when swimming in free space, the cell body can only reorient by thermal noise.

This motion can be modelled as a run-reverse pattern, characterised by a persistence parameter $\kappa = \langle \cos\theta_t \rangle$ and a mean path length $v_s \lambda_r^{-1}$ [122] (see §2.2.1). Here θ_t is the angle between tumbling events, which for a run-reverse pattern is $\theta_t = \pi$, hence $\kappa = -1$. The swimming speed is v_s and λ_r^{-1} is the mean arrival time for a reversal event, which we assume follows an exponential distribution. In the absence of thermal noise, the velocity correlation function is given by $\mathscr{C}(t) = v_s^2 e^{-2\lambda_r t}$. Assuming that the process that generates the chirality change is independent from thermal noise, the velocity correlation function including thermal noise is then simply given by $\mathscr{C}(t) = v_s^2 e^{-2(\lambda_r + D_r)t}$, where $D_r = k_B \Theta \zeta_r^{-1}$

is the rotational diffusion coefficient, with k_B the Boltzmann constant and Θ the absolute temperature. Here we use ζ_r to denote the rotational drag coefficient, given approximately by $\zeta_r \simeq \pi\mu L^3/3\ln(L/R)$, where L and R are the length and radius of *Spiroplasma*, and μ is the dynamic viscosity of the medium [145]. Integrating twice $\mathscr{C}(t)$ and taking the long-time limit, we obtain the effective diffusion constant $4D_e = 3D_\perp + v_s^2/(2D_r + 2\lambda_r)$, where $D_\perp = k_B\Theta\zeta_\perp^{-1}$ is the translational thermal diffusion coefficient. Note that the translational drag $\zeta_\perp$ is given by Eq. (3.30) with $\zeta_\perp^h = 4\pi\mu L/\ln(L/R)$ [145]. This result is consistent with the analysis presented by Wada and Netz [49], and extends it to include persistence that, for a run-reverse motion, hinders diffusion.

Chemotaxis

It is also known that *Spiroplasma* cells can perform chemotaxis. Although it is not yet fully understood, it has been observed that the presence of certain amino acids changes the reversal rate of kink propagation, and the cell appears to twitch [46, 52, 53]. When viewed as a run-reverse motion with rotational diffusion, a change in the reversal rate modifies the mean path length. Indeed a lower reversal rate in high attractant concentration regions results in longer trajectories before a change in the direction of motion occurs, as a result the random walk is biased up the gradient. Experimental observations have shown that the biochemical machinery that controls chemotaxis in *Spiroplasma* is unrelated to the conventional two-component system of other bacteria such as *E. coli* [46]. Nevertheless, given the small size of *Spiroplasma*, we can still assume that, similar to *E. coli*, *Spiroplasma* can only measure differences in chemical concentrations over time. Under this assumption, the de Gennes model for chemotaxis can be applied [132]. In this approximation, the drift speed of the cell is given by $v_d = v_s^2|\nabla c|\lambda_k G(K)/(2\lambda_k + 2D_r)^2$ where the function G is given by $G(K) = \int e^{-2(\lambda_k + D_r)t}K(t)\,\mathrm{d}t$ and $K(t)$ is the cell memory kernel satisfying the adaptability condition $\int_0^\infty K\,\mathrm{d}t = 0$ (see §2.2.2). The experimental observations of Liu et al. [46] suggest that *Spiroplasma eriocheiris* performs chemotaxis without adaptation. On the other hand, Daniels and Longland [53] observed that *Spiroplasma melliferum* responds only to gradients and not absolute values of concentration, which suggest adaptation. In any case, the de Gennes model is appropriate, as we can assume either that the timescale for adaptation is very large but finite or that *Spiroplasma* can sense changes in concentrations instantaneously [134] (see §6.3.1).

Outlook

Further extensions to our model could consider the presence of non-homogeneous viscosity fields. It is known that *Spiroplasma*, as other helical shaped bacteria, swims faster in more

viscous environments [52, 70, 71]. While the swimming speed increases, the kink velocity remains the same. As proposed by Magariyama and Kudo [146], in a linear-polymer solution, the motion of a slender rod is restricted mostly in the perpendicular direction to its axis, as long as its length is much larger than the characteristic size of the polymer network. In that case, we can approximate the new drag ratio by $\beta_p \simeq (\mu_0/\mu_p)\beta$ where μ_p is the viscosity of the polymeric solution and μ_0 that of the standard medium. Assuming that the inter-kink distance does not depend on the viscosity of the medium and noticing that at leading order $|\mathbf{x}_T| \propto (3+\cos\theta-\beta)$, we should expect larger swimming velocities for increasing viscosity. Besides an increase in swimming speed, it would also be possible for a non homogeneous viscosity field to generate a torque that reorient the cell body. Like the bacterium *H. pylori* living in the mucous layer in the stomach [74], *Spiroplasma* should then be able to display viscotaxis [78].

Chapter 4

Swimming Across Viscosity Gradients

4.1 Introduction

Recently, motivated by the process through which *H. pylori* crosses the intestinal mucus layer, Gonzalez et al. [147] conducted an experimental study on the dynamics of helical swimmers moving through the interface between two immiscible fluids. Depending on the orientation of the swimmer and the different stages of penetration (in particular whether the head or the tail reaches first the interface), the interface was shown to dramatically affect the swimmer. However, interfacial tension is believed to not play a significant role in the mucus zone, where instead high viscosity gradients are dominant. This led to a different experimental set up in which the swimmer moves across a solution of variable viscosity (see details in §4.2 below). The results show that the swimmer slows down as it crosses from a region of low to high viscosity head-forward (i.e. in the pusher mode) but that it speeds up when it approaches the interface with its tail forward (puller mode). In contrast, the swimmer always slows down when it moves down the gradient, regardless of its orientation. Here we propose a model to explain this results.

Inspired by a previous study on viscotaxis [78], we assume that the standard Newtonian Stokes drag laws are locally valid, and that the swimming behaviour is determined by an instantaneous balance between viscous propulsion and drag. For motion up the viscosity gradient, our model predicts a decrease (resp. increase) in the swimming speed for pusher head-forward (resp. puller tail-forward) orientation, which is consistent with the experimental observations. Due to the reversibility of Stokes flows, our model predicts the opposite behaviour when the swimmer moves down the gradient. However, the opposite is observed in experiments. Further analysis of the experiments reveal that when the swimmer moves down the gradient it entrains a portion of the high-viscosity fluid into the low-viscosity region, regardless of its orientation. This drift volume increases the apparent density of the swimmer,

thereby slowing it down due to gravitational forces. Including a buoyancy term in our model to account for this effect allow the theoretical predictions to come closer to the experimental observations.

This chapter is organised as follows. In §4.2 we describe the synthetic swimmer, its characteristic geometrical parameters and the experimental setup. The experimental results are presented in §4.3, with a focus on the swimming speed as a function of the swimmer position relative to the fluid interface. The mathematical model for a sharp viscosity gradient is developed in §4.4 and its extension for a continuous viscosity profile is presented in §4.5. We next compare our model with the experimental results in §4.6; a modified model that takes into account the fluid entrainment is discussed at the end of this section. Finally, we discuss our results in §4.7.

4.2 Experimental setup

A synthetic swimmer is used to analyse the dynamics of a microorganism moving in environments of variable viscosity. The helical swimmer developed by the group of Roberto Zenit at the National University of Mexico (UNAM), is shown schematically in Fig. 4.1(a), it consists of a cylindrical head and a right-handed helical tail, both of which are rigid; pictures of the swimmer are shown in §4.3. The head of the swimmer contains a small magnet and is made to rotate at a fixed rate by the action of an external magnetic field. Details on the setup can be found in Ref. [148]. The speed of the swimmer can be controlled by changing the rotation rate of the external magnetic field, and the swimmer remains force-free throughout. The swimmer moves vertically in either the upwards or downwards direction and the swimming orientation (head or tail forward) can also be changed. Since the helical tail is chiral, reversing the rotation direction of the tail leads to pusher and puller mode swimming.

A viscosity gradient is produced by slowly superposing two miscible viscous liquids onto each other. They are placed, in sequence, in a transparent tank initially leading to a two-layer sharp viscosity gradient, as shown in Fig. 4.1(b). The bottom liquid is prepared by mixing glucose (530 ml) and water (100 ml), to have a viscosity of approximately $\mu_+ = 2.74$ Pa $\cdot$ s, at room temperature. To ensure that the interface remains horizontal, a small amount of salt is added to this liquid (30 g of NaCl) to increase its density slightly, $\rho_+ = 1367.4$ kg/m^3. The viscosity and density of the top fluid are $\mu_- = 0.55$ Pa $\cdot$ s and $\rho_- = 1309.7$ kg/m^3, respectively.

The container, with dimensions $8.9\times8.9\times18$ cm^3, with the swimmer inside is placed within the rotating Helmholtz coil, as in previous experiments [87, 88, 147]. To reduce the crystallization of the glucose solutions at the free surface, the container is kept closed at all

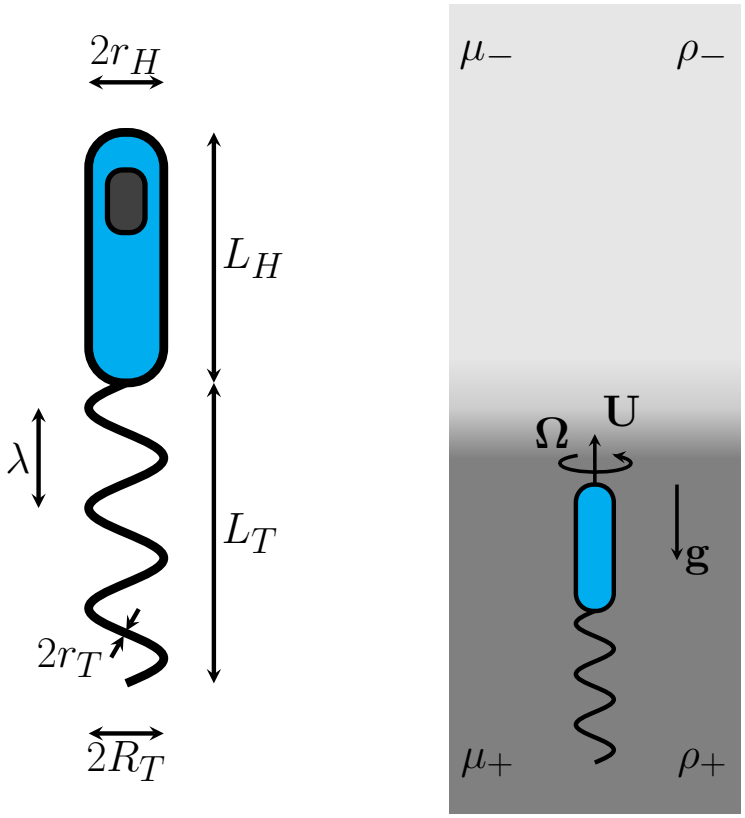

Fig. 4.1 Experimental setup. (a) Schematic representation of the helical swimmer. The dimensions of the device are: $2r_H = 4.5$ mm; $L_H = 16$ mm; $L_T = 16$ mm; $\lambda = 5.3$ mm; $2R_T = 4.5$ mm; and the pitch angle $\psi = 45^\circ$. The thickness of the wire is $2r_T = 0.9$ mm. (b) In this example, the swimmer moves head-forward from a high-to-low viscosity fluid through a sharp gradient and here gravity is pointing downwards. Note that in all figures the dark and light gray denote high and low viscosity regions, respectively.

times. As explained above, the system is slightly density-stratified. Therefore, the swimmer cannot be neutrally buoyant in both top and bottom fluids. The density of the swimmer is adjusted to make it as close as possible to that of the light fluid: $\rho_{\text{swimmer}} \approx 1270$ kg/m^3. Hence, the swimmer is slightly buoyant for both fluids.

All experiments are conducted at a fixed rotation rate of the swimmer, $\Omega/2\pi = 2.92$ Hz and the swimmer moves at a constant terminal swimming speed, $U_0 \simeq 1.5 - 3.5$ mm/s in one of the fluids. Due to the slight density mismatch the terminal speed is different for each fluid and for each direction of motion. The maximum Reynolds number is $Re = 0.035$, using μ_-, r_H and the maximum swimming speed $U_0 = 3.3$ mm/s, as the characteristic viscosity, length and speed.

4.2.1 Evolution of the viscosity gradient in time

If left undisturbed, the two-fluid layer slowly mix, leading to a diffuse viscosity gradient [Fig. 4.2 (b)]. By conducting experiments at different times after the two-layer fluid is first prepared, the influence of the strength of the viscosity gradient on the swimming process can be tested. The thickness of the viscosity gradient is quantified by applying the following procedure. A dye is added to the low viscosity gradient, this allows to track the concentration of glucose and assign a pixel-intensity to it. We calculate the concentration gradient along the z-axis at time t by solving the diffusion equation

$$\frac{\partial C}{\partial t} = D\frac{\partial^2 C}{\partial z^2}, \tag{4.1}$$

where D is the diffusivity and z the distance from the initial interface. Using the Green's function method and the initial distribution $C(z,0) = C_0(1-\theta(z))$, where $\theta(z)$ is the Heaviside step function, we obtain the viscosity distribution as

$$\frac{C(z,t)}{C_0} = \frac{1}{2}\left(1 - \text{erf}\left(\frac{z}{\sqrt{\Delta^2/2}}\right)\right), \tag{4.2}$$

where $\text{erf}(x)$ is the error function, $\Delta = 2\sqrt{2Dt}$ is the width of the transition region and C_0 is the initial glucose concentration on the high viscosity fluid. Next, we assume that the viscosity field μ is related to the concentration C through the Arrhenius equation $\mu(C) = Ae^{BC/C_0}$, where the constants A and B depend on the properties of the fluid mixture [149].

We show in Fig. 4.2 (b) the viscosity profile obtained experimentally (data points) with the pixel intensity corresponding to the viscosity of each fluid. Here $z = 0$ denotes the position of the fluid interface. The plot is presented in terms of the dimensionless distance

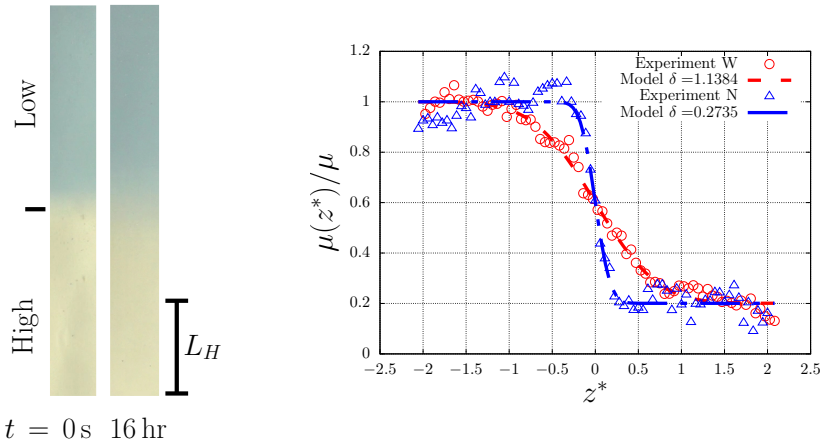

Fig. 4.2 (a) The viscosity gradients at $t = 0$ and 16 hours. (b) Normalized viscosity, $\mu(z)/\mu$, as a function of normalized distance from the interface, $z^* = z/L_H$. Data points represent the pixel intensity, which serves as a proxy for the viscosity profile soon after the initial setup ($\delta = \Delta/L_H = 0.2735$) and sixteen hours afterwards ($\delta = 1.1384$). Dashed lines represent the best fit of the Arrhenius equation $\mu(C) = Ae^{BC/C_0}$ with C/C_0 given by Eq. (4.2), and $A = \mu_-$ and $B = \ln(\mu_+/\mu_-)$.

$z^* = z/L_H$, where L_H is the length of the head. Negative values of z^* correspond to the bottom fluid, which is more viscous than the high-viscosity fluid located at $z^* > 0$. Choosing A and B so that the viscosity profile matches the initial configuration at $t = 0$, that is $A = \mu_-$ and $B = \ln(\mu_+/\mu_-)$, we can fit the Arrhenius equation to the experimental data (with C/C_0 given by Eq. (4.2)) and find the thickness of the transition region $\delta = \Delta/L_H$ as a function of time. The fits are shown in Fig. 4.2 as dashed lines. In the case where the measurement is conducted soon after the gradient is set up, referred to as a "narrow gradient" (N) in what follows, a value of $\delta = 0.2735$ closely fits the data. For experiments conducted sixteen hours after the setup, which we will refer to as "wide gradient" (W), the value of $\delta = 1.1384$ closely reproduces the experiments.

It is possible to determine the fluid density, $\rho(z,t)$ in a similar way. Assuming an initial condition $\rho(z) = \rho' + \theta(z)(\rho - \rho')$, an expression analogous to Eq. (4.2) can be obtained for $\rho(z,t)$.

4.2.2 Four different swimmer-viscosity interactions

Four distinct swimmer-viscosity interactions can be considered. First, the swimmer can move head-forward (pusher mode) or tail-forward (puller mode). Additionally, the swimmer can be made to swim across the interface from low to high viscosity (i.e. from μ_- to μ_+) or from

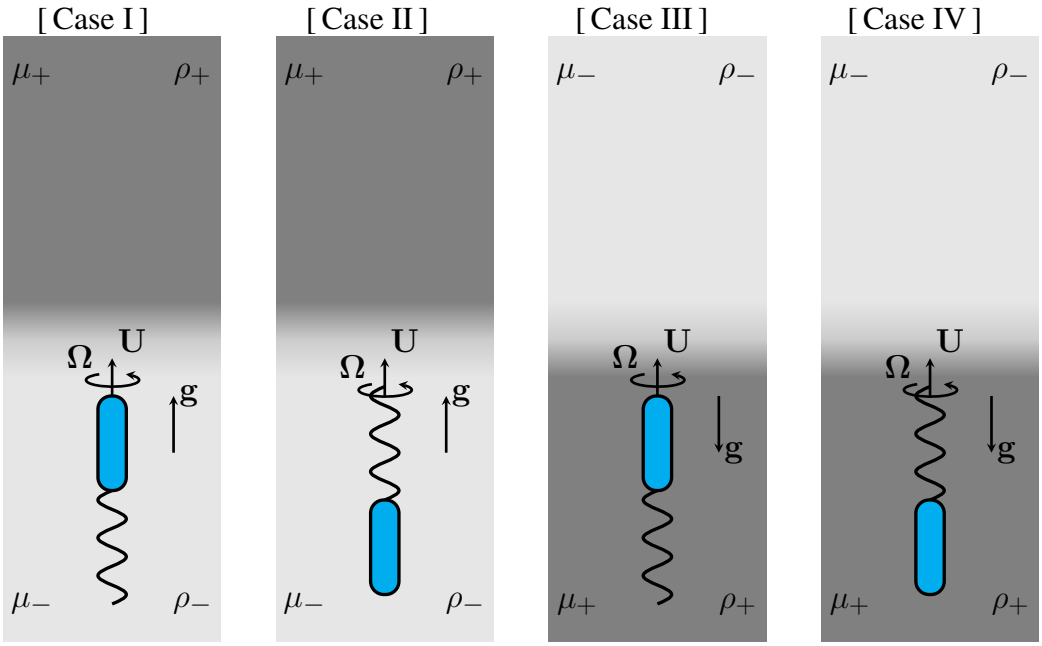

Fig. 4.3 The four swimmer-viscosity interaction configurations for motion across the viscosity gradient. In all cases $\mu_- < \mu_+$ and the motion is in the upwards direction; note that gravity points upwards in (a) and (b), and downwards in (c) and (d). Notice as well the change in the sense of rotation of the tail, depending on its orientation. All conditions are described in Table 4.1.

CASE	DIRECTION	GRADIENT
I	head-forward (pusher)	positive
II	tail-forward (puller)	positive
III	head-forward (pusher)	negative
IV	tail-forward (puller)	negative

Table 4.1 The four possible swimmer-viscosity interactions depicted in Fig. 4.3.

high to low viscosity (i.e. from μ_+ to μ_-). These four scenarios are depicted schematically in Fig. 4.3 and summarized in Table 4.1. In what follows, we will refer to the viscosity gradient as being positive when the swimmer moves from a low to a high viscosity region, or negative in the opposite case, from high to low.

Before each experiment is conducted, the swimmer is slowly placed in the desired initial position and alignment, as far as possible from the interface, such that the viscosity gradient is not significantly disturbed. The motion is recorded with a video camera (920×1080 pixels, Sony RX10II, 60 frames per second), using the same distance from the setup to the camera and lens magnification for all experiments. If the traveling time of the swimmer across the two-fluid layer is smaller than the diffusion time, the viscosity gradient can be considered

to be approximately constant. Although, in principle, it is possible to conduct experiments considering different values of the viscosity gradient we only consider two cases here: a narrow gradient (N, δ=0.274) and a wide gradient (W, δ=1.138), as described above with a viscosity ratio $\mu_+/\mu_- \simeq 5$.

4.3 Experimental results

We now analyse the four configurations described in Table 4.1, for which we find significantly contrasting behaviors. In all experiments, the position z measures the distance from the leading edge of the swimmer to the undisturbed interface; negative and positive z values denote therefore locations before and after reaching the interface, respectively.

4.3.1 Case I: Head-first, positive viscosity gradient

In the first case, the swimmer is placed initially at the upper part of the tank. The rotating magnetic field forces the swimmer to move downwards, it quickly reaches the steady-state speed, $U_0^{\mu_-} = 1.75$ mm/s. After the interaction with the interface, the swimmer attains a new steady-state speed $U_0^{\mu_+} = U_+ = 2.5$ mm/s. The mismatch in the swimming speeds comes from the density stratification of the fluid solution.

In Fig. 4.4 we show a sequence of images illustrating the crossing process. The time is given in dimensionless terms, $t^* = tU_+/L_H$, and $t^* = 0$ represents the instant at which the swimmer (in this case the head) first reaches the interface. Along with the images, Fig. 4.5 (a) shows the normalized position of the swimmer, $z^* = z/L_H$, as a function of the normalized time, t^* (note that the images have been flipped so that the swimmer appears to move upwards); Fig. 4.5 (b) shows the normalized speed U/U_+ as a function of z^*.

As the swimmer approaches the viscosity gradient, its speed progressively decreases, Fig. 4.4 (a-b). When the head of the swimmer begins to cross the interface [$z^* \approx 0$, Fig. 4.4 (b)], the speed decreases sharply reaching a minimum value at $z^* \approx 0.5$. During this period, the speed is so small that the measurement becomes inaccurate (very small displacement in between frames), characterized by the noisy velocity in the region $0.2 < z^* < 1$. Once the head has completely passed, the swimmer experiences two different viscous environments simultaneously: the head is in the high-viscosity region while the tail is in the low-viscosity domain [Fig. 4.4 (c)]. Shortly after the head has crossed, the swimmer rapidly increases its speed [Fig. 4.4 (d)]. Once the tail has completely gone through the interface, the swimmer attains a new steady-state speed, $z^* > 2$ [Fig. 4.4 (e)–(f)]. For the two values considered experimentally, the thickness of the viscosity gradient does not seem to affect the process

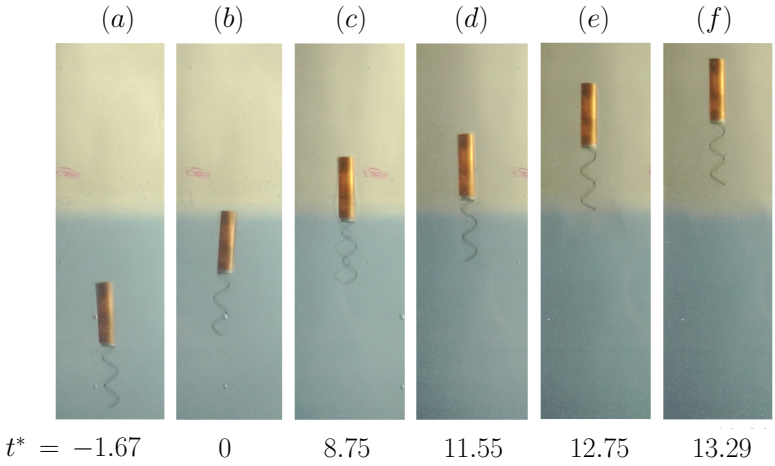

Fig. 4.4 Case I: Time sequence of the head-forward (pusher) swimmer crossing a positive viscosity gradient, for δ=0.274 (narrow gradient). Images have been flipped so that the swimmer appears to move upwards.

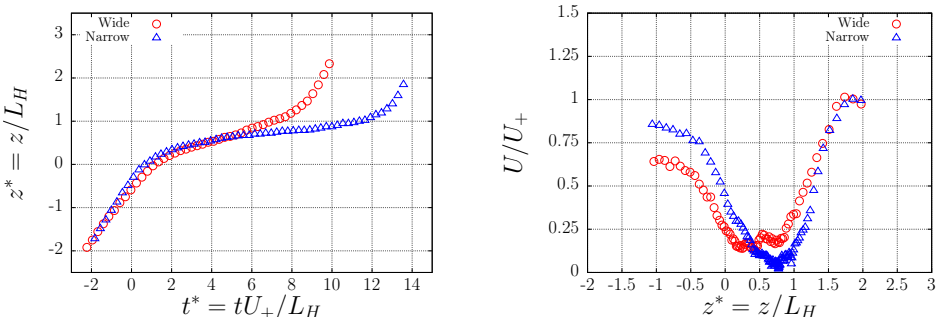

Fig. 4.5 Case I dynamics, i.e. head-forward (pusher) swimmer crossing a positive viscosity gradient: (a) Dimensionless position, $z*$, as function of t^* (b) Normalized speed U/U_+ as a function of position z^*. At $t^* \approx 0$ the swimmer reaches the interface, located at $z^* \approx 0$.

significantly. However, we note that when the gradient is sharp, the swimmer spends a longer time at the interface than in the case of the wider viscosity gradient.

4.3.2 Case II: Tail-first, positive viscosity gradient

The second case is similar to the previous one, but with the tail oriented towards the interface. By reversing the rotation direction of the magnetic field, the swimmer is made to move tail-forward (puller mode). In Fig. 4.6 we show an image sequence of the process. The corresponding position and speed of the swimmer are plotted in Fig. 4.7.

As in the previous case, the swimmer moves at a constant speed when it is relatively far from the interface, see Fig. 4.6 (a). In contrast with the previous case, when the tail of the swimmer reaches the interface, the swimming speed increases sharply, Fig. 4.6 (b).

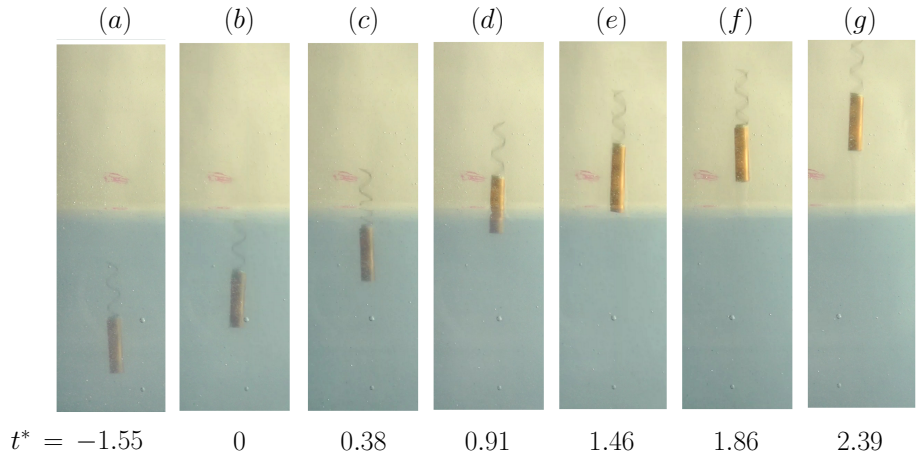

Fig. 4.6 Case II: Time sequence of the tail-forward (puller) swimmer crossing a positive viscosity gradient, for δ=0.274 (narrow gradient). Images are flipped so that the swimmer appears to move upwards.

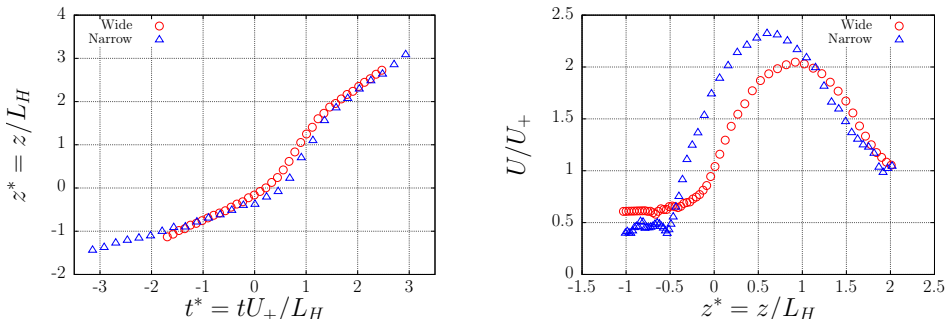

Fig. 4.7 Case II dynamics for a tail-forward (puller) swimmer in a positive viscosity gradient: (a) Position $z*$ as function of t^* (b) Normalized speed U/U_+ as a function of position z^*. At $t^* \approx 0$ the swimmer reaches the interface, located at $z^* \approx 0$.

The swimmer continues accelerating until the head reaches the interface, Fig. 4.6 (c). The maximum speed reached is nearly twice that of the steady speed in the more viscous fluid. As the head crosses the interface, the swimming speed decreases until it reaches a new constant value, see Fig. 4.6 (f). The process can be observed clearly in the two plots that show normalized position and speed in Fig. 4.7. As in the previous case, the thickness of the viscosity gradient does not significantly change the process.

4.3.3 Case III: Head-first, negative viscosity gradient

In the third case, the swimmer moves up from the bottom of the tank, head-forward (i.e. in pusher mode) across a negative viscosity gradient. Since low-*Re* dynamics is time reversible, we should expect the dynamics to be the same as that in Case II, that is, the swimmer should

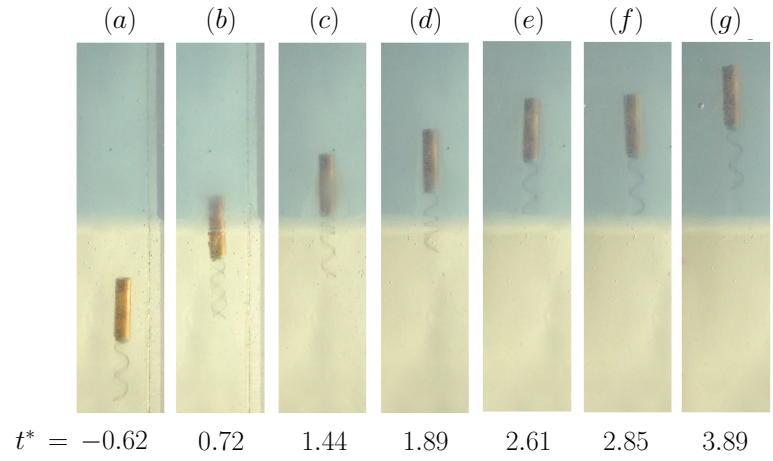

Fig. 4.8 Case III: Time sequence of the head-forward (pusher) swimmer crossing a negative viscosity gradient, for δ=0.274 (narrow gradient).

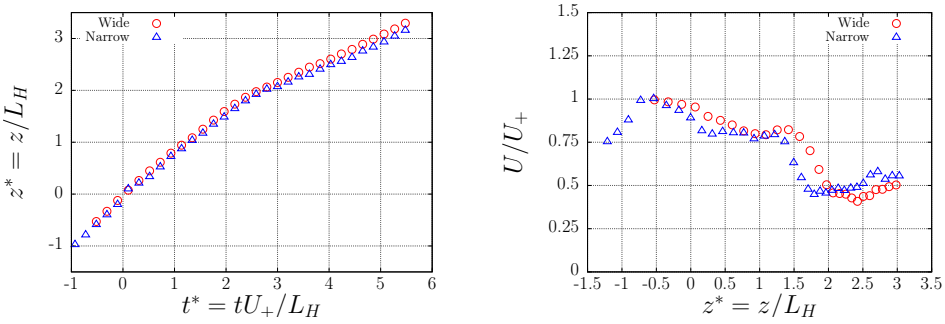

Fig. 4.9 Case III dynamics for a head-forward swimmer (pusher) crossing a negative viscosity gradient: (a) Position $z*$ as function of t^* (b) Normalized speed U/U_+ as a function of position z^*. At $t^* \approx 0$ the swimmer reaches the interface, located at $z^* \approx 0$.

increase its speed as it crosses the interface. Interestingly, the opposite is observed. The swimmer decreases its speed as it crosses the interface. In Fig. 4.8 we show snapshots of the crossing process at different times. The swimmer appears to entrain some of the bottom fluid with it as it crosses the interface, Fig. 4.8 (b) and (c). This might be the reason for the counter intuitive dynamics. We show the position and speed of the swimmer in Fig. 4.9. Again, the width of the viscosity gradient does not seem to play an important role.

4.3.4 Case IV: Tail-first, negative viscosity gradient

The final case considers the dynamics of the swimmer moving tail-forward from the high to low viscous fluid (negative gradient). From reversing time direction in Case I, we should expect the swimmer to decrease its speed. Although this is the case, the speed does not recover until the swimmer has completely crossed the gradient $z^* \simeq 2$, in contrast to Case I in

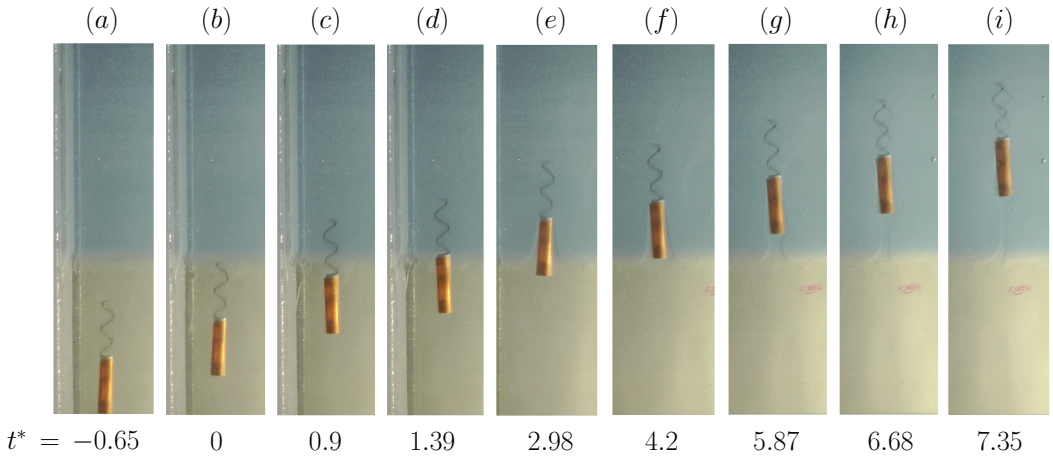

Fig. 4.10 Case IV: Time sequence of the tail-forward swimmer crossing the viscosity gradients from high to low viscosity.

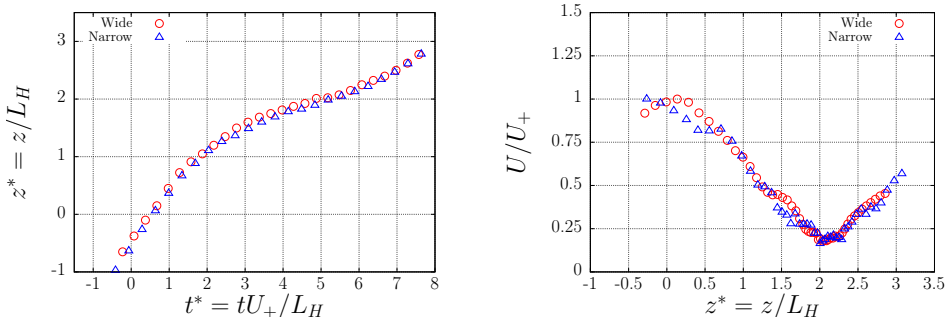

Fig. 4.11 Case IV dynamics for tail-forward (puller) swimming crossing negative viscosity gradient: (a) Position $z*$ as function of t^* (b) Normalized speed U/U_+ as a function of position z^*. At $t^* \approx 0$ the swimmer reaches the interface, located at $z^* \approx 0$.

which the swimmer increases its speed as soon as the tail meets the interface $z^* \simeq 1$. In this case the swimmer also entrains fluid with it. It is possible that the extra volume of drifted fluid prevents the swimmer from increasing its speed sooner. A sequence of images of the dynamics are shown in Fig. 4.10 and we show the position and speed of the swimmer in Fig. 4.11 (as in all previous cases, Fig. 4.10 only illustrates the motion in the case of a narrow viscosity gradient).

4.4 Discrete interface model

As shown in the experiments above, a rich dynamical process results from the intricate balance between drag and thrust for a swimmer straddling two domains of different viscosities. Since the two-fluid solution is naturally stratified (the more-viscous fluid is denser), buoyancy may

also play an important role in the process. Based on these observations, we now propose a model to describe the motion of a swimmer immersed in a fluid of non-homogeneous viscosity. Following the experimental setup, the rigid swimmer consists of a cylindrical head and a helical tail. It rotates at a fixed angular speed $\mathbf{\Omega}$, causing the tail to rotate and push on the surrounding fluid, thus propelling the swimmer forward with velocity $\mathbf{U}$. The size of the swimmer, velocity of motion and the viscosity of the fluid media are such that inertia can be neglected and we are in the creeping flow conditions. Assuming that the classical resistive-force theory of slender filaments [119] remains applicable locally at each point along the swimmer, the force per unit length acting on the swimmer is given by (see §2.1.2.2)

$$\mathbf{f} = -\zeta_{\perp}\mathbf{u} + \left(\zeta_{\perp} - \zeta_{\parallel}\right)(\mathbf{u}\cdot\boldsymbol{\tau})\boldsymbol{\tau}, \tag{4.3}$$

where $\zeta_{\perp}$ and $\zeta_{\parallel}$ are, respectively, the perpendicular and parallel drag coefficients per unit length given by [120]

$$\zeta_{\parallel}^{H,T} \approx \frac{2\pi\mu}{\ln\left(L_{H,T}/r_{H,T}\right)}, \tag{4.4}$$

where the superscripts denote head (H) and tail (T). We also ignore hydrodynamic interactions between the tail and the head, an assumption that we can check a posteriori to be reasonable given the comparison between the model and the experimental results Using force balance we can then relate the swimming velocity to the angular velocity with a linear relationship, $\mathbf{U} = S\mathbf{\Omega}$, with a prefactor S that can be determined for different viscosity profiles. We start below with a sharp (step) function, which is a good approximation to a mixture of two miscible fluids of different viscosities at early times. We will next generalise to a continuous profile. We then complete the model by adding the effect of gravity to our calculations. The predictions of the model are finally compared against experimental data.

4.4.1 Sharp viscosity gradient

We start by analysing the motion at early times when the gradient in viscosity is sharp. In this case we can model the fluid as two semi-infinite domains with viscosity

$$\mu(z) = \begin{cases} \mu_1 = \mu' & z \leq 0 \\ \mu_2 = \mu & 0 \leq z \end{cases}, \tag{4.5}$$

where $z = 0$ denotes the location of the interface (see Fig. 1). The analysis below will be valid for any viscosity distribution and any orientation. Indeed, if we express the swimming speed as a function of the distance from the head to the fluid interface, instead of the vertical coordinate z, we can describe the dynamics in cases I and III (head-forward negative and

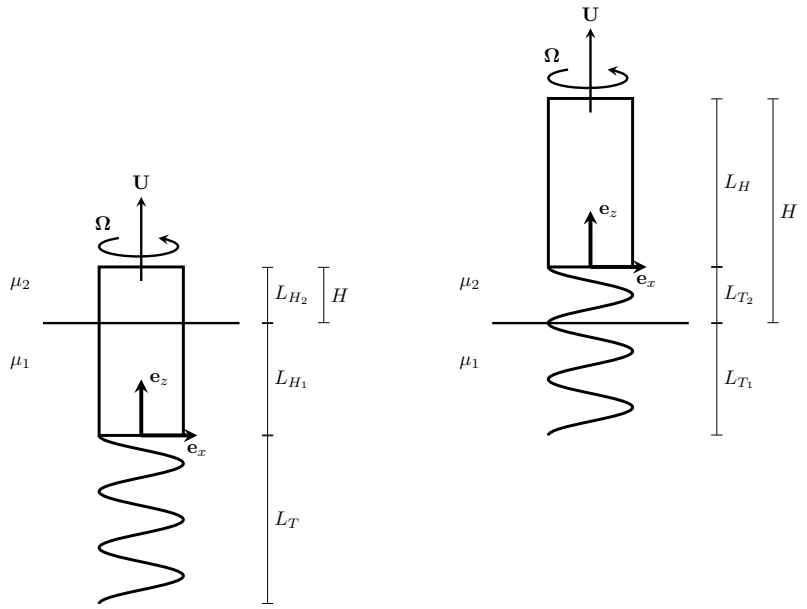

Fig. 4.12 Helical swimmer crossing a sharp viscosity gradient.

positive gradient) by taking $\mu' < \mu$ and $\mu < \mu'$, respectively. As discussed in §4.5.1, the tail-forward dynamics then follows from the reversibility of Stokes flow.

4.4.2 Head-first interaction

4.4.2.1 Head crossing

When the head crosses the viscosity gradient first (Fig. 4.12, left), we model the drag exerted on each part of the head, as that experienced in an infinite fluid of viscosity $\mu_1 = \mu'$ or $\mu_2 = \mu$. The total viscous drag on the head is therefore given by

$$\mathbf{F}_D = -\left[\zeta^H_{\parallel_1} L_{H_1} + \zeta^H_{\parallel_2} L_{H_2}\right] U\mathbf{e}_z = -\zeta^H_{\parallel_1}\left[L_{H_1} + \frac{\mu_2}{\mu_1} L_{H_2}\right] U\mathbf{e}_z, \tag{4.6}$$

where $L_{H_{1,2}}$ are the lengths of the portions of the head above and below the interface (which therefore change in time as the swimmer moves through the interface). The resistance coefficients $\zeta^H_{\parallel_{1,2}}$ are proportional to the corresponding local viscosities and depend on the geometry of the head [150]. The tail is modelled as a right-handed helix of radius R and pitch angle ψ. We parametrise it using the arc-length $s = R\varphi/\sin\psi$, where φ is the azimuthal coordinate. The position $\mathbf{x}(s,t)$ of a material point on the tail is therefore given by (see Fig. 4.12)

$$\mathbf{x}(s,t) = R\cos(2\pi s/\ell + \Omega t)\mathbf{e}_x + R\sin(2\pi s/\ell + \Omega t)\mathbf{e}_y + (Ut + bs)\,\mathbf{e}_z, \tag{4.7}$$

where $\ell = 2\pi R/\sin\psi$ is the arc-length per helical turn and $b = \cos\psi$. The tangent ($\boldsymbol{\tau}$) and velocity vectors ($\mathbf{u}$) are obtained by differentiation with respect to s and t respectively

$$\boldsymbol{\tau}(s) = -\sin\psi\sin(2\pi s/\ell + \Omega t)\mathbf{e}_x + \sin\psi\cos(2\pi s/\ell + \Omega t)\mathbf{e}_y + \cos\psi\mathbf{e}_z, \tag{4.8}$$

$$\mathbf{u}(s) = -R\Omega\sin(2\pi s/\ell + \Omega t)\mathbf{e}_x + R\Omega\cos(2\pi s/\ell + \Omega t)\mathbf{e}_y + U\mathbf{e}_z. \tag{4.9}$$

The total hydrodynamic force exerted on the helix is then obtained using resistive-force theory as

$$\begin{aligned}\mathbf{F}_p &= -\int_0^{L_T/\cos\psi} \zeta_{\perp_1}^T\mathbf{u} + \left(\zeta_{\parallel_1}^T - \zeta_{\perp_1}^T\right)(\mathbf{u}\cdot\boldsymbol{\tau})\boldsymbol{\tau}\,\mathrm{d}s \\ &= -\zeta_{\perp_1}^T\int_0^{L_T/\cos\psi} \mathbf{u} + \left(\beta^T - 1\right)(\mathbf{u}\cdot\boldsymbol{\tau})\boldsymbol{\tau}\,\mathrm{d}s,\end{aligned} \tag{4.10}$$

where $\zeta_{\perp_1}^T$, $\zeta_{\parallel_1}^T$ are the perpendicular and parallel drag coefficients for the helix center line filament and $\beta^T = \zeta_{\parallel_1}^T/\zeta_{\perp_1}^T$, approximately equal to $1/2$ in the slender limit [119]. Ignoring end effects, the propulsive force acts mainly in the z direction, therefore we evaluate

$$\begin{aligned}\mathbf{e}_z\cdot\mathbf{F}_p &= -\zeta_{\perp_1}^T\int_0^{L_T/\cos\psi}\left[U + \left(\beta^T - 1\right)b(\Omega R\sin\psi + Ub)\right]\mathrm{d}s \\ &= -\frac{\zeta_{\perp_1}^T L_T}{\cos\psi}\left[U\left(1 + \left(\beta^T - 1\right)\cos^2\psi\right) + \left(\beta^T - 1\right)\Omega R\sin\psi\cos\psi\right].\end{aligned} \tag{4.11}$$

We obtain the swimming velocity in terms of the angular velocity, by imposing the free swimming condition $\mathbf{e}_z\cdot(\mathbf{F}_p + \mathbf{F}_D) = 0$. The swimming speed is then given by

$$U = \frac{\zeta_{\perp_1}^T L_T\left(1-\beta^T\right)R\sin\psi\cos\psi\Omega}{\zeta_{\parallel_1}^H\cos\psi\left(L_{H_1} + \frac{\mu_2}{\mu_1}L_{H_2}\right) + \zeta_{\perp_1}^T L_T\left(1 + (\beta^T - 1)\cos^2\psi\right)}. \tag{4.12}$$

Using the condition $L_{H_1} + L_{H_2} = L_H$ and defining $\lambda \equiv L_T/L_H$, $\xi \equiv \zeta_{\perp_1}^T/\zeta_{\parallel_1}^H$ and $\ell_H \equiv L_{H_2}/L_H$, we can write the swimming speed as a function of $\ell_H = h$ as

$$U_1(h) = \frac{\xi\lambda\left(1-\beta^T\right)R\sin\psi\cos\psi\Omega}{\cos\psi\left(1 + \dfrac{\mu_2 - \mu_1}{\mu_1}h\right) + \xi\lambda\left(1 + (\beta^T - 1)\cos^2\psi\right)}, \tag{4.13}$$

where $h \equiv H/L_H$ is the dimensionless position of the swimmer's head.

4.4.2.2 Tail crossing

After the head has crossed the interface completely ($h = 1$) the force balance changes. In this case, the head is completely immersed in the fluid of viscosity μ_2 and the drag on the head is given by

$$\mathbf{F}_D = -\zeta^H_{\parallel_2} L_H U \mathbf{e}_z. \tag{4.14}$$

On the other hand, the propulsive force from the tail as it crosses the interface (Fig. 4.12, right) is now given by

$$\mathbf{e}_z \cdot \mathbf{F}_p = -\frac{\zeta^T_{\perp_1} L_{T_1} + \zeta^T_{\perp_2} L_{T_2}}{\cos\psi} \left[U\left(1 + \left(\beta^T - 1\right)\cos^2\psi\right) + \left(\beta^T - 1\right)\Omega R \sin\psi\cos\psi \right], \tag{4.15}$$

where β^T is independent of the viscosities. Applying the free swimming condition along z, we then obtain the swimming speed

$$U = \frac{\xi\lambda\left(\dfrac{\mu_2}{\mu_1} + \dfrac{\mu_1 - \mu_2}{\mu_1}\ell_T\right)\left(1 - \beta^T\right) R \sin\psi\cos\psi\Omega}{\cos\psi\dfrac{\mu_2}{\mu_1} + \xi\lambda\left(\dfrac{\mu_2}{\mu_1} + \dfrac{\mu_1 - \mu_2}{\mu_1}\ell_T\right)\left(1 + (\beta^T - 1)\cos^2\psi\right)}, \tag{4.16}$$

where we have used the fact that $\zeta^T_{\perp_2}/\zeta^H_{\parallel_2} = \zeta^T_{\perp_1}/\zeta^H_{\parallel_1} = \xi$ and defined $\ell_T \equiv L_{T_1}/L_T$. The position of the top part of the head is now $H = L_H[1 + \lambda(1 - \ell_T)]$, so we can rewrite Eq. (4.16) in terms of h as follows

$$U_2(h) = \frac{\xi\left(\lambda + \dfrac{\mu_2 - \mu_1}{\mu_1}(h-1)\right)\left(1 - \beta^T\right) R \sin\psi\cos\psi\Omega}{\cos\psi\dfrac{\mu_2}{\mu_1} + \xi\left(\lambda + \dfrac{\mu_2 - \mu_1}{\mu_1}(h-1)\right)\left(1 + (\beta^T - 1)\cos^2\psi\right)}. \tag{4.17}$$

4.4.2.3 Summary

In the calculations above we obtained that $U_1(\ell_H = 0) = U_2(\ell_T = 0) = U_0$, so the swimming speeds are identical when the swimmer is completely immersed in either of the two fluids. The final speed of the swimmer is then given parametrically by

$$U(h) = \begin{cases} U_0 & h < 0, \\ U_1(h) & 0 \le h \le 1, \\ U_2(h) & 1 < h < 1 + \lambda, \\ U_0 & 1 + \lambda < h. \end{cases} \tag{4.18}$$

We further note that the information about the direction of motion is only embedded in the values of the viscosities, hence Eq. (4.18) is the swimming speed in case I when $\mu_1 = \mu' < \mu_2 = \mu$, and case III for the choice $\mu < \mu'$.

4.4.3 Swimmer position

When the head crosses the interface, the swimming speed is of the form

$$U_1(h) = \frac{A_1}{B_1 + C_1 h}\Omega, \tag{4.19}$$

where

$$A_1 = \xi\lambda(1-\beta^T)R\sin\psi\cos\psi, \tag{4.20}$$
$$B_1 = \cos\psi + \xi\lambda(1+(\beta^T-1)\cos^2\psi), \tag{4.21}$$
$$C_1 = \frac{\mu_2-\mu_1}{\mu_1}\cos\psi. \tag{4.22}$$

On the other hand, when the tail crosses the interface, the speed is of the form

$$U_2(h) = \frac{A_2 + D_2 h}{B_2 + C_2 h}\Omega, \tag{4.23}$$

where

$$A_2 = \xi\lambda'(1-\beta^T)R\sin\psi\cos\psi, \tag{4.24}$$
$$D_2 = \xi\frac{\mu_2-\mu_1}{\mu_1}(1-\beta^T)R\sin\psi\cos\psi, \tag{4.25}$$
$$B_2 = \cos\psi\frac{\mu_2}{\mu_1} + \xi\lambda'(1+(\beta^T-1)\cos^2\psi), \tag{4.26}$$
$$C_2 = \xi\frac{\mu_2-\mu_1}{\mu_1}(1+(\beta^T-1)\cos^2\psi), \tag{4.27}$$

where $\lambda' = \lambda - (\mu_2-\mu_1)/\mu_1$.

The swimming speed is the derivative with respect to time of the position of the head, therefore to find the position we need to integrate the ordinary differential equation

$$L_H\frac{\mathrm{d}h_i}{\mathrm{d}t} = U_i(h). \tag{4.28}$$

That equation is separable and can be integrated to obtain $h_1(t)$ and $h_2(t)$ as solutions of

$$B_1 h_1 + C_1 \frac{h_1^2}{2} = \frac{A_1}{L_H}\Omega t, \tag{4.29}$$

$$L_H \left[\frac{D_2 B_2 - A_2 C_2}{D_2^2} \ln\left(\frac{A_2 + D_2 h_2}{A_2 + D_2} \right) + \frac{C_2}{D_2}(h_2 - 1) \right] = \Omega(t - T_1), \tag{4.30}$$

where $T_1 = L_H(2B_1 + C_1)/(2A_1\Omega)$ satisfies $h(T_1) = 1$, that is, T_1 is the time at which the head has fully crossed the interface. Taking the condition $h(0) = 0$, we then chose the positive branch of Eq. (4.29) so the position of the head for $0 \leq t \leq T_1$ is given by

$$h_1 = \frac{B_1}{C_1} \left[\left(1 + 2\frac{A_1 C_1 \Omega t}{L_H B_1^2} \right)^{1/2} - 1 \right]. \tag{4.31}$$

In the second period, $T_1 \leq t \leq T_2$, the position of the head is given implicitly as the solution of

$$\cos\psi \ln\left(1 + \frac{\mu_2 - \mu_1}{\lambda \mu_1}(h_2 - 1) \right) + C_2(h_2 - 1) = \frac{D_2}{L_H}\Omega(t - T_1), \tag{4.32}$$

where we used equations Eq. (4.24)-Eq. (4.27) while $T_2 = L_H \left[\cos\psi \ln(\mu_2/\mu_1) + C_2\lambda \right]/(D_2\Omega) + T_1$ is the time at which the tail has completely crossed the interface, solution to $h_2(T_2) = 1 + \lambda$. As the swimming speed is constant, $U = U_0$, for $h \leq 0$ and $1 + \lambda \leq h$, or equivalently $t \leq 0$ and $T_2 \leq t$, the position of the head as a function of time is given by

$$h(t) = \begin{cases} U_0 t & t \leq 0, \\ h_1(t) & 0 \leq t \leq T_1, \\ h_2(t) & T_1 \leq t \leq T_2, \\ 1 + \lambda + U_0(t - T_2) & T_2 \leq t. \end{cases} \tag{4.33}$$

4.4.4 Buoyancy

In order to maintain a stable two-fluid configuration, the fluids must have different densities. Experimentally, salt was added to the high-viscosity fluid to slightly increase its density. The effect on the swimmer is to add a buoyancy term in the force balance equation $(\mathbf{F}_D + \mathbf{F}_p + \mathbf{F}_g) \cdot \mathbf{e}_z = 0$, where the buoyancy term is given by

$$\mathbf{F}_{g1} = \left[\pi R^2 \left(L_{H_1}(\rho_H - \rho_1) + L_{H_2}(\rho_H - \rho_2) \right) + \pi a^2 \frac{L_T}{\cos\psi}(\rho_T - \rho_1) \right] \mathbf{g}, \tag{4.34}$$

for $0 \leq h \leq 1$ and

$$\mathbf{F}_{g2} = \left[\pi R^2 L_H(\rho_H - \rho_2) + \frac{\pi a^2}{\cos\psi}\left(L_{T_1}(\rho_T - \rho_1) + L_{T_2}(\rho_T - \rho_2)\right)\right]\mathbf{g}, \tag{4.35}$$

for $1 \leq h \leq 1+\lambda$. Here ρ_H and ρ_T are the effective densities of the head and the helical tail respectively, the density of fluid $i = 1,2$ is denoted by ρ_i and $\mathbf{g}$ is the gravitational acceleration. As none of these expressions contain the swimming speed U explicitly, we can modify Eq. (4.13) and Eq. (4.17) to include an extra buoyancy term U_{gi} on the right hand side, given by

$$U_{g1} = \frac{(\mathbf{F}_{g1}\cdot\mathbf{e}_z)\cos\psi}{\zeta^H_{\parallel_1}\cos\psi\left(L_{H_1} + \frac{\mu_2}{\mu_1}L_{H_2}\right) + \zeta^T_{\perp_1}L_T\left(1 + (\beta^T - 1)\cos^2\psi\right)}, \tag{4.36}$$

$$U_{g2} = \frac{\mathbf{F}_{g2}\cdot\mathbf{e}_z\cos\psi}{\zeta^H_{\parallel_2}\cos\psi L_H + \left(\zeta^T_{\perp_1}L_{T_1} + \zeta^T_{\perp_1}L_{T_2}\right)\left(1 + (\beta^T - 1)\cos^2\psi\right)}. \tag{4.37}$$

Defining the typical buoyancy speed $u^H_{gi} \equiv \pi R^2(\rho_H - \rho_i)\mathbf{g}\cdot\mathbf{e}_z/\zeta^H_{\parallel_i}$ we can then write

$$U_{g1} = \frac{u^H_{g1}}{B_1 + C_1 h}\left[\left(1 + \frac{\rho_1 - \rho_2}{\rho_H - \rho_1}h\right)\cos\psi + \lambda\frac{a^2}{R^2}\frac{\rho_T - \rho_1}{\rho_H - \rho_1}\right], \tag{4.38}$$

$$U_{g2} = \frac{u^H_{g2}}{B_2 + C_2 h}\left[\cos\psi + (h-1)\frac{a^2}{R^2}\frac{\rho_1 - \rho_2}{\rho_H - \rho_2} + \lambda\frac{a^2}{R^2}\frac{\rho_T - \rho_1}{\rho_H - \rho_2}\right], \tag{4.39}$$

where B_i and C_i are as given in Eqs. (4.21), (4.22), (4.26) and (4.27).

4.5 Continuous interface model

At short times after depositing the fluids in the tank, the interface between the two fluid mixture is sharp and the analysis of Section 4.4.1 is appropriate. At later times however, the components responsible for the increase in the viscosity of the fluid mixture diffuse, and therefore so does the viscosity profile (see our measurements in §4.2.1). Therefore, we need to include into our calculations for the swimming speed, the case in which the viscosity distribution is continuous. We can achieve this by using a local drag coefficient $\zeta^{H,T}_{\perp,\parallel}(\mu(z))$ in the resistive force calculation above. Here, $\mu(z)$ represents the local viscosity of the fluid at some point on the swimmer's body at a distance z from the fluid interface. Considering a viscosity profile $\mu(z)$ such that $\mu(z \to -\infty) \to \mu'$ and $\mu(z \to \infty) \to \mu$ (see Fig. 4.13), the

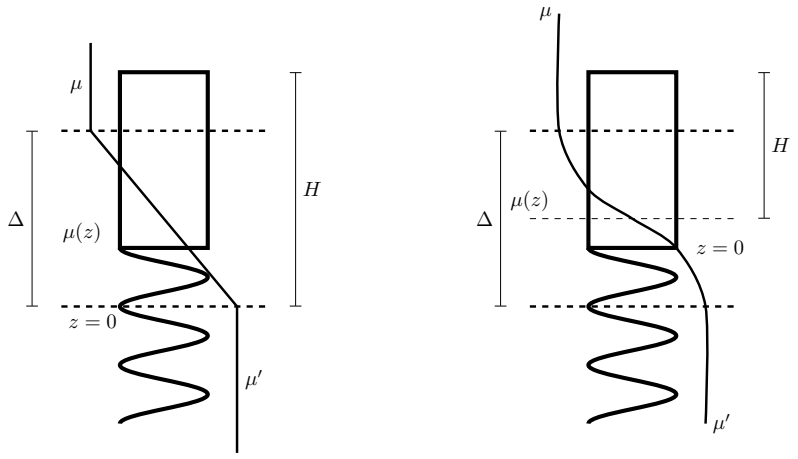

Fig. 4.13 Continuous viscosity gradient with a transition region of size Δ. Left, a linear viscosity profile between two fluid layers of viscosities μ' and μ. Right, a diffuse layer with $\Delta \sim \sqrt{Dt}$, where D is the diffusivity of $\mu(z)$.

drag, propulsion and buoyancy forces are given by

$$\mathbf{e}_z \cdot \mathbf{F}_D = -\int_{H-L_H}^{H} \zeta_{\parallel}^{H}(\mu(z)) U \, \mathrm{d}z = -\zeta_{\parallel}^{H}(\mu') L_H U \int_{h-1}^{h} \frac{\tilde{\mu}(z)}{\mu'} \, \mathrm{d}z, \tag{4.40}$$

$$\begin{aligned} \mathbf{e}_z \cdot \mathbf{F}_p &= -\int_0^{L_T/\cos\psi} \zeta_{\perp}^{T}(\mu(z(s))) \, \mathrm{d}s \left[U\left(1 + (\beta^T - 1)\cos^2\psi\right) + (\beta^T - 1)\Omega R \sin\psi\cos\psi \right] \\ &= -\frac{\zeta_{\perp}^{T}(\mu') L_H}{\cos\psi} \int_{h-1-\lambda}^{h-1} \frac{\tilde{\mu}(z)}{\mu'} \, \mathrm{d}z \left[U\left(1 + (\beta^T - 1)\cos^2\psi\right) \right. \\ &\qquad \left. + (\beta^T - 1)\Omega R \sin\psi\cos\psi \right], \end{aligned} \tag{4.41}$$

$$\mathbf{F}_g = \pi R^2 L_H \left[\int_{h-1}^{h} [\rho_H - \tilde{\rho}(z)] \, \mathrm{d}z + \frac{a^2}{R^2 \cos\psi} \int_{h-1-\lambda}^{h-1} [\rho_T - \tilde{\rho}(z)] \, \mathrm{d}z \right] \mathbf{g}, \tag{4.42}$$

where $\tilde{\mu}(z) = \mu(L_H z)$, $\tilde{\rho}(z) = \rho(L_H z)$ with $\rho(z)$ the continuous density distribution of the fluid along z. Applying the free swimming condition $\mathbf{F}_D + \mathbf{F}_p + \mathbf{F}_g = 0$, and solving for U, we find the swimming speed in the continuous case

$$U(h) = \frac{\xi \left(\int_{h-1-\lambda}^{h-1} \frac{\mu(z)}{\mu'} \, \mathrm{d}z \right) (1 - \beta^T) \sin\psi\cos\psi R\Omega + (\mathbf{F}_g \cdot \mathbf{e}_z \cos\psi / \zeta_{\parallel}^{H} L_H)}{\cos\psi \left(\int_{h-1}^{h} \frac{\mu(z)}{\mu'} \, \mathrm{d}z \right) + \xi \left(\int_{h-1-\lambda}^{h-1} \frac{\mu(z)}{\mu'} \, \mathrm{d}z \right) (1 + (\beta^T - 1)\cos^2\psi)}, \tag{4.43}$$

Notice that the transition between μ' and μ does not have to be monotonic, but in order to apply this model to the experiments presented in §4.3, we will chose a monotonic viscosity profile, with a transition region $\delta \equiv \Delta / L_H$, such as the linear and diffuse distributions depicted

in Figure 4.13. Again, the dynamics in cases I and III are obtained by setting $\mu' < \mu$ and $\mu < \mu'$, respectively. The position of the swimmer as a function of time $h(t)$ can then be obtained by solving the ordinary differential equation

$$L_H \frac{\mathrm{d}h}{\mathrm{d}t} = U(h). \tag{4.44}$$

Note that this might not be solvable analytically for an arbitrary viscosity profile, but it is straightforward to do numerically. As a final remark, we can recover the swimming speed in the two-fluid case, by setting $\tilde{\mu}(z<0) = \mu'$, $\tilde{\mu}(z>0) = \mu$ in Eq. (4.43). And in general, for any discrete number of fluid layers the swimming speed is obtained by replacing the integrals in Eq. (4.43) by the appropriate sums.

4.5.1 Head-first vs tail-forward approach

The calculations above were all carried out in the case where the head of the swimmer crosses the interface first (pusher mode). Since the motion is dominated by viscosity, expressions for the speed when the swimmer approaches the interface with the tail first may then be obtained by time reversal. Indeed, time reversal of Stokes flow corresponds to the map $\{U, \Omega, h, \mu', \mu\} \mapsto \{-U, -\Omega, -h, \mu, \mu'\}$, therefore the tail-forward approach is obtained by evaluating Eq. (4.43) at $h' = -h + \lambda + 1$, where the translation $\lambda + 1$ comes from the fact that $h' = 0$ corresponds to the moment when the tail meets the fluid interface. Note that we need to be careful with the sign of the gravitational field, and to remember that in the experiments, the high viscosity fluid always sits at the bottom, so $\mathbf{F}_g \cdot \mathbf{e}_z < 0$ when the swimmer crosses from high to low viscosity and vice-versa.

4.5.2 Model predictions: Parameter dependence

Before comparing the model predictions with the experimental data, we explore the impact of the different parameters of the problem on the swimming speed. One of the advantages of the model developed here is that it allows us to explore a wider set of conditions than those attainable experimentally. In this and the following section we will adopt the convention $\mu' < \mu$ for clarity. This means that, when the swimmer moves up the gradient, $\mu(h \to -\infty) \to \mu'$ and $\mu(h \to \infty) \to \mu$. When the swimmer moves down the gradient, we swap μ' and μ. Furthermore, we will use the terminology defined in Table 4.1 to refer to the different swimming conditions.

To simplify the interpretation of predictions, we first neglect buoyancy; in such a case, the time-reversal symmetry between the head-forward and tail-forward is exact. The dimensional

parameters we are left with are the sizes of the swimmer (L_H, r_H, L_T, r_T) and the pitch of the helical tail (P_T). Another length scale is the size of the transition region (Δ) or, equivalently, the time at which the experiment is performed after the two-fluid mixture is set up. We will keep the proportions of the head fixed as well as the pitch and thickness of the helical filament so that we are left with two dimensionless parameters: $\delta = \Delta/L_H$ and $\lambda = L_h/L_H$, which quantify the relative size of the transition region and the size of the tail compared to the head of the swimmer. Finally, we will also consider variations in the viscosity ratio of the initial two mixture fluid, i.e. μ/μ'.

In Fig. 4.14 we first show the swimming speed as a function of the distance between the head and the fluid-fluid interface (normalised by the initial, and terminal, speed U_0). We assume that the viscosity varies linearly between the two experimental values, $\mu' = \mu_- = 0.55$ Pa$\cdot$s and $\mu = \mu_+ = 2.74$ Pa$\cdot$s, and we take the head and tail to have the same lengths, i.e. $\lambda = 1$. In panel (a) we consider Case I, and the fluid interface is located at $h = 0$. The speed is constant when the swimmer is completely immersed on the low viscosity fluid. As the head crosses the interface, the drag increases but the propulsion stays the same, therefore the speed decreases. Once the tail meets the interface, the propulsion starts to increase thereby compensating the drag, and thus the speed increases until it plateaus back to a constant speed. Panel (b) shows the speed of the swimmer in Case III. Here the drag reduces as the head traverses the interface, hence the swimming speed increases until the tail meets the interface, when the propulsion starts decreasing, compensating for the lower drag. This continues until the swimmer is completely immersed in the top fluid, at which point the speed reaches a new constant value.

The speed of the swimmer in Case II (tail-forward) may be obtained by reflecting Fig. 4.14 (b) on the vertical axis $h = 1$, with h now measured from the tip of the tail to the interface. Similarly for Case IV, we reflect Fig. 4.14 (a). Notice that for $\lambda = 1$, this reflection corresponds to the transformation $h \to -h + 1 + \lambda$. In general, for arbitrary λ, we need to reflect on the axis $h = (1+\lambda)/2$ in order to obtain the swimming speed in the tail forward scenarios. Therefore, the behaviour of the swimming speed is reversed in the tail first approach: the swimming speed increases when it crosses from low to high viscosity and vice-versa.

We next show in Fig. 4.15 (a) and (b) analogous graphs to those in Fig. 4.14 for a diffusive viscosity gradient with different values of the transition length scale $\Delta = 2\sqrt{2Dt}$. The behaviour is seen to be qualitatively the same as in the linear case. We also show the position of the swimmer as a function of time for the same conditions in Fig. 4.15 (c) and (d). The evolution of the position is seen to not strongly depend on the width of the viscosity transition region, with the strongest variability occurring for Case I [panel (c)].

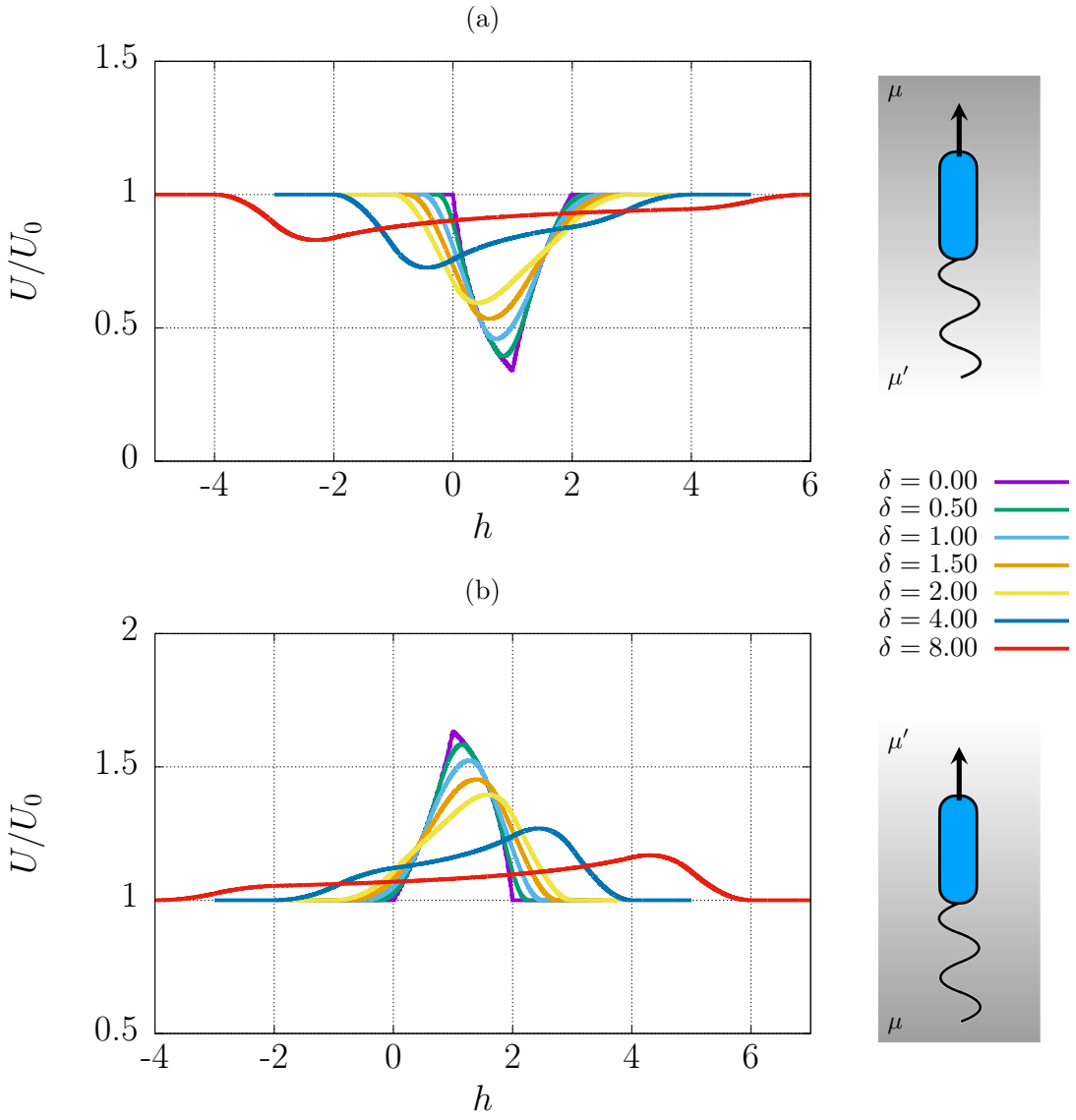

Fig. 4.14 Swimming speed in a linear viscosity gradient for different widths of the transition region. (a) Case I, (b) Case III. The viscosities of the semi-infinite fluids on either side of the interface are given by the experimental values, i.e. $\mu' = \mu_- = 0.55$ Pa·s and $\mu = \mu_+ = 2.74$ Pa·s. The length of the tail and head are the same, i.e. $\lambda = 1$, and the swimmer is neutrally buoyant in both fluids. The diagrams on the right indicate the direction of motion, with dark and light gray representing high (μ) and low viscosity (μ') respectively. The values are normalised by the terminal speed U_0.

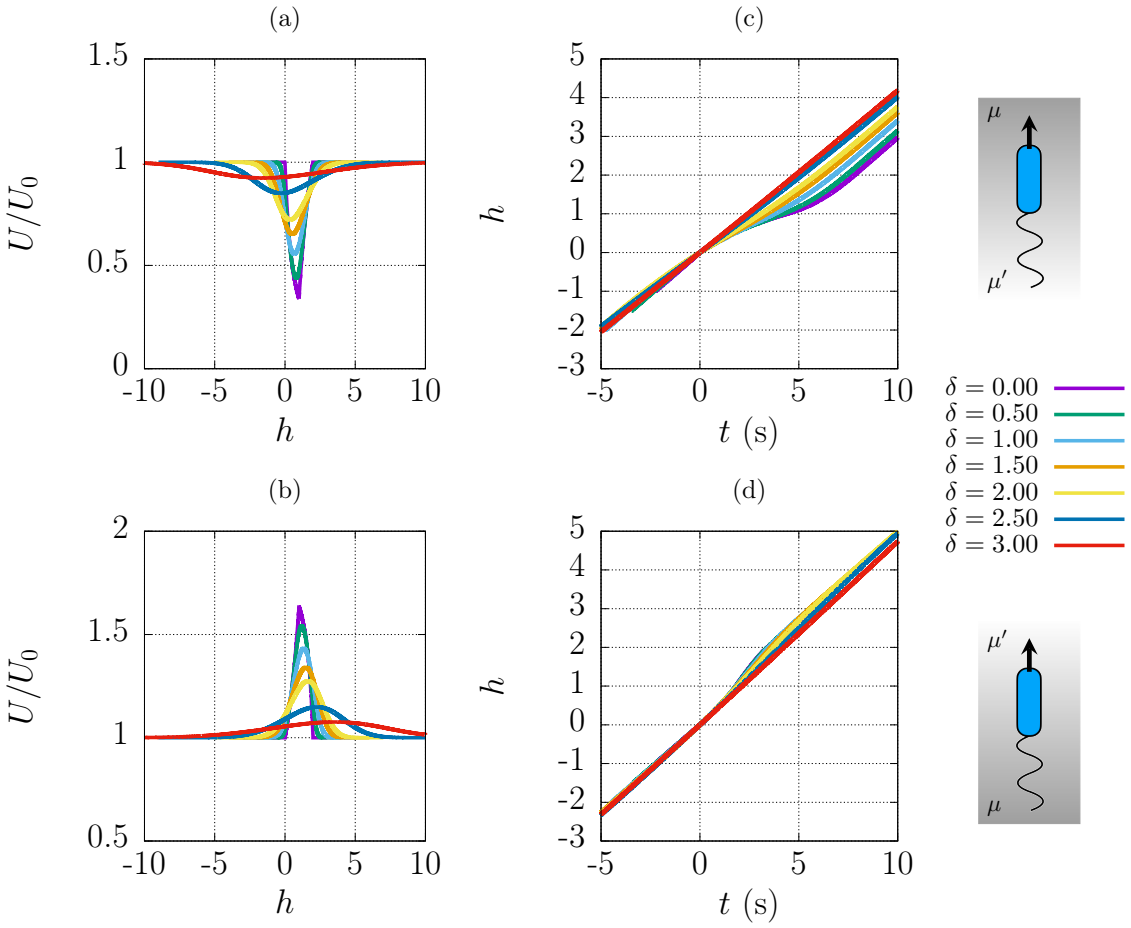

Fig. 4.15 Swimming speed and position in a diffusive viscosity gradient for different widths of the transition region. (a) Case I, (b) Case III. The parameters $\{\mu/\mu', \lambda\}$ are the same as in Fig. 4.14.

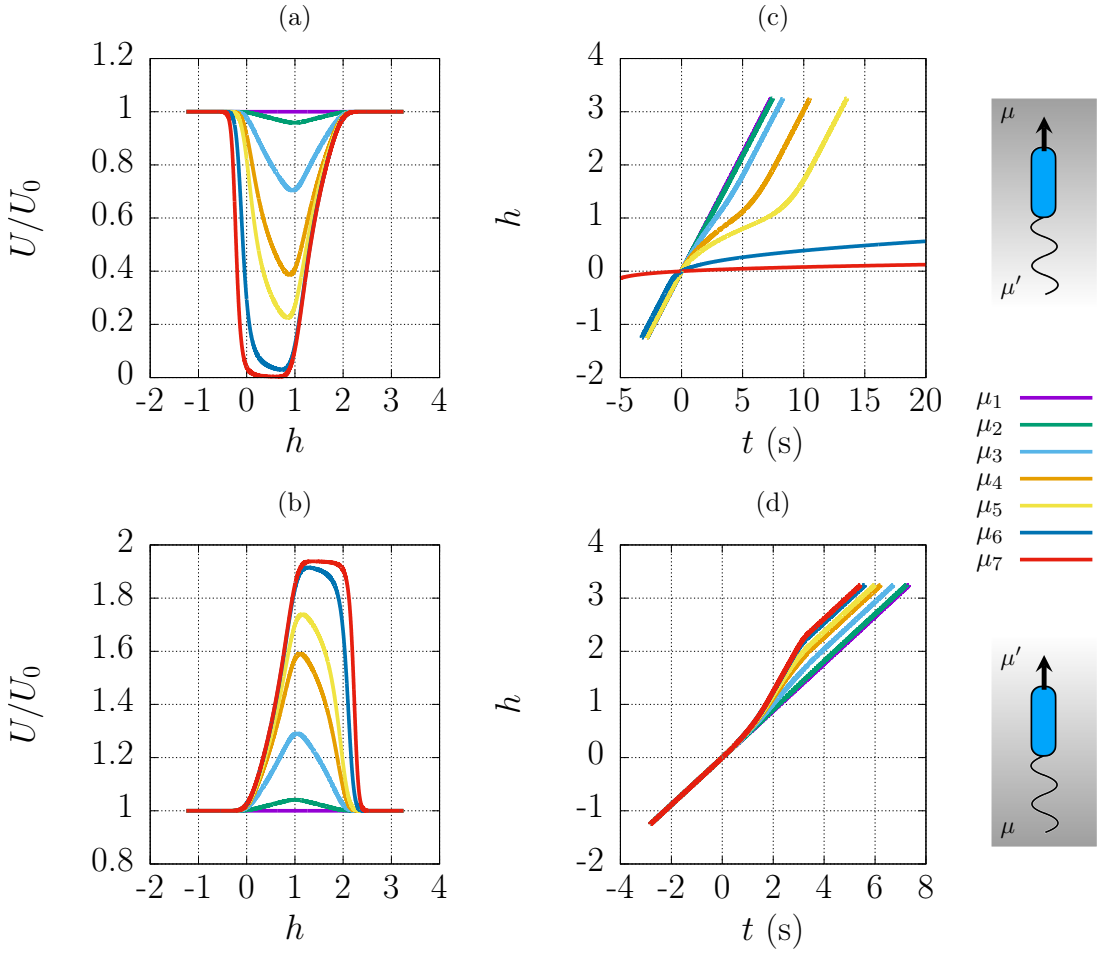

Fig. 4.16 Swimming speed and position in a diffusive viscosity gradient for different values of the viscosity ratio: $\mu_i/\mu' = 1.0$, 1.1, 2.0, 5.0, 10.0, 100.0 and 1000.0. (a), (c) Speed and position, Case I; (b), (d) Speed and position, Case III. The width of the transition region is $\delta = \Delta/L_H = 0.25$, the viscosity of the top fluid is $\mu' = \mu_- = 0.55$ Pa·s and $\lambda = 1$.

The behaviour of the swimmer dynamics with increasing values of the viscosity ratio (μ/μ') is shown in Fig. 4.16 (for values $\delta = 0.25$ and $\lambda = 1$). As could have been expected, the viscosity ratio greatly influences the amount by which the speed of the swimmer changes as it crosses the interface. In particular, when motion occurs from low to high viscosity, it is possible for the swimmer to spend an arbitrarily long time crossing the gradient if the viscosity ratio is large (see Fig. 4.16 (a) and (c)). In contrast, the effect on the dynamics when the swimmer crosses from high to low viscosity is less pronounced, with the time spent crossing the gradient decreasing by about 30% when the viscosity ratio is a thousand times larger.

The impact of the dimensionless length of the tail (λ) is next plotted in Fig. 4.17, for

which we use the same size of the transition region and the viscosity values used in Fig. 4.14. The speed of the swimmer is seen to increase with the length of its tail, as expected since it is the tail that generates propulsion. We further observe that the time the swimmer takes to cross the interface decreases with λ in both cases. We also observe that the speed changes less for swimmers with long tails; indeed, if the tail is much larger than the size of the transition region, then the propulsion remains almost the same during a crossing event. Therefore, we expect swimmers with short tails to be less efficient at crossing the interface.

When buoyancy is considered, many additional parameters impact the penetration dynamics, in particular the relative densities between the swimmer's tail, head and the densities of the fluids. We did not explore all the dependencies, but it is important to point out two possible scenarios. In the situation where the bottom fluid is significantly denser than the top one, the swimmer could end up trapped at the interface between the two fluids in two different ways. Case (i) is the one where the head dominates the weight of the swimmer and case (ii) when the tail does. In case (i) the densities of the head and tail can be chosen in such a way that the propulsion is sufficiently large for the swimmer to cross the interface when moving head forwards down the viscosity gradient (assuming the bottom fluid is also the more viscous one) but then for the relative weight of the head in the top fluid to be so large that it opposes any further propulsion. Symmetrically, in case (ii), when the tail dominates the weight of the swimmer, it would be possible for the head of the swimmer, moving head first, to be light enough so as to provide buoyancy able to cancel the propulsion generated by the tail when the swimmer moves up the gradient. In both cases the swimmer would thus end up being trapped at the interface, like a buoy.

4.6 Comparison with experiments

4.6.1 Positive viscosity gradient

In this section we compare the predictions of our model to the experiments of §4.3. We begin with the situation where the swimmer crosses the interface from the low to the high-viscosity domain and we start by analysing Case I, in which the head approaches the interface first. The swimmer moves at a constant speed when it is completely immersed in fluid 1. When the head reaches the interface, based on the results from the previous section, we expect the speed to decrease due to an increase in drag experienced by the head. When the tail meets the interface, the propulsion should then start to increase until it compensates the higher drag, achieving a constant terminal speed. Indeed, both Eq. (4.43) and the experimental data confirm this.

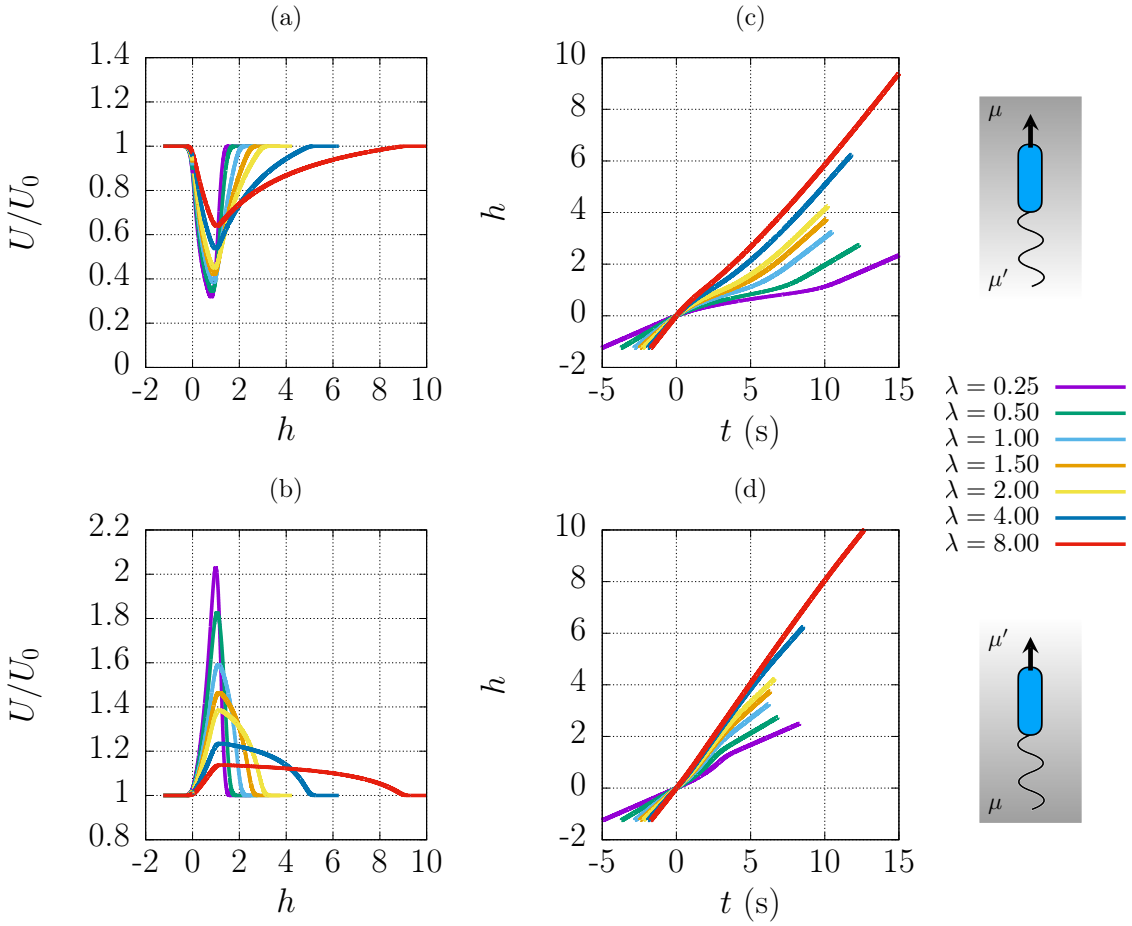

Fig. 4.17 Swimming speed and position in a diffusive viscosity gradient for different values of the tail to head size ratio, λ. (a), (c) Speed and position, Case I; (b), (c) Speed and position, Case III. The width of the transition region is $\delta = \Delta/L_H = 0.25$ and the viscosity ratio is the same as in Fig. 4.14 (experimental values).

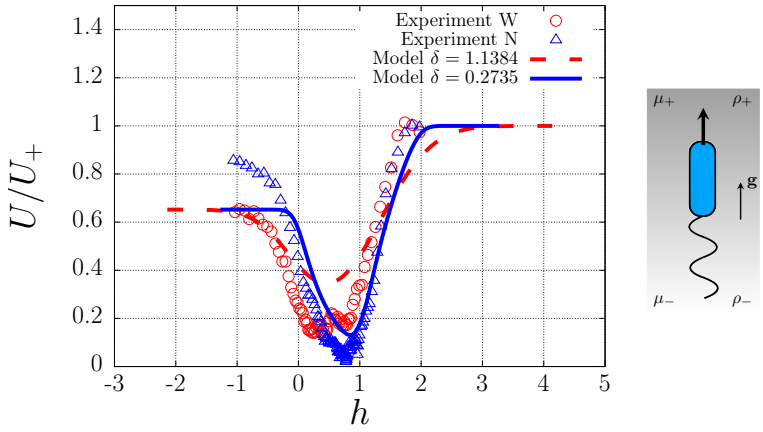

Fig. 4.18 Comparison between experiments and data for Case I (i.e. head-forward (pusher) swimmer crossing a positive viscosity gradient): Speed of the swimmer as a function of the dimensionless position of the head h with respect to the interface located at $h = 0$. The speed is normalised by the speed in the fluid of high viscosity, $U_+ = U(h \to \infty)$. We display the measurements early after the viscosity gradient has been set up ([N]arrow gradient): triangles (experiment) and blue solid line (model), and sixteen hours after ([W]ide gradient): circles (experiment) and red dashed line (model).

We plot in Fig. 4.18 the speed of the swimmer (normalised by the swimming speed in the high-viscosity fluid) as a function of the dimensionless position of the head h; the swimmer starts from the low-viscosity fluid ($\mu' = \mu_- = 0.55\,\mathrm{Pa\cdot s}$) and approaches the interface head-forward. We compare the experimental data against our model, Eq. (4.43), using the experimental parameters, i.e. $\lambda = 1$, $\mu = \mu_+ = 2.74$ Pa·s, $\rho' = \rho_- = 1310$ kg/m^3, $\rho = \rho_+ = 1370$ kg/m^3 and an average density $\rho_s = 1270$ kg/m^3 for the swimmer. The size of the transition region δ is obtained by the procedure described in §4.2.1. With no additional fitting parameters, we observe that our model matches the experiments very well specially at early times [in the narrow viscosity gradient, indicated by (N)]. The model is able to predict also that the speed reduction decreases with an increase in the thickness of the fluid interface, δ.

Note that the swimming speed drops dramatically to less than 10% of its initial value when crossing the interface. This is a result of the combination of drag and buoyancy: as the swimmer crosses the interface, its velocity is reduced both by an increase in drag and by an increase in buoyancy (since the swimmer is slightly buoyant in both fluids, this is the least favourable case).

In contrast to the head first approach, in Case II (tail-forward motion) we expect the swimmer to speed up as it traverses the viscosity gradient, this as a result of an increase in propulsion. When the head meets the interface, the drag increases and the speed should

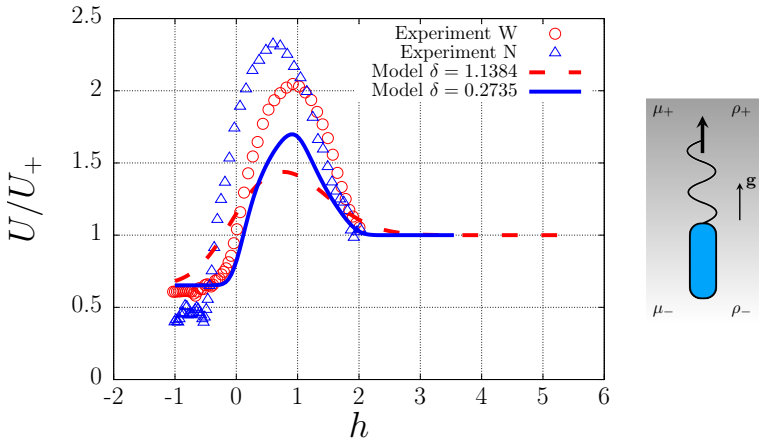

Fig. 4.19 Comparison between experiments and data for Case II (tail-forward (puller) swimmer in a positive viscosity gradient). The speed of the swimmer is plotted as a function of the dimensionless position of the tail h with respect to the interface located at $h = 0$, and the speed is normalised by that in the high-viscosity fluid, $U_+ = U(h \to \infty)$. We show the measurements soon after the viscosity gradient has been set up ([N]arrow gradient case): triangles (experiment) and blue solid line (model), as well as sixteen hours after the start of the experiment ([W]ide gradient case): circles (experiment) and red dashed line (model).

decrease, until the swimmer achieves a constant speed. Both our model in Eq. (4.43) and the experiments agree with this behaviour, as shown in Fig. 4.19; we use the same values for the parameters λ and ρ_s as in Figs. 4.18 and 4.21. The position h is now measured from the tip of the tail to the interface. We swap the values of the viscosities and densities $\mu' = \mu_+$, $\mu = \mu_-$, $\rho' = \rho_+$ and $\rho = \rho_-$, to be consistent with reversibility and the speed is still normalised by U_+. Here, we also observe that the model can reproduce the experimental behaviour, especially at early times. It can also capture the reduction of the increase in speed with the width of the transition region δ.

4.6.2 Negative viscosity gradient

We now move on to the case where the swimmer crosses the interface from the high to the low-viscosity region, that is swimming down the gradient. To compare the results against our model, Eq. (4.43), we use the same set of the parameters: $\mu' = \mu_+ = 2.74\,\mathrm{Pa\cdot s}$, $\mu = \mu_- = 0.55\,\mathrm{Pa\cdot s}$, $\rho' = \rho_+ = 1370\,\mathrm{kg/m^3}$, $\rho = \rho_- = 1310\,\mathrm{kg/m^3}$, $\rho_s = 1270\,\mathrm{kg/m^3}$ and $\lambda = 1$. The width of the transition region, δ, is obtain as before by fitting Eq. (4.2) to the experimental data.

In Case III (head-forward) we expect to see a behaviour opposite to that of Case I. Again, the swimmer travels at constant speed when it is completely immersed in the high viscosity

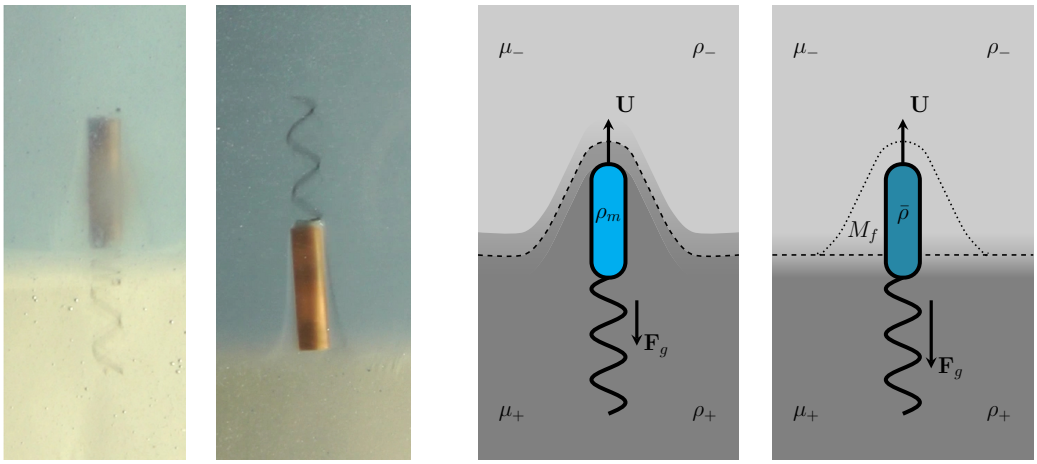

Fig. 4.20 Viscous entrainment of the high-viscosity fluid by the swimmer. (a) Experimental picture showing the swimmer moving down the gradient and entraining some of the high-viscosity fluid as it crosses the interface, regardless of its orientation relative to the interface. (b) The entrained fluid accounts for an increase in the apparent density of the swimmer from $\rho_s = M_s/V_s$ to $\bar{\rho} = [1+\alpha(h)]\rho_s$, where α depends on the mass of fluid dragged along with the swimmer, $M_f = \rho_f V_f$, as given in Eq. (4.45).

fluid. As predicted by our model, when the head crosses the interface we would expect the drag experienced by the swimmer to decrease, resulting in an increase in the swimming speed. Then, when the tail reaches the interface, the propulsion should decrease, compensating for the reduced drag, until the swimming speed reaches a constant value. However, the experimental data show a completely different behaviour. We plot in Fig. 4.21 a comparison between the experimental data and the predictions of Eq. (4.43) (theoretical predictions are shown in thin lines). In the experiments, the swimmer seems to maintain a constant speed as the head crosses the interface. When the tail then meets the interface, the speed starts decreasing. It is only once the swimmer has fully crossed and is completely immersed in the low viscosity fluid that the speed starts to increase.

Based on experimental observations, we hypothesise that this counter-intuitive behaviour is due to the head of the swimmer entraining a significant amount of high-viscosity fluid with it as it crosses into the low-viscosity region, thereby increasing its effective density and being slowed down. We show experimental evidence of this entrainment in Fig. 4.20 (a).

It is difficult to precisely calculate the amount of fluid that the swimmer entrains. However, we can use our model to show that an increase in the effective swimmer density leads to theoretical results closer to what is observed experimentally. In order to do that, we assume that the swimmer has an average density ρ_s which increases by a height-dependent

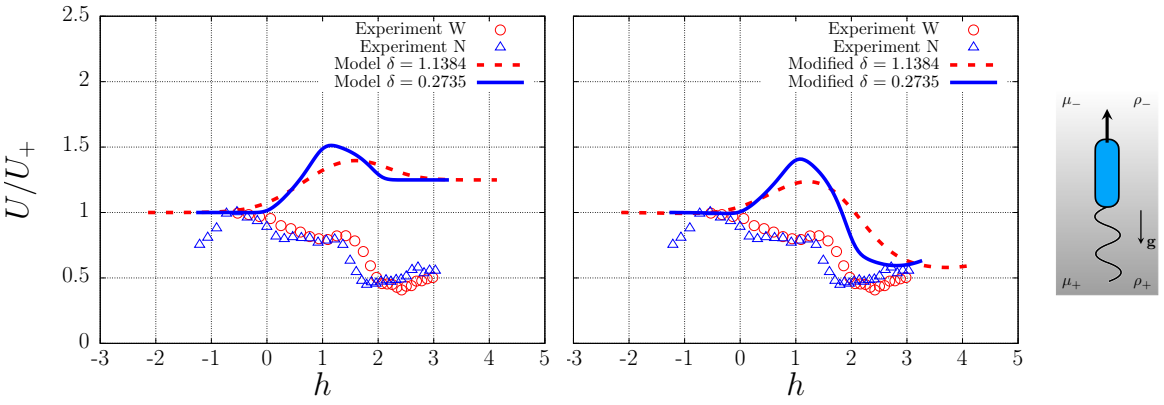

Fig. 4.21 Comparison between experiments and data for Case III (i.e. head-first swimmer (pusher) crossing a negative viscosity gradient). We plot the dimensionless speed of the swimmer as a function of the dimensionless position of the head h measured relative to the interface located at $h = 0$. The speed of the swimmer is normalised by the speed in the high viscosity fluid, $U_+ = U(h \to -\infty)$. We display the measurements early after the viscosity gradient has been set up ([N]arrow gradient): triangles (experiment) and blue solid line (model), and sixteen hours after ([W]ide gradient): circles (experiment) and red dashed line (model). The figure on the left show the predictions of the original model, not taking into account entrainment, while the plot on the right the modified model with variable buoyancy and $\alpha_{max} = 0.1$.

fraction $\alpha(h)$ as $[1+\alpha(h)]\rho_s$. The increase is set explicitly by the relation

$$\bar{\rho}(h) = [1+\alpha(h)]\rho_s = \frac{M_s + M_f(h)}{V_s + V_f(h)}, \tag{4.45}$$

where $\{M_s, V_s\}$, $\{M_f, V_f\}$ are the masses and volumes of the swimmer and the entrained fluid (see Fig. 4.20(b)). Therefore the maximum increase in density is obtained in the limit $1 \ll V_f/V_s$ and is given by $\alpha_{max} = (\rho_f - \rho_s)/\rho_s$. Once the density reaches its maximum, the fluid slides-off and the density decreases. This observation is consistent with previous calculations for the drift volume entrained by organisms in density stratified media [151]. At small Peclet number (i.e. for advection dominated by diffusion), the drift volume is a symmetric function of the distance to a reference line and it decreases as the swimmer moves away [151]. For finite Peclet number, the drift volume remains symmetric provided the Richardson number is small (i.e. for buoyancy negligible compared to viscous stresses). Here we assume the shape remains symmetric and we set α to be a Gaussian function with variance $[(1+\lambda)/2+\delta]^2$ and maximum α_{max} at $h = 1+\lambda+\delta$. This means that: (i) the changes in apparent density are negligible before the swimmer meets the interface, (ii) the maximum increase in density occurs when the swimmer has fully crossed the interface, and

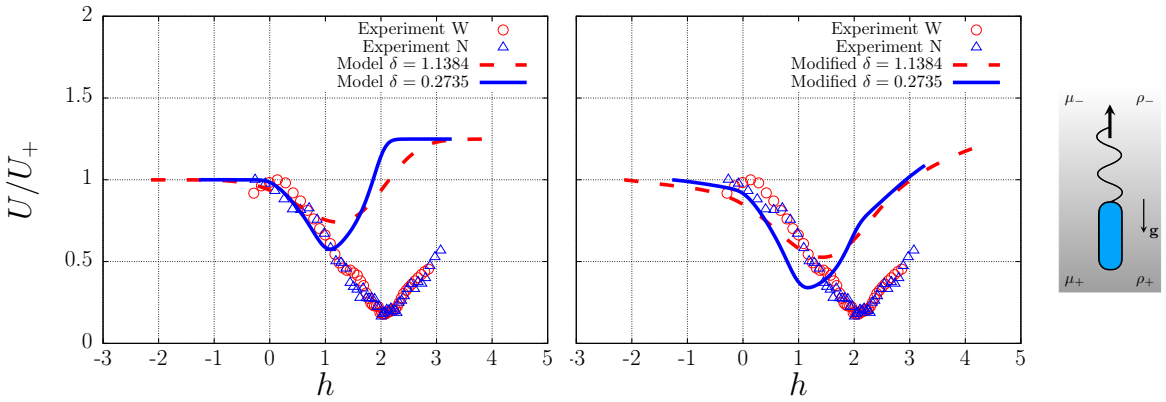

Fig. 4.22 Comparison between experiments and data for Case IV (tail-first swimmer (puller) crossing the viscosity gradients from high to low viscosity): Speed of the swimmer as a function of the dimensionless position of the tail h with respect to the interface located at $h = 0$. Values for the speed are normalised by the speed in the high viscosity fluid $U_+ = U(h \to -\infty)$. We display the measurements early after the viscosity gradient has been set up ([N]arrow gradient): triangles (experiment) and blue solid line (model), and sixteen hours after ([W]ide gradient): circles (experiment) and red dashed line (model). The figure on the left show the predictions of the original model while the plot on the right the modified model with variable buoyancy and $\alpha_{max} = 0.1$.

(iii) most of the dragged fluid slides off after the swimmer has travelled the same distance it did before accumulating the maximum amount of entrained fluid. Although this approach is a phenomenological way to account for the effect of the drift volume, it shows that an increase in the effective swimmer density plays an important role in the dynamics. We show in Fig. 4.21 the predictions of the modified model with the increase in density as thick lines. This new model is now able to capture the qualitative features observed in experiments.

We finally address the situation in Case IV with a swimmer approaching the interface tail-forward (puller case). Here we expect the swimming speed to slow down as the swimmer crosses the gradient as a result of a decrease in propulsion. As soon as the head meets the interface the drag should decrease, compensating for the lower propulsion, until the speed reaches a constant value. However we can see in Fig. 4.22 that, in the experiments, the swimmer does not speed up until it has completely crossed the viscosity gradient ($h = 0$), unlike the predictions from the original model (thin lines). An increase in the effective density of the swimmer due to entrainment of the high-viscosity fluid might here also be at the origin of this result. We use the modified model outlined above and plot its predictions in Fig. 4.22 as thick lines; we see that the new model is able to come closer to the experimental data. As for case II, here h is measured from the tip of the tail and we flip the values of the viscosities and densities to be consistent with reversibility, $\mu' = \mu_-$, $\mu = \mu_+$, $\rho' = \rho_-$ and

$\rho = \rho_+$.

Since the viscosity of the bottom fluid is five times larger than that of the top fluid, the deformation of the interface and the amount of fluid that the swimmer carries with it are much smaller when it moves up the gradient (small entrainment of the low-viscosity fluid into the other one) than when it moves down the gradient (larger entrainment of the large-viscosity fluid). Therefore the correction to the buoyancy forces in cases I and II do not need to be included.

4.7 Conclusions

Summary

In this chapter, we present a joint experimental-theoretical study of the dynamics of synthetic magnetic helical swimmers moving across viscosity gradients between two miscible fluids. The viscosity gradients are seen to play a significant role in the swimming dynamics.

For motion up the viscosity gradient, there are two possible behaviours: first, for up the gradient motion, if the swimmer moves head-forward (pusher mode), its speed reduces due to an increase in drag. On the other hand, the swimmer speeds up when it swims tail-forward (puller mode), due to an increase in the viscous propulsion. When the swimmer moves from high to low-viscosity regions, the opposite behaviour is expected, i.e. the swimming speed should increase if the swimmer moves head-forward and decrease if it moves tail-forward. However, we observe in experiments that the swimmer slows down in both cases. We hypothesise that buoyancy forces, resulting from entrainment of the high-viscosity fluid, are responsible for such counter-intuitive behaviour: as the swimmer traverses the gradient, it drags a large amount of fluid with it, increasing its apparent mass and slowing it down. We show evidence of this mechanism by modifying our model to include a buoyant term that increases as the swimmer advances. Although our model is able to capture many of the experimental features, it makes a number of simplifying assumptions, in particular hydrodynamic interactions between the head and the tail are neglected and drift is modelled in an ad-hoc fashion. We believe that improvements are possible and we hope to pursue them in future work.

Outlook

Since we only focus on swimming motion parallel to the viscosity gradient, our model cannot tackle the issue of viscotaxis for single swimmers. However, our results suggest that, regardless of the viscous entrainment, it is always harder for a pusher-like swimmer to swim up the gradient and that the opposite is true for a puller-like swimmer. Therefore, in addition

to the reorientation of chiral swimmers in viscosity gradients [78], our results point to both positive and negative collective viscotaxis as being not only possible but governed solely by the motility pattern of the cells.

Specifically, let us consider microorganisms which perform a run-and-tumble dynamics, as is the case for many bacteria [123, 152], and therefore swimmers that repeatedly stop their motion to change direction. For simplicity, we can assume that the swimmer's mode is always the same, i.e. that it always remains a puller or a pusher. For example the bacterium *E. coli* remains a pusher during its swimming motion. If the motility pattern of the swimmer has a large positive directional persistence (i.e. the swimming direction after a reorientation event is close to the previous direction), then pusher-like swimmers would be predicted to statistically accumulate in regions of high viscosity (collective positive viscotaxis), because individual swimmers would spend more time in regions were they swim slower. The opposite situation would happen for puller-like swimmers (negative collective viscotaxis). In contrast, if the directional persistence is negative (i.e. reorientation angles larger than 90° on average), then pusher swimmers would exhibit negative collective viscotaxis while pullers would display positive viscotaxis.

The situation is more complex for bacteria such as *H. pylori* that can switch between swimming modes [137] or *V. alginolyticus* that exhibits a bi-modal motility pattern with two different persistence parameters [152]. In the case of *H. pylori*, persistence is negative and the cell switches between pusher and puller modes during its locomotion. Using our results, we predict that a swimmer with this type of motility would accumulate in regions of high viscosity. This, in turn, would be advantageous for the cell as it would tend to spend longer times in the high-viscosity mucus layer that protects the stomach, ultimately leading to penetration and colonization of the stomach wall.

The reorientation towards, or away from, the gradient might of course modify the collective viscotactic effect. A recent theoretical study concluded that a squirmer swimming in a weak viscosity gradient will always reorient towards the direction of decreasing viscosity (negative viscotaxis), regardless of the swimming mode, puller or pusher [84]. This effect has been confirmed experimentally for the puller-like alga *C. reinhardtii* [153, 154], independently. These studies showed that the green algae reorients against the viscosity gradient and perform collective negative viscotaxis. These results would seem to support our findings, however *C. reinhardtii* swims at constant propulsive force rather than with a constant beating rate, therefore its swimming speed decreases with increasing viscosity. Therefore at small viscosity ratios it is possible to observe a slight positive viscotactic effect, whereas for large viscosity ratios the viscous torque is strong enough so that the algae move away from high-viscosity regions. Another theoretical study found that positive viscotaxis is possible

for a dumbbell swimmer which is driven by a force pulling on its leading pole while negative viscotaxis happens for a dumbbell which is pushed on its back pole [78]. This suggests that a pusher-like swimmer such as *E. coli* might also exhibit negative viscotaxis. However, a detail calculation of the hydrodynamic torque on a rotating helix due to an imbalance in the viscosity that it experiences is still lacking and therefore further investigation would be necessary to draw definite conclusions.

The idealized system considered here was aimed to emulate biological processes. In particular the one by which bacteria are capable of penetrating mucus layers or membranes to cause infections. Even in this simplified situation, the process is seen to exhibit rich dynamics. We hope that this first study will motivate further work on swimming in viscosity-stratified fluids.

Chapter 5

Diffusion and Chemotaxis of Bacteria-Driven Micro-swimmers

5.1 Introduction

A detailed mathematical analysis of the motility properties of bacteria-driven microswimmers is essential for their optimal design and fabrication. In this chapter, we thus develop a stochastic model for bio-hybrid spherical microswimmers with *E. coli* bacteria attached to their surface. We derive analytical expressions for the rotational diffusion coefficient and the mean squared displacement (MSD), based on the following assumptions: (i) low-Reynolds number flow, (ii) a large number of uniformly attached bacteria, (iii) negligible thermal noise compared to the random activity of each cell and (iv) run-and-tumble dynamics for each bacterium.

The chapter is organised as follows. We describe the mathematical model and the details of the simulations in §5.2. In §5.3 we derive expressions for the diffusivity and effective velocity of the microswimmers. First, we consider the situation where the chemical environment is homogeneous. Next, we investigate the effects of external chemical gradients, assuming a linear response of each one of the attached bacteria. We show in particular that the microswimmers inherit the chemotactic capabilities of the bacteria that propel them. Our analytical results are validated against numerical simulations and past experimental results [16, 90–93]. Finally, we conclude with a general discussion in §5.4.

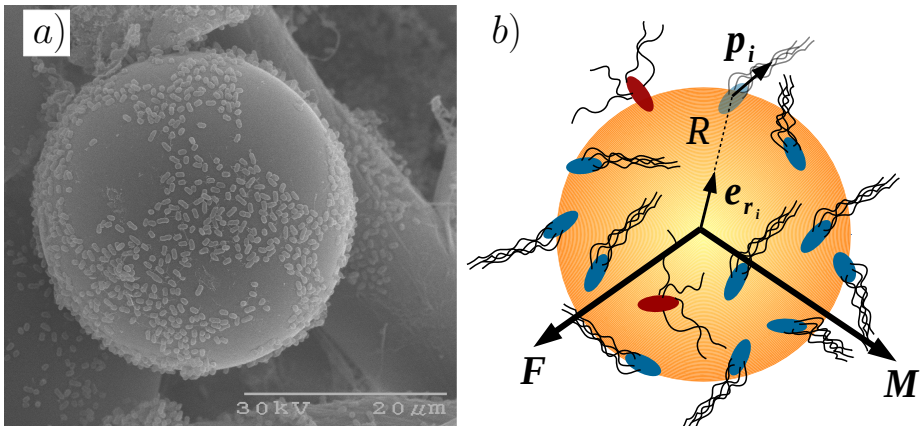

Fig. 5.1 Bacteria-driven microswimmer. (*a*) Scanning electron microscope (SEM) image of a 30 μm diameter bead with surface-attached bacteria. The individual cells are seen as small dots on the smooth surface of the bead (reprinted by permission from Kim et al. [155]. Copyright 2012 from Springer Nature). (*b*) Schematic representation of a bacteria-driven particle of radius R. The unit vectors $\mathbf{e}_{r_i}$ and $\mathbf{p_i}$ define the position and orientation of the i-th bacterium. The total hydrodynamic force, $\mathbf{F}$, and torque, $\mathbf{M}$, are the sum of the applied forces and torques by each bacterium, $-f\mathbf{p}_i$ and $-Rf\left(\mathbf{e}_{r_i}\times\mathbf{p}_i\right)$ respectively.

5.2 Mathematical model and numerical simulations

5.2.1 Micro-swimmers in homogeneous environments

Following previous studies [91, 92], we model the microswimmers as passive spherical particles of radius R with a number N of uniformly distributed bacteria attached to their surface (see Fig. 5.1). Reported densities of attachment in experiments range from one bacterium per 12 μm^2 up to one per 7 μm^2 [93]. The bacteria are assumed to be fixed in position and orientation with respect to the surface of the particle. This condition is satisfied in practice by using strong chemical binding such as streptavidin-biotin interactions [92]. Previous numerical investigations suggest that the direction of the flagellar bundle is unaffected by the fluid flow in the vicinity of the swimmer [91], therefore the flagellar bundle is assumed to align with the orientation of the cell body with no change as the swimmer moves.

Each cell is assumed to perform its own, independent run-and-tumble dynamics. The reaction torques in the running and tumbling states have magnitudes $|\mathbf{M}_R|\simeq 0.7\,\text{pN}\mu\text{m}$ and $|\mathbf{M}_T|\simeq 0.4\,\text{pN}\mu\text{m}$ respectively [92]. These torques can be neglected if we focus on sufficiently large particles such that $|\mathbf{M}_{R,T}|\sqrt{\langle\sin^2\alpha\rangle_\alpha}\ll fR$, where $f\sim 0.3-0.48\,\text{pN}$ is the average propulsive force exerted by each bacterium [92, 93] and the angle α defined in Fig. 5.2 denotes the orientation of the bacterium flagella bundle with respect to the radial

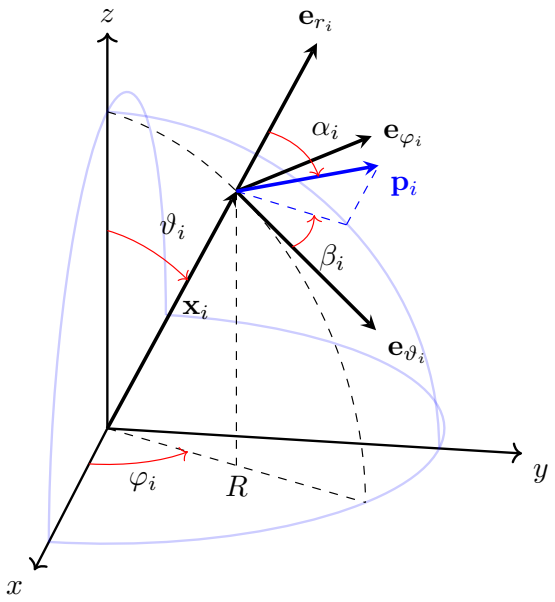

Fig. 5.2 Notation for the location and orientation of each bacterium on the surface of the particle. The i-th bacterium is located at $\mathbf{x}_i = R\mathbf{e}_{r_i}$ where R is the radius of the particle and $\mathbf{e}_{r_i}$ is the radial unit vector defined by the polar and azimuth angles ϑ_i and φ_i with respect to the body frame $\{x,y,z\}$. The orientation of the bacterium relative to the bead surface is given by the unit vector $\mathbf{p}_i$, which is the radial unit vector defined by the polar and azimuth angles α_i and β_i with respect to the local spherical coordinate system $\{\mathbf{e}_{\vartheta_i}, \mathbf{e}_{\varphi_i}, \mathbf{e}_{r_i}\}$. Each bacterium is assumed to push on the fluid along $\mathbf{p}_i$ and thus to exert a force on the particle along $-\mathbf{p}_i$.

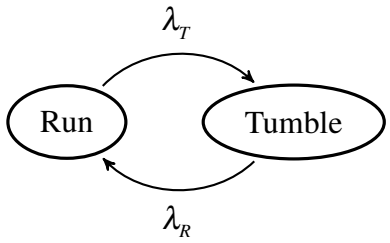

Fig. 5.3 The run-and-tumble motility pattern as a two-state Markov chain with transition rates λ_R and λ_T from the tumbling to the running state and vice-versa, respectively. Typical values of these rates for *E. coli* in homogeneous environments (no chemical gradients) are $\lambda_T^{-1} = 0.9$ s and $\lambda_R^{-1} = 0.1$ s [125].

direction. In other words, for large particles, the reorientation of the swimmer is dominated by the moment-arm torque induced by the propulsive forces of the cells. Finally, thermal noise can also be neglected as it induces typical forces three orders of magnitude smaller than the propulsive forces from the bacteria.

We model therefore each bacterium as a two-state machine which exerts a force of magnitude f when running and no force when tumbling. The transition between the running and the tumbling states is modelled as a continuous time Markov chain with transition rates λ_R and λ_T from the tumbling to the running state and vice-versa, respectively (see Fig. 5.3). The values for *E. coli* in homogeneous environments (no chemical gradients) are $\lambda_R \simeq 10\ \mathrm{s}^{-1}$ and $\lambda_T \simeq 10/9\ \mathrm{s}^{-1}$. Furthermore, the swimming motion occurs at low Reynolds number $Re \simeq 10^{-4}$ [125]. The linear and angular velocities of the microswimmer, denoted by $\mathbf{V}$ and $\boldsymbol{\omega}$, are obtained by force and moment balance using Stokes law

$$\mathbf{F} = 6\pi\mu R\mathbf{V} = -f\sum_{i=1}^{N}\varepsilon_i\mathbf{p}_i, \tag{5.1}$$

$$\mathbf{M} = 8\pi\mu R^3\boldsymbol{\omega} = -fR\sum_{i=1}^{N}\varepsilon_i\mathbf{e}_{r_i}\times\mathbf{p}_i, \tag{5.2}$$

where μ is the dynamic viscosity of the fluid, $\mathbf{F}$ and $\mathbf{M}$ are the total force and torque applied by the surface-attached cells, while $\mathbf{e}_{r_i}$ and $\mathbf{p}_i$ are unit vectors which determine the position and orientation of the i-th bacterium (see Figs. 5.1b and 5.2). Specifically, each bacterium is assumed to push on the fluid along the direction $\mathbf{p}_i$ of its bundle of flagellar filaments and thus to exert a force on the particle along $-\mathbf{p}_i$. In equations Eq. (5.1) and Eq. (5.2), the stochastic variable ε_i determines the state of the i-th bacterium with $\varepsilon_i = 1$ when running and $\varepsilon_i = 0$ when tumbling. The position and orientation of the microswimmer evolve in time

according to

$$\dot{\mathbf{X}} = \mathbf{V}, \tag{5.3}$$

$$\dot{\mathbf{n}} = \boldsymbol{\omega} \times \mathbf{n}, \tag{5.4}$$

where the dot denotes a derivative with respect to time and $\mathbf{n}$ is a body-fixed unit vector. We integrate Eq. (5.3) numerically using an Euler method and Eq. (5.4) using the mid point method presented in Refs. [156, 157] with a time step $\mathrm{d}t = 0.01$ s. We consider 10^4 different configurations, sampling the geometrical angles ϑ_i, φ_i, α_i and β_i, which describe the location and orientation of the cells on the bead surface (see Fig. 5.2), from uniform distributions in the intervals $[0,\pi]$, $[0,2\pi)$, $[\alpha_{\max},\alpha_{\min}]$ and $[0,2\pi)$ respectively. The maximum and minimum deviation angles from the radial direction are $\alpha_{\min} = 30^\circ$ and $\alpha_{\max} = 85^\circ$ following Ref. [91].

5.2.2 Run-and-tumble dynamics

If we denote by $p_R(t)$ and $p_T(t)$ the probabilities of finding a particular bacterium in the running and the tumbling states respectively, the master equation for the run-and-tumble dynamics is given by

$$\begin{bmatrix} \dot{p}_R \\ \dot{p}_T \end{bmatrix} = \begin{bmatrix} -\lambda_T & \lambda_R \\ \lambda_T & -\lambda_R \end{bmatrix} \begin{bmatrix} p_R \\ p_T \end{bmatrix}, \tag{5.5}$$

where λ_R and λ_T are the transitions rates defined earlier. The system in Eq. (5.5) can be easily integrated by considering the normalisation condition $p_R + p_T = 1$, with the result

$$\begin{bmatrix} p_R \\ p_T \end{bmatrix} = \begin{bmatrix} \dfrac{\lambda_R}{\lambda_R+\lambda_T} + Ae^{-(\lambda_R+\lambda_T)t} \\ \dfrac{\lambda_T}{\lambda_T+\lambda_R} - Ae^{-(\lambda_R+\lambda_T)t} \end{bmatrix}, \tag{5.6}$$

where A is a constant determined by the initial state of the bacterium. In particular, if the bacterium is running at time $t = 0$ we have $p_R(0) = 1$, hence

$$\begin{bmatrix} p_{RR} \\ p_{TR} \end{bmatrix} = \begin{bmatrix} \dfrac{\lambda_R + \lambda_T e^{-(\lambda_R+\lambda_T)t}}{\lambda_R+\lambda_T} \\ \dfrac{\lambda_T - \lambda_T e^{-(\lambda_R+\lambda_T)t}}{\lambda_R+\lambda_T} \end{bmatrix}, \tag{5.7}$$

where we denote by $p_{RR}(t)$, $p_{TR}(t)$ the probability for a bacterium to be running or tumbling at time t given that it was running at time $t = 0$. Furthermore, in the steady state, the results

of Eq. (5.6) reduce to

$$\begin{bmatrix} p_R^s \\ p_T^s \end{bmatrix} = \begin{bmatrix} \dfrac{\lambda_R}{\lambda_R+\lambda_T} \\ \dfrac{\lambda_T}{\lambda_T+\lambda_R} \end{bmatrix}. \tag{5.8}$$

In our numerical simulations, we assume that we have waited long enough so that the system has reached the steady state. We therefore determine the state of the variables ε_i by sampling a pseudo random number r_i from a uniform distribution and comparing it with p_R^s for the first step and $p_{RR}(\mathrm{d}t)$, $p_{RT}(\mathrm{d}t)$ for the following steps. Here p_{RT} is obtained from Eq. (5.6) by taking $p_R(0) = 0$. In the steady state, the mean of the variables $\varepsilon_i(t)$ is

$$\langle \varepsilon_i(t) \rangle = P(\varepsilon_i(t) = 1) = p_R^s = \frac{\lambda_R}{\lambda_R+\lambda_T}, \tag{5.9}$$

while the time autocorrelation is given by

$$\begin{aligned} \big\langle \varepsilon_i(t)\varepsilon_j(s) \big\rangle &= P(\varepsilon_i(t) = 1, \varepsilon_j(s) = 1) \\ &= P(\varepsilon_j(s) = 1 | \varepsilon_i(t) = 1) p_R^s. \end{aligned} \tag{5.10}$$

If the bacteria behave independently from each other, the probability of the j-th bacterium being running at time s, given that the i-th bacterium is also running at time t, is $p_{RR}(|s-t|)$ for $i = j$ and p_R^s otherwise. Hence

$$\big\langle \varepsilon_i(t)\varepsilon_j(s) \big\rangle = \left(p_R^s\right)^2 \left(1 + \delta_{ij} \frac{\lambda_T}{\lambda_R} e^{-(\lambda_R+\lambda_T)|s-t|}\right). \tag{5.11}$$

We will use equations Eq. (5.9) and Eq. (5.11) to evaluate the MSD bellow.

5.2.3 Chemotaxis of bacteria-driven microswimmers

Chemotaxis is included numerically in our model by modifying the tumbling rate of each bacterium according to $\lambda_T = \lambda_T^{(0)}(1 - Q(t))$ where $Q(t)$ is given as in Eq. (2.17). We make the simplifying assumption that the particle is permeable to the chemical so that the chemical gradient is not perturbed by its presence. In general, we should evaluate $C(\mathbf{r}(t))$ in Eq. (2.17) at the position of each cell. However, if we consider shallow gradients such that $k|\nabla c|R \ll 1$, then it is appropriate to neglect variations in concentration along the surface of the particle and substitute the position of the centre of the microswimmer for $\mathbf{r}(t)$ in Eq. (2.17).

We run the simulation from the previous sections for an ensemble of 10^4 beads, now evaluating the tumbling rate at each step using Eq. (2.17) with $\mathbf{r}(t)$ taken to be the posi-

tion of the centre of the bead. We further take the position of the two impulses in the kernel to coincide with the maximum and minimum of the response kernel measured by Segall et al. [126], *i.e.* $t_1 \simeq 1\,\mathrm{s}$ and $t_2 \simeq 3\,\mathrm{s}$. The intensity of the response is taken as $k = |K|_{max} \times 1\,\mathrm{s} \simeq 0.3\,\mu\mathrm{M}^{-1}$ [133]. As we require the second term in brackets in Eq. (2.17) to remain small and $\mathbf{r}(t) \sim U_e(t_2 - t_1)$, where $U_e \sim 10\,\mu\mathrm{m/s}$ is the swimming speed of the microswimmers [93], we choose $k|\nabla c| \sim 10^{-3} - 10^{-2}\,\mu\mathrm{m}^{-1}$, which corresponds to concentration gradients $|\nabla c| \sim 3 \times 10^{-3} - 3 \times 10^{-2}\,\mathrm{mM/mm}$, so that $k|\nabla c|R \sim 10^{-2} - 10^{-1}$ and the tumbling rate is reduced by approximately one tenth. The chemical gradient is set up along the z direction.

5.3 Theoretical and numerical results

We start this section with the description of the three-dimensional trajectories of the microswimmers as obtained numerically and we observe that for long time-scales these become three-dimensional random walks. We then introduce a coarse-grain model to describe the diffusive behaviour of the microswimmers. We define the rotational diffusion coefficient, D_r, the effective speed, U_e, the effective diffusion coefficient, D_e and derive analytical expressions for each one of them. Next, we show that in the presence of a non uniform chemical concentration field, to which the bacteria respond chemotactically, the microswimmers perform a biased random walk and we quantify their response in terms of a drift speed v_d, for which we derive an analytical expression. Throughout this section, we validate the analytical results against our numerical simulations.

5.3.1 Three-dimensional trajectories of bacteria-driven microswimmers

We present first the results in isotropic environments, i.e. constant concentration field and thus constant tumbling rate. Typical trajectories for the centre of the particle, resulting from numerical integration of equations (5.3) and (5.4), are shown in Fig. 5.4. At short time scales, the applied force and torque are nearly constant and the resulting trajectories are noisy helices. For a given distribution of attached bacteria, the average force and torque acting on the particles in the steady state are given by

$$\langle \mathbf{F} \rangle_{\varepsilon} = -f \sum_{i=1}^{N} \langle \varepsilon_i \rangle_{\varepsilon} \, \mathbf{p}_i = -f p_R^s \sum_{i=1}^{N} \mathbf{p}_i, \tag{5.12}$$

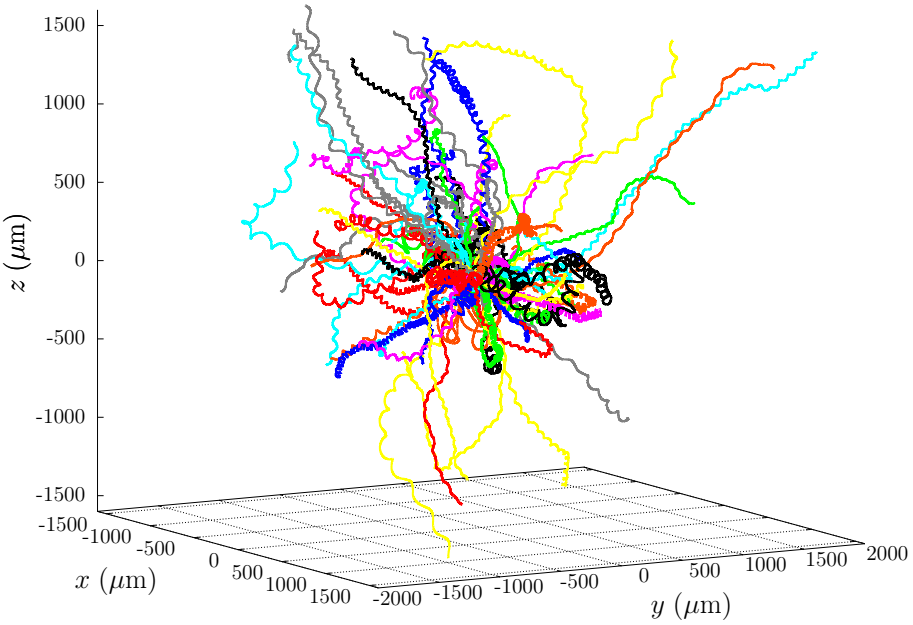

Fig. 5.4 Typical trajectories of bacteria-driven microswimmers of radius $R = 10\,\mu$m with bacteria density $\rho = 1/12\ \mu\text{m}^{-2}$, individual propulsive forces $f = 0.48$ pN, and transition rates $\lambda_T^{-1} = 0.9$ s and $\lambda_R^{-1} = 0.1$ s. The simulation time is $t = 5/(3D_r) \simeq 224$ s, where D_r is given by Eq. (5.31). One hundred different realisations are shown.

$$\langle \mathbf{M} \rangle_\varepsilon = -fR \sum_{i=1}^{N} \langle \varepsilon_i \rangle_\varepsilon (\mathbf{e}_{r_i} \times \mathbf{p}_i) = -fRp_R^s \sum_{i=1}^{N} (\mathbf{e}_{r_i} \times \mathbf{p}_i), \tag{5.13}$$

where $\langle \cdot \rangle_\varepsilon$ denotes the average over the probability distribution Eq. (5.6). Defining the vectors $\mathbf{a} \equiv \sum \mathbf{p}_i$ and $\mathbf{b} \equiv \sum (\mathbf{e}_{r_i} \times \mathbf{p}_i)$, we can express the average radius and pitch of the trajectories as follows

$$\mathscr{R} = \frac{4}{3} R^2 \frac{|\langle \mathbf{F} \rangle_\varepsilon \times \langle \mathbf{M} \rangle_\varepsilon|}{|\langle \mathbf{M} \rangle_\varepsilon|^2} = \frac{4}{3} R \frac{|\mathbf{a} \times \mathbf{b}|}{|\mathbf{b}|^2}, \tag{5.14}$$

$$\mathscr{P} = \frac{8\pi}{3} R^2 \frac{|\langle \mathbf{F} \rangle_\varepsilon \cdot \langle \mathbf{M} \rangle_\varepsilon|}{|\langle \mathbf{M} \rangle_\varepsilon|^2} = \frac{8\pi}{3} R \frac{|\mathbf{a} \cdot \mathbf{b}|}{|\mathbf{b}|^2}. \tag{5.15}$$

In contrast, at longer times the trajectories become three-dimensional random walks and their diffusive behaviour determines the motility properties of the microswimmers. It is well known in the theory of Brownian motion that for a random walk governed by rotational diffusion, the MSD is given by [130]

$$\left\langle r^2(t) \right\rangle = 2\tau_r^2 U_e^2 \left(\frac{t}{\tau_r} + e^{-t/\tau_r} - 1 \right), \tag{5.16}$$

where the angle brackets $\langle\cdot\rangle$ denote ensemble average, U_e is the effective speed at which the bead moves and τ_r is the orientation correlation time, which is the time scale of decay for the orientation correlation function, $\langle \mathbf{n}(0)\cdot\mathbf{n}(t)\rangle$. In other words, τ_r is the time it takes the microswimmer to forget its initial orientation. For short time scales, that is $t \ll \tau_r$, Eq. (5.16) reduces to $\langle r^2(t)\rangle = U_e^2 t^2$, which represents ballistic motion. On the other hand, for time scales such that $\tau_r \ll t$ the MSD is linear in t, a dependence typical in diffusion processes. The constant of proportionality is the effective diffusion coefficient which is defined in three dimensions by

$$6D_e \equiv \lim_{t\to\infty} \frac{\langle r^2(t)\rangle}{t} = 2U_e^2\tau_r. \tag{5.17}$$

Since D_e is a macroscopic property of the microswimmers, it is likely that a simplified description of the trajectories ignoring the microscopic details would still lead to the same result. Furthermore, ignoring the fine structure of the driving mechanism will render the chemotaxis analysis more tractable (see §5.3.3). Inspired by this we propose a coarse grained model as described in the next section. We will use this model to derive analytical expressions for U_e, τ_r and D_e.

5.3.2 Coarse-grained modelling

We start by observing that the trajectories of the microswimmers such as those illustrated in Fig. 5.4 and Fig. 5.5a consist of almost undisturbed helical paths interrupted by sudden changes in direction. We thus construct a coarse-grain model replacing every helical trajectory by a straight path along an average axis denoted by $\hat{\mathbf{u}}_k$ for the kth path (see Fig. 5.5b). Each straight path is travelled at a constant speed U_e for an average time T. The resulting trajectory is therefore a chain of equal-length links. The polar and azimuthal angles between consecutive paths $\hat{\mathbf{u}}_{i-1}$ and $\hat{\mathbf{u}}_i$ are denoted by θ_i and ϕ_i respectively. We further take ϕ_i as uniformly distributed, due to homogeneity of the space.

In polymer physics, a mathematically-identical setup is used in the freely-rotating chain model of a polymer. In this context, the length of the chain links is defined by the Kuhn length as [128, 129]

$$b \equiv \lim_{L\to\infty} \frac{\langle r^2(t)\rangle}{L(t)} = L(T), \tag{5.18}$$

where $L(t)$ is the maximum possible length that the trajectory can have at time t. In order to find L, we need to calculate the average speed at which the particle moves along the coarse-grain trajectory.

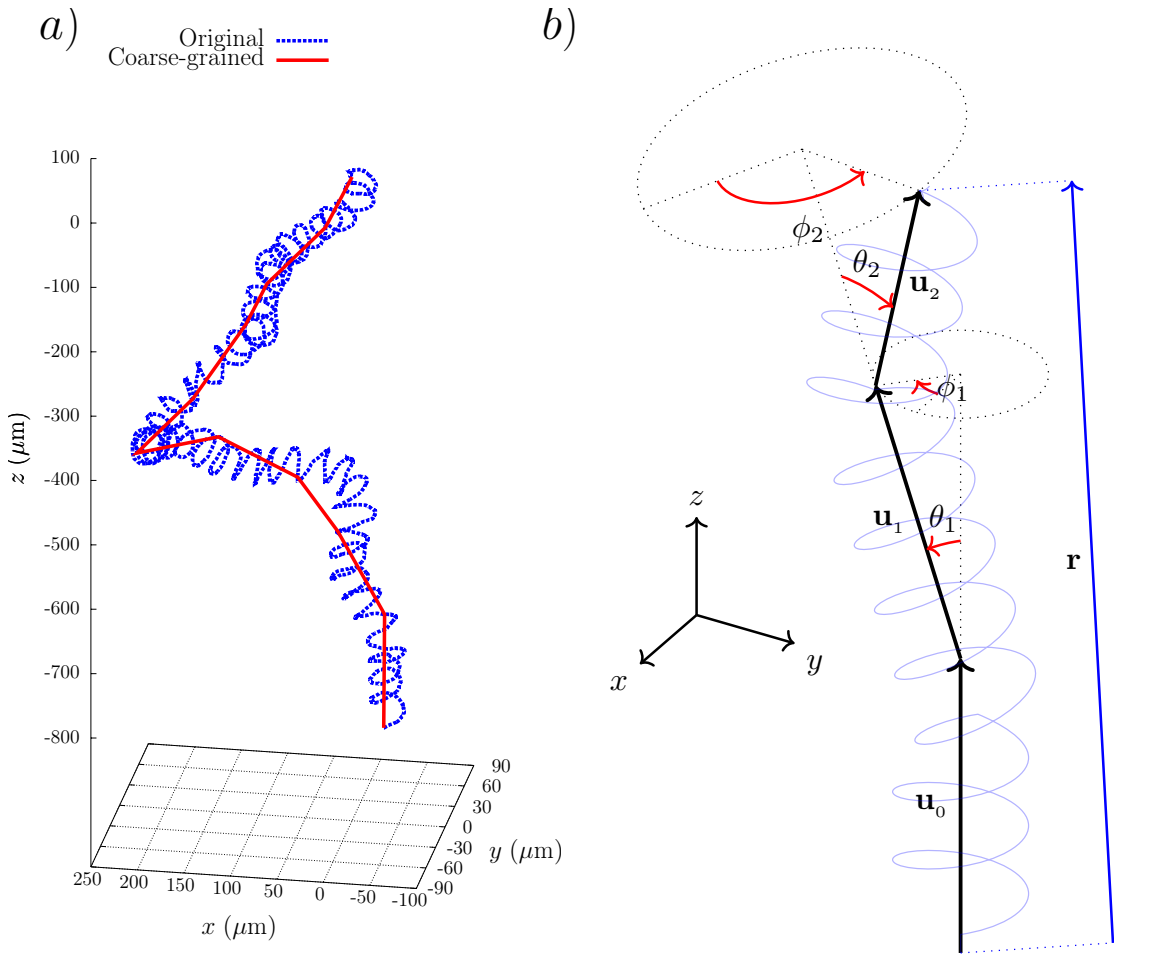

Fig. 5.5 Coarse graining the trajectories of particles. (*a*) Typical trajectory of a bacteria-driven microswimmer with parameters: radius $R = 10\,\mu$m, cell density $\rho = 1/12\ \mu\text{m}^{-2}$, propulsive force $f = 0.48$ pN, and transition rates $\lambda_T^{-1} = 0.9$ s and $\lambda_R^{-1} = 0.1$ s. The simulation time is $t = 5/(3D_r) \simeq 224\,$s, where D_r is given by Eq. (5.31). The path of the swimmer is plotted in dotted blue line and can be approximated by a coarse-grain trajectory in the form of a random walk (solid red line). (*b*) The coarse-grain trajectory is analogous to a freely rotating chain with equal-length links. The angle between two consecutive paths $\hat{\mathbf{u}}_{i-1}$ and $\hat{\mathbf{u}}_i$ is denoted by θ_i and the internal angle of rotation, denoted by ϕ_i, is the angle between the planes generated by $\{\hat{\mathbf{u}}_{i-2}, \hat{\mathbf{u}}_{i-1}\}$ and $\{\hat{\mathbf{u}}_{i-1}, \hat{\mathbf{u}}_i\}$.

5.3.2.1 Effective speed

We define the effective speed as the ensemble average projection of the velocity along the angular velocity, that is

$$U_e^2 \equiv \left\langle \frac{\left(\langle \mathbf{V} \rangle_\varepsilon \cdot \langle \boldsymbol{\omega} \rangle_\varepsilon\right)^2}{|\langle \boldsymbol{\omega} \rangle_\varepsilon|^2} \right\rangle_{\mathbf{p}} = \left(\frac{f p_R^s}{6\pi\mu R}\right)^2 \left\langle \left(\mathbf{a} \cdot \hat{\mathbf{b}}\right)^2 \right\rangle_{\mathbf{p}} \tag{5.19}$$

where $\langle \cdot \rangle_{\mathbf{p}}$ denotes the average over configurations. For a large number of bacteria N, we may assume that the vector $\mathbf{a}$ is uniformly distributed on the sphere and therefore $\left\langle \left(\mathbf{a} \cdot \hat{\mathbf{b}}\right)^2 \right\rangle_{\mathbf{p}} = \left\langle |\mathbf{a}|^2 \right\rangle_{\mathbf{p}} / 3$. Substitution in Eq. (5.19) yields

$$U_e^2 = \left(\frac{f p_R^s}{6\pi\mu R}\right)^2 \frac{1}{3} \sum_{i,j}^{N} \left\langle \mathbf{p}_i \cdot \mathbf{p}_j \right\rangle_{\mathbf{p}} = \frac{N}{3} \left(\frac{f}{6\pi\mu R} \frac{\lambda_R}{\lambda_R + \lambda_T}\right)^2 \tag{5.20}$$

where we have assumed that the bacteria behave independently of each other, that is $\left\langle \mathbf{p}_i \cdot \mathbf{p}_j \right\rangle = \delta_{i,j}$. Notice that p_R^s is the fraction of time that the bacteria exert a force on the sphere, hence the effective speed is simply the average swimming speed of each bacterium $v_0 \equiv f p_R^s / (6\pi\mu R)$ multiplied by the average number of bacteria pushing along the axis of the helical path $\sqrt{N/3}$. Notably, for a fixed density of attached bacteria, U_e is independent of the size of the microswimmer as $N \sim R^2$, this is in agreement with the numerical results of Arabagi et al. [91]. On the other hand, U_e is proportional to the square root of the number of bacteria, which is in agreement with the experimental results of Behkam et al. [93].

Note that the definition of the effective speed in Eq. (5.19) requires $|\langle \boldsymbol{\omega} \rangle_\varepsilon| \neq 0$; if the distribution of bacteria is truly uniform this is not possible since in this case the total torque Eq. (5.13) vanishes. In a similar way, for a truly uniform distribution of bacteria, the total force, Eq. (5.12), also vanishes and therefore the swimming speed should vanish in the limit $N \to \infty$. This limit is not achievable for real bacteria since they have a finite size which bounds the number of bacteria that can attach to the surface. Therefore Eq. (5.20) and the calculations hereafter are only valid for particle size and density of attachment such that N is large enough for the distribution of bacteria to be considered uniform, but finite so that small fluctuations allow for small, but finite, linear and angular velocities.

Since the arc lenght of a helix is the same as that of a straight line traversed at the same speed, the maximum length of the microswimmer's trajectory, $L(t)$, can be obtained by considering the square root of Eq. (5.19) in the limit when $\langle \mathbf{V} \rangle_\varepsilon$ is parallel to $\langle \boldsymbol{\omega} \rangle_\varepsilon$ and multiplying the result by t. In this case $\left\langle \left(\mathbf{a} \cdot \hat{\mathbf{b}}\right)^2 \right\rangle_{\mathbf{p}} = \left\langle |\mathbf{a}|^2 \right\rangle_{\mathbf{p}}$ and $L(t) = \sqrt{3} U_e t$. Therefore,

using Eq. (5.17) we find

$$\tau_r = \frac{3}{2}T\cdot \tag{5.21}$$

From rotational diffusion [120, 136], the correlation time is related to the rotational diffusion coefficient D_r, in d spatial dimensions, by $\tau_r = [(d-1)D_r]^{-1}$. Therefore, for our microswimmer $T^{-1} = 3D_r$. The value of D_r depends on the distribution of the torque that acts on the microswimmer, for example, reorientation due to thermal noise yields $D_r^T = k_B T/8\pi\mu R^3$ from the Stokes-Einstein relation [120]. In the next section we will calculate the value of D_r explicitly, considering the variance of the torque $\mathbf{M}$ given by Eq. (5.2).

5.3.2.2 Rotational diffusion coefficient

We now calculate the rotational diffusion coefficient for the particle by considering the variance of its angular displacement. The orientation of the microswimmer at time t can be obtained from its initial orientation by applying the rotation matrix $\mathbf{R}(t) = \exp[\mathbf{\Gamma}(t)]$, where $\mathbf{\Gamma}$ is a matrix such that for any vector $\mathbf{v}$ we have $\mathbf{\Gamma v} = \boldsymbol{\gamma}\times\mathbf{v}$, with $\boldsymbol{\gamma}$ the angle vector[1]

$$\boldsymbol{\gamma}(t) = \int_0^t \boldsymbol{\omega}(s)\mathrm{d}s. \tag{5.22}$$

Given an orthonormal basis $\mathscr{B} = \{\mathbf{e}_i\}_{i=1}^3$, the components of $\boldsymbol{\gamma}$ on $\mathscr{B}$ satisfy $\langle\cos|\gamma_i|\rangle = e^{-D_r t}$, which in the Gaussian limit (thermal noise [136]) reduces to $\mathrm{Var}[\gamma_i] = 2D_r t$, where $\mathrm{Var}[\cdot]$ denotes the variance. For large N we may assume that $\boldsymbol{\gamma}$ is spherically uniform, thus we define the rotational diffusion coefficient as

$$6D_r \equiv \lim_{t\to\infty}\frac{\left[\left\langle|\boldsymbol{\gamma}|^2\right\rangle - |\langle\boldsymbol{\gamma}\rangle|^2\right]}{t}, \tag{5.23}$$

Substituting Eq. (5.2) in Eq. (5.22) leads to

$$\boldsymbol{\gamma} = -\frac{f}{8\pi\mu R^2}\int_0^t\sum_{i=1}^N \varepsilon_i(s)\,(\mathbf{e}_{r_i}(s)\times\mathbf{p}_i(s))\mathrm{d}s \equiv \int_0^t\sum_{i=1}^N \varepsilon_i(s)\mathbf{c}_i(s)\,\mathrm{d}s, \tag{5.24}$$

where Eq. (5.24) defines the vectors $\mathbf{c}_i(s)$. The variance of the angle vector for a fixed configuration of attached bacteria is then given by

$$\mathrm{Var}\,[\boldsymbol{\gamma}] = \int_0^t\int_0^t\sum_{i,j}^N\left[\left\langle\varepsilon_i(s_1)\varepsilon_j(s_2)\right\rangle_\varepsilon - \left(p_R^s\right)^2\right]\mathbf{c}_i(s_1)\cdot\mathbf{c}_j(s_2)\mathrm{d}s_2\mathrm{d}s_1$$

[1] Strictly, we should include the time ordering operator as in Eq. (3.5), however, we can ignore time order as we will consider all possible realizations of the angular velocity of the microswimmer.

$$= \int_0^t \int_0^t \left[p_R^s p_{RR}(|s_2 - s_1|) - \left(p_R^s\right)^2 \right] \sum_{i=1}^{N} \mathbf{c}_i(s_1) \cdot \mathbf{c}_i(s_2) \mathrm{d}s_2 \mathrm{d}s_1$$

$$= \int_0^t \int_0^t p_R^s p_T^s e^{-(\lambda_R + \lambda_T)|s_2 - s_1|} \sum_{i=1}^{N} \mathbf{c}_i(s_1) \cdot \mathbf{c}_i(s_2) \mathrm{d}s_2 \mathrm{d}s_1 . \tag{5.25}$$

For large N we may replace the sum by N times the average over configurations

$$\sum_{i=1}^{N} \mathbf{c}_i(s_1) \cdot \mathbf{c}_i(s_2) \simeq N \left(\frac{f}{8\pi\mu R^2} \right)^2 \left\langle (\mathbf{e}_{r_i} \times \mathbf{p}_i)_{s_1} \cdot (\mathbf{e}_{r_i} \times \mathbf{p}_i)_{s_2} \right\rangle_{\mathbf{c}_i}, \tag{5.26}$$

where the subscript $\mathbf{c}_i$ denotes that the average is taken over the distributions of $\mathbf{e}_{r_i}$ and $\mathbf{p}_i$, which is equivalent to the average over the angles ϑ_i, φ_i, α_i and β_i. As the positions and orientations of the bacteria are identically and independently distributed, the correlation function on the right hand side of Eq. (5.26) does not depend on i, hence

$$\left\langle (\mathbf{e}_r \times \mathbf{p})_{s_1} \cdot (\mathbf{e}_r \times \mathbf{p})_{s_2} \right\rangle_{\mathbf{c}} = \frac{1}{N} \sum_{i,j} \left\langle (\mathbf{e}_{r_i} \times \mathbf{p}_i)_{s_1} \cdot \left(\mathbf{e}_{r_j} \times \mathbf{p}_j\right)_{s_2} \right\rangle_{\mathbf{c}}$$

$$= \frac{1}{N} \langle \mathbf{b}(s_1) \cdot \mathbf{b}(s_2) \rangle_{\mathbf{c}} = \frac{1}{N} \left\langle |\mathbf{b}|^2 \right\rangle_{\mathbf{c}} \left\langle \hat{\mathbf{b}}(s_1) \cdot \hat{\mathbf{b}}(s_2) \right\rangle_{\mathbf{c}} . \tag{5.27}$$

Remembering that $\mathbf{b}$ defines the direction of motion in our coarse-grain model, we have

$$\left\langle \hat{\mathbf{b}}(s_1) \cdot \hat{\mathbf{b}}(s_2) \right\rangle_{\mathbf{c}} = \frac{1}{U_e^2} \mathscr{C}(|s_2 - s_1|) = e^{-2D_r|s_2 - s_1|}, \tag{5.28}$$

where we have used the fact that the orientation autocorrelation function is given by $\mathscr{C}(t) = e^{-2D_r t}$. On the other hand, since α_i is the angle between $\mathbf{e}_{r_i}$ and $\mathbf{p}_i$ and the bacterial distributions are independent and identical, then $\left\langle |\mathbf{b}|^2 \right\rangle_{\mathbf{c}} = N \left\langle \sin^2 \alpha \right\rangle_{\alpha}$. Therefore

$$\sum_{i=1}^{N} \mathbf{c}_i(s_1) \cdot \mathbf{c}_i(s_2) \simeq N \left(\frac{f}{8\pi\mu R^2} \right)^2 \left\langle \sin^2 \alpha \right\rangle_{\alpha} e^{-2D_r|s_2 - s_1|}. \tag{5.29}$$

Note that, in doing this approximation, we are ignoring the periodic component of the correlation function of the vectors $\mathbf{c}_i$. As it can be seen in Fig. 5.7 this decays on a time scale shorter than τ_r and, since we are interested on the diffusive behaviour of the microswimmer,

we can ignore it[2]. A substitution of Eq. (5.29) into Eq. (5.24) yields

$$\begin{aligned}\mathrm{Var}[\boldsymbol{\gamma}] &= \frac{2Nf^2\left\langle\sin^2\alpha\right\rangle_\alpha}{\left(8\pi\mu R^2\right)^2}\int_0^t\int_{s_1}^t p_R^s p_T^s e^{-(\lambda_R+\lambda_T+2D_r)(s_2-s_1)}\mathrm{d}s_2\mathrm{d}s_1 \\ &= \frac{2Nf^2\left\langle\sin^2\alpha\right\rangle_\alpha}{\left(8\pi\mu R^2\right)^2}p_R^s p_T^s\left(\frac{t}{\lambda_R+\lambda_T+2D_r}\right) \\ &+ \frac{2Nf^2\left\langle\sin^2\alpha\right\rangle_\alpha}{\left(8\pi\mu R^2\right)^2}p_R^s p_T^s\left(\frac{e^{-(\lambda_R+\lambda_T+2D_r)t}-1}{(\lambda_R+\lambda_T+2D_r)^2}\right).\end{aligned} \tag{5.30}$$

We expect the rotational diffusion time scale to be larger than the running and tumbling times, *i.e.* to be in the limit $D_r \ll (\lambda_R+\lambda_T)$, which will be verified later. In this limit, Eq. (5.30) simplifies to

$$D_r = \left(\frac{f}{8\pi\mu R^2}\right)^2\frac{N\left\langle\sin^2\alpha\right\rangle_0\lambda_R\lambda_T}{3(\lambda_R+\lambda_T)^3}+\mathscr{O}\left(\frac{2D_r}{(\lambda_R+\lambda_T)^4}\right). \tag{5.31}$$

We note that D_r vanishes for $\alpha_i = 0$, and indeed if all the bacteria are oriented in the radial direction they produce no moment-arm torque from their propulsive force and there is no change in the orientation of the particle. To treat this case one must include the effect of the reaction torques, the calculations are however more complicated since the direction of $\mathbf{M}_T$ varies in time with respect to the direction of $\mathbf{M}_R$. On the other hand, the effects of thermal diffusion (which had been neglected) can be easily included by adding $6D_T t$ to the MSD and by replacing D_r by $D_r + D_r^T$ where $D_T = k_B T/6\pi\mu R$ and $D_r^T = k_B T/8\pi\mu R^3$ are the thermal translational and rotational diffusion coefficients respectively.

For a microswimmer immersed in water the viscosity is $\mu \simeq 10^{-3}\,\mathrm{pNs}/\mu\mathrm{m}^2$. With the parameters $f \simeq 5\times10^{-1}\,\mathrm{pN}$, $\lambda_R \simeq 10\,\mathrm{s}^{-1}$, $\lambda_T \simeq 1\mathrm{s}^{-1}$ and $\rho \simeq 10^{-1}\mu\mathrm{m}^{-2}$, we obtain

$$D_r \simeq (2\,\mu\mathrm{m}^2\mathrm{s}^{-1})\left\langle\sin^2\alpha\right\rangle_\alpha R^{-2}. \tag{5.32}$$

Therefore Eq. (5.31) is valid as long as we have $(0.2\,\mu\mathrm{m}^2)\left\langle\sin^2\alpha\right\rangle_\alpha R^{-2} \ll 1$. For a uniform distribution of angle of attachment in the range $[\alpha_{\min},\alpha_{\max}]$, $\left\langle\sin^2\alpha\right\rangle_\alpha \simeq 0.71$, hence the condition $D_r \ll (\lambda_R+\lambda_T)$ is accomplished provided that the particle is sufficiently large, $R \gtrsim 3\,\mu\mathrm{m}$. We now proceed to calculate the microswimmers effective diffusion coefficient.

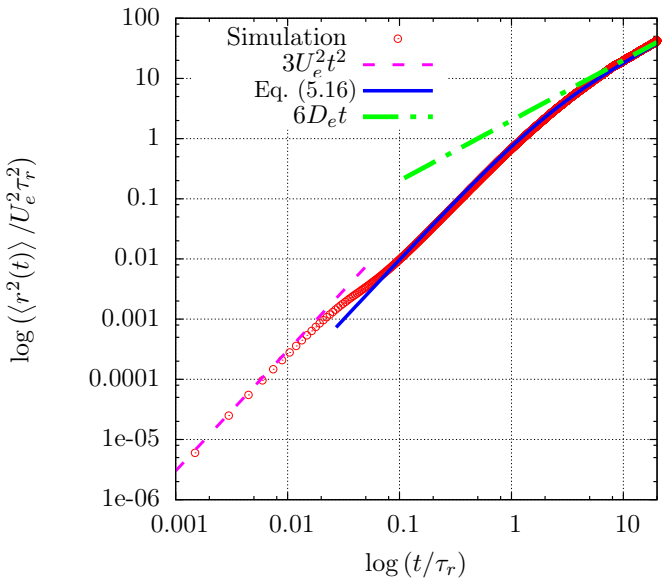

Fig. 5.6 Mean squared displacement of bacteria-driven microswimmers as a function of time, for fixed radius $R = 10\,\mu$m and density of cells $\rho = 1/12\,\mu\text{m}^{-2}$. The parameters f, λ_T and λ_R are the same as in Fig. 5.4. Circles: mean values for 10^4 different numerical realisations. Solid blue line; theory from Eq. (5.16). Dashed dotted green line: asymptotic diffusive behaviour $\langle r^2\rangle = 6D_et$ and D_e given by Eq. (5.33). Dashed magenta line: instantaneous ballistic evolution of the MSD, $\langle r^2\rangle = 3U_e^2t^2$. Note that time is measured in units of $\tau_r \simeq 68\,$s.

5.3.2.3 Long-time diffusion of bacteria-driven microswimmers

We now use the results above to obtain an analytical expression for the effective diffusion coefficient, D_e, defined by Eq. (5.17). Substitution of equations Eq. (5.20) and Eq. (5.31) into Eq. (5.17) with $\tau_r^{-1} = 2D_r$ leads to

$$6D_e = \frac{16}{9}\frac{R^2\lambda_R\left(\lambda_R+\lambda_T\right)}{\lambda_T\left\langle\sin^2\alpha\right\rangle_\alpha}. \tag{5.33}$$

Our result makes two predictions with important consequences for experiments: (i) for a setup with a uniform density of surface-attached bacteria, we predict that the long-time diffusion coefficient increases with the square of the size of the particle; (ii) the diffusion constant is, perhaps surprisingly, independent of the value of the propulsive force exerted by each bacterium. Recall however that diffusion is obtained in the “long-time" limit, which is defined as $t \gg D_r^{-1} \sim f^{-2}$ and therefore a variation in the value of f changes this limit. Note that when $\alpha_i = \pi/2$ for all i, we obtain a maximum value for the rotational diffusion and therefore a minimum value of the linear diffusion. In contrast, when $\alpha_i = 0$ for all swimmers we obtain a singular expression for the diffusion coefficient, due to the fact that there is no reorientation as discussed in §5.3.2.2. This result might appear counter intuitive, as one would expect that a large number of uniformly distributed radial forces acting on a sphere should account for no net thrust. However, this is only true if the time autocorrelation of the forces decays to zero. As the autocorrelation of the epsilon variables decays to a finite value, $(p_R^s)^2$ from Eq. (5.11), so does the velocity correlation function, hence the ballistic motion. Thermal fluctuations would make the particle reorient nevertheless, recovering a finite diffusivity. Tilting the forces away from the radial direction allows for reorientation of the sphere, reducing the probability of finding a given force pointing in the same direction at two different times accounting for a vanishing autocorrelation at large time-scales, hence the long-time diffusive behaviour for the case $\alpha_i \neq 0$.

We next validate our analytical results against numerical simulations. In Fig. 5.6 we show a log-log plot of the MSD as a function of time for a microswimmer of radius $R = 10\,\mu$m, with density of attached bacteria $\rho = 1/12\ \mu\text{m}^{-2}$, a propulsive force $f = 0.48$ pN and transition rates $\lambda_T^{-1} = 0.9$ s and $\lambda_R^{-1} = 0.1$ s. Time is measured in units of $\tau_r \simeq 68$s. At very short times $t \lesssim \tau_r/100 \sim \lambda_T^{-1} = 0.9\,$s, the force and torque remain constant and therefore the MSD is simply the instantaneous mean squared velocity multiplied by the time squared, that is $\left\langle r^2\right\rangle = 3U_e^2t^2$ (dashed magenta line). The solid blue line is Eq. (5.16) and, for times-scales shorter than τ_r, is ballistic with a MSD approximately $\left\langle r^2\right\rangle \simeq U_e^2t^2$. On the other hand, for

[2]The torque $\mathbf{M}$ fluctuates around its mean $\langle\mathbf{M}\rangle_\varepsilon \propto \mathbf{b}$ on a time-scale in the order of λ_T^{-1} which as seen below is much smaller than τ_r.

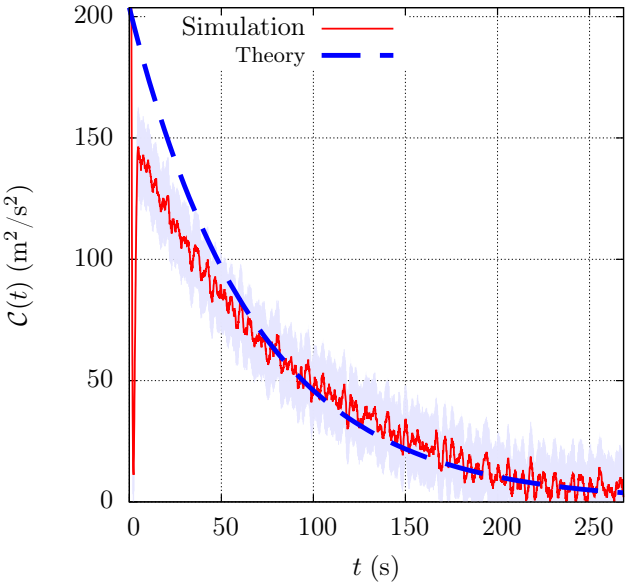

Fig. 5.7 Velocity correlation function of a bacteria-driven microswimmer of radius $R = 10\,\mu$m and density of bacteria $\rho = 1/12\,\mu\text{m}^{-2}$. The parameters f, λ_T and λ_R are the same as in Fig. 5.4. The solid line shows the average over 10^4 realisations and the shaded region the standard deviation. The dashed line is the theoretical prediction from $\mathscr{C}(t) = e^{-2D_r t}$ with D_r given by Eq. (5.31).

time-scales larger than τ_r, the MSD approaches the asymptotic limit $\langle r^2 \rangle \simeq 6D_e t$ represented by the dashed dotted green line, with D_e given by Eq. (5.33).

On Fig. 5.7 we illustrate the exponential decay of the velocity correlation function (solid red line) for the same microswimmer. The dashed line is the theoretical prediction of $\mathscr{C}(t) = e^{-2D_r t}$ with $D_r = (2\tau_r^{-1})$ and U_e given by equations Eq. (5.31) and Eq. (5.20) respectively. The shaded region is the (numerical) standard deviation. The coarse-grain model captures accurately the late time behaviour of the computational results. Finally, Fig. 5.8 shows the dependence of D_e with the bead radius R, for a microswimmer with the same set of parameters f, ρ, λ_R and λ_T. The red circles and error bars represent the numerical mean and the standard deviation of D_e, which where obtained from a linear fit to the MSD in the regime $t > 3\tau_r$. The dashed blue line represents our theoretical prediction Eq. (5.33), which agrees very well with the numerical results. The inset in Fig. 5.8 confirms that D_e is independent of the propulsive force of the individual bacteria, f.

5.3.3 Chemotaxis of bacteria-driven microswimmers

In the previous sections, we analysed the motion of the microswimmers in chemically-homogeneous environments. Here we consider the case where instead the surrounding

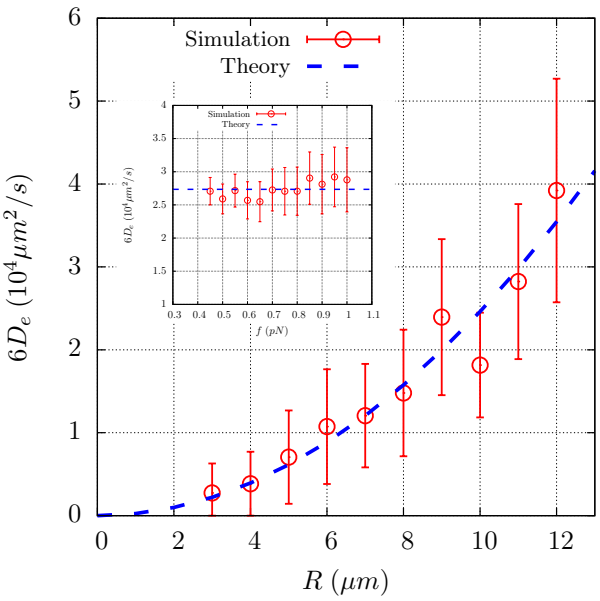

Fig. 5.8 Effective diffusion coefficient of bacteria-driven microswimmer as a function of the bead radius, R, for fixed density of cells $\rho = 1/12\,\mu\text{m}^{-2}$. The parameters f, λ_T and λ_R are the same as in Fig. 5.4. Inset shows D_e as a function of the propulsive force f, for a microswimmer of radius $R = 10/,\mu\text{m}$ and the same set of parameters. Mean values are shown in circles, error bars represent one standard deviation above and below the mean and the dashed line is the theoretical prediction of Eq. (5.33).

environment has a (weak) gradient of a solute to which the cells respond chemotactically. The question then emerges, whether the chemotaxis of individual cells translates to chemotaxis of the particle to which they are attached? The answer is not obvious *a priori* since bacteria in diametrically opposite positions on the particle can modify its motion in a symmetric fashion and as a result the chemotactic response can be vanishing. Experiments show however that the microswimmers perform indeed chemotaxis [90, 92]. Here we rationalise this result using the coarse grained model developed in the last section and we give an analytical expression for the chemotactic drift, which is validated against numerical simulations.

5.3.3.1 Chemotactic drift speed

As illustrated in the inset of Fig. 5.9, when the tumbling rate varies according to Eq. (2.17), the trajectories are biased in the direction of increasing concentration (positive z) and the drift increases with the magnitude of the chemical gradient. This result can be rationalised observing that the coarse-grain model developed in §5.3.2 can be interpreted as follows: the microswimmers are run-and-tumble particles with rate $1/T$, swimming speed U_e, persistence parameter $\langle \cos\theta \rangle = 0$ and subject to rotational diffusion with intensity $2D_r$. In the limit

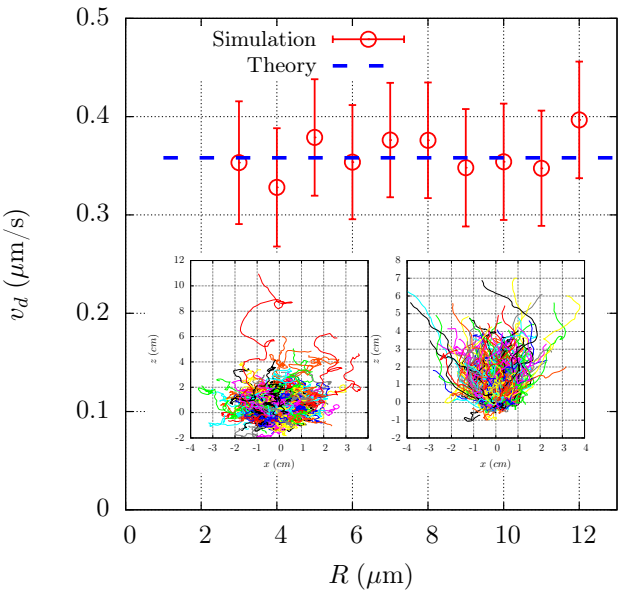

Fig. 5.9 Drift speed of bacteria-driven microswimmers as a function of the bead radius, R, for fixed cell density. The parameters ρ, f and λ_R are the same as in Fig. 5.4, $\lambda_0^{-1} = 0.9$ s and $k|\nabla c| = 0.005\,\mu\text{m}^{-1}$. Symbols show mean values from the simulations, error bars represent the standard deviation and the dashed line is the theoretical prediction in Eq. (5.37). The inset shows the biased trajectories in the direction of the chemical gradient for $k|\nabla c| = 0.01$ (left) and $k|\nabla c| = 0.05$ (right) with each figure showing 10^3 trajectories for a microswimmer of radius $R = 10\,\mu$m and the same set of parameters. In all cases, the simulation time is $t = 50/(3D_r) \simeq 2240$ s, where D_r is given by Eq. (5.31).

$k|\nabla c|R \ll 1$ the tumbling rate of each individual bacterium changes by the same fraction $Q(t) = \int K(t-s)c(s)\,\mathrm{d}s$ as in Eq. (2.17). Since $T^{-1} = 3D_r$ and $D_r \propto \lambda_R\lambda_T/(\lambda_T+\lambda_R)^3$, we find

$$\frac{1}{T(t)} = \frac{1}{T_0}\left(1 - \int_{-\infty}^{t} K(t-t')c(t')\mathrm{d}t'\right) + \mathscr{O}\left(|\nabla c|\frac{\lambda_T^{(0)}}{\lambda_R^2}\right), \tag{5.34}$$

this means that for shallow gradients, the tumbling rate for the microswimmer decreases in the same fashion as the tumbling rate for an individual bacterium, as long as $\lambda_T^{(0)} \ll \lambda_R$. Therefore, we can use the results of §2.2.2 to calculate the chemotactic drift for bacteria-driven microswimmers, the result is

$$v_d = \frac{|\nabla c|U_e^2 T_0^{-1}}{3(T_0^{-1}+2D_r)^2}\int K(s)e^{-(T_0^{-1}+2D_r)s}\,\mathrm{d}s. \tag{5.35}$$

It is known that $K(t)$ vanishes for $t > 4s$ [126]. Furthermore, D_r decreases quadratically with increasing R, therefore for sufficiently large radius of the particle we have $2D_r s \ll 1$ for all

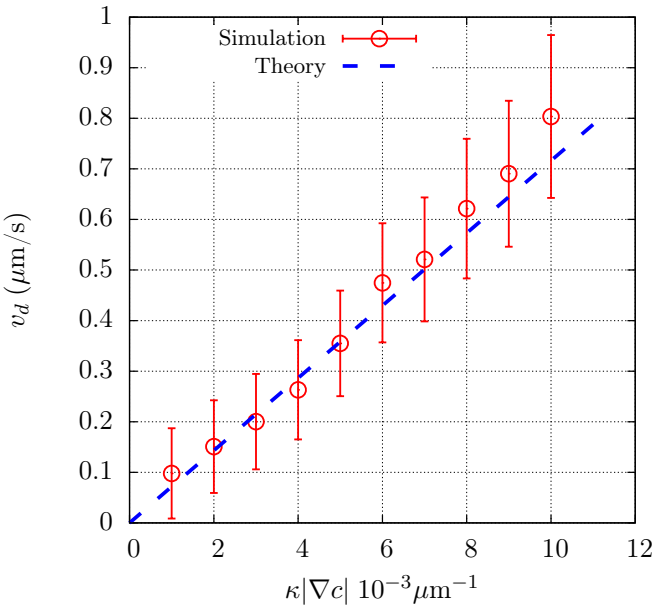

Fig. 5.10 Drift speed of bacteria-driven microswimmers as a function of $k|\nabla c|$ for a particle of fixed radius $R = 10\,\mu$m, The parameters ρ, f and λ_R are the same as in Fig. 5.4. The remaining parameters are the same as in Fig. 5.9. Symbols show mean values from the simulations, error bars represent the standard deviation and the dashed line is our prediction from Eq. (5.37).

relevant values of s (for example, when $R = 10\,\mu$m and $\rho = 1/12\,\mu\mathrm{m}^{-2}$, $2D_r \simeq 0.015\,\mathrm{s}^{-1}$) and we may then expand the exponential in the last line of Eq. (5.35) to first order in the rotational diffusion coefficient. This leads to the general prediction for drift velocity

$$v_d = -\frac{|\nabla c|U_e^2}{3(1+2D_rT_0)}\int_0^\infty K(s)s\mathrm{d}s = -\frac{|\nabla c|U_e^2}{5}\int_0^\infty K(s)s\mathrm{d}s. \tag{5.36}$$

where we have used Eq. (5.21) which leads to $T_0^{-1} = 3D_r$. Our prediction for v_d is seen to be independent of the radius of the particle and is linear in the concentration gradient. For the particular choice of $K(t) = k[\delta(t-t_1) - \delta(t-t_2)]$ used in our computations, we obtain

$$v_d = \frac{k|\nabla c|U_e^2(t_2-t_1)}{5}. \tag{5.37}$$

These results are validated against our simulations in Figs. 5.9 and 5.10. In Fig. 5.9 we first plot v_d as a function of R for fixed $k|\nabla c|$, $t_1 = 1\,\mathrm{s}$, $t_2 = 3\,\mathrm{s}$, $\lambda_0^{-1} = 0.9$ s and the same set of parameters f, ρ and λ_R as in the isotropic case. Correspondingly, we plot in Fig. 5.10 the drift speed as a function of $k|\nabla c|$ for fixed radius $R = 10\,\mu$m and the same set of parameters. Once again, the red circles and error bars represent the numerical values of the mean and standard

deviation of v_d. These values were obtained from a linear fit to the average displacement in the regime $t > 10\tau_r$. The dashed blue lines represent the prediction of Eq. (5.37) and we can observe that the agreement with the numerical results is excellent.

5.4 Discussion

Summary

In this chapter, we developed a coarse-grain model that allows to accurately predict the diffusive behaviour of bacteria-driven microswimmers, both in homogeneous environments and in the presence of (weak) chemical gradients. The analytical expressions for the effective diffusion coefficient D_e (Eq. 5.33) and the chemotactic drift speed v_d (Eq. 5.37) were validated against numerical simulations using the stochastic model presented in §5.2.1 with Eq. (2.17) for the chemotactic change of the tumbling rate of the bacteria. We found that the effective swimmer velocity, U_e, is independent of the swimmer size, but increases with the square root of the number of surface-attached bacteria N, when N is large. On the other hand, the rotational diffusion coefficient, D_r, increases linearly with N and is inversely proportional to the particle radius R, in contrast with the thermal rotational diffusion coefficient D_r^T which decreases as R^{-3}. For shallow chemical gradients $k|\nabla c|R \ll 1$, we found that the microswimmers respond chemotactically if we assume that each bacterium on its surface does, and that the resulting chemotactic drift speed is proportional to $|\nabla c|$ and independent of R, the latter being a consequence of the bacteria being constrained by the bead and each bacterium experiencing the same change in concentration.

Comparison with experiments

The expression we obtained for the effective velocity can be directly compared with experimental results. Behkam et al. reported $U_e = 14.8 \pm 1.1\,\mu$m/s for microswimmers of radius $R = 10\,\mu$m and densities of attachment between one bacterium per $12\,\mu\text{m}^2$ and $7\,\mu\text{m}^2$ with $f \simeq 0.48\,$pN [93]. In comparison, our model predicts $U_e \simeq 12.99 - 17.42\,\mu$m/s, in good agreement. The same study also reported that the swimming speed increases with the square root of the number of bacteria N, for $N \geq 10$, as predicted theoretically. The same scaling result was reported by Arabagi et al. [91] and Zhuang et al. [92]. Furthermore, both of these studies reported swimming velocities independent of the particle radius in homogeneous environments as well as in the presence of a chemical gradient, again confirming our theoretical results. Unfortunately there are no past experimental measurements of the effective diffusion coefficient. In their numerical simulations however, Arabagi et al. [91] reported the value $D_e = 15185\,\mu\text{m}^2/\text{s}$ for a bead of radius $R = 20\,\mu$m and $f \simeq 0.48\,$pN, in good agreement with

Eq. (5.33) which predicts $D_e \simeq 15802\,\mu\mathrm{m}^2/\mathrm{s}$. Regarding the chemotactic drift of particles with surface-attached bacteria, Zhuang et al. [90, 92] found that v_d is proportional to the magnitude of the chemical gradient and that it is independent of the particle size, both of which are predicted by Eq. (5.37).

Outlook

The analytical results in this chapter will be useful for the practical design of bacteria-driven microswimmers. The model can be extended to include other steering strategies such as phototaxis, pH-taxis and external electromagnetic fields [97, 101]. The assumption of a chemically permeable particle could also be relaxed, and the perturbation to the concentration field by the presence of the particle (and the cells) should be solved for. Another possible extension is the study of deformable random walkers, inspired by experiments with bacteria-driven microswimmers in which *E. coli* are attached to red blood cells [158]. One of the ultimate applications of bacteria-driven microswimmers is targeted drug delivery, which requires a suspension of these particles to move collectively. A mathematical description of the collective behaviour of multiple microswimmers is therefore needed and this requires an explicit consideration of their hydrodynamic interactions. The interactions depend critically on the distribution of attached bacteria on the surface of each particle, which can be controlled using micro-manipulation [159] and nanoprinting methods [19, 160]. A theory including hydrodynamic interactions, taking clues from classical work on active fluids [33, 161] will therefore allow to move bacteria-driven microswimmers closer to applications.

Chapter 6

Near-surface run-and-tumble

6.1 Introduction

A swimming bacterium can be modelled mathematically as a run-and-tumble particle (RTP), which is an active swimmer that moves at a constant speed v_0 for an average interval of time λ_T^{-1}, a run, before changing its direction of motion, a tumble. The rate at which tumbles occur is λ_T and they last for λ_R^{-1} which is the inverse of the running rate. Usually the running rate is much bigger than the tumbling rate, that is $\lambda_T \ll \lambda_R$, hence we can neglect the duration of the tumbling event and consider the changes in direction as instantaneous. The reorientation angle between consecutive paths β_0 is considered to be isotropic and can be characterised by a persistence parameter $\alpha = \langle \cos\beta_0 \rangle$. In practice we are interested in the long time behaviour of the RTP and we can ignore fluctuations in the running time and the tumbling angle.

A bacterium swimming in the bulk will exhibit quasi-straight runs. In this case the trajectory will resemble a random chain with straight links (see. Fig. 6.1). In contrast when the bacterium moves next to a solid boundary, the runs become circular (see Fig. 6.2) as a result of hydrodynamic interactions with the wall. In this chapter we analyse the long time behaviour of an RTP in both cases, free-swimming (straight paths) and swimming next to a wall (circular paths). The calculations are similar for both cases, therefore we start analysing the free-swimming case, recovering classical results. In §6.2 we model run-and-tumble as a jump diffusion process of constant rate λ_T, this allows us to derive an evolution equation for the probability distribution $P(\mathbf{x},\mathbf{p},t)$ of finding the RTP at position $\mathbf{x}$, with orientation $\mathbf{p}$ at time t. We treat the particular case of exponentially distributed waiting times in §6.2.2.1 and we derive analytical expressions for the effective diffusion coefficient D_e. We introduce chemotaxis in §6.3 by allowing the tumbling rate to depend on a chemical concentration gradient $\lambda_T(t) = \lambda_T[C(\mathbf{x}(t))]$. In the case in which the concentration field changes slowly,

we can expand P in powers of the concentration gradient $|\nabla C|$ and compute the chemotactic drift v_d, which follows from the first moment of the position.

We generalise the calculations to the circle swimming case in §6.4. We calculate expressions for the diffusivity and chemotactic drift, and show that both are always lower when the RTP moves in circles. The effects of thermal fluctuations are discussed in §6.5, along with a general discussion and comparison with previous models. Throughout the chapter we focus on motion in two dimensions, but the analysis can be easily generalised to one or three dimensions. Such two-dimensional motion can be achieved by strong confinement, for example, if the cells swim in a thin fluid film squeezed between two solid plates then run-and-tumble with straight paths is observed [116]. When one of the surfaces is removed, then circle swimming can be recovered [112].

6.2 Free-swimming run-and-tumble

When swimming in the bulk, the trajectory of an RTP can be seen as a series of straight paths of equal length v_0/λ_T and directions $\{\mathbf{p}_i\}_{i=0}^{N}$, such that $\mathbf{p}_i \cdot \mathbf{p}_{i+1} = \alpha$ (with equal probability for positive or negative tumbling angle), see Fig. 6.1. In this section we calculate the late time motility properties of an RTP moving in free space. We proceed by considering the random walk depicted in Fig 6.1 as a continuous process in time, this will allow us to derive a Fokker–Planck like equation for the probability distribution of the position of the particle. We can then calculate the moments of the position of the RTP, from which we can determine the diffusivity and the randomisation time.

6.2.1 Equations of Motion

We consider a particle moving in two dimensions with position $\mathbf{x} = x\mathbf{e}_x + y\mathbf{e}_y$ and velocity $\mathbf{v} = v_0\mathbf{p}$, where v_0 is a constant speed and $\mathbf{p} = \cos\beta\mathbf{e}_x + \sin\beta\mathbf{e}_y$ is a unit vector with orientation β. The set $\{\mathbf{e}_x, \mathbf{e}_y\}$ is the Cartesian basis for the Euclidean two dimensional space. Naturally, the position of the RTP evolves according to $\dot{\mathbf{x}} = \mathbf{v}$. On the other, the orientation angle β will evolve according to $\dot{\beta} = \omega(t)$, where ω is an stochastic process determined by the tumbling dynamics. Since tumbles occur at discrete points in time, the angular velocity ω can be written as follows

$$\omega(t) = \sum_{i=0}^{N(t)} \beta_i \delta(t - t_i), \tag{6.1}$$

where $N(t)$ is a counting process with probability $P_n(N)$, β_i is the tumbling angle which is distributed according to a density function $q(\beta_i)$, and $\delta(t)$ is the Dirac delta. Given the

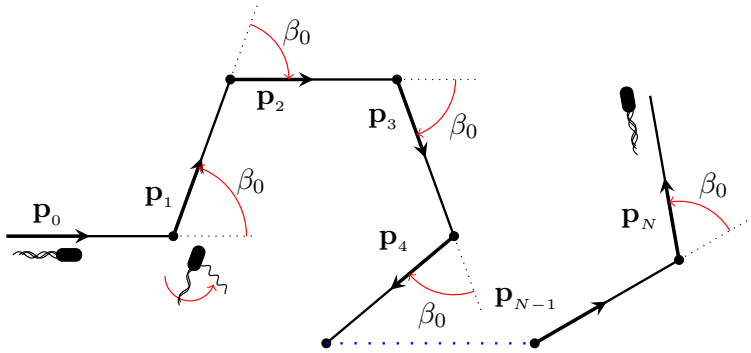

Fig. 6.1 Run and tumble trajectory in two dimensional flat space. The trajectory consists of straight paths of equal length v_0/λ_T with directions $\{\mathbf{p}_i\}_{i=0}^N$ such that $\mathbf{p}_i \cdot \mathbf{p}_{i+1} = \alpha$, with α the persistence parameter.

singular nature of $\delta(t)$, it is more convenient to consider equations for the increments in position and orientation: $\delta\mathbf{x} = \mathbf{x}(t+\tau) - \mathbf{x}(t)$ and $\delta\beta = \beta(t+\tau) - \beta(t)$, during a small interval of time τ. The evolution equations can then be written in the Ito convention as [162]

$$\delta x = v_0 \cos\beta(t)\tau, \tag{6.2}$$

$$\delta y = v_0 \sin\beta(t)\tau, \tag{6.3}$$

$$\delta\beta = \int_t^{t+\tau} \omega(t')\,\mathrm{d}t' = \sum_{i=1}^{N(\tau)} \beta_i. \tag{6.4}$$

Both the position and orientation of the RTP are random variables, this means that all the knowledge we can have about them will depend on the probability distribution $P(\mathbf{x},\beta,t)$ of finding the particle at position $\mathbf{x}$ with orientation β at time t. The idea now is to obtain an evolution equation for P, with the aid of equations Eq. (6.2)-Eq. (6.4). When the noise increments $\delta\beta$ are normally distributed, the resulting equation is called the Fokker–Planck equation, hence we will refer to the evolution equation of P as the generalised Fokker–Planck equation [163].

6.2.2 The generalised Fokker–Planck equation

In this section we derive the evolution equation for the probability $P(\mathbf{x},\beta,t)$, following the analysis presented by Denisov et al. in [163]. We start by defining the double Fourier transform of P as follows

$$P_{\mathbf{k},\ell}(t) = \int_{\mathbb{R}^2}\int_{-\pi}^{\pi} e^{-i\mathbf{k}\cdot\mathbf{x} - i\ell\beta} P(\mathbf{x},\beta,t)\,\mathrm{d}\beta\,\mathrm{d}\mathbf{x}$$

$$= \left\langle e^{-i\mathbf{k}\cdot\mathbf{x}-i\ell\beta} \right\rangle = \mathscr{F}_{\mathbf{k},\ell}\left[P(\mathbf{x},\beta,t)\right]. \tag{6.5}$$

We now calculate the probability increment $\delta P_{\mathbf{k},\ell} = P_{\mathbf{k},\ell}(t+\tau) - P_{\mathbf{k},\ell}(t)$, where the time interval τ is vanishing small. Taylor expanding at first order in τ we obtain

$$\delta P_{\mathbf{k},\ell}(t) = \left\langle e^{-i\mathbf{k}\cdot\mathbf{x}-i\ell\beta} \left[e^{-i\tau\mathbf{k}\cdot\left(\dot{x}\frac{\partial\mathbf{x}}{\partial x}+\dot{y}\frac{\partial\mathbf{x}}{\partial y}\right)-i\ell\delta\beta} - 1 \right] \right\rangle, \tag{6.6}$$

Expanding the exponentials and ignoring terms of order $\tau\delta\beta$ and higher, we have

$$\delta P_{\mathbf{k},\ell}(t) = \left\langle e^{-i\mathbf{k}\cdot\mathbf{x}-i\ell\beta} \left(e^{-i\ell\delta\beta} - 1 \right) \right\rangle - i\tau \left\langle \mathbf{k}\cdot\left(\dot{x}\frac{\partial\mathbf{x}}{\partial x} + \dot{y}\frac{\partial\mathbf{x}}{\partial y} \right) e^{-i\mathbf{k}\cdot\mathbf{x}-i\ell\beta} \right\rangle. \tag{6.7}$$

Using integration by parts and equations Eq. (6.2)-Eq. (6.4) we can show that the second term can be written as

$$-\tau\mathscr{F}_{\mathbf{k},\ell}\left[\left(\frac{\partial}{\partial x}\dot{x} + \frac{\partial}{\partial y}\dot{y} \right) P(\mathbf{x},\beta,t) \right] = -\tau\mathscr{F}_{\mathbf{k},\ell}\left[\nabla\cdot(\dot{\mathbf{x}}P(\mathbf{x},\beta,t))\right]. \tag{6.8}$$

The first term in Eq. (6.7) is obtained by calculating the average over the random variable $\delta\beta$ as follows

$$\begin{aligned} \left\langle e^{-i\mathbf{k}\cdot\mathbf{x}-i\ell\beta} \left(e^{-i\ell\delta\beta} - 1 \right) \right\rangle &= \int P(\mathbf{x},\beta,t) e^{-i\mathbf{k}\cdot\mathbf{x}-i\ell\beta} \int \left(e^{-i\ell\zeta} - 1 \right) F(\zeta,\tau)\,\mathrm{d}\zeta\,\mathrm{d}x\,\mathrm{d}y\,\mathrm{d}\beta \\ &= \int P(\mathbf{x},\beta,t) e^{-i\mathbf{k}\cdot\mathbf{x}-i\ell\beta} \left(F_\ell(\tau) - 1\right) \mathrm{d}x\,\mathrm{d}y\,\mathrm{d}\beta, \end{aligned} \tag{6.9}$$

where $F(\zeta,\tau)$ is the probability distribution of the stochastic process $\delta\beta$ and $F_\ell(\tau)$ its Fourier transform. Taking the limit as $\tau \to 0$ of Eq. (6.7) and then the inverse Fourier transform we obtain the generalised Fokker–Planck equation

$$\frac{\partial}{\partial t}P(\mathbf{x},\beta,t) = -v_0\left(\cos\beta\frac{\partial}{\partial x} + \sin\beta\frac{\partial}{\partial y} \right) P(\mathbf{x},\beta,t) + \int P(\mathbf{x},\zeta,t)\Phi(\beta-\zeta)\,\mathrm{d}\zeta, \tag{6.10}$$

where $\Phi(\zeta)$ is defined as

$$\Phi(\zeta) = \lim_{\tau\to 0}\frac{1}{\tau}\left(F(\zeta,\tau) - \delta(\zeta)\right). \tag{6.11}$$

We note that this expression is valid for any process $\delta\beta$, not necessarily the one given in Eq. (6.1). For example, when the reorientations are due to thermal noise, $\delta\beta$ follows a Gaussian distribution with variance $2D$, therefore $F_\ell(\tau) = e^{-D\tau\ell^2} \simeq 1 - D\tau\ell^2$, after taking

the inverse Fourier transform Eq. (6.10) reduces to

$$\frac{\partial}{\partial t}P = D\nabla\cdot(\nabla P) - v_0\left(\cos\beta\frac{\partial}{\partial x}+\sin\beta\frac{\partial}{\partial y}\right)P = \nabla\cdot\left[-\dot{\mathbf{x}}P + D\nabla P\right], \tag{6.12}$$

which is the well-known Fokker–Planck equation. Next we calculate Φ for the run-and-tumble process Eq. (6.1).

6.2.2.1 Run-and-tumble diffusion

For convenience, we will consider that the number of tumbles follows a Poisson distribution with rate λ_T, which is a good approximation according to experimental observations of tumbling bacteria [125]. In this case $P_n(N(t)) = (\lambda_T t)^n e^{-\lambda_T t}/n!$ and we can calculate $F(\zeta,\tau) = \langle\delta(\zeta-\delta\beta)\rangle$ using the law of total expectation as follows

$$\begin{aligned} F(\zeta,\tau) &= \sum_{n=0}^{\infty}\langle\delta(\zeta-\delta\beta)|N(\tau)=n\rangle\, P_n(\tau) \\ &= P_0(\tau)\delta(\zeta) + \sum_{n=1}^{\infty}P_n(\tau)\int\delta(\zeta-\delta\beta)\prod_j q(\beta_j)\,\mathrm{d}\beta_j, \end{aligned} \tag{6.13}$$

where $q(\beta_j)$ is the probability distribution of the tumbling angles. At first order in τ, only the terms with P_0 and P_1 survive, as $\delta\beta = \beta_1$ for $N(t) = 1$ we have

$$F(\zeta,\tau) = (1-\lambda_T\tau)\delta(\zeta) + \lambda_T\tau q(\zeta) + \mathscr{O}(\tau^2), \tag{6.14}$$

and hence, $\Phi(\beta) = \lambda_T\left(q(\beta)-\delta(\beta)\right)$. We ignore fluctuations on the tumbling angle between consecutive events, so that $q(\beta) = (\delta(\beta-\beta_0)+\delta(\beta+\beta_0))/2$, in this case the Fokker–Planck equation is

$$\begin{aligned} \frac{\partial P}{\partial t} &= -v_0\left(\cos\beta\frac{\partial}{\partial x}+\sin\beta\frac{\partial}{\partial y}\right)P(x,y,\beta,t) \\ &\quad + \frac{\lambda_T}{2}\left[P(x,y,\beta-\beta_0,t)+P(x,y,\beta+\beta_0,t)\right] - \lambda_T P(x,y,\beta,t). \end{aligned} \tag{6.15}$$

We solve the equation following an approach similar to that used in references [164] and [165]. We decompose P in Fourier modes

$$P(\mathbf{x},\beta,t) = \frac{1}{2\pi}\sum_{n\in\mathbb{Z}} e^{in\beta-\lambda_T t g(n)}p_n(\mathbf{x},t), \tag{6.16}$$

where $g(n) = 1 - \cos(n\beta_0)$ is chosen so that the left-hand-side and the terms proportional to λ_T in Eq. (6.15) cancel. Substituting Eq. (6.16) into Eq. (6.15) gives the hierarchy equations

$$\frac{\partial p_n}{\partial t} = -\frac{v_0}{2} \sum_{\sigma=\{-1,1\}} e^{-\lambda_T (g(n+\sigma)-g(n))t} \hat{\ell}_\sigma p_{n+\sigma}, \tag{6.17}$$

where $\hat{\ell}_\sigma = \partial/\partial x + i\sigma \partial/\partial y$. Note that the moments of $\cos(n\beta)$ involve only the $n-$th Fourier modes $p_{\pm n}$, in particular p_0 corresponds to the probability distribution of finding the RTP at position $\mathbf{x}$ at time t, regardless of its orientation. Moreover, since $\langle x \rangle = \int v_0 \langle \cos\beta(t') \rangle \, \mathrm{d}t'$, and $\langle x^2 \rangle = v_0^2 \int\int \langle \cos\beta(t') \cos\beta(t'') \rangle \, \mathrm{d}t'' \, \mathrm{d}t'$, we should expect only a few of the Fourier modes to be relevant. In fact we can show that truncating the hierarchy at $n = \pm 1$ already gives the correct result for the mean and mean squared displacement (see §6.5). Therefore, we consider the hierarchy equations

$$\dot{p}_0(\mathbf{x},t) = -\frac{v_0}{2} e^{-\lambda_\alpha t} \left(\hat{\ell}_1 p_1(\mathbf{x},t) + \hat{\ell}_{-1} p_{-1}(\mathbf{x},t) \right), \tag{6.18}$$

$$\dot{p}_{\pm 1}(\mathbf{x},t) = -\frac{v_0}{2} e^{-\lambda_\alpha t} \hat{\ell}_{\mp 1} p_0(\mathbf{x},t), \tag{6.19}$$

where $\lambda_\alpha = \lambda_T(1-\alpha)$. Differentiating Eq. (6.18) with respect to time we find that the marginal distribution p_0 evolves according to the telegrapher's equation

$$\ddot{p}_0 + \lambda_\alpha \dot{p}_0 - \frac{v_0^2}{2} \Delta p_0 = 0, \tag{6.20}$$

where $\Delta = \nabla \cdot \nabla$ is the Laplace operator. The general solution can be obtained by expanding p_0 in planar wave modes $e^{i\mathbf{q}\cdot x}$. Then applying the initial conditions $p_0|_{t=0} = \delta(\mathbf{x})$ and $[\partial p_0/\partial t]_{t=0} = 0$, we obtain

$$p_0(\mathbf{x},t) = \frac{1}{(2\pi)^2} \int G\left(\lambda_\alpha t/2, 2v_0^2 q^2/\lambda_\alpha^2\right) e^{i\mathbf{q}\cdot\mathbf{x}} \, \mathrm{d}\mathbf{q}, \tag{6.21}$$

where

$$G_q(t) = G(\xi(t), \zeta(\mathbf{q})) = e^{-\xi} \left[\cosh\left(\xi\sqrt{1-\zeta}\right) + \frac{\sinh\xi\sqrt{1-\zeta}}{\sqrt{1-\zeta}} \right]. \tag{6.22}$$

We can now calculate the moments of the position vector $\mathbf{x}$. The mean vanishes of course, because the system is invariant under rotations. The variance on the other follows from the fact that $|\mathbf{x}|^2 e^{i\mathbf{q}\cdot\mathbf{x}} = -\Delta_q e^{i\mathbf{q}\cdot\mathbf{x}}$ and the integral representation of the delta function. Here $\Delta_q = \partial^2/\partial q_x^2 + \partial^2/\partial q_y^2$ is the Laplacian in the q space. Hence, applying the formal definition

of the average and integrating by parts we have

$$\left\langle |\mathbf{x}|^2 \right\rangle = \frac{1}{(2\pi)^2} \int\int |\mathbf{x}|^2 G_q e^{i\mathbf{q}\cdot\mathbf{x}} \,\mathrm{d}\mathbf{q}\,\mathrm{d}\mathbf{x} = -\int G_q \Delta_q \delta(\mathbf{q})\,\mathrm{d}\mathbf{q} = -\left[\Delta_q G_q\right]_{\mathbf{q}=\mathbf{0}}. \tag{6.23}$$

From equation Eq. (6.22), we have that $\nabla_q G_q = (4v_0^2/\lambda_\alpha^2)(\partial G/\partial\zeta)\mathbf{q}$ and taking the divergence we find $[\Delta_q G_q]_{\mathbf{q}=\mathbf{0}} = 2(4v_0^2/\lambda_\alpha^2)[\partial G_q/\partial\zeta]_{\zeta=0}$, where the factor of 2 comes from the divergence of $\mathbf{q}$ in two dimensions. Substituting in Eq. (6.23) and using $\xi = \lambda_\alpha t/2$ we obtain

$$\begin{aligned}\left\langle |\mathbf{x}|^2 \right\rangle &= -\frac{4v_0^2}{\lambda_\alpha^2} e^{-\xi} \left(-\xi \sinh\xi - \xi\cosh\xi + \sinh\xi\right) = \frac{4v_0^2}{\lambda_\alpha^2} e^{-\xi}\left(\xi e^{\xi} + \frac{e^{-\xi} - e^{\xi}}{2}\right) \\ &= \frac{2v_0^2}{\lambda_\alpha^2}\left(\lambda_\alpha t + e^{-\lambda_\alpha t} - 1\right) = 2v_0^2\tau_r^2\left(\frac{t}{\tau_r} + e^{-t/\tau_r} - 1\right),\end{aligned} \tag{6.24}$$

where we defined the correlation time $\tau_r = \lambda_\alpha^{-1}$. Equation Eq. (6.24) is the well known result derived by Lovely and Dahlquist [122] for the mean squared displacement of an RTP in planar space with an effective diffusivity $4D_e = 2v_0^2\tau_r$.

6.3 Run-and-tumble chemotaxis

Inspired by bacterial chemotaxis, we will assume that our RTP changes its tumbling rate λ_T in response to a chemical concentration gradient $C(\mathbf{x})$ on the plane. Following the classical de Gennes analysis [132], we assume that the tumbling rate changes as $\lambda_T(t) = \lambda_T^{(0)}(1 - Q(t))$, where $\lambda_T^{(0)}$ is the tumbling rate in a homogeneous environment and the fraction Q depends on the history of the RTP trajectory as follows

$$Q(t) = \int_{-\infty}^{t} K(t-s)C(\mathbf{x}(s))\mathrm{d}s. \tag{6.25}$$

The kernel $K(t)$ is usually considered to be a bilobed function such that $\int K\mathrm{d}t = 0$, a property which accounts for adaptation. This means that for a constant concentration field the tumbling rate is $\lambda_T^{(0)}$. We now consider a linear chemical concentration gradient

$$C(\mathbf{x}(t)) = C_0 + |\nabla C|\mathbf{x}(t)\cdot\mathbf{e}_x, \tag{6.26}$$

with constant intensity $|\nabla C|$. The constant C_0 is a reference concentration that we can ignore as we assume adaptation. It is customary to approximate the memory kernel by a sum of impulses $K(t) = \sum k_i \delta(t - T_i)$, where k_i is the intensity of the response at time T_i and satisfies $\sum k_i = 0$. A special case is that of instantaneous changes according to the orientation of the

RTP with respect to the chemical concentration gradient. In this case the dynamics is still Markovian, that means that the probability distribution only depends on the present state and not on the previous history. We address this case first in order to get some intuition on the calculations. Then we will include details of the RTP trajectory history by introducing a set of internal variables that will take care of the particle's memory.

6.3.1 Non-adaptive chemotaxis

The instantaneous sensing limit is obtained by considering the memory kernel with only two spikes at times $T_1 = T$ and $T_2 = T + \tau$ with intensities $k_1 = k_2 = k/(v_0\tau)$, in this case $\lambda_T(t) = \lambda_T^{(0)}(1 - k|\nabla C|(x(t-T) - x(t-T-\tau)/(v_0\tau)))$. Then, taking the simultaneous limit $\tau \to 0$, $T \to 0$ we obtain

$$\lambda_T(t) = \lambda_T^{(0)}\left(1 - k|\nabla C|\frac{\dot{x}(t)}{v_0}\right) = \lambda_T^{(0)} + \varepsilon\lambda_T^{(1)}(t), \tag{6.27}$$

where $\varepsilon = k|\nabla C|$ and $\lambda_T^{(1)} = -\lambda_T^{(0)}\dot{x}(t)/v_0 = -\lambda_T^{(0)}\cos\beta$. This means that the RTP biases its tumbling rate, depending on its instantaneous orientation with respect to the gradient. For shallow gradients, the parameter ε will be small and we can make an asymptotic expansion of the probability distribution $P(\mathbf{x},\beta,t)$ as follows

$$\begin{aligned}
P(\mathbf{x},\beta,t) &= \frac{1}{2\pi}\sum_{n\in\mathbb{Z}} e^{in\beta - \lambda_T^{(0)} t g(n) - \varepsilon\int\lambda^{(1)}(t')\mathrm{d}t' g(n)}\left(p_n^{(0)} + \varepsilon p_n^{(1)} + \mathscr{O}\left(\varepsilon^2\right)\right) \\
&= \frac{1}{2\pi}\sum_{n\in\mathbb{Z}} e^{in\beta - \lambda_T^{(0)} t g(n)}\left[p_n^{(0)} + \varepsilon\left(p_n^{(1)} - \int\lambda^{(1)}(t')\mathrm{d}t' g(n) p_n^{(0)}\right)\right] + \mathscr{O}\left(\varepsilon^2\right) \\
&= \frac{1}{2\pi}\sum_{n\in\mathbb{Z}} e^{in\beta - \lambda_T^{(0)} t g(n)}\left[p_n^{(0)} + \varepsilon\left(p_n^{(1)} + \frac{\lambda_T^{(0)}}{v_0} x g(n) p_n^{(0)}\right)\right] + \mathscr{O}\left(\varepsilon^2\right) \\
&= P^{(0)} + \varepsilon P^{(1)} + \mathscr{O}\left(\varepsilon^2\right).
\end{aligned} \tag{6.28}$$

Taking the time derivative we find for the first order correction

$$\dot{P}^{(1)} = \frac{1}{2\pi}\sum_{n\in\mathbb{Z}} e^{in\beta - \lambda_T^{(0)} t g(n)}\left[\left(\frac{\partial}{\partial t} - \lambda_T^{(0)} g(n)\right)\left(p_n^{(1)} + \frac{\lambda_T^{(0)}}{v_0} x g(n) p_n^{(0)}\right)\right]. \tag{6.29}$$

On the other hand, expanding Eq. (6.15) in powers of ε, we find for the first correction

$$\dot{P}^{(1)} = -\nabla\cdot\left(\dot{\mathbf{x}}P^{(1)}\right) + \frac{\lambda_T^{(0)}}{2}\left(P_+^{(1)} + P_-^{(1)} - 2P^{(1)}\right) + \frac{\lambda_T^{(1)}}{2}\left(P_+^{(0)} + P_-^{(0)} - 2P^{(0)}\right), \tag{6.30}$$

where $P_{\pm}^{(0,1)} = P^{(0,1)}(\mathbf{x}, \beta \pm \beta_0, t)$. Substituting Eq. (6.28) into Eq. (6.30) we obtain

$$\dot{P}^{(1)} = -\nabla \cdot \left(\dot{\mathbf{x}} P^{(1)}\right) - \frac{1}{2\pi} \sum_{n\in\mathbb{Z}} e^{in\beta - \lambda_T^{(0)} t g(n)} \lambda_T^{(0)} g(n) \left(p_n^{(1)} + \frac{\lambda_T^{(0)}}{v_0} x g(n) p_n^{(0)} \right) - \frac{1}{2\pi} \sum_{n\in\mathbb{Z}} e^{in\beta - \lambda_T^{(0)} t g(n)} \lambda_T^{(1)} g(n) p_n^{(0)}. \tag{6.31}$$

The second term cancels the term proportional to $\lambda_T^{(0)}$ in Eq. (6.29). Then comparing terms of the same order in n we find the hierarchy equations

$$\dot{p}_n^{(1)} + \frac{\lambda_T^{(0)}}{v_0} x g(n) \dot{p}_n^{(0)} = -\frac{v_0}{2} \sum_{\sigma=\{1,-1\}} e^{-\lambda_T^{(0)} t (g(n+\sigma) - g(n))} \left[\hat{\ell}_\sigma p_{n+\sigma}^{(1)} + \frac{\lambda_T^{(0)}}{v_0} g(n+\sigma) \hat{\ell}_\sigma x p_{n+\sigma}^{(0)} - \frac{\lambda_T^{(0)}}{v_0} g(n+\sigma) p_{n+\sigma}^{(0)} \right]. \tag{6.32}$$

Again we truncate the hierarchy at first order. In this case, using $g(0) = 0$ and $g(\pm 1) = 1 - \alpha$ we get the system of equations

$$\dot{p}_0^{(1)} = -\frac{v_0}{2} e^{-\lambda_\alpha^{(0)} t} \left[\hat{\ell}_1 \left(p_1^{(1)} + \frac{\lambda_\alpha^{(0)}}{v_0} x p_1^{(0)} \right) + \hat{\ell}_{-1} \left(p_{-1}^{(1)} + \frac{\lambda_\alpha^{(0)}}{v_0} x p_{-1}^{(0)} \right) \right] + \frac{\lambda_\alpha^{(0)}}{2} e^{-\lambda_\alpha^{(0)} t} \left(p_1^{(0)} + p_{-1}^{(0)} \right) \tag{6.33}$$

$$\dot{p}_{\pm 1}^{(1)} = -\frac{\lambda_\alpha^{(0)}}{v_0} x \dot{p}_{\pm 1}^{(0)} - \frac{v_0}{2} e^{\lambda_\alpha^{(0)} t} \hat{\ell}_{\mp 1} p_0^{(1)}. \tag{6.34}$$

We turn this into a evolution equation for $p_0^{(1)}$, by taking the time derivative of Eq. (6.33), the result is

$$\ddot{p}_0^{(1)} + \lambda_\alpha^{(0)} \dot{p}_0^{(1)} - \frac{v_0^2}{2} \Delta p_0^{(1)} = \frac{\lambda_\alpha^{(0)}}{2} e^{-\lambda_\alpha^{(0)} t} \left(\dot{p}_1^{(0)} + \dot{p}_{-1}^{(0)} \right). \tag{6.35}$$

The right hand side is simplified by using Equations Eq. (6.18) and Eq. (6.19). The evolution of the first order correction to the probability of finding the particle at position $\mathbf{x}$ at time t, regardless of its orientation is

$$\ddot{p}_0^{(1)} + \lambda_\alpha^{(0)} \dot{p}_0^{(1)} - \frac{v_0}{2} \Delta p_0^{(1)} = -\frac{\lambda_\alpha^{(0)} v_0}{2} \frac{\partial}{\partial x} p_0^{(0)}. \tag{6.36}$$

Multiplying by x and integrating over the whole domain we find the evolution of the first correction to the mean displacement in the direction of the chemical gradient

$$\langle \ddot{x} \rangle^{(1)} + \lambda_\alpha^{(0)} \langle \dot{x} \rangle^{(1)} = -\frac{\lambda_\alpha^{(0)} v_0}{2} \int_{-\infty}^{\infty} x \frac{\partial}{\partial x} p_0^{(0)} \mathrm{d}x = \frac{\lambda_\alpha^{(0)} v_0}{2}. \tag{6.37}$$

Integrating once and using $\langle \dot{x} \rangle (t=0) = 0$, we find

$$\langle \dot{x} \rangle^{(1)} = \frac{\lambda_\alpha^{(0)} v_0}{2} \int_0^t e^{-\lambda_\alpha^{(0)}(t-t')} \mathrm{d}t' = \frac{v_0}{2} \left(1 - e^{-\lambda_\alpha^{(0)} t} \right). \tag{6.38}$$

From this we can deduce that the chemotactic drift is

$$v_d = \varepsilon \lim_{t\to\infty} \langle \dot{x} \rangle^{(1)} = k|\nabla C| \frac{v_0}{2}, \tag{6.39}$$

which agrees with the de Gennes model [134] and the calculations of Schnitzer [127].

6.3.2 Adaptive chemotaxis

We now assume that the tumbling rate depends on the history of the trajectory as

$$\lambda_T(t) = \lambda_T^{(0)} (1 - k|\nabla C| x(t-T)) = \lambda_T^{(0)} + \varepsilon \lambda_T^{(1)}, \tag{6.40}$$

where now $\varepsilon = k|\nabla C| v_0 / \lambda_T^{(0)}$ and $\lambda_T^{(1)} = -\left(\lambda_T^{(0)}\right)^2 x(t-T)/v_0$. In this case, the dynamics is no longer Markovian and it is necessary to consider the infinite set of joint probability distributions of observing positions $\mathbf{x}, \mathbf{x}', \mathbf{x}'', \ldots$ at times $t, t', t'', \ldots$. Calculating this distributions is extremely difficult and we might not have any hope of finding them. Fortunately, we can recover the Markovian structure if we consider three extra internal variables $x' = x(t-T)$, $\beta' = \beta(t-T)$ and $\Lambda = \int_0^t \lambda_T^{(1)}(t') \mathrm{d}t'$. Then, we have to consider the probability distribution $P(\mathbf{x}, \beta, x', \beta', \Lambda, t)$ of finding the RTP at position $\mathbf{x} = (x, y)$ with orientation β and internal state (x', β', Λ). Repeating the steps to derive the Fokker-Planck equation, we obtain

$$\begin{aligned} \dot{P}(\mathbf{x}, \beta, x', \Lambda, t) = &-v_0 \left(\cos\beta \frac{\partial}{\partial x} + \sin\beta \frac{\partial}{\partial y} - \frac{\left(\lambda_T^{(0)}\right)^2}{v_0^2} x' \frac{\partial}{\partial \Lambda} \right) P(\mathbf{x}, \beta, x', \Lambda, t) \\ &+ \frac{\lambda_T(t)}{2} \left(P(\mathbf{x}, \beta - \beta_0, x', \Lambda, t) + P(\mathbf{x}, \beta + \beta_0, x', \Lambda, t) - 2P(\mathbf{x}, \beta, x', \Lambda, t) \right) \\ &- v_0 \int \cos\beta' \frac{\partial}{\partial x'} P(\mathbf{x}, \beta, x', \beta', \Lambda, t) \, \mathrm{d}\beta'. \end{aligned} \tag{6.41}$$

In the derivation above we used the fact that $\dot{x}' = v_0 \cos\beta'$, $\dot{\Lambda} = \lambda_T^{(1)} = -\left(\lambda_T^{(0)}\right)^2 x'/v_0$ and we averaged over β', since the orientation at $t-T$ is irrelevant for the chemotactic drift. Expanding in Fourier modes with $p_n^{(i)} = p_n^{(i)}(\mathbf{x}, x', \beta', \Lambda, t)$, and making an asymptotic expansion in powers of ε as in Eq. (6.28) we find the hierarchy equations for the zeroth order and first order correction

$$\dot{p}_0^{(0)} = -\frac{v_0}{2} e^{-\lambda_\alpha^{(0)} t}\left[\hat{\ell}_1 p_1^{(0)} + \hat{\ell}_{-1} p_{-1}^{(0)}\right] + \frac{\left(\lambda_T^{(0)}\right)^2}{v_0} x' \frac{\partial}{\partial \Lambda} p_0^{(0)} - v_0 \int \cos\beta' \frac{\partial}{\partial x'} p_0^{(0)}\, \mathrm{d}\beta', \tag{6.42}$$

$$\dot{p}_{\pm 1}^{(0)} = -\frac{v_0}{2} e^{\lambda_\alpha^{(0)} t} \hat{\ell}_{\mp 1} p_0^{(0)} + \frac{\left(\lambda_T^{(0)}\right)^2}{v_0} x' \frac{\partial}{\partial \Lambda} p_{\pm 1}^{(0)} - v_0 \int \cos\beta' \frac{\partial}{\partial x'} p_{\pm 1}^{(0)}\, \mathrm{d}\beta', \tag{6.43}$$

$$\begin{aligned}\dot{p}_0^{(1)} = &-\frac{v_0}{2} e^{-\lambda_\alpha^{(0)} t}\left[\hat{\ell}_1\left(p_1^{(1)} - \Lambda(1-\alpha) p_1^{(0)}\right) + \hat{\ell}_{-1}\left(p_{-1}^{(1)} - \Lambda(1-\alpha) p_{-1}^{(0)}\right)\right] \\ &+ \frac{\left(\lambda_T^{(0)}\right)^2}{v_0} x' \frac{\partial}{\partial \Lambda} p_0^{(1)} - v_0 \int \cos\beta' \frac{\partial}{\partial x'} p_0^{(1)}\, \mathrm{d}\beta',\end{aligned} \tag{6.44}$$

$$\begin{aligned}\dot{p}_{\pm 1}^{(1)} = &\Lambda(1-\alpha)\dot{p}_{\pm 1}^{(0)} - \frac{v_0}{2} e^{\lambda_\alpha^{(0)} t} \hat{\ell}_{\mp 1} p_0^{(1)} + \frac{\left(\lambda_T^{(0)}\right)^2}{v_0} x' \frac{\partial}{\partial \Lambda}\left(p_{\pm 1}^{(1)} - \Lambda(1-\alpha) p_{\pm 1}^{(0)}\right) \\ &+ \frac{\lambda_\alpha^{(0)} \lambda_T^{(0)}}{v_0} x' p_{\pm 1}^{(0)} - v_0 \int \cos\beta' \frac{\partial}{\partial x'}\left(p_{\pm 1}^{(1)} - \Lambda(1-\alpha) p_{\pm 1}^{(0)}\right) \mathrm{d}\beta'.\end{aligned} \tag{6.45}$$

Again we have truncated the hierarchy at the first modes. Notice that after averaging equations Eq. (6.42) and Eq. (6.43) over x' and Λ, we recover equations Eq. (6.18) and Eq. (6.19). The idea now is to calculate $\langle \dot{x} \rangle^{(1)}$ to do so we start by taking the average of equations Eq. (6.44) and Eq. (6.45) with respect to y, x' and Λ, on doing so, the last two terms in both equations drop. We can then take the time derivative to obtain

$$\begin{aligned}\ddot{p}_0^{(1)}(x,t) = &-\lambda_\alpha^{(0)} \dot{p}_0^{(1)}(x,t) + \frac{v_0^2}{2} \Delta p_0^{(1)}(x,t) - \frac{\lambda_\alpha^{(0)} \lambda_T^{(0)}}{2} e^{-\lambda_\alpha^{(0)} t} \int x' \frac{\partial}{\partial x} p_1^{(0)}(x, x', t)\, \mathrm{d}x' \\ &- \frac{\lambda_\alpha^{(0)} \lambda_T^{(0)}}{2} e^{-\lambda_\alpha^{(0)} t} \int x' \frac{\partial}{\partial x} p_{-1}^{(0)}(x, x', t)\, \mathrm{d}x'\end{aligned} \tag{6.46}$$

Multiplying by x and averaging we get

$$\begin{aligned}\langle \ddot{x} \rangle^{(1)} + \lambda_\alpha^{(0)} \langle \dot{x} \rangle^{(1)} &= \frac{\lambda_\alpha^{(0)} \lambda_T^{(0)}}{v_0} \int x x' \left[-\frac{v_0}{2} e^{-\lambda_\alpha^{(0)} t} \frac{\partial}{\partial x}\left(p_1^{(0)}(x, x', t) + p_{-1}^{(0)}(x, x', t)\right)\right] \mathrm{d}x' \mathrm{d}x \\ &= \frac{\lambda_\alpha^{(0)} \lambda_T^{(0)}}{v_0} \frac{v_0}{e} e^{-\lambda_\alpha^{(0)} t} \int x' \left(p_1^{(0)}(x', t) + p_{-1}^{(0)}(x', t)\right) \mathrm{d}x' \mathrm{d}x.\end{aligned} \tag{6.47}$$

To obtain the second line in Eq. (6.47) we integrated by parts and used the fact that the probability distribution vanishes at infinity. Now, from Eq. (6.16) and the orthogonality of the Fourier basis, we have

$$\left\langle x' \cos\beta \right\rangle^{(0)} = \frac{1}{2} e^{-\lambda_\alpha^{(0)} t} \int x' (p_1^{(0)}(x',t) + p_{-1}^{(0)}(x',t))\, \mathrm{d}x'. \tag{6.48}$$

Therefore, denoting $\dot{x} = v_x = v_0 \cos\beta$, the evolution of the mean displacement is given by

$$\begin{aligned} \langle \ddot{x} \rangle^{(1)} + \lambda_\alpha^{(0)} \langle \dot{x} \rangle^{(1)} &= \frac{\lambda_\alpha^{(0)} \lambda_T^{(0)}}{v_0} \langle v_x(t) x(t-T) \rangle^{(0)} \\ &= \frac{\lambda_\alpha^{(0)} \lambda_T^{(0)}}{v_0} \int_0^{t-T} \left\langle v_x(t) v_x(t') \right\rangle^{(0)} \mathrm{d}t'. \end{aligned} \tag{6.49}$$

To finish, we remember that, at zeroth order, the distribution of orientations is isotropic, therefore $\langle v_x(t) v_x(t') \rangle^{(0)} = \langle \mathbf{v}(t) \cdot \mathbf{v}(t') \rangle^{(0)} / 2$, where $\mathbf{v} = \dot{\mathbf{x}}$ and as the RTP moves at constant speed we find $\langle v_x(t) v_x(t') \rangle^{(0)} = v_0^2 c(t-t')/2$, where $c(t) = e^{-\lambda_\alpha^{(0)} t}$ is the orientation correlation function. Solving Eq. (6.49) for $\langle \dot{x} \rangle^{(1)}$ we find

$$\begin{aligned} \langle \dot{x} \rangle^{(1)} &= v_0 \frac{\lambda_\alpha^{(0)} \lambda_T^{(0)}}{2} \int_0^t e^{-\lambda_\alpha^{(0)}(t-t')} \int_0^{t'-T} e^{-\lambda_\alpha^{(0)}(t'-t'')}\, \mathrm{d}t''\, \mathrm{d}t' \\ &= v_0 \frac{\lambda_T^{(0)}}{2} \int_0^t e^{-\lambda_\alpha^{(0)}(t-t')} \left(e^{-\lambda_\alpha^{(0)} T} - e^{-\lambda_\alpha^{(0)} t'} \right) \mathrm{d}t' \\ &= v_0 \frac{\lambda_T^{(0)}}{2\lambda_\alpha^{(0)}} \left[e^{-\lambda_\alpha^{(0)} T} - e^{-\lambda_\alpha^{(0)} t} (\lambda_\alpha^{(0)} t + e^{-\lambda_\alpha^{(0)} T}) \right] \end{aligned} \tag{6.50}$$

Hence, the chemotactic drift for a single impulse kernel $K(t) = k\delta(t-T)$ is

$$v_d = \varepsilon \lim_{t\to\infty} \langle \dot{x} \rangle^{(1)} = \varepsilon v_0 \frac{\lambda_T^{(0)}}{2\lambda_\alpha^{(0)}} e^{-\lambda_\alpha^{(0)} T} = \frac{k v_0^2 |\nabla C|}{2\lambda_\alpha^{(0)}} e^{-\lambda_\alpha^{(0)} T}, \tag{6.51}$$

the drift for a general kernel is then obtained by integrating over T, the result is

$$v_d = \frac{v_0^2 |\nabla C| \lambda_\alpha^{(0)} \tau_r^2}{2} \int_0^\infty e^{-\lambda_\alpha^{(0)} T} K(T)\, \mathrm{d}T, \tag{6.52}$$

which is the de Gennes chemotactic drift [132].

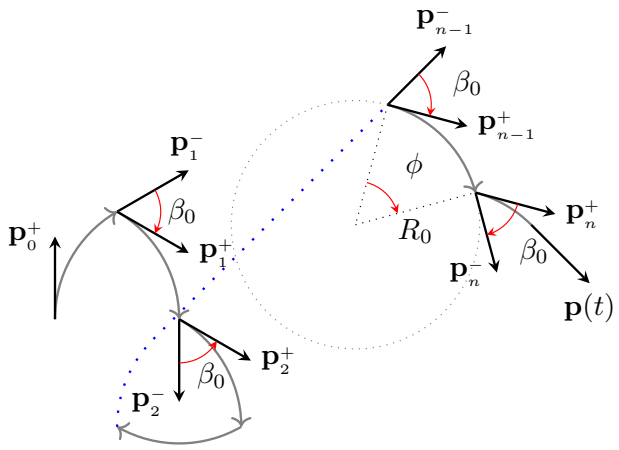

Fig. 6.2 Run-and-Tumble pattern for a circle swimmer. The circular trajectories are shown in gray. The unit vectors $\mathbf{p}_i^-$ and $\mathbf{p}_i^+$ represent the direction of motion just before and after the i-th tumble. The tumbling angle is β_0 and $\phi = \omega_0/\lambda_T$ where ω_0 is the angular velocity of the circular trajectories. The radius of the trajectories is denoted by R_0.

6.4 Run-and-tumble near boundaries

When a bacterium swims next to a wall, hydrodynamic interactions generate a torque perpendicular to the surface, as a result, the cell rotates and moves in circular trajectories (see Fig. 6.2). It is known that the radius of the trajectory is an increasing function of the distance to the wall [166]. Here we assume that the RTP moves at a stable distance from the wall, in this case the radius R_0 of the trajectories is fixed and the cell rotates with angular velocity $\mathbf{\Omega} = \pm\mathbf{e}_z\omega_0$, where $\omega_0 = v_0/R_0$. The sign is determined by the swimming mode, it is positive for a pusher and negative for a puller [112]. In this section we generalise the method above to include a deterministic rotation. We show that diffusivity and chemotaxis are always lower for a circle swimmer, suggesting that hydrodynamic interactions hinder motility of an RTP.

6.4.1 Diffusion

When the RTP undergoes a deterministic rotation at angular velocity ω_0 the Langevin equation for the orientation angle, β, becomes

$$\dot{\beta} = \omega(t) + \omega_0. \tag{6.53}$$

This contributes with an extra term proportional to ω_0 in the drift term of the generalised Fokker–Planck equation Eq. (6.15). Therefore, the probability distribution evolves according

to

$$\frac{\partial P}{\partial t} = -v_0\left(\cos\beta\frac{\partial}{\partial x}+\sin\beta\frac{\partial}{\partial y}+\frac{\omega_0}{v_0}\frac{\partial}{\partial\beta}\right)P(x,y,\beta,t) + \frac{\lambda_T}{2}\left[P(x,y,\beta-\beta_0,t)+P(x,y,\beta+\beta_0,t)\right]-\lambda_T P(x,y,\beta,t). \tag{6.54}$$

Using the same Fourier expansion as before, Eq. (6.16), we find the hierarchy equations

$$\frac{\partial p_n}{\partial t} = -\frac{v_0}{2}\sum_{\sigma=\{-1,1\}} e^{-\lambda_T(g(n+\sigma)-g(n))t}\hat{\ell}_\sigma p_{n+\sigma} - in\omega_0 p_n, \tag{6.55}$$

which leads to the evolution equation

$$\ddot{p}_0+\lambda_\alpha\dot{p}_0-\frac{v_0^2}{2}\Delta p_0+\omega_0^2\int_0^t e^{-\lambda_\alpha(t-t')}\frac{\partial p_0}{\partial t'}\,\mathrm{d}t' = 0. \tag{6.56}$$

We can solve this equation by expressing p_0 as a superposition of planar waves, that is $p_0(\mathbf{x},t)=(2\pi)^{-2}\int f_q(t)e^{i\mathbf{q}\cdot\mathbf{x}}\,\mathrm{d}\mathbf{q}$ and then applying the Laplace transform to Eq. (6.56). Using the same initial conditions for p_0 as in §6.2.2.1, we find that the function $f_q(t)$ satisfies $f_q(0)=1$ and $\dot{f}_q(0)=0$. Applying the Laplace transform we find that, the Laplace transform of f_q, $F_q(s)=\int_0^\infty e^{-st}f_q(t)\,\mathrm{d}s$, is given by

$$F_q(s) = \frac{(\lambda_\alpha+s)^2+\omega_0^2}{s[(s+\lambda_\alpha)^2+\omega_0^2]+v_0^2q^2(\lambda_\alpha+s)/2} = \frac{1}{s+v_0^2q^2\mathscr{C}(s)/2}, \tag{6.57}$$

where $\mathscr{C}(s)=(\lambda_\alpha+s)/((\lambda_\alpha+s)^2+\omega_0^2)$ is the Laplace transform of the orientation correlation function $c(t)=\cos(\omega_0 t)e^{-\lambda_\alpha t}$. To calculate the moments of the position vector we can again exploit the fact that $\mathbf{x}^n e^{i\mathbf{q}\cdot\mathbf{x}}=(-i\nabla_q)^n e^{i\mathbf{q}\cdot\mathbf{x}}$. Again, the first moment of the position vanishes, on the other hand the second moment is given in the Laplace domain by

$$\begin{aligned}\left\langle|\mathbf{x}(s)|^2\right\rangle &= \frac{1}{(2\pi)^2}\int|\mathbf{x}|^2 f_q(t)e^{i\mathbf{q}\cdot\mathbf{x}-st}\,\mathrm{d}\mathbf{x}\,\mathrm{d}\mathbf{q}\,\mathrm{d}t = -\int\Delta_q F_q(s)e^{i\mathbf{q}\cdot\mathbf{x}}\,\mathrm{d}\mathbf{x}\,\mathrm{d}\mathbf{q}\\ &= -\int\Delta_q F_q(s)\delta(\mathbf{q})\,\mathrm{d}\mathbf{q} = -\left[\Delta_q F_q(s)\right]_{\mathbf{q}=0} = 2v_0^2\frac{\mathscr{C}(s)}{s^2}.\end{aligned} \tag{6.58}$$

In the first line we used the definition of the Laplace transform and the first equation on the second line follows from the Fourier representation of the delta function. Using the convolution theorem and the fact that $1/s^2$ is the Laplace transform of t, we find

$$\left\langle|\mathbf{x}(t)|^2\right\rangle = 2v_0^2\int_0^t(t-t')\cos(\omega_0 t')e^{-\lambda_\alpha t'}\,\mathrm{d}t'$$

$$= 2v_0^2 \mathscr{R}\left[\frac{1}{(\lambda_\alpha - i\omega_0)^2}\left((\lambda_\alpha - i\omega_0)t + e^{(\lambda_\alpha - i\omega_0)t} - 1\right)\right]$$
$$= 2v_0^2\tau_{r,\omega_0}^2\left[\frac{t}{\tau_{r,\omega_0}} + \left(e^{-\lambda_\alpha t}\cos(\omega_0 t) - 1\right)\left(1-\Gamma^2\right) - 2\Gamma e^{-\lambda_\alpha t}\sin(\omega_0 t)\right], \quad (6.59)$$

where Γ is the dimensionless ratio between tumbling and rotation timescales, $\Gamma = \omega_0/\lambda_\alpha$. The correlation time is given in this case by

$$\tau_{r,\omega_0} \equiv \lim_{t\to\infty}\int_0^t c(t')\,\mathrm{d}t' = \frac{\lambda_\alpha}{\lambda_\alpha^2 + \omega_0^2} = \frac{\tau_r}{1+\Gamma^2}, \quad (6.60)$$

where τ_r is the correlation time in the non-interacting case. The diffusion coefficient for a circular RTP is obtained from the MSD Eq. (6.59) in the limit $\tau_{r,\omega_0} \ll t$ as follows

$$4D_{e,\omega_0} \equiv \lim_{t\to\infty}\frac{\left\langle|\mathbf{x}(t)|^2\right\rangle}{t} = 2v_0^2\tau_{r,\omega_0} = \frac{2v_0^2\lambda_\alpha}{\lambda_\alpha^2+\omega_0^2} = \frac{4D_e}{1+\Gamma^2}, \quad (6.61)$$

where D_e is the diffusivity in the non-interacting case. Equation Eq. (6.60) tells us that hydrodynamic interactions hinder diffusion of the RTP. Moreover $D_{e,\omega_0} \to 0$ for both $\lambda_\alpha \to 0$ and $\lambda_\alpha \to \infty$. Indeed if the tumbling rate is infinite, the RTP does not move at all, on the other hand if the tumbling rate vanishes the RTP moves in a closed circular trajectory. In contrast to the non interacting case in which the diffusivity grows without limit as the tumbling rate decreases, a circular RTP has an optimum tumbling rate $\lambda_\alpha = |\omega_0|$. Therefore, the maximum diffusivity for an interacting RTP is $4D_{e,\omega_0}^{max} = v_0^2/|\omega_0|$. This is in agreement with the analytic results of Martens et al. [114] and the numerical simulations of Guccione et al. [116].

6.4.2 Chemotaxis

For a circle swimming RTP, the master equation has an extra term proportional to ω_0 that contributes with extra terms $\mp i\omega_0 p_{\pm1}^{(0)}$ and $\mp i\omega_0\left(p_{\pm1}^{(1)} - \Lambda(1-\alpha)p_{\pm1}^{(0)}\right)$ on the right hand sides of equations Eq. (6.43) and Eq. (6.45) respectively. The evolution equation for the zeroth mode modifies as follows

$$\ddot{p}_0^{(1)}(x,t) + \lambda_\alpha^{(0)}\dot{p}_0^{(1)}(x,t) - \frac{v_0^2}{2}\Delta_C p_0^{(1)}(x,t) = -\frac{\lambda_\alpha^{(0)}\lambda_T^{(0)}}{2}e^{-\lambda_\alpha^{(0)}t}\int x'\frac{\partial}{\partial x}p_1^{(0)}(x,x',t)\,\mathrm{d}x'$$
$$-\frac{\lambda_\alpha^{(0)}\lambda_T^{(0)}}{2}e^{-\lambda_\alpha^{(0)}t}\int x'\frac{\partial}{\partial x}p_{-1}^{(0)}(x,x',t)\,\mathrm{d}x'$$
$$+i\frac{v_0\omega_0}{2}e^{-\lambda_\alpha^{(0)}t}\int\frac{\partial}{\partial x}\left(p_1^{(1)}(x,\Lambda,t) - \Lambda(1-\alpha)p_1^{(0)}(x,\Lambda,t)\right)\mathrm{d}\Lambda$$

$$-i\frac{v_0\omega_0}{2}e^{-\lambda_\alpha^{(0)}t}\int\frac{\partial}{\partial x}\left(p_{-1}^{(1)}(x,\Lambda,t)-\Lambda(1-\alpha)p_{-1}^{(0)}(x,\Lambda,t)\right)\mathrm{d}\Lambda. \tag{6.62}$$

Multiplying by x and averaging we find

$$\langle\ddot{x}\rangle^{(1)}+\lambda_\alpha^{(0)}\langle\dot{x}\rangle^{(1)}=\frac{\lambda_\alpha^{(0)}\lambda_T^{(0)}}{v_0}\int_0^{t-T}\left\langle v_x(t)v_x(t')\right\rangle^{(0)}\mathrm{d}t'+i\frac{v_0\omega_0}{2}e^{-\lambda_\alpha^{(0)}t}\left[I_+^{(1)}-I_-^{(1)}\right], \tag{6.63}$$

where

$$\begin{aligned}I_\pm^{(1)}&=\int x\frac{\partial}{\partial x}\left(p_{\pm1}^{(1)}(x,\Lambda,t)-\Lambda(1-\alpha)p_{\pm1}^{(0)}(x,\Lambda,t)\right)\mathrm{d}\Lambda\mathrm{d}x\\&=-\int p_{\pm1}^{(1)}(\Lambda,t)-\Lambda(1-\alpha)p_{\pm1}^{(0)}(\Lambda,t)\,\mathrm{d}\Lambda.\end{aligned} \tag{6.64}$$

Hence, from the orthogonality of the Fourier basis we find

$$I_+^{(1)}-I_-^{(1)}=2ie^{\lambda_\alpha^{(0)}t}\langle\sin\beta\rangle^{(1)}. \tag{6.65}$$

To find $\langle\sin\beta\rangle^{(1)}$ we now use the master equation for $P^{(1)}$. Including the extra drift term due to deterministic rotation and denoting the volume element by $\mathrm{d}V=\mathrm{d}\mathbf{x}\mathrm{d}\beta\mathrm{d}x'\mathrm{d}\beta'\mathrm{d}\Lambda$ we obtain

$$\begin{aligned}\frac{\mathrm{d}}{\mathrm{d}t}\langle\sin\beta\rangle^{(1)}&=-\int\sin\beta\nabla\cdot\left(\mathbf{x}P^{(1)}\right)\mathrm{d}V+\frac{\lambda_T^{(0}}{2}\int\sin\beta\left(P_+^{(1)}+P_-^{(1)}-2P^{(1)}\right)\mathrm{d}V\\&+\frac{1}{2}\int\lambda_T^{(1)}\sin\beta\left(P_+^{(0)}+P_-^{(0)}-2P^{(0)}\right)\mathrm{d}V\\&=\frac{\lambda_T^{(0)}}{2}\int\left(\sin\left(\beta-\beta_0\right)+\sin\left(\beta+\beta_0\right)-2\sin\beta\right)P^{(1)}\,\mathrm{d}V-\omega_0\int\sin\beta\frac{\partial P^{(1)}}{\partial\beta}\,\mathrm{d}V\\&-\frac{\left(\lambda_T^{(0)}\right)^2}{2v_0}\int x'\left(\sin\left(\beta-\beta_0\right)+\sin\left(\beta+\beta_0\right)-2\sin\beta\right)P^{(0)}\,\mathrm{d}V\\&=\omega_0\langle\cos\beta\rangle^{(1)}-\lambda_\alpha^{(0)}\langle\sin\beta\rangle^{(1)}+\frac{\lambda_T^{(0)}\lambda_\alpha^{(0)}}{v_0}\left\langle x'\sin\beta\right\rangle^{(0)}.\end{aligned} \tag{6.66}$$

The last term can be written as

$$\begin{aligned}\left\langle x'\sin\beta\right\rangle^{(0)}&=v_0\int_0^{t-T}\left\langle\cos\beta(t')\sin\beta(t)\right\rangle^{(0)}\mathrm{d}t'=\frac{1}{v_0}\int_0^{t-T}\left\langle v_x(t')v_y(t)\right\rangle^{(0)}\mathrm{d}t'\\&=\frac{v_0}{2}\int_0^{t-T}e^{-\lambda_\alpha^{(0)}(t-t')}\sin\omega_0(t-t')\,\mathrm{d}t',\end{aligned} \tag{6.67}$$

where we used the correlation function $\langle v_x(t)v_y(t')\rangle = (v_0^2/2)e^{-\lambda_\alpha^{(0)}|t-t'|}\sin\omega_0|t-t'|$. Therefore, we find

$$\begin{aligned}\langle\sin\beta\rangle^{(1)} &= \int_0^t e^{-\lambda_\alpha^{(0)}(t-t')}\left(\omega_0\langle\cos\beta(t')\rangle^{(1)} + \frac{\lambda_T^{(0)}\lambda_\alpha^{(0)}}{v_0}\langle x(t'-T)\sin\beta(t')\rangle^{(0)}\right)\mathrm{d}t' \\ &= \frac{\omega_0}{v_0}\int_0^t e^{-\lambda_\alpha^{(0)}(t-t')}\frac{\mathrm{d}}{\mathrm{d}t'}\langle x(t')\rangle^{(1)}\,\mathrm{d}t' \\ &+ \frac{\lambda_T^{(0)}\lambda_\alpha^{(0)}}{2}\int_0^t e^{-\lambda_\alpha^{(0)}(t-t')}\int_0^{t'-T} e^{-\lambda_\alpha^{(0)}(t'-t'')}\sin\omega_0(t'-t'')\,\mathrm{d}t''\,\mathrm{d}t'. \end{aligned} \tag{6.68}$$

Hence, the first moment of the position evolves according to

$$\begin{aligned}\langle\ddot{x}\rangle^{(1)} + \lambda_\alpha\langle\dot{x}\rangle^{(1)} + \omega_0^2\int_0^t e^{-\lambda_\alpha^{(0)}(t-t')}\langle\dot{x}\rangle^{(1)}\,\mathrm{d}t' &= \frac{\lambda_T^{(0)}\lambda_\alpha^{(0)}}{v_0}\int_0^{t-T}\langle v_x(t)v_x(t')\rangle^{(0)}\,\mathrm{d}t' \\ - v_0\omega_0\frac{\lambda_T^{(0)}\lambda_\alpha^{(0)}}{2}\int_0^t e^{-\lambda_\alpha^{(0)}(t-t')}\int_0^{t'-T} e^{-\lambda_\alpha^{(0)}(t'-t'')}\sin\omega_0(t'-t'')\,\mathrm{d}t''\,\mathrm{d}t', \end{aligned} \tag{6.69}$$

or equivalently

$$\begin{aligned}\langle\dot{x}\rangle^{(1)} + \omega_0^2\int_0^t\int_0^{t'} e^{-\lambda_\alpha^{(0)}(t-t'')}\langle\dot{x}\rangle^{(1)}\,\mathrm{d}t''\,\mathrm{d}t' &= \frac{v_0\lambda_T^{(0)}\lambda_\alpha^{(0)}}{2}\int_0^t\int_0^{t'-T} e^{-\lambda_\alpha^{(0)}(t-t'')}\cos\omega_0(t'-t'')\,\mathrm{d}t''\,\mathrm{d}t' \\ - v_0\omega_0\frac{\lambda_T^{(0)}\lambda_\alpha^{(0)}}{2}\int_0^t\int_0^{t'}\int_0^{t''-T} e^{-\lambda_\alpha^{(0)}(t-t''')}\sin\omega_0(t''-t''')\,\mathrm{d}t'''\,\mathrm{d}t''\,\mathrm{d}t', \end{aligned} \tag{6.70}$$

where we have used the correlation function $\langle v_x(t)v_x(t')\rangle = (v_0^2/2)e^{-\lambda_\alpha^{(0)}|t-t'|}\cos\omega_0|t-t'|$. Noting that the integrands diverge as $e^{\lambda_\alpha^{(0)}t}$ and are multiplied by a factor $e^{-\lambda_\alpha^{(0)}t}$, we find the long-time-limit solution

$$\begin{aligned}\lim_{t\to\infty}\langle\dot{x}\rangle^{(1)} &= \frac{v_0\lambda_T^{(0)}}{2(1+\Gamma^2)}\lim_{t\to\infty}\int_0^{t-T} e^{-\lambda_\alpha^{(0)}(t-t')}\left(\cos\omega_0(t-t') - \Gamma\sin\omega_0(t-t')\right)\mathrm{d}t' \\ &= \frac{v_0\lambda_T^{(0)}\lambda_\alpha^{(0)}\tau_{r,\omega_0}^2}{2}e^{-\lambda_\alpha^{(0)}T}\left((1-\Gamma^2)\cos\omega_0 T - 2\Gamma\sin\omega_0 T\right). \end{aligned} \tag{6.71}$$

Therefore, the chemotactic drift for an RTP swimming in circles near to a solid boundary is

$$v_d = \frac{v_0^2|\nabla C|\lambda_\alpha^{(0)}\tau_{r,\omega_0}^2}{2}\int_0^\infty e^{-\lambda_\alpha^{(0)}T}\left((1-\Gamma^2)\cos\omega_0 T - 2\Gamma\sin\omega_0 T\right)K(T)\,\mathrm{d}T. \tag{6.72}$$

This result agrees with previous calculations by Bearon and Pedley [167] for an RTP that rotates due to a shear flow and that bias its tumbling rate instantaneously, according to its orientation with respect to a chemical concentration gradient that points in the same direction as the flow. In this case the drift is given by

$$v_d^{\text{inst}} = \frac{k'|\nabla C|v_0}{2}\lambda_\alpha^{(0)}\tau_{r,\omega_0} = \frac{k'|\nabla C|v_0}{2(1+\Gamma^2)}, \tag{6.73}$$

which is obtained from Eq. (6.72), using a kernel with two spikes of intensity $k'/(v_0\tau)$ at times T and $T+\tau$, such as the one used in §6.3.1. We observe that in both cases, adaptive and non-adaptive chemotaxis, the drift speed decays to zero when the rotation rate is large compared to the tumbling rate $1 \ll \Gamma$. Moreover, the chemotactic response function, Eq. (6.71) not only decays but oscillates with frequency ω_0, this means that for certain values of Γ it is possible to obtain vanishing and even a negative drift. It is possible to observe negative chemotaxis indeed, as shown in Fig. 6.3. We plot the drift as a function of Γ, for different values of the persistence parameter. We use a kernel with two spikes of the same intensity but opposite signs, at times $T_1 = 1$ s and $T_2 = 3$ s, which is a good approximation of the kernel used by *E. coli* [127]. The red symbols are obtained by solving numerically the Langevin equations and the solid curve represents the prediction of Eq. (6.71). The inset in Fig. 6.3 shows the drift in the non-adaptive case. Intuitively, negative chemotaxis arises from the fact that there is a down-the-gradient bias in the distribution of orientations at the beginning of a run due to circular motion (see Fig 6.4).

6.5 Discussion

Summary

In this chapter we analysed the motion of an active swimmer that performs run-and-tumble motion. This is a simple, but general model for a swimming bacterium. We explored two cases: i) free-swimming, in which the swimmer moves in an unbound fluid with straight runs, and ii) circle-swimming, in which the particle follows circular runs due to the action of a hydrodynamic torque. We derive analytical expressions for the diffusivity and chemotactic drift of the RTP in both cases, using a Fokker-Planck equation. We showed that for an RTP, diffusion and chemotaxis are hindered by hydrodynamic interactions with a solid boundary.

Traditionally one would calculate the orientation correlation function using the polymer analogy, as described in §2.2.1. This method has two disadvantages, first it can not be used to calculate higher order moments of the position. Second, analytical expressions can only be obtained for Poissonian tumble events. The Fokker-Planck approach presented here

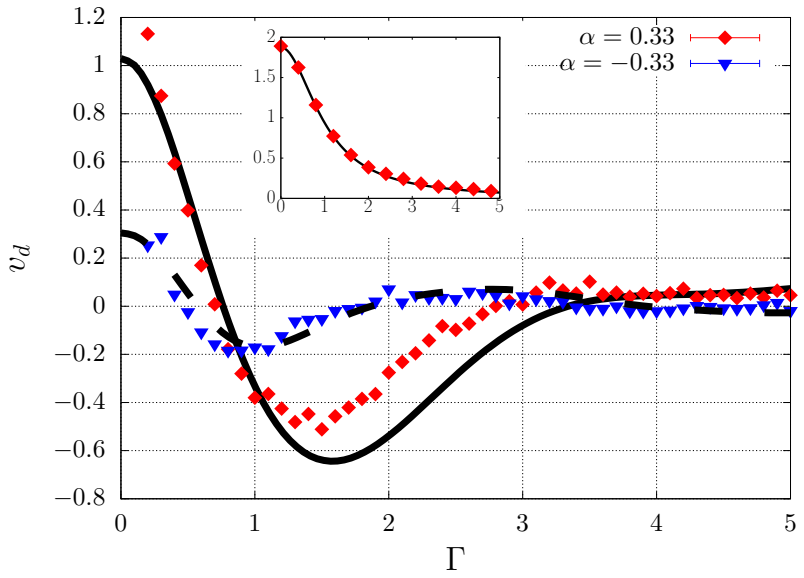

Fig. 6.3 Chemotactic drift for a circle swimming RTP as a function of the ratio of rotation to tumbling rate Γ. Symbols show the chemotactic drift obtained by numerical integration of the Langevin equations for two different values of the persistence parameter (a) $\alpha = 0.33$ (*E. coli*), (b) $\alpha = -0.33$. The solid line shows the prediction of Eq. (6.72). The inset shows the drift in the non-adaptive case, Eq. (6.73), for $\alpha = 0.33$.

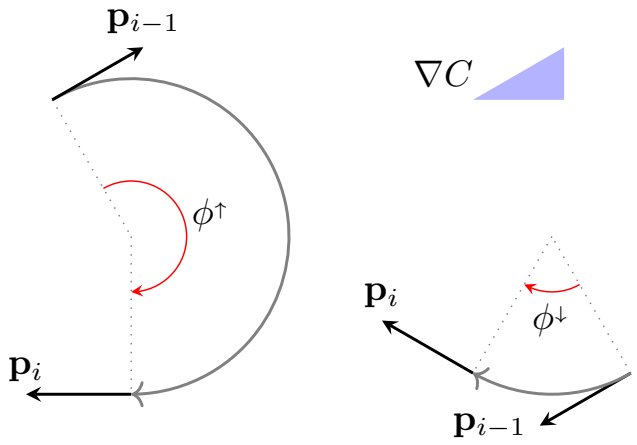

Fig. 6.4 Down-gradient bias of the initial orientation of a run in the case $0 < \alpha$. On the left a trajectory that starts heading up the gradient after the $(i-1)$-th tumble. On the right a trajectory that starts heading down the gradient after the $(i-1)$-th tumble. Since the running time is increased when the bacterium swims up the chemoattractant gradient, the rotation angles satisfy $\phi^{\downarrow} < \phi^{\uparrow}$ and the condition $0 < \alpha$ implies that the the next run is most likely to initiate heading down the gradient.

allows to calculate higher order moments, at least approximately, and it can also be used to consider power law distributions of running times, leading to Lévy dynamics and anomalous diffusion [163].

Consistency with previous results

Throughout this chapter, we pointed out how classical results for the diffusivity and chemotactic drift of a run-and-tumble particle can be recovered using the Fokker–Planck equation and its solution in terms of the moments of the cosine of the orientation angle. The Fokker–Planck approach has been used previously by Celani and Vergassola to calculate the optimal chemotactic kernel [133]. Similarly to the approach presented here, in order to preserve the Markov property, they introduced a set of internal variables that measure the chemotactic response at time t, analogously to our variable Λ. In the hydrodynamic limit (see run-and-tumble in one and three dimensions below) the Fokker-Planck equation reduces to $\dot{\rho} + \nabla \cdot (v_d P) = \Delta(D_e P)$ where v_d is given by Eq. (6.51) in agreement with our calculations.

In the case of circle swimming, we found that both diffusion and chemotaxis are hindered. The diffusivity is always smaller for a circle swimmer than for an RTP with straight runs. On the other hand, the chemotactic drift is not only lower, it can actually be negative. This result was derived previously by Locsei and Pedley in the case of an RTP swimming in a shear flow [135]. In this case the parameter Γ is the ratio between the shear and tumbling rates.

Thermal noise

The equations of motion for a $2D$-run-and-tumble particle under the action of thermal fluctuations are

$$\begin{aligned} \dot{\mathbf{x}} &= \mathbf{v} + \boldsymbol{\xi}(t), \\ \dot{\beta} &= \omega(t) + \Omega(t), \end{aligned} \tag{6.74}$$

where $\mathbf{v}$ and ω are as before and $\boldsymbol{\xi}$ as well as Ω are Gaussian processes characterised by $\langle \boldsymbol{\xi} \rangle = \mathbf{0}$, $\langle \xi_i(t)\xi_j(t') \rangle = 2D_T \delta_{ij}\delta(t-t')$ and $\langle \Omega \rangle = 0$, $\langle \Omega(t)\Omega(t') \rangle = 2D_r\delta(t-t')$, where D_T and D_r are the translational and rotational diffusion coefficients. Since the forces exerted on a swimming bacteria due to thermal fluctuations are roughly two orders of magnitude smaller than the propulsion forces generated by their flagella, it is reasonable to model the tumbling motion and thermal noise as independent processes. This means that the probability distribution $F(\boldsymbol{\zeta}, \eta_1, \eta_2, t)$ of observing a realization $\boldsymbol{\zeta}$, η_1 and η_2 of the translational Brownian noise, run-and-tumble and rotational Brownian noise at the same moment in time, t, can split in the product $F_{\boldsymbol{\xi}}(\boldsymbol{\zeta}, t)F_{\omega}(\eta_1, t)F_{\Omega}(\eta_2, t)$, where $F_{\boldsymbol{\xi}}$, F_{ω} and F_{Ω}

are the probability distributions of observing each realization independently. Repeating the derivation in §6.2.2 we find for that the Fourier transform of the function Φ in Eq. (6.10) is now given by

$$\Phi_{\mathbf{k},\ell} = \lim_{\tau\to 0}\frac{1}{\tau}\left(F_{\xi_x,k_x}(\tau)F_{\xi_y,k_y}(\tau)F_{\omega,\ell}(\tau)F_{\Omega,\ell}(\tau)-1\right), \tag{6.75}$$

where $F_{\gamma,m}$ is the Fourier transform of F_γ on the m-space, $\gamma=\xi_x,\xi_y,\eta_1,\eta_2$, $m=k_x,k_y,\ell$. Since $\tau\to 0$ we have $F_{\gamma,m}\to 1$, we can write $F_{\gamma,m}=1-(1-F_{\gamma,m})=1-\Phi_{\gamma,m}$, where $0<\Phi_{\gamma,m}\ll 1$ and hence $\Phi_{\mathbf{k},\ell}$ splits in a sum over the functions $\Phi_{\gamma,m}$. Therefore the generalised Fokker–Planck equation for a run-and-tumble particle that undergoes Brownian diffusion is given by

$$\begin{aligned}\frac{\partial}{\partial t}P &= -\nabla\cdot(\dot{\mathbf{x}}P)+\mathscr{F}^{-1}\left[P_{\mathbf{k},\ell}\left(\Phi_{\xi_x,k_x}+\Phi_{\xi_y,k_y}+\Phi_{\omega,\ell}+\Phi_{\Omega,\ell}\right)\right]\\ &= \nabla\cdot(-\dot{\mathbf{x}}P+D_T\nabla P)+D_r\frac{\partial^2}{\partial\beta^2}P+\lambda_T\int P(\mathbf{x},\zeta,t)\Phi_\omega(\beta-\zeta)\,\mathrm{d}\zeta\\ &= \nabla\cdot(-\dot{\mathbf{x}}P+D_T\nabla P)+D_r\frac{\partial^2}{\partial\beta^2}P+\frac{\lambda_T}{2}\left(P_++P_--2P\right),\end{aligned} \tag{6.76}$$

where we have used the fact that the generating processes for Brownian noise follow a normal distribution and we have assumed that the tumbles follow a Poisson process as in §6.2.2.1. To solve this equation we can expand again in Fourier modes as follows

$$P(\mathbf{x},\beta,t)=\sum_{n\in\mathbb{Z}}e^{in\beta-(D_rn^2+\lambda_Tg(n))t}p_n(\mathbf{x},t). \tag{6.77}$$

Substitution in Eq. (6.76) gives the hierarchy equations

$$\dot{p}_n=-\frac{v_0}{2}\sum_{\sigma=\{-1,1\}}e^{-\left[\lambda_T(g(n+\sigma)-g(n))+D_r\left((n+\sigma)^2-n^2\right)\right]t}\hat{\ell}_\sigma p_{n+\sigma}+D_T\Delta p_n. \tag{6.78}$$

In this case, the zeroth mode evolves according to

$$\ddot{p}_0+(\lambda_\alpha+D_r-2D_T\Delta)\,\dot{p}_0-\left((\lambda_\alpha+D_r)D_T+\frac{v_0^2}{2}\right)\Delta p_0+D_T^2\Delta^2p_0=0. \tag{6.79}$$

Using the plane wave expansion we find the same solution as in Eq. (6.21), with G_q satisfying $\ddot{G}_q+\left(\lambda_\alpha+D_r+2D_Tq^2\right)\dot{G}_q+q^2\left(D_T^2q^2+D_T(\lambda_\alpha+D_r)+v_0^2/2\right)G_q=0$. In this case, the MSD is given by

$$\left\langle|\mathbf{x}|^2\right\rangle=2\tau_r\left(2D_T+v_0^2\tau_r\right)\left(\frac{t}{\tau_r}+e^{-t/\tau_r}-1\right), \tag{6.80}$$

where now the randomisation time is given by $\tau_r^{-1} = \lambda_\alpha + D_r$. We recover the appropriate limits $\left\langle |\mathbf{x}|^2 \right\rangle \simeq v_0^2 t$ and $\left\langle |\mathbf{x}|^2 \right\rangle \simeq 4D_e t = (4D + 2v_0^2\tau_r)t$. Additionally in the limit of negligible activity, that is $v_0, \lambda_T, D_r \to 0$ we recover normal diffusion $\left\langle |\mathbf{x}|^2 \right\rangle = 4D_T t$.

We now calculate the chemotactic drift. Assuming that the rotational diffusivity is independent of the chemical concentration gradient and considering the fact that the terms containing the Laplacian of the probability density do not contribute to the first moment of the position, we find that $\langle x \rangle^{(1)}$ evolves according to Eq. (6.49) with $\lambda_\alpha^{(0)} \mapsto \lambda_\alpha^{(0)} + D_r$ on the left-hand side. Therefore the chemotactic drift including rotational diffusion is

$$v_d = \frac{v_0^2 |\nabla C| \lambda_\alpha^{(0)}}{2\left(\lambda_\alpha^{(0)} + D_r\right)^2} \int_0^\infty e^{-\left(\lambda_\alpha^{(0)} + D_r\right)T} K(T)\,\mathrm{d}T, \tag{6.81}$$

in agreement with the calculations of Locsei [134]. The calculations for the circle swimming case are similar.

Run-and-tumble in one and three dimensions

As we mention before, the method presented here can be generalised to one and three dimensions. The one dimensional case is trivial, since we can consider the $2D$ case with a full turn after a tumble, that is $\beta_0 = \pi$. In this case the MSD is given by Eq. (6.24), replacing $|\mathbf{x}|^2 \mapsto x^2$. Therefore the diffusivity for a $1D$-RTP is $D_e = v_0^2\tau_r$, with $\tau_r^{-1} = 2\lambda_T$. Similarly, the chemotactic drift in $1D$ is twice as large as that of a $2D$-RTP. The $3D$ case is slightly more interesting, although we can anticipate that the RTP will have a diffusivity and drift 3 times less than those of a $1D$-RTP. In three dimensions the tumble term in the generalised Fokker–Planck equation, Eq. (6.15), can be replaced by an integral over the transition probability of going from an orientation $\mathbf{p}' \mapsto \mathbf{p}$ after a tumble. Denoting by $W(\mathbf{p},\mathbf{p}')\,\mathrm{d}\mathbf{p}$ the transition probability, the generalised Fokker–Planck equation is

$$\dot{P}(\mathbf{x},\mathbf{p},t) = -\nabla\cdot(\dot{\mathbf{x}}P(\mathbf{x},\mathbf{p},t)) + \lambda_T\left(\int W(\mathbf{p},\mathbf{p}')P(\mathbf{x},\mathbf{p}',t)\,\mathrm{d}\mathbf{p}' - P(\mathbf{x},\mathbf{p},t)\right). \tag{6.82}$$

To solve this equation, we introduce the *hydrodynamic tensors* $\rho = \int P\,\mathrm{d}\mathbf{p}$, $\mathbf{P} = \int \mathbf{p}P\,\mathrm{d}\mathbf{p}$ and $\mathbf{Q} = \int (\mathbf{pp} - \mathbf{1}/3)P\,\mathrm{d}\mathbf{p}$, with $\mathbf{1}$ the identity matrix. These tensors correspond to the density of particles, polarization field and nematic field, respectively [165]. Using Eq. (6.82), with $\dot{\mathbf{x}} = v_0\mathbf{p}$ we find that the density and polarization field evolve according to

$$\begin{aligned}
\dot{\rho} &= -v_0\int \nabla\cdot(\mathbf{p}P)\,\mathrm{d}\mathbf{p} = -v_0\nabla\cdot\mathbf{P} \\
\dot{\mathbf{P}} &= -v_0\int \nabla\cdot(\mathbf{p}P)\mathbf{p}\,\mathrm{d}\mathbf{p} - \lambda_T\mathbf{P} + \lambda_T\int \mathbf{p}P(\mathbf{p}')W(\mathbf{p},\mathbf{p}')\,\mathrm{d}\mathbf{p}'\mathrm{d}\mathbf{p}
\end{aligned} \tag{6.83}$$

$$= -v_0 \nabla \cdot \mathbf{Q} - \frac{v_0}{3} \nabla \rho - \lambda_\alpha \mathbf{P}, \tag{6.84}$$

where we have used the fact that $\int \mathbf{p}' W(\mathbf{p}, \mathbf{p}') \, \mathrm{d}\mathbf{p} = \alpha \mathbf{p}'$. Strictly speaking, we would need the evolution equation for $\mathbf{Q}$ and higher rank tensors, but as we will see, the MSD does not depend on higher rank tensors, which is the reason why truncating the Fourier expansion at order one in the $2D$ case works. Taking the time derivative of ρ we find

$$\ddot{\rho} = v_0^2 \nabla \cdot (\nabla \cdot \mathbf{Q}) + \frac{v_0^2}{3} \Delta \rho - \lambda_\alpha \dot{\rho}. \tag{6.85}$$

Multiplying by $|\mathbf{x}|^2$ and averaging we obtain the evolution equation for the MSD

$$\begin{aligned} \frac{\partial^2}{\partial t^2} \left\langle |\mathbf{x}|^2 \right\rangle + \lambda_\alpha \frac{\partial}{\partial t} \left\langle |\mathbf{x}|^2 \right\rangle &= \frac{v_0^2}{3} \int |\mathbf{x}|^2 \Delta \rho \, \mathrm{d}\mathbf{x} + v_0^2 \int |\mathbf{x}|^2 \nabla \cdot (\nabla \cdot \mathbf{Q}) \, \mathrm{d}\mathbf{x} \\ &= 2v_0^2 + v_0^2 \int \mathbf{Q} \colon \nabla^2 |\mathbf{x}|^2 \, \mathrm{d}\mathbf{x} = 2v_0^2. \end{aligned} \tag{6.86}$$

To obtain the second equality we integrate by parts and $\mathbf{A} \colon \mathbf{B} = A_{ij} B_{ij}$ (Einstein convention) denotes the scalar product of two second rank symmetric tensors $\mathbf{A}$ and $\mathbf{B}$. The last equality follows from $\Delta |\mathbf{x}|^2 = 2 \nabla \cdot \mathbf{x} = 6$ in three dimensions, $\nabla^2 |\mathbf{x}|^2 = 2\mathbf{1}$, and the fact that $\mathbf{Q}$ is traceless. We find that the MSD in three dimensions evolves in the same way as it does in the planar case, therefore the solution is given by Eq. (6.15) and the diffusivity of a $3D$-RTP is $D_e = v_0^2 \tau_r / 3$, as expected. Similarly we can find that the drift is given by Eq. (6.52) with the 2 replaced by a 3 in the denominator. Finally, when we include thermal noise, we only need to replace $D_r \mapsto 2D_r$.

Biological relevance

It is clear that a three dimensional RTP serves as a model for a bacterium moving in free-space and that a circle swimmer in two dimensions represents near-surface swimming. What about a one dimensional RTP or a circle swimmer in three dimensions? The $1D$ case is relevant for the motion of a bacterium in a capillary tube, when the radius of the capillary is comparable to the size of the bacterium, tumbles are suppressed and reversals occur more often, in this case the motion becomes effectively one dimensional [113]. On the other hand, a bacterium that moves in the presence of a background flow with shear, will experience a torque that curves its trajectory. Locsei and Pedley [135], calculated the drift for an ellipsoidal RTP in a shear flow, and concluded that the effects of negative chemotaxis decreased for elongated particles and suggested that it could be hard to observe negative chemotaxis in experiments. The existence of an optimal tumbling rate for diffusion in the near-surface case, unlike in

the free-swimming case, suggest that bacteria might have evolved to maximise the extend of space that they can explore through run-and-tumble motion when swimming in confinement rather than in the bulk. This is consistent with the fact that microorganisms are actually found in constricted environments such as wet soil and mucus layers. However, the results for circle swimming chemotaxis show that negative drift occur at a rotation rate comparable to the optimal tumbling rate $\Gamma \sim 1$. Therefore, a circle swimmer would find itself unfit for locating a food source or escaping from predators, pointing to an evolutionary disadvantage. This suggests the need of clustering and biofilm formation to overcome such disadvantage. Moreover, the fact that chemotaxis is rendered ineffective in near-surface swimming supports the observation that chemotaxis plays a minor role in biofilm formation [168].

Outlook

In this chapter we presented preliminary results of a larger study that focuses on the motion of run-and-tumble particles moving in surfaces with curvature. This is relevant both biologically and experimentally. Chemotaxis is often measured using capillary assays [106, 113], in such cases bacteria tend to engage in near-surface-motion and curve their trajectories. Curved trajectories arise either by the effect of hydrodynamic interactions or the intrinsic curvature of the capillaries. Biologically, chemotaxis plays a relevant role for nutrient search in confined environments. Although chemotaxis does not enhance migration in porous media [169], it contributes to an increase in the residence time in the vicinity of a chemoattractant source [170], a desirable characteristic for soil bioremediation applications. Therefore, further development of a mathematical model for bacterial motion in confined environments and surfaces with curvature will be required.

Chapter 7

Conclusions

7.1 Summary

The fundamental principles behind the hydrodynamic and statistic aspects of low-*Re* swimming were discussed in Chapter 2. We made emphasis on two facts: i) the directional anisotropy of drag forces acting on a slender rod allows for propulsion by flagellar beating and ii) the macroscopic trajectory of many different low-*Re* swimmers can be described by a simple but general random walk model. We discussed applications and further details of these facts in the rest of the thesis.

Hydrodynamics

In Chapter 3 we presented a hydrodynamic model to describe the motility of the bacterium *Spiroplasma*, which swims by progressively shifting the chirality of its body. We confirmed previous experimental and theoretical results, specifically: i) swimming motion occurs in the opposite direction of kink propagation, ii) the optimum cell shape corresponds to a helix of pitch angle $\phi = 35^\circ$ and iii) the swimming stroke induces no net rotation. The first two observations have been derived before [48–50] by means of a complex simulation and a mathematical model that include full details of the geometry and elastic nature of the cell body. However, these did not provide any insights on property iii) of *Spiroplasma* motility. In contrast, although our model ignores fine details of the cell's body geometry, it uncovers the underlying symmetry that constrains *Spiroplasma* to move in a straight line, without sacrificing predictive power. Perhaps the extra details of the full elasto-hydrodynamic model obscured the underlying symmetry of the swimming gait. In this case, a simple resistive-force model is powerful enough to describe the motion of *Spiroplasma*.

In a similar way, the resistive force model proves itself useful in the description of the

dynamics of a helical swimmer moving in a viscosity gradient. Indeed, in Chapter 4 we show that assuming local validity of Stokes laws of motion is enough to capture the complex dynamics observed in experiments of a synthetic swimmer crossing a viscosity stratified fluid. Both experimental results and our hydrodynamic model point to the fact that a pusher-like swimmer will always find it harder to navigate the gradient from low to high viscosity. Note that *Spiroplasma* acts as a pusher when it moves forwards and as a puller when it moves backwards, similarly to *H. pylori*. Therefore, the same arguments in the concluding section of Chapter 4 imply that *Spiroplasma* will statistically accumulate in regions of high viscosity, which is in turn advantageous for the bacterium, since it is able to swim faster in such environments. This supports the experimental observation of positive viscotaxis in *Spiroplasma* [52] and other helical bacteria such as *Spirochetes* [69–71].

As mentioned above, a full understanding of viscotaxis requires further study. In addition to calculating the hydrodynamic torque on a helical filament due to variations in the viscosity that it experiences along its body, at least two other problems come immediately to our mind. i) First, extending the run-and-tumble model to explicitly derive expressions for the viscotactic drift and the effective diffusion coefficient of a bacterium moving in a viscosity gradient. ii) Second, and perhaps more interesting, is an inhomogeneous viscosity distribution enough to break the time symmetry of a reciprocal swimmer and allow it swim? One way to answer this question is to find an example of a reciprocal swimmer that can move in a viscosity gradient. A quick calculation for the two arm scallop using resistive force theory in the spirit of Chapter 4 show that the velocity of the scallop, U, is proportional to the rate of change of the angle of aperture θ, both in a homogeneous and inhomogeneous viscosity field. This means that the position of the scallop, X, is independent of the stroke rate $\dot{\theta}$. Therefore, in one cycle $\theta \mapsto \theta' \mapsto \theta$ the displacement vanishes and the scallop theorem holds. In their calculations for microswimmers composed by joint active spheres, Liebchen et al. found a similar result for a swimmer with axial symmetry [78]. This does not mean that the scallop theorem holds in a viscosity gradient for any reciprocal swimmer. It could be possible that enabling hydrodynamic interactions and viscosity advection in the resistive force calculation for the two arm scallop lead to a different result. Another way to proceed could be proving the symmetry brake in a perturbative way, similarly to how it has been done for the non-zero-*Re* case [118]. The proof by Ishimoto and Yamada, relies solely on the Lorentz reciprocal theorem [171] and there exists a version of the theorem that includes viscosity advection [77].

Statistics

The second part of this thesis focused on the statistical aspects of low-*Re* swimming.

In Chapter 5, we presented an application of the run-and-tumble model to describe the motion of a particular type of hybrid microswimmers that consist of passive particles coated with swimming bacteria. The substrate particle serves as cargo and in some cases as steering device, while bacteria enable propulsion and sensing. We showed that a coarse-grain description of the microswimmer trajectory allows us to consider the microswimmer as a run-and-tumble particle itself. The characteristic parameters of the run-and-tumble motion, swimming speed, persistence and running time, result as a combination of the individual contributions of each one of the attached bacteria. Surprisingly, the diffusivity of such particles increases with its size, in contrast with passive Brownian particles whose diffusivity decreases with it. We also showed that the microswimmers inherit the chemotactic ability of their propelling bacteria. In this case the chemotactic drift is independent of the swimmer size, but increases linearly with the number of attached bacteria, when they are uniformly distributed on the surface. These results should be relevant to improve the design of microswimmers for biomedical applications in the future.

Finally, in Chapter 6 we discussed how near-surface motion affects the motility of swimming bacteria. It is well known that bacteria and in general microswimmers, tend to accumulate on surfaces and it has been observed that, during near-surface swimming, their motility is hindered. To rationalise this, we studied the motion of a run-and-tumble particle moving on a planar surface and found that both diffusivity and chemotactic drift decrease when the particle moves in circles as compared to the case in which it performs straight runs. Strikingly, we found that in the case of chemotaxis, it is possible to modulate the tumbling rate with respect to the rotation rate induced by hydrodynamic interactions, so as to observe chemorepulsion in a chemoattractant field.

Negative chemotaxis occurs at values of the rotation rate comparable to the tumbling rate. In turn, the diffusion coefficient is maximum in the same range of rotation rates. This points out to a disadvantage for a microswimmer that performs run-and-tumble chemotaxis. The same result was found by Locsei and Pedley [135] in the case of a bacterium swimming on a shear flow. They concluded however, that the effect of negative chemotaxis is lowered when the cell body is elongated and suggested that it would be practically impossible to measure this effect experimentally. Another limiting factor that would prevent the experimental observation of negative chemotaxis, is the fact that in nature there is a non-zero probability that a bacterium escapes from the surface after a tumble. Additionally, previous numerical simulations have shown that in strong confinement (swimming in a narrow microfluidic channel for example) circular trajectories are suppressed [116, 172].

Even if hydrodynamic interactions in near-surface swimming do not induce circular motion, there are other cases in which confinement can induce circular trajectories. We can

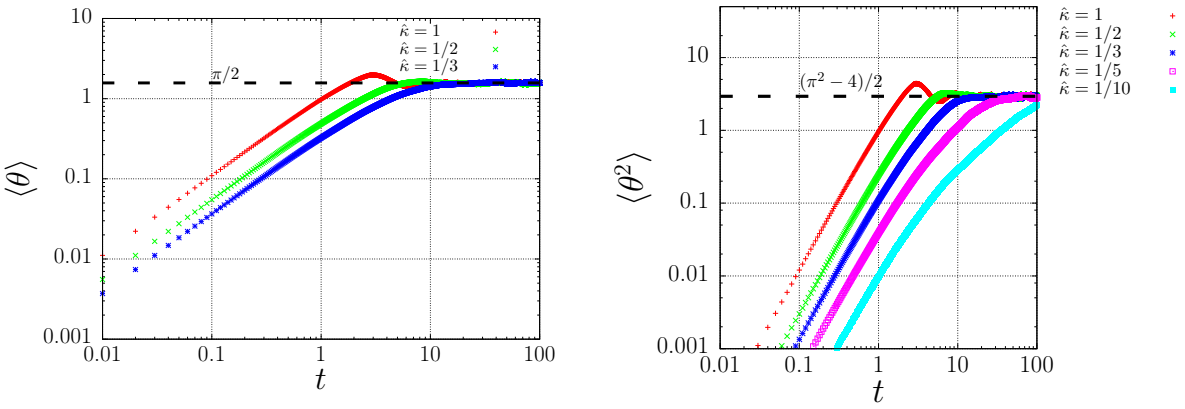

Fig. 7.1 Run-and-tumble particle on a spherical surface. First two moments of the polar displacement θ for different values of the curvature, normalised by the run length, $\hat{\kappa} = v_0\lambda_T^{-1}R^{-1}$. (a) The mean displacement is ballistic at short times and converges to $\langle\theta\rangle_\infty = \pi/2$ as t increases. (b) The mean squared displacement is also ballistic at short times and converges to $\langle\theta^2\rangle_\infty = (\pi^2-4)/2$ as t increases. A diffusive regime is only achieved for large values of the spherical surface radius, that is $\hat{\kappa} \ll 1$.

think for example of a thin spherical shell filled with fluid in which bacteria can swim. In this case circular motion arises from the intrinsic curvature of the surface and the control parameter is the ratio between the run length and the radius of the sphere, that is $\hat{\kappa} = v_0/R\lambda_T$. For a spherical RTP, the variable of interest is the polar angle θ. In contrast to the planar case, the compactness of the sphere enforces convergence of the mean polar position to a constant value $\langle\theta\rangle_\infty$ in the long time limit. For example in a homogeneous environment, an RTP that starts moving from the north pole, $\theta = 0$, will end up being found, on average, at the equator. Indeed, after the swimmer has been moving for a period of time much longer than R/v_0, the RTP looses all memory of directionality, and north and south become equivalent for it, therefore $\langle\theta\rangle_\infty = \pi/2$ in this case [see Fig. 7.1(a)]. A similar argument applies to the mean squared polar displacement that converges to $\langle\theta^2\rangle_\infty = (\pi^2-4)/2$.

The generalised Fokker–Planck equation for an RTP moving on a spherical surface is analogous to Eq. (6.15) with a slightly different advection term. In the polar approximation (ignoring hydrodynamic tensors of rank $3 \leq r$), the marginal distribution $p_0(\theta,\phi,t)$ satisfies the telegrapher equation $\ddot{p}_0 + \lambda_\alpha \dot{p}_0 = (v_0^2/2R^2)\Delta_{LB}p_0$, where $\Delta_{LB} = (1/\sin\theta)(\partial_\theta \sin\theta\,\partial_\theta) + (1/\sin^2\theta\,\partial_{\phi^2})$ is the spherical Laplace–Beltrami operator. In this case the steady state solution is a constant $p_0^s = (4\pi)^{-1}$ which leads to the steady state values $\langle\theta\rangle_\infty = \pi/2$ and $\langle\theta^2\rangle_\infty = (\pi^2-4)/2$, as observed (see Fig. 7.1).

When the RTP moves in a chemical concentration gradient ∇C, the geodesic displacement will still converge to a constant value in the long time limit. This value will be different from

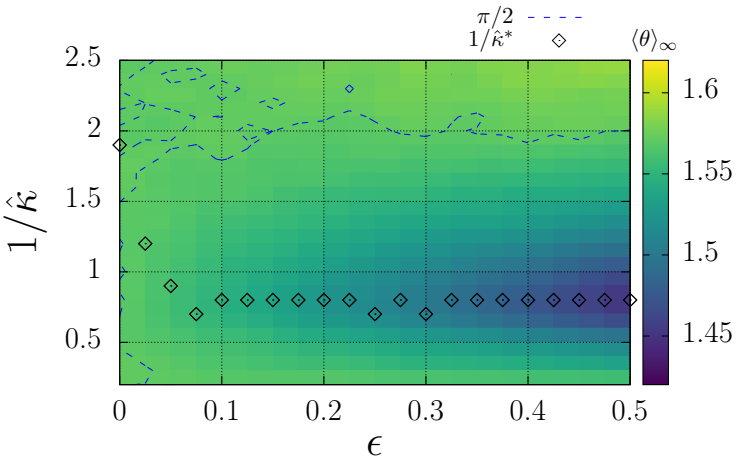

Fig. 7.2 Chemotactic drift for a run-and-tumble particle moving on the surface of a sphere. The RTP starts moving from the north pole $\theta = 0$ with an isotropic distribution of orientations. We consider a chemical concentration $C = C_0 - 3C_1 R\cos\theta/2$, with C_0 and C_1 constants, and a chemotactic kernel with two spikes of intensity k at times $T_1 = 1$ s and $T_2 = 3$ s. The plot show the steady state geodesic displacement, $\langle\theta\rangle_\infty$, for different values of the intensity parameter $\varepsilon = kC_1 v_0/\lambda_T^{(0)}$ and the control parameter $\hat{\kappa}^{-1} = R\lambda_T^{(0)}/v_0$. The black symbols represent the position of the lowest mean displacement.

$\pi/2$ depending on the direction of ∇C with respect to the initial position. We can imagine for example a concentration field that increases with the cosine of the polar angle, in such a case, an RTP that starts moving from the north pole, will end up being found, on average, at an angle $\pi/2 < \langle\theta\rangle_\infty$ if it performs positive chemotaxis, or $\langle\theta\rangle_\infty < \pi/2$ if it performs negative chemotaxis. Simulations suggest that it is indeed possible to observe negative chemotaxis, for values of the radius of curvature on the order of the run length (see Fig. 7.2). Interestingly, the higher negative drift occur for the same value of the curvature, regardless of the intensity of the chemotactic response (black symbols). Notice that if we interpret v_0/R as an angular velocity, this result is analogous to that of circle swimmers on the plane. An adaptation of the calculations in Chapter 6 to this case should lead to proper analytical expressions to help us better understand chemotaxis on surfaces with curvature.

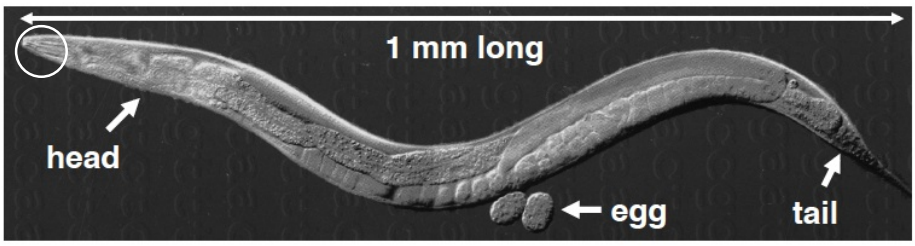

Fig. 7.3 The nematode *C. elegans* (adapted from Chuang Lab https://sites.google.com/site/chioufenchuanglab/research/c-elegans). It is millimiter size non-parasitic transparent nematode, naturally found in temperate soil environments. There are no female worms, only males and hermaphrodites as the one shown here. The white circle at the tip of the head indicates the position of the pair of the amphids, which work as chemoreceptors [176].

7.2 Outlook: Run-and-tumble models for higher organisms

As a final remark, we would like to point out the generality of the run-and-tumble model once again. As we discussed, it can describe the motility of a large set of different bacteria as well as that of artificial microswimmers. It can even be used to describe the motion of animals with a nervous system. Even when an organism has total control over its actions, locomotion can be affected by the conditions of the environment in which it moves. Irregularities of the landscape and unexpected events can give rise to seemingly random behaviours, regardless of the fact that the individual actions taken by the organism are deterministic. Consider for example the nematode *Caenorhabditis elegans* (see Fig. 7.3), when crawling in agar its trajectories resemble a random walk, similar to that produced by the run-and-tumble motion of the bacterium *E. coli* [28, 173]. In fact, previous studies have shown that the run-and-tumble model can capture diffusion [174, 175] and chemotaxis [176, 177] of *C. elegans*. However there are some aspects which are yet to be understood.

The nematode's chemotactic strategy is similar to that of *E. coli* (see Fig. 7.4), in the sense that both organisms try to move for as long as possible in the direction of increasing concentration of chemoattractant, before changing directions [28]. Moreover, the bias in running time is correlated to measurements of the concentration experienced at previous times [176]. This suggest the existence of an internal mechanism that allows the worm to display memory. There is also experimental evidence of adaptation, this means that *C. elegans* moves the same way in environments of different, but constant concentrations of chemoattractants.

Chemotaxis in *C. elegans* differs from bacterial chemotaxis in several aspects. First, more than one reorientation mechanism or phenotype, are involved: i) Pirouettes, discrete events analogous to tumbles in *E. coli* are suppressed when the organism moves towards the chemoattractant source, and triggered when it moves away, the latter in contrast to *E. coli*, whose tumble rate changes only when it moves towards the source. A further distinction is that a pirouette consists of more than one phenotype, usually a reversal in orientation and an omega turn [177], in contrast to bacterial tumbles, but similar to other bacterial strategies such as the run-reverse-flick motility pattern of *V. alginolyticus* [138]. ii) Weathervaning, as opposed to pirouettes, is a continuous mechanism that produces a change in the instantaneous curvature of the trajectory so as to reorient the worm towards the source. Numerical simulations have shown that both mechanisms must be used in parallel, in order to perform chemotaxis effectively [177]. Notably, *C. elegans* is capable to sense chemical gradients, by temporal and spatial comparison, unlike *E. coli* which can only perform the former. Temporal sensing is mainly associated to changes in pirouette behaviour, whereas spatial sensing correlates to wheathervaning. Another difference is that after a pirouette it is more likely for *C.elegans* to be oriented facing the source (regardless of its orientation before the pirouette) [176], as opposed to *E. coli* whose tumble angle is the same both in homogeneous and chemically stratified environments [28].

These facts suggest that a description similar to the de Gennes model for chemotaxis could also account for *C. elegans* chemotaxis [132, 134]. This model would require extra complexity however, in order to account for error correction during a pirouette. Ignoring weathervaning for the moment, one option could be to coarse grain the different phenotypes involved in a pirouette into a single reorientation event of finite duration. We can then consider that during this event, a constant torque, but no force, acts on the worm for a period of time τ that depends on the change in concentration $\partial C/\partial t$ experienced in the recent past. Another approach would be to consider a multimodal random walk, with instantaneous reorientation events of different types. We can then consider that the running events in between have lengths that depend on $\partial C/\partial t$. The first method is simpler and it might be possible to find closed analytical expressions for the chemotactic drift. The second approach is more complicated, but still tractable within the framework of continuous random walks [115, 123], although the expressions obtained for the drift are more involved and more difficult to interpret. In any case, a more detailed observation and analysis of the locomotion of *C. elegans* during a pirouette would be required. In particular, experimental studies should attempt to estimate the distributions for the arrival times and rotation angles of the different reorientation events.

Weathervaning could be further included in the random walk model, by considering an

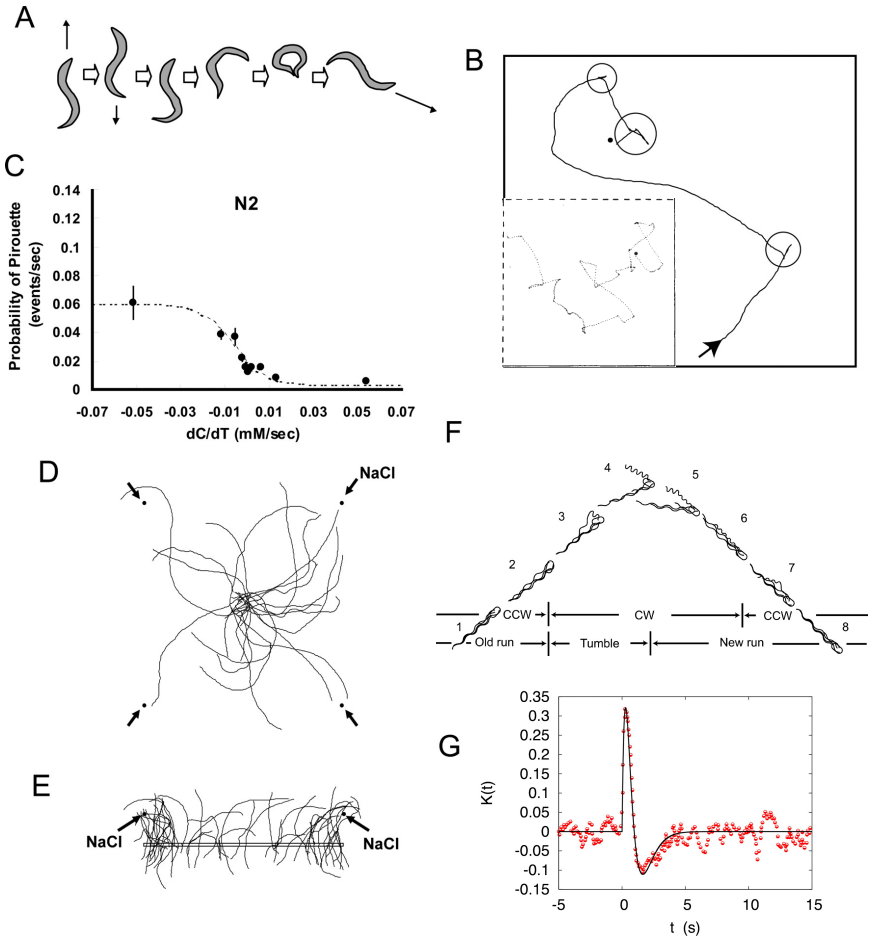

Fig. 7.4 Behavioral mechanisms in *C. elegans* and *E. coli* chemotaxis (Adapted from Iino and Yoshida 2009 [177]). A) A pirouette consists of a reversal and an omega turn. B) Typical trajectory, black dot indicates chemoattractant source and circles pirouettes, inset shows *E. coli* run and tumble track (adapted from Berg and Brown 1972 [28]). C) Evidence of pirouette mechanism, the probability of observing a pirouette increases with negative values of $\partial C/\partial t$. D) and E) Evidence of weathervaning mechanism, the trajectories curve towards the chemoattractant source, indicated by the black dots. F) Run-and-tumble mechanism in *E. coli* (adapted from Darnton et al. 2007 [178]). G) *E. coli* Chemotactic memory kernel $K(t)$ measures changes in the concentration field $\partial C/\partial t \simeq \int K(t-t')C(t')\mathrm{d}t'$, tumbling probability increases when $\partial C/\partial t$ is negative. The areas of the two lobes cancel, which is a signature of adaptation to a constant concentration (adapted from Celani and Vergassola 2010 [133]).

external torque acting on the organism's body as it crawls, analogously to the hydrodynamic torque that curves *E. coli* runs when it swims next to a solid surface [112]. Run-and-tumble diffusion and chemotaxis of circular swimmers was addressed in Chapter 6 and elsewhere before [114, 135], but only for the case in which the curvature of the trajectories, determined by the hydrodynamic torque, is independent of the chemical gradient. For *C. elegans*, the ad hoc torque should depend on the angle between the orientation vector $\mathbf{p}$ during a run and the concentration gradient $|\nabla C|\mathbf{e}$. Something as simple as considering the magnitude to be proportional to $1-\mathbf{p}\cdot\mathbf{e}$ would result in trajectories that curve towards a chemoattractant source. Weathervaning could also be included by considering the intrinsic curvature of the trajectories to depend on ∇C, in a similar way that has been done to describe spermatozoa chemotaxis [179].

An extra step of complexity is left to address, there is no detailed measurement of the memory kernel that *C. elegans* uses. Assuming we have knowledge of the distributions of arrival times and reorientation angles, we can define some measure of efficiency, such as maximum nutrient uptake, and perform an optimization analysis to obtain the optimum kernel shape [133].

Further details of the dynamics can be included by relating the parameters in the random walk model to the so called *eigenworms* which serve as coordinates in the space of possible shapes that *C. elegans* can adopt [174]. Understanding how the dynamics changes in shape space in response to a chemical cue might facilitate experimental measurements of the chemotactic kernel. Moreover, a combination of a random walk model with shape dynamics constitute a powerful tool to study species variability and to relate locomotive behaviour to the physiology of the nematode's nervous system [174, 175, 180].

7.3 Conclusions

The swimming strategy adopted by a microorganism is determined by the physical constraints that its environment imposes on it. The dominant role of viscous forces leads to the prevalence of wave-like structures in microswimmers, both biological and man made. On the other hand, the small size of a microorganism makes it highly susceptible to the action of fluctuations. Without any propulsion or control mechanisms, a microorganism would be doomed to rely entirely on diffusion to explore its habitat. Therefore, it does not come as a surprise that many microorganisms have evolved to display self propulsion, sensing and control.

The work presented here explores two different but related aspects of bacterial motility, hydrodynamics and statistics. Hydrodynamics deals with the fine details of the machinery

that enables bacteria to swim, as well as the motion at small scales. On the other hand, the movement of a microswimmer at long spatio-temporal scales is statistic in nature. Mathematical models that combine both aspects are necessary to understand the navigation strategies observed in bacterial populations. As an example, statistical analysis of the run-and-tumble model allows us to predict macroscopic behaviours observed in bacterial populations that display motility, such as diffusion and taxis (Chapter 5 and Chapter 6). Interestingly, the parameters in the run-and-tumble model are determined by the microscopic details of the swimming strategy of each microswimmer. Therefore it is possible to use hydrodynamic modelling to predict the values of the model parameters in cases when experimental observations of the swimming trajectories are not available. Indeed, the results in Chapter 3 allowed us to determine the persistence parameter of *Spiroplasma* and suggested a mechanism, based purely on hydrodynamics, for navigation in viscosity gradients. Similarly in Chapter 6, using the run-and-tumble model and the fact that hydrodynamic interactions with boundaries result in curved trajectories, we predicted a negative effect in the chemotactic strategy of *E. coli*, when it swims in a confined environment.

Noise sources represent a challenge in analysing experimental data. Since a macroscopic low-*Re* swimmer is less susceptible to thermal noise, it is easier to perform controlled experiments using artificial swimmers such as the one studied in Chapter 4. Taking advantage of the scalability of low-*Re* flow, we can use the results of these experiments to understand the motility of swimming microorganisms. To further investigate the viscotactic mechanism suggested by our hydrodynamic model for *Spiroplasma*, we analysed the motion of an artificial helical swimmer moving in a viscosity gradient in Chapter 4. Through experimental observation and mathematical modelling, we found that it is indeed possible to achieve collective viscotaxis solely by hydrodynamic effects, supporting the findings of Chapter 3. The viscotactic mechanism points to a biological advantage for *H. pylori* to colonise the stomach wall. In this sense, mathematical modelling of swimming bacteria helps us understand pathogenicity and devise strategies to prevent diseases. In the same way, modelling suggest possible ways to harness motility for good. For example, in Chapter 5, we show that it is possible to use bacteria to fabricate particles capable of performing chemotaxis, which can potentially be used for targeted drug delivery. Similarly, negative chemotaxis predicted for bacteria swimming in confinement (Chapter 6) could be harnessed to enhance bioremediation, or as a sorting mechanism for bacterial populations with large variations in tumbling rates.

In conclusion, the results presented in this thesis contribute to the understanding of bacterial motility and low-*Re* swimmers in general. Furthermore, these results may be useful

for future developments in biophysics, including applications to targeted drug delivery and microrobotics.

References

[1] D. Bray, *Cell Movements* (Garland Science, 2000).

[2] E. M. Purcell, "Life at low Reynolds number," Am. J. Phys. **45**, 3–11 (1977).

[3] G. I. Taylor, "Analysis of the swimming of microscopic organisms," Proc. Roy. Soc. Lond. A. **209**, 447–461 (1951).

[4] G. J. Hancock, "The self-propulsion of microscopic organisms through liquids," Proc. Roy. Soc. Lond. A. **217**, 96–121 (1953).

[5] J. Lighthill, "Flagellar hydrodynamics," SIAM Review **18**, 161–230 (1976).

[6] A. T. Chwang and T. Y. Wu, "A note on the helical movement of micro-organisms," Proc. Roy. Soc. Lond. B. **178**, 327–346 (1971).

[7] E. M. Purcell, "The efficiency of propulsion by a rotating flagellum," P. Natl. Acad. Sci. U.S.A. **94**, 11307–11311 (1997).

[8] R. Yasuda, H. Noji, K. Kinosita, and M. Yoshida, "F1-ATPase is a highly efficient molecular motor that rotates with discrete 120° steps," Cell **93**, 1117–1124 (1998).

[9] H. C. Berg, *E. coli in Motion* (Springer New York, 2004).

[10] S. Chattopadhyay, R. Moldovan, C. Yeung, and X. L. Wu, "Swimming efficiency of bacterium escherichiacoli," Proceedings of the National Academy of Sciences **103**, 13712–13717 (2006).

[11] R. Dreyfus, J. Baudry, M. L. Roper, M. Fermigier, H. A. Stone, and J. Bibette, "Microscopic artificial swimmers," Nature **437**, 862–865 (2005).

[12] A. Ghosh and P. Fischer, "Controlled propulsion of artificial magnetic nanostructured propellers," Nano Lett. **9**, 2243–2245 (2009).

[13] L. Zhang, J. J. Abbott, L. Dong, B. E. Kratochvil, D. Bell, and B. J. Nelson, "Artificial bacterial flagella: Fabrication and magnetic control," Appl. Phys. Lett. **94**, 064107 (2009).

[14] H.-W. Huang, M. S. Sakar, A. J. Petruska, S. Pané, and B. J. Nelson, "Soft micromachines with programmable motility and morphology," Nature Communications **7** (2016), 10.1038/ncomms12263.

[15] R. K. Soong, "Powering an inorganic nanodevice with a biomolecular motor," Science **290**, 1555–1558 (2000).

[16] N. Darnton, L. Turner, K. Breuer, and H. C. Berg, "Moving fluid with bacterial carpets," Biophys. J. **86**, 1863–1870 (2003).

[17] A. Julius, M. Sakar, E. Steager, U. Cheang, M. Kim, V. Kumar, and G. Pappas, "Harnessing bacterial power in microscale actuation," in *2009 IEEE International Conference on Robotics and Automation* (IEEE, 2009) pp. 1004–1009.

[18] S. Martel, "Bacterial microsystems and microrobots," Biomed. Microdevices **14**, 1033–1045 (2012).

[19] R. W. Carlsen and M. Sitti, "Bio-hybrid cell-based actuators for microsystems," Small **10**, 3831–3851 (2014).

[20] Z. Hosseinidoust, B. Mostaghaci, O. Yasa, B.-W. Park, A. V. Singh, and M. Sitti, "Bioengineered and biohybrid bacteria-based systems for drug delivery," Adv. Drug Deliver. Rev. **106**, 27 – 44 (2016).

[21] H. Ceylan, J. Giltinan, K. Kozielski, and M. Sitti, "Mobile microrobots for bioengineering applications," Lab Chip **17**, 1705–1724 (2017).

[22] J. Katuri, X. Ma, M. M. Stanton, and S. Sánchez, "Designing micro- and nanoswimmers for specific applications," Accounts Chem. Res. **50**, 2–11 (2017).

[23] L. Schwarz, M. Medina-Sánchez, and O. G. Schmidt, "Hybrid biomicromotors," Appl. Phys. Rev. **4**, 031301 (2017).

[24] H. Wang and M. Pumera, "Micro/nanomachines and living biosystems: From simple interactions to microcyborgs," Adv. Funct. Mater. **28**, 1705421 (2018).

[25] J. Bastos-Arrieta, A. Revilla-Guarinos, W. E. Uspal, and J. Simmchen, "Bacterial biohybrid microswimmers," Front. Robot. AI **5**, 97 (2018).

[26] R. Brown, "XXVII. a brief account of microscopical observations made in the months of june, july and august 1827, on the particles contained in the pollen of plants and on the general existence of active molecules in organic and inorganic bodies," Philos. Mag. **4**, 161–173 (1828).

[27] Z. D. Blount, "The unexhausted potential of e. coli," eLife **4** (2015), 10.7554/elife.05826.

[28] H. C. Berg and D. A. Brown, "Chemotaxis in escherichia coli analysed by three-dimensional tracking," Nature **239**, 500–504 (1972).

[29] M. Erhardt, "Strategies to block bacterial pathogenesis by interference with motility and chemotaxis," in *How to Overcome the Antibiotic Crisis : Facts, Challenges, Technologies and Future Perspectives*, edited by M. Stadler and P. Dersch (Springer International Publishing, 2016) pp. 185–205.

[30] M. A. Matilla and T. Krell, "The effect of bacterial chemotaxis on host infection and pathogenicity," FEMS Microbiol. Rev. **42** (2017), 10.1093/femsre/fux052.

[31] J. Elgeti, R. G. Winkler, and G. Gompper, "Physics of microswimmers—single particle motion and collective behavior: a review," Rep. Prog. Phys. **78**, 056601 (2015).

[32] D. B. Dusenbery, *Living at micro scale: the unexpected physics of being small* (Harvard University Press, 2009).

[33] M. C. Marchetti, J.-F. Joanny, S. Ramaswamy, T. B. Liverpool, J. Prost, M. Rao, and R. A. Simha, "Hydrodynamics of soft active matter," Rev. Mod. Phys. **85**, 1143 (2013).

[34] M. E. Cates, "Diffusive transport without detailed balance in motile bacteria: does microbiology need statistical physics?" Rep. Prog. Phys. **75**, 042601 (2012).

[35] J. B. Waterbury, J. M. Willey, D. G. Franks, F. W. Valois, and S. W. Watson, "A cyanobacterium capable of swimming motility," Science **230**, 74–76 (1985).

[36] K. Ehlers and G. Oster, "On the mysterious propulsion of *Synechococcus*," PLoS ONE **7**, e36081 (2012).

[37] R. F. Whitcomb, "The genus *Spiroplasma*," Annu. Rev. Microbiol. **34**, 677–704 (1980).

[38] J. W. Shaevitz, J. Y. Lee, and D. A. Fletcher, "*Spiroplasma* swim by a processive change in body helicity," Cell **122**, 941–945 (2005).

[39] N. W. Charon and S. F. Goldstein, "Genetics of motility and chemotaxis of a fascinating group of bacteria: The *Spirochetes*," Annu. Rev. Genet. **36**, 47–73 (2002).

[40] S. Trachtenberg and R. Gilad, "A bacterial linear motor: cellular and molecular organization of the contractile cytoskeleton of the helical bacterium *Spiroplasma melliferum* BC3," Mol. Microbiol. **41**, 827–848 (2002).

[41] R. Gilad, A. Porat, and S. Trachtenberg, "Motility modes of *Spiroplasma melliferum* BC3: a helical, wall-less bacterium driven by a linear motor," Mol. Microbiol. **47**, 657–669 (2003).

[42] S. Trachtenberg, R. Gilad, and N. Geffen, "The bacterial linear motor of *Spiroplasma melliferum* BC3: from single molecules to swimming cells," Mol. Microbiol. **47**, 671–697 (2003).

[43] S. Trachtenberg, S. B. Andrews, and R. D. Leapman, "Mass distribution and spatial organization of the linear bacterial motor of *Spiroplasma citri* R8A2," J. Bacteriol. **185**, 1987–1994 (2003).

[44] S. Trachtenberg, "The cytoskeleton of *Spiroplasma*: A complex linear motor," J. Mol. Microb. Biotech. **11**, 265–283 (2006).

[45] S. Trachtenberg, "Shaping and moving a *Spiroplasma*," J. Mol. Microb. Biotech. **7**, 78–87 (2004).

[46] P. Liu, H. Zheng, Q. Meng, N. Terahara, W. Gu, S. Wang, G. Zhao, D. Nakane, W. Wang, and M. Miyata, "Chemotaxis without conventional two-component system, based on cell polarity and aerobic conditions in helicity-switching swimming of *Spiroplasma eriocheiris*," Front. Microbiol. **8**, 58 (2017).

[47] D. Nakane, T. Ito, and T. Nishizaka, "Coexistence of two chiral helices produces kink translation in *Spiroplasma* swimming," J. Bacteriol **202**, e00735–19 (2020).

[48] J. Yang, C. W. Wolgemuth, and G. Huber, "Kinematics of the swimming of *Spiroplasma*," Phys. Rev. Lett. **102**, 218102 (2009).

[49] H. Wada and R. R. Netz, "Model for self-propulsive helical filaments: Kink-pair propagation," Phys. Rev. Lett. **99**, 108102 (2007).

[50] H. Wada and R. R. Netz, "Hydrodynamics of helical-shaped bacterial motility," Phys. Rev. E. **80**, 021921 (2009).

[51] D. Takahashi, I. Fujiwara, and M. Miyata, "Phylogenetic origin and sequence features of MreB from the wall-less swimming bacteria *Spiroplasma*," Biochem. Biophys. Res. Commun. **533**, 638–644 (2020).

[52] M. J. Daniels, J. M. Longland, and J. Gilbart, "Aspects of motility and chemotaxis in *Spiroplasmas*," Microbiology **118**, 429–436 (1980).

[53] M. J. Daniels and J. M. Longland, "Chemotactic behavior of *Spiroplasmas*," Curr. Microbiol. **10**, 191–193 (1984).

[54] G. Jékely, J. Colombelli, H. Hausen, K. Guy, E. Stelzer, F. Nédélec, and D. Arendt, "Mechanism of phototaxis in marine zooplankton," Nature **456**, 395 (2008).

[55] R. R. Bennett and R. Golestanian, "A steering mechanism for phototaxis in *Chlamydomonas*," J. R. Soc. Interface **12**, 20141164 (2015).

[56] A. Giometto, F. Altermatt, A. Maritan, R. Stocker, and A. Rinaldo, "Generalized receptor law governs phototaxis in the phytoplankton *Euglena gracilis*," P. Natl. Acad. Sci. U.S.A. **112**, 7045–7050 (2015).

[57] C. Lozano, B. ten Hagen, H. Löwen, and C. Bechinger, "Phototaxis of synthetic microswimmers in optical landscapes," Nat. Commun. **7**, 12828 (2016).

[58] B. Dai, J. Wang, Z. Xiong, X. Zhan, W. Dai, C.-C. Li, S.-P. Feng, and J. Tang, "Programmable artificial phototactic microswimmer," Nat. Nanotechnol. **11**, 1087 (2016).

[59] S. Klumpp and D. Faivre, "Magnetotactic bacteria," Eur. Phys. J. Spec. Top. **225**, 2173–2188 (2016).

[60] J.-F. Rupprecht, N. Waisbord, C. Ybert, C. Cottin-Bizonne, and L. Bocquet, "Velocity condensation for magnetotactic bacteria," Phys. Rev. Lett. **116**, 168101 (2016).

[61] N. Waisbord, C. T. Lefèvre, L. Bocquet, C. Ybert, and C. Cottin-Bizonne, "Destabilization of a flow focused suspension of magnetotactic bacteria," Phys. Rev. Fluids **1**, 053203 (2016).

[62] A. Bahat, I. Tur-Kaspa, A. Gakamsky, L. C. Giojalas, H. Breitbart, and M. Eisenbach, "Thermotaxis of mammalian sperm cells: A potential navigation mechanism in the female genital tract," Nat. Med. **9**, 149 (2003).

[63] Y. Li, Y. Zhao, X. Huang, X. Lin, Y. Guo, D. Wang, C. Li, and D. Wang, "Serotonin control of thermotaxis memory behavior in nematode *Caenorhabditis elegans*," PLOS One **8**, e77779 (2013).

[64] T. Bickel, G. Zecua, and A. Würger, "Polarization of active janus particles," Phys. Rev. E **89**, 050303 (2014).

[65] B. ten Hagen, F. Kümmel, R. Wittkowski, D. Takagi, H. Löwen, and C. Bechinger, "Gravitaxis of asymmetric self-propelled colloidal particles," Nat. Commun. **5**, 4829 (2014).

[66] A. I. Campbell and S. J. Ebbens, "Gravitaxis in spherical janus swimming devices," Langmuir **29**, 14066–14073 (2013).

[67] A. I. Campbell, R. Wittkowski, B. ten Hagen, H. Löwen, and S. J. Ebbens, "Helical paths, gravitaxis, and separation phenomena for mass-anisotropic self-propelling colloids: Experiment versus theory," J. Chem. Phys. **147**, 084905 (2017).

[68] M. Eisenbach, *Chemotaxis* (World Scientific Publishing Company, 2004).

[69] M. G. Petrino and R. Doetsch, "'viscotaxis', a new behavioural response of *Leptospira interrogans (biflexa)* strain b16," Microbiology **109**, 113–117 (1978).

[70] K. Takabe, H. Tahara, M. S. Islam, S. Affroze, S. Kudo, and S. Nakamura, "Viscosity-dependent variations in the cell shape and swimming manner of *Leptospira*," Microbiology **163**, 153–160 (2017).

[71] G. E. Kaiser and R. N. Doetsch, "Enhanced translational motion of *Leptospira* in viscous environments," Nature **255**, 656–657 (1975).

[72] P. Illien, R. Golestanian, and A. Sen, "'fuelled'motion: phoretic motility and collective behaviour of active colloids," Chem. Soc. Rev. **46**, 5508–5518 (2017).

[73] P. Romanczuk, M. Bär, W. Ebeling, B. Lindner, and L. Schimansky-Geier, "Active brownian particles," Eur. Phys. J. Spec. Top. **202**, 1–162 (2012).

[74] S. A. Mirbagheri and H. C. Fu, "*Helicobacter pylori* couples motility and diffusion to actively create a heterogeneous complex medium in gastric mucus," Phys. Rev. Lett. **116**, 198101 (2016).

[75] K. M. Ottemann and A. C. Lowenthal, "*Helicobacter pylori* uses motility for initial colonization and to attain robust infection," Infect. Immun. **70**, 1984–1990 (2002).

[76] M. Laumann and W. Zimmermann, "Focusing and splitting of particle streams in microflows via viscosity gradients," Eur. Phys. J. E **42**, 108 (2019).

[77] N. Oppenheimer, S. Navardi, and H. A. Stone, "Motion of a hot particle in viscous fluids," Phys. Rev. Fluids **1**, 014001 (2016).

[78] B. Liebchen, P. Monderkamp, B. ten Hagen, and H. Löwen, "Viscotaxis : Microswimmer navigation in viscosity gradients," Phys. Rev. Lett. **120**, 208002 (2018).

[79] M. Y. Sherman, E. O. Timkina, and A. N. Glagolev, "Viscosity taxis in *Escherichia coli*," FEMS Microbiol. Lett. **13**, 137–140 (1982).

[80] M. Lighthill, "On the squirming motion of nearly spherical deformable bodies through liquids at very small reynolds numbers," Commun. Pur. Appl. Math. **5**, 109–118 (1952).

[81] J. R. Blake, "A spherical envelope approach to ciliary propulsion," J. Fluid Mech. **46**, 199–208 (1971).

[82] T. J. Pedley, "Spherical squirmers: models for swimming micro-organisms," IMA J. Appl. Math. **81**, 488–521 (2016).

[83] P. S. Eastham and K. Shoele, "Axisymmetric squirmers in stokes fluid with nonuniform viscosity," Phys. Rev. Fluids **5**, 063102 (2020).

[84] C. Datt and G. J. Elfring, "Active particles in viscosity gradients," Phys. Rev. Lett **123** (2019), 10.1103/PhysRevLett.123.158006.

[85] E. Lauga, *The fluid dynamics of cell motility* (Cambridge University Press, Cambridge U.K., 2020).

[86] C. Bechinger, R. Di Leonardo, H. Löwen, C. Reichhardt, G. Volpe, and G. Volpe, "Active particles in complex and crowded environments," Rev. Mod. Phys. **88**, 045006 (2016).

[87] S. Gómez, F. A. Godínez, E. Lauga, and R. Zenit, "Helical propulsion in shear-thinning fluids," J. Fluid Mech. **812**, R3 (2017).

[88] F. A. Godínez, L. Koens, T. D. Montenegro-Johnson, R. Zenit, and E. Lauga, "Complex fluids affect low-reynolds number locomotion in a kinematic-dependent manner," Exp. Fluids **56**, 97 (2015).

[89] M. Sitti, "Voyage of the microrobots," Nature **458**, 1121 (2009).

[90] J. Zhuang and M. Sitti, "Chemotaxis of bio-hybrid multiple bacteria-driven microswimmers," Sci. Rep-UK **6**, 32135 (2016).

[91] V. Arabagi, B. Behkam, E. Cheung, and M. Sitti, "Modeling of stochastic motion of bacteria propelled spherical microbeads," J. Appl. Phys. **109**, 114702 (2011).

[92] J. Zhuang, B.-W. Park, and M. Sitti, "Propulsion and chemotaxis in bacteria-driven microswimmers," Adv. Sci. **4**, 1700109 (2017).

[93] B. Behkam and M. Sitti, "Effect of quantity and configuration of attached bacteria on bacterial propulsion of microbeads," Appl. Phys. Lett. **93**, 223901 (2008).

[94] O. Schauer, B. Mostaghaci, R. Colin, D. Hürtgen, D. Kraus, M. Sitti, and V. Sourjik, "Motility and chemotaxis of bacteria-driven microswimmers fabricated using antigen 43-mediated biotin display," Sci. Rep. **8**, 9801 (2018).

[95] S. Cho, S. J. Park, S. Y. Ko, J.-O. Park, and S. Park, "Development of bacteria-based microrobot using biocompatible poly(ethylene glycol)," Biomed. Microdevices **14**, 1019–1025 (2012).

[96] V. D. Nguyen, J.-W. Han, Y. J. Choi, S. Cho, S. Zheng, S. Y. Ko, J.-O. Park, and S. Park, "Active tumor-therapeutic liposomal bacteriobot combining a drug (paclitaxel)-encapsulated liposome with targeting bacteria (salmonella typhimurium)," Sensor. Actuat. B-Chem. **224**, 217 – 224 (2016).

[97] E. B. Steager, M. S. Sakar, D. H. Kim, V. Kumar, G. J. Pappas, and M. J. Kim, "Electrokinetic and optical control of bacterial microrobots," J. Micromech. Microeng. **21**, 035001 (2011).

[98] B. Behkam and M. Sitti, "Bacterial flagella-based propulsion and on/off motion control of microscale objects," Appl. Phys. Lett. **90**, 023902 (2007).

[99] M. M. Stanton, J. Simmchen, X. Ma, A. Miguel-López, and S. Sánchez, "Biohybrid janus motors driven by escherichia coli," Adv. Mater. Interfaces **3**, 1500505 (2015).

[100] S. J. Park, S.-H. Park, S. Cho, D.-M. Kim, Y. Lee, S. Y. Ko, Y. Hong, H. E. Choy, J.-J. Min, J.-O. Park, and S. Park, "New paradigm for tumor theranostic methodology using bacteria-based microrobot," Sci. Rep. UK **3**, 3394 (2013).

[101] E. Steager, C.-B. Kim, J. Patel, S. Bith, C. Naik, L. Reber, and M. J. Kim, "Control of microfabricated structures powered by flagellated bacteria using phototaxis," Appl. Phys. Lett. **90**, 263901 (2007).

[102] R. W. Carlsen, M. R. Edwards, J. Zhuang, C. Pacoret, and M. Sitti, "Magnetic steering control of multi-cellular bio-hybrid microswimmers," Lab Chip **14**, 3850–3859 (2014).

[103] M. R. Edwards, R. W. Carlsen, and M. Sitti, "Near and far-wall effects on the three-dimensional motion of bacteria-driven microbeads," Appl. Phys. Lett. **102**, 143701 (2013).

[104] J. Männik, R. Driessen, P. Galajda, J. E. Keymer, and C. Dekker, "Bacterial growth and motility in sub-micron constrictions," P. Natl. Acad. Sci. USA **106**, 14861–14866 (2009), http://www.pnas.org/content/106/35/14861.full.pdf .

[105] P. Sartori, E. Chiarello, G. Jayaswal, M. Pierno, G. Mistura, P. Brun, A. Tiribocchi, and E. Orlandini, "Wall accumulation of bacteria with different motility patterns," Phys. Rev. E **97**, 022610 (2018).

[106] L. Ping, V. Wasnik, and E. Emberly, "Bacterial motion in narrow capillaries," FEMS Microbiol. Ecol. **91**, 1–7 (2015).

[107] A. P. Berke, L. Turner, H. C. Berg, and E. Lauga, "Hydrodynamic attraction of swimming microorganisms by surfaces," Phys. Rev. Lett. **101**, 038102 (2008).

[108] G. Li and J. X. Tang, "Accumulation of microswimmers near a surface mediated by collision and rotational brownian motion," Phys. Rev. Lett. **103**, 078101 (2009).

[109] G. Li, J. Bensson, L. Nisimova, D. Munger, P. Mahautmr, J. X. Tang, M. R. Maxey, and Y. V. Brun, "Accumulation of swimming bacteria near a solid surface," Phys. Rev. E **84**, 041932 (2011).

[110] S. Bianchi, F. Saglimbeni, and R. D. Leonardo, "Holographic imaging reveals the mechanism of wall entrapment in swimming bacteria," Phys. Rev. X **7**, 011010 (2017).

[111] P. D. Frymier, R. M. Ford, H. C. Berg, and P. T. Cummings, "Three-dimensional tracking of motile bacteria near a solid planar surface," P. Natl. Acad. Sci. U.S.A. **92**, 6195–6199 (1995), http://www.pnas.org/content/92/13/6195.full.pdf .

[112] E. Lauga, W. R. DiLuzio, G. M. Whitesides, and H. A. Stone, "Swimming in circles: Motion of bacteria near solid boundaries," Biophys. J. **90**, 400 – 412 (2006).

[113] H. Berg and L. Turner, "Chemotaxis of bacteria in glass capillary arrays. escherichia coli, motility, microchannel plate, and light scattering," Biophys. J. **58**, 919–930 (1990).

[114] K. Martens, L. Angelani, R. Di Leonardo, and L. Bocquet, "Probability distributions for the run-and-tumble bacterial dynamics: An analogy to the lorentz model," Eur. Phys. J. E **35**, 84 (2012).

[115] F. Detcheverry, "Generalized run-and-turn motions: From bacteria to Lévy walks," Phys. Rev. E **96**, 012415 (2017).

[116] G. Guccione, D. Pimponi, P. Gualtieri, and M. Chinappi, "Diffusivity of *E. coli*-like microswimmers in confined geometries: The role of the tumbling rate," Phys. Rev. E **96**, 042603 (2017).

[117] E. Lauga and T. R. Powers, "The hydrodynamics of swimming microorganisms," Rep. Prog. Phys. **72**, 096601 (2009).

[118] K. Ishimoto and M. Yamada, "A coordinate-based proof of the scallop theorem," SIAM J. Appl. Math. **72**, 1686–1694 (2012).

[119] R. G. Cox, "The motion of long slender bodies in a viscous fluid part 1. general theory," J. Fluid. Mech. **44**, 791–810 (1970).

[120] M. Doi and H. See, *Introduction to Polymer Physics* (Oxford University Press, USA, 1996).

[121] J. Gray and G. Hancock, "The propulsion of sea-urchin spermatozoa," J. Exp. Biol. **32**, 802–814 (1955).

[122] P. S. Lovely and F. Dahlquist, "Statistical measures of bacterial motility and chemotaxis," J. Theor. Biol. **50**, 477 – 496 (1975).

[123] J. Taktikos, H. Stark, and V. Zaburdaev, "How the motility pattern of bacteria affects their dispersal and chemotaxis," PLoS ONE **8**, e81936 (2013).

[124] E. Lauga, "Bacterial hydrodynamics," Annu. Rev. Fluid Mech. **48**, 105–130 (2016).

[125] S. M. Block, J. E. Segall, and H. C. Berg, "Impulse responses in bacterial chemotaxis," Cell **31**, 215–226 (1982).

[126] J. E. Segall, S. M. Block, and H. C. Berg, "Temporal comparisons in bacterial chemotaxis." P. Natl. Acad. Sci. USA **83**, 8987–8991 (1986).

[127] M. J. Schnitzer, "Theory of continuum random walks and application to chemotaxis," Phys. Rev. E **48**, 2553–2568 (1993).

[128] M. Rubinstein and R. H. Colby, *Polymer Physics (Chemistry)* (Oxford University Press, 2003).

[129] H. Yamakawa, *Helical Wormlike Chains in Polymer Solutions* (Springer Berlin Heidelberg, 1997).

[130] S. Chandrasekhar, "Stochastic problems in physics and astronomy," Rev. Mod. Phys. **15**, 1–89 (1943).

[131] V. Sourjik and N. S. Wingreen, "Responding to chemical gradients: bacterial chemotaxis," Curr. Opin. Cell Biol. **24**, 262 – 268 (2012).

[132] P.-G. de Gennes, "Chemotaxis: the role of internal delays," Eur. Biophys. J. **33**, 691–693 (2004).

[133] A. Celani and M. Vergassola, "Bacterial strategies for chemotaxis response," P. Natl. Acad. Sci. USA **107**, 1391–1396 (2010).

[134] J. T. Locsei, "Persistence of direction increases the drift velocity of run and tumble chemotaxis," J. Math. Biol. **55**, 41–60 (2007).

[135] J. T. Locsei and T. J. Pedley, "Run and tumble chemotaxis in a shear flow: The effect of temporal comparisons, persistence, rotational diffusion, and cell shape," Bull. Math. Biol. **71**, 1089–1116 (2009).

[136] J. Saragosti, P. Silberzan, and A. Buguin, "Modeling e. coli tumbles by rotational diffusion. implications for chemotaxis," PLOS ONE **7**, 1–6 (2012).

[137] J. D. Antani, A. X. Sumali, T. P. Lele, and P. P. Lele, "Anisotropic random walks reveal chemotaxis signaling output in run-reversing bacteria," bioRxiv (2020).

[138] L. Xie, T. Altindal, S. Chattopadhyay, and X.-L. Wu, "Bacterial flagellum as a propeller and as a rudder for efficient chemotaxis," P. Natl. Acad. Sci. U.S.A. **108**, 2246–2251 (2011).

[139] H. Hotani, "Light microscope study of mixed helices in reconstituted *Salmonella* flagella," J. Mol. Biol. **106**, 151–166 (1976).

[140] R. E. Goldstein, A. Goriely, G. Huber, and C. W. Wolgemuth, "Bistable helices," Phys. Rev. Lett. **84**, 1631–1634 (2000).

[141] R. E. Johnson, "An improved slender-body theory for stokes flow," J. Fluid Mech. **99**, 411–431 (1980).

[142] F. Alouges, A. DeSimone, L. Giraldi, Y. Or, and O. Wiezel, "Energy-optimal strokes for multi-link microswimmers: Purcell's loops and taylor's waves reconciled," New J. Phys. **21**, 043050 (2019).

[143] O. Pironneau and D. F. Katz, "Optimal swimming of flagellated micro-organisms," J. Fluid Mech. **66**, 391–415 (1974).

[144] E. Lauga and C. Eloy, "Shape of optimal active flagella," J. Fluid Mech. **730** (2013), 10.1017/jfm.2013.370.

[145] M. Doi, *The Theory of Polymer Dynamics (International Series of Monographs on Physics)* (Oxford University Press, 1988).

[146] Y. Magariyama and S. Kudo, "A mathematical explanation of an increase in bacterial swimming speed with viscosity in linear-polymer solutions," Biophys. J. **83**, 733–739 (2002).

[147] J. Gonzalez-Gutierrez, S. Osorio-Ramirez, F. J. Solorio-Ordaz, and R. Zenit, "Dynamics of a helical swimmer crossing an interface between two immiscible fluids," Phys. Rev. Fluids **4**, 083102 (2019).

[148] F. A. Godínez, O. Chávez, and R. Zenit, "Note: Design of a novel rotating magnetic field device," Rev. Sci. Instrum. **83**, 066109 (2012).

[149] M. Mathlouthi and J. Génotelle, "Rheological properties of sucrose solutions and suspensions," in *Sucrose* (Springer US, 1995) pp. 126–154.

[150] S. Kim and J. S. Karrila, *Microhydrodynamics: Principles and Selected Applications.* (Butterworth-Heinemann, Boston, MA, 1991).

[151] V. A. Shaik and A. M. Ardekani, "Far-field flow and drift due to particles and organisms in density-stratified fluids," Phys. Rev. E **102**, 063106 (2020).

[152] K. M. Taute, S. Gude, S. J. Tans, and T. S. Shimizu, "High-throughput 3d tracking of bacteria on a standard phase contrast microscope," Nat. Commun. **6** (2015), 10.1038/ncomms9776.

[153] S. Coppola and V. Kantsler, "Green algae scatter off sharp viscosity gradients," Sci. Rep. **11** (2021), 10.1038/s41598-020-79887-7.

[154] M. R. Stehnach, N. Waisbord, D. M. Walkama, and J. S. Guasto, "Viscophobic turning dictates microalgae transport in viscosity gradients," Nature Phys. (2021), 10.1038/s41567-021-01247-7.

[155] D. Kim, A. Liu, E. Diller, and M. Sitti, "Chemotactic steering of bacteria propelled microbeads," Biomed. Microdevices **14**, 1009–1017 (2012).

[156] J. C. Simo, N. Tarnow, and M. Doblare, "Non-linear dynamics of three-dimensional rods: Exact energy and momentum conserving algorithms," Int. J. Numer. Meth. Eng. **38**, 1431–1473 (1995).

[157] E. Zupan and M. Saje, "Integrating rotation from angular velocity," Adv. Eng. Softw. **42**, 723 – 733 (2011).

[158] Y. Alapan, O. Yasa, O. Schauer, J. Giltinan, A. F. Tabak, V. Sourjik, and M. Sitti, "Soft erythrocyte-based bacterial microswimmers for cargo delivery," Sci. Robotics **3**, eaar4423 (2018).

[159] Á. Barroso, S. Landwerth, M. Woerdemann, C. Alpmann, T. Buscher, M. Becker, A. Studer, and C. Denz, "Optical assembly of bio-hybrid micro-robots," Biomed. Microdevices **17**, 26 (2015).

[160] S. Rozhok, C.-F. Shen, P.-L. Littler, Z. Fan, C. Liu, C. Mirkin, and R. Holz, "Methods for fabricating microarrays of motile bacteria," Small **1**, 445–451 (2005).

[161] F. Jülicher, S. W. Grill, and G. Salbreux, "Hydrodynamic theory of active matter," Rep. Prog. Phys. **81**, 076601 (2018).

[162] H. Risken, *The Fokker-Planck Equation* (Springer Berlin Heidelberg, 1989).

[163] S. I. Denisov, W. Horsthemke, and P. Hänggi, "Generalized fokker-planck equation: Derivation and exact solutions," Eur. Phys. J. B **68**, 567–575 (2009).

[164] F. J. Sevilla and L. A. G. Nava, "Theory of diffusion of active particles that move at constant speed in two dimensions," Phys. Rev. E **90** (2014), 10.1103/physreve.90.022130.

[165] P. Castro-Villarreal and F. J. Sevilla, "Active motion on curved surfaces," Phys. Rev. E **97** (2018), 10.1103/physreve.97.052605.

[166] J. Hu, A. Wysocki, R. G. Winkler, and G. Gompper, "Physical sensing of surface properties by microswimmers – directing bacterial motion via wall slip," Sci. Rep. **5** (2015), 10.1038/srep09586.

[167] R. N. Bearon and J. T. Pedley, "Modelling run-and-tumble chemotaxis in a shear flow," Bull. Math. Biol. **62**, 775–791 (2000).

[168] L. A. Pratt and R. Kolter, "Genetic analysis of escherichia coli biofilm formation: roles of flagella, motility, chemotaxis and type i pili," Mol. Microbiol. **30**, 285–293 (2002).

[169] J. W. Barton and R. M. Ford, "Determination of effective transport coefficients for bacterial migration in sand columns." Appl. Environ. Microb. **61**, 3329–3335 (1995), https://aem.asm.org/content/61/9/3329.full.pdf .

[170] K. Duffy, R. Ford, and P. Cummings, "Residence time calculation for chemotactic bacteria within porous media," Biophys. J. **73**, 2930 – 2936 (1997).

[171] J. Happel and H. Brenner, *Low Reynolds number hydrodynamics* (Springer Netherlands, 1981).

[172] H. Shum and E. A. Gaffney, "Hydrodynamic analysis of flagellated bacteria swimming near one and between two no-slip plane boundaries," Phys. Rev. E **91** (2015), 10.1103/PhysRevE.91.033012.

[173] N. A. Croll, "Components and patterns in the behaviour of the nematode caenorhabditis elegans," J. Zool. **176**, 159–176 (2009).

[174] G. J. Stephens, B. Johnson-Kerner, W. Bialek, and W. S. Ryu, "From modes to movement in the behavior of caenorhabditis elegans," PLoS ONE **5**, e13914 (2010).

[175] S. J. Helms, W. M. Rozemuller, A. C. Costa, L. Avery, G. J. Stephens, and T. S. Shimizu, "Modelling the ballistic-to-diffusive transition in nematode motility reveals variation in exploratory behaviour across species," J. R. Soc. Interface **16**, 20190174 (2019).

[176] J. T. Pierce-Shimomura, T. M. Morse, and S. R. Lockery, "The fundamental role of pirouettes in caenorhabditis elegans chemotaxis," J. Neurosci. **19**, 9557–9569 (1999).

[177] Y. Iino and K. Yoshida, "Parallel use of two behavioral mechanisms for chemotaxis in caenorhabditis elegans," J. Neurosci. **29**, 5370–5380 (2009).

[178] N. C. Darnton, L. Turner, S. Rojevsky, and H. C. Berg, "On torque and tumbling in swimming escherichia coli," J. Bacteriol. **189**, 1756–1764 (2007).

[179] B. M. Friedrich and F. Jülicher, "Chemotaxis of sperm cells," P. Natl. Acad. Sci. USA **104**, 13256–13261 (2007).

[180] A. E. X. Brown, E. I. Yemini, L. J. Grundy, T. Jucikas, and W. R. Schafer, "A dictionary of behavioral motifs reveals clusters of genes affecting caenorhabditis elegans locomotion," P. Natl. Acad. Sci. **110**, 791–796 (2013).